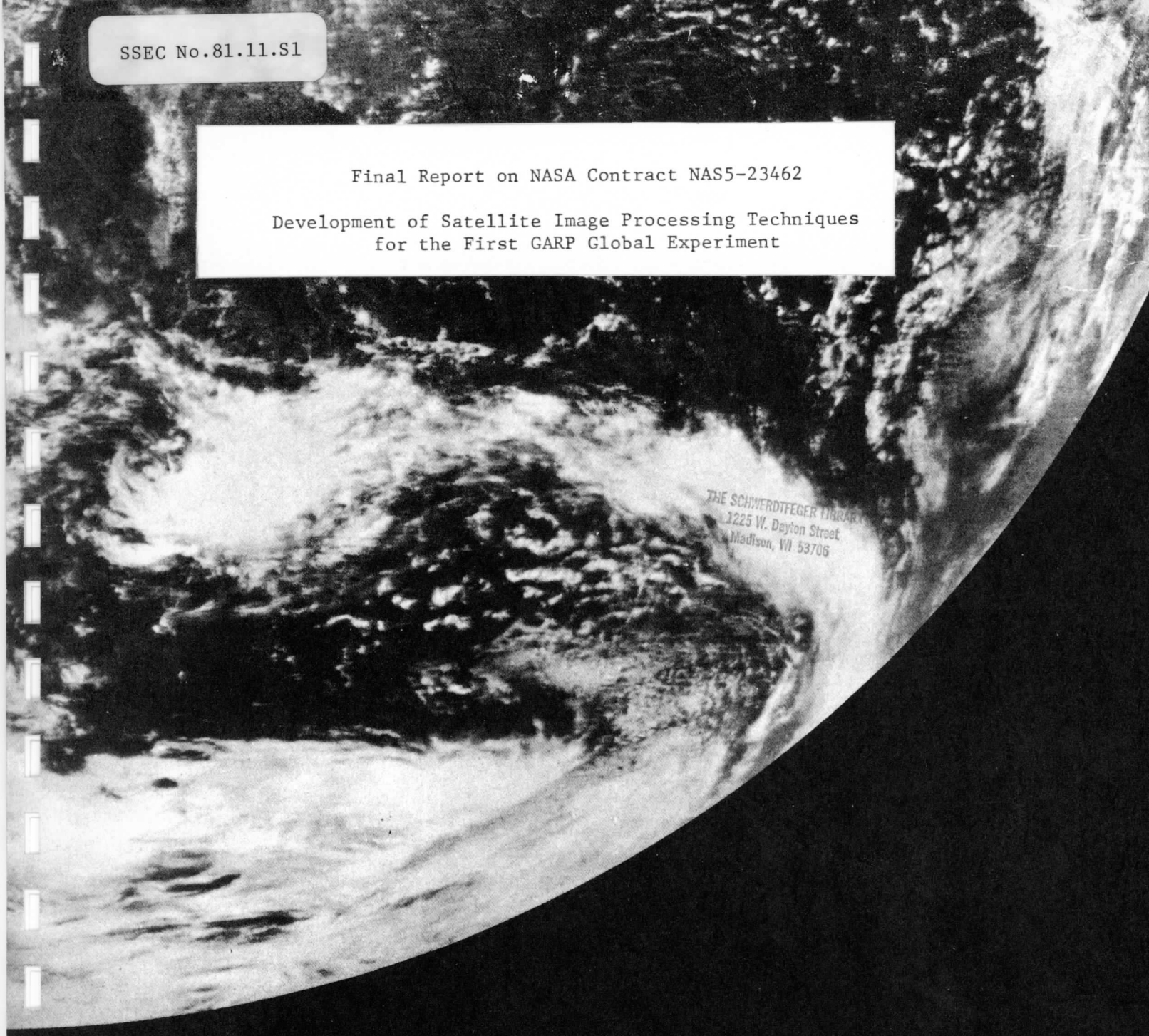

Final Report on NASA Contract NAS5-23462

Development of Satellite Image Processing Techniques for the First GARP Global Experiment

A REPORT

from the space science and engineering center
the university of wisconsin-madison
madison, wisconsin

Final Report on NASA Contract NAS5-23462

Development of Satellite Image Processing Techniques for the First GARP Global Experiment

Verner S. Suomi, Principal Investigator
Frederick R. Mosher
Donald P. Wylie
Jan-Hwa Chu
Sanjay S. Limaye
Anne Marie LeBlanc
Vincent D. Condella, Jr.

Space Science and Engineering Center
University of Wisconsin-Madison
1225 West Dayton Street
Madison, Wisconsin 53706

November 1981

Index

INTRODUCTION

FREDERICK R. MOSHER

This Project Report contains research done with full or partial support of the National Aeronautics and Space Administration's contract NAS5-23462. The ultimate objective of this effort was to develop the basis for the operational systems using GOES VISSR data to:

1) Estimate rainfall and latent heating using data from satellite images, and
2) Objectively measure cloud climatological parameters such as fractional cloud cover, cloud height, cloud type, cloud thickness and cloud top temperatures which are required to determine the effect of global cloudiness on radiation.

A considerable amount of work on this contract was devoted to the development of the scientific basis for determining rainfall and cloud parameters. The techniques developed with this contract have been picked by the operational community. The rainfall determination algorithms are being used by NOAA's Agristar program for rainfall determination over agricultural areas. The cloud climatology techniques are being incorporated into the International Satellite Cloud Climatology Program (ISCCP) which will make a five year cloud climatology starting January 1983.

The first effort on this contract was a feasibility study which established who are the potential users of cloud measurement and rainfall data, what are their requirements, what is currently available to meet these requirements, how adequate are the currently available techniques, and what developments would be required to meet the potential user requirements. The report on this feasibility study is contained in Section I of this report.

Section II describes the development of a rain estimation technique using geostationary data which can be applied to extratropical areas. Earlier rain estimation techniques such as Griffith et al. (1978) and Stout et al. (1979) were confined to the tropical regions. When these techniques were applied to mid-latitude storms, they failed because of the air mass differences between tropical and extratropical regions. In this section Wylie shows how a cumulus cloud model can be used to account for differing temperature and moisture profiles. This rain estimation technique is applicable to a wide variety of weather situations and geographical areas.

The ability to specify rain areas generally depends upon being able to identify growing cloud systems. The man-interactive approach to this identification problem has been quite successful. However, if these techniques for rain estimation are ever to be automated, cloud growth needs to be objectively identified. In satellite images, differences between successive images are caused by two factors: cloud growth or dissipation and cloud advection. Section III describes an attempt to identify cloud growth by remapping the satellite image according to the wind field to account for advection and then taking the differences between the successive images.

The cloud census portions of this contract require techniques to measure cloud height, thickness, cloud type, fractional cloud cover, and number of clouds. The bases for many of these techniques was developed in the cloud height determination by Mosher (1975). A cloud thickness program was developed as part of the cloud tracking effort, but it used light intensities derived from plane parallel light scattering theory as a data base. Recent Monte Carlo studies of average finite cloud brightness have shown that plane parallel theory can be significantly in error. It was hypothesized that while the average finite cloud brightness could cause problems in relating cloud

brightness to thickness, parts of the cloud away from the cloud edges would have light scattering closer to that of plane parallel theory. Since there was no light scattering model which could handle the brightness variation across a finite cloud without exhorbitant computer expense, a new light scattering model was developed. This new finite cloud model and the results using the model are described in Section IV.

Cloud typing depends upon the ability of a system to recognize cloud height, size and texture. Fourier analysis techniques are traditional means of analyzing size and texture variation in one dimensional phenomena, but little work on cloud images has been done because of the two-dimensional character of the data. Section V describes an attempt at performing a two dimensional fourier analysis of satellite images.

Clouds effect the global radiation budget. Clouds are the biggest factor in determining the incoming solar radiation. Section VI describes the development of an empirical relationship which relates visible and infrared digital data to incoming solar radiation.

Section VII describes a cloud census performed for a data set of eight days from GATE Phase III. This study used a point-by-point cloud classification threshold technique, determined three cloud types based on cloud top height, subdivided these cloud types into thick (convectively active) and thin clouds, and then produced cloud size and area distributions.

The study in Section VII produced cloud size and area distributions using two dimensional images. Processing data in two dimensions requires a considerable amount of computer memory and time. Section VIII mdescribes a study to produce one dimensional cloud size distributions by processing data long a line. This study also describes the use of a minimum brightness composite technique to determine the land brightness so that cloud cover

determination can be made over regions without a uniform background.

Measurements of clouds are interesting, but to be most useful meteorologically they must be related to the state of the atmosphere. The techniques in the numerical models which account for the cumulus convective effects require verification using real data. Studies of the correlations among the magnitude and spatial distribution of convective mass flux, large scale vertical motion, and convective cloud amount must be done before general circulation models can correctly describe the tropics. The GATE experiment was designed to provide data to determine these relationships. However, the radiosonde wind data of much of the GATE wa of poor quality. Since this is the only data set before FGGE which could be used for these diagnostic studies in conjunction with a satellite cloud census, an editing effort was undertaken. Section IX describes the editing effort and some of the preliminary results of the diagnostic studies. Section X then describes how this wind data was combined with thermodynamic fields and radiation divergence calculated from geostationary images of clouds. Heat and moisture budgets were computed in the environment of GATE convective systems.

REFERENCES

Griffith, C. E., W. L. Woodley, P. G. Grube, D. W. Martin, J. Stout and D. N. Sikdar, 1978. Rain estimation from geostationary satellite imagery--visible and infrared studies. Mon. Wea. Rev., 106, 1153-1171.

Mosher, Frederick R., 1975. SMS Cloud Heights. Final Report on Contract NAS5-23296, Mac-Computer Interactive Data Access System (McIDAS). SSEC, University of Wisconsin-Madison, pp. (3-1)-(3-29).

Stout, J., D. W. Martin and D. N. Sikdar, 1979. Estimating GATE rainfall from geostationary satellite images. Mon. Wea. Rev., 107, 585-598.

Survey of User Requirements and Available Data Sources for Rainfall Estimation and Cloud Climatologies

Frederick R. Mosher
Donald P. Wylie

Space Science and Engineering Center
University of Wisconsin-Madison
1225 West Dayton Street
Madison, Wisconsin 53706

April 1977

I. Introduction

The objective of the effort discussed in this report will be to develop systems using GOES VISSR data to:

1) Estimate convective rainfall and latent heating using data from satellite images
2) Measure cloud parameters objectively.

The effort has three projected phases. The first phase is a feasibility study. The second will be a technique development program, and the final phase will be demonstration and transfer of the techniques to appropriate users. This report will discuss the progress made on the first phase.

The efforts during this phase have been to determine:

1) Who are the potential users of cloud measurement and rainfall data and what are their requirements.
2) What is currently available to meet these requirements.
3) How adequate are the currently available techniques.
4) What developments would be required to meet the potential user requirements.

The discussion of these efforts will be separated into two sections, one on cloud census and the other on rainfall estimation.

II. Cloud Census

The following classes of potential users have been contacted.

1. General circulation modeling (GCM) and climate modeling groups
2. Tropical and GATE research groups
3. Pilot and aviation groups
4. Forecast groups

5. Cloud wind measurement groups

6. Mesoscale forecast research

The requirements of the different groups are quite different as are the currently available products. The different groups will be discussed separately as to requirements, currently available cloud products, adequacy of the currently available products for their needs, and developments which would be required to fully meet the needs of the group.

A. GCM and climate modeling groups

For time scales of greater than 2-4 days, radiation becomes one of the main forcing functions of the atmosphere's circulation. Of the many factors which influence the radiation budget of an area, the factor which is the largest and most variable is cloudiness. Clouds can be considered to be "the shutters of earth." Data from meteorological satellites show clouds to be organized by the large scale flow. Hence there is a strong internal feedback mechanism between radiation, the circulation of the atmosphere, and clouds. If the circulation of the atmosphere is to be modeled for periods longer than 2-4 days, the linkages between large-scale atmospheric variables, cloudiness, and radiation must be firmly established. Of these linkages, the relationship between cloudiness and atmospheric variables is the weakest.

1. Requirements

The requirements for cloud information vary with the different types of climate models. The simplest climate models are the vertically and zonally averaged atmospheric models which address the mean radiative equilibrium heat balance of the earth such as those of Budyko (1969), Sellers (1973), and Bryson and Dittberner (1976). In these models the cloudiness is set at a mean effective fractional cloud cover and maintained as a constant with the assumption being that cloud cover variations are negligible

on the hemispheric scale over the past century. All these simple models are looking for external changes which affect the atmospheric climate. However, even in these simple climate models, sensitivity analysis shows cloudiness to be a major factor. In the Bryson and Dittberner model (1976) the effective fractional cloud cover was assigned to be .40. Sensitivity analysis showed a 1% variation in that value caused a .5°K change in the Northern Hemispheric mean surface temperature. The observed change over the period 1880-1945 was .6°K.

Even in the more complex climate models, the treatment of cloudiness is still rather crude. In the Geophysical Fluid Dynamic Laboratory (GFDL) general circulation model (GCM) the clouds for radiational purposes are specified from annual mean observed distributions of clouds which varies with latitude and height, but not longitude or time (Manabe et al., 1974). In the NCAR model (Kasahara and Washington, 1971) and the GISS model (Somerville et al., 1974) the clouds are determined by dynamical processes. While the monthly mean cloudiness does resemble the observed mean cloudiness, the instantaneous cloud fields have little relationship to observed clouds.

Studies of the sensitivity of the global climate to changes in cloudiness have shown the climate to be very sensitive to cloud variations. Schneider (1972) has shown that an increase in the cloud amount will decrease the global average surface temperature,while an increase in the effective cloud top height will increase the surface temperature. An increase of the effective cloud height from the present 5.5 km to 6.1 km could raise the surface temperature by 2°K. An increase in fractional cloud cover per se from 50% to 58% should decrease the surface temperature by 2°K.

Observed cloudiness is required by all climate models either as an input parameter for the simpler models or as a verification tool by the more

complex models. The need to obtain cloud observations has been reflected in the GARP requirements (GARP Special Report No. 14). Because of the sensitivity of the climate to cloudiness, the GARP program has specified the desired measurement of cloudiness with the following specifications:

space resolution	100 km
time resolution	1 day
period of measurement	FGGE
desired accuracy	1 km vertical 1° cloud top temperature 5% amount
observing technique	subjective analysis of RAOB and satellite imagery

This data would be used in several ways. The simpler models require an "effective" fractional cloud cover of opaque clouds. Present estimates range from 40% (Bryson and Dittberner, 1976) to 50% (Budyko, 1969). Existing GCM models which input climatical clouds for radiation calculation such as the GFDL model require average cloud distributions as a function of position and height. Other GCM models such as the NCAR, UCLA, and GISS models require observations to verify the existing cloud parameterization routines. The development of the next generation of cloud parameterization techniques will also require detailed cloud data.

2. Existing Observations

There are two types of cloudiness observations. One is average cloud cover over a period and the other is detailed cloud measurements. The average cloud cover is useful for inputs to simpler models and for qualitative verification of more complex models. The detailed cloud measurements are required for cloud parameterization studies. The cloud climatology studies available and their sufficiency will be discussed first, followed by existing systems of detailed cloud measurements.

a. Cloud Climatologies

The first, and in many cases still the standard cloud climatology, was Telegadas and London (1954). This study was done before the age of the satellite and is limited to mainly land based observations. However it contains information on average cloud types and the heights of these cloud types as a function of latitude in addition to observations of total cloud cover. Satellite data from the early TIROS, ESSA, and NOAA satellites have been used by Miller and Feddes (1971), Sadler and Harris (1970), Schutz and Gates (1971), Van Loon (1972), Clapp (1964), and others to produce climatologies of total cloud cover based on analysis of fractional cloud cover of grids on visual satellite images. These satellite climatologies contained no information on the vertical distribution of clouds or information on cloud types. These fractional cloud cover climatologies are presently being used by modelers as a qualitative verification because they are the only data available.

However the present cloud climatologies do not provide enough information. As stated by Arakawa (1975):

> "Obviously any cloud modelling must be verified and tuned. It is therefore necessary to establish a global climatology of the geographical and seasonal distribution of the clouds, in which the high, middle, and low clouds are treated separately, and if possible, by cloud type. The climatology of total cloudiness, which is all that is presently available, is of very little help in modeling clouds and cloud processes."

b. Current Cloud Measurement Programs

One of the currently operational cloud measurement systems which potentially could be used for cloud parameterization is the Air Force three dimensional Nephanalysis (3DNEPH) model (Coburn, 1971). This system

produces an objective three-dimensional cloud field analysis with a horizontal grid spacing of approximately 25 nautical miles and 15 vertical layers with the highest vertical resolution at the earth's surface. The 3DNEPH uses as its inputs all the available data which could be related to cloud fields: surface observations, radiosonde soundings, aircraft reports, and meteorological satellites. The 3DNEPH has a modular data processing design based on decision tree type logic. It handles a very large volume of input data and generates global analyses of cloud type, weather, maximum tops, minimum bases, total cloud cover and percent cloud amounts at 15 levels. This data is used for Air Force requirements which will be described later in this report in the section on aviation requirements. The 3DNEPH is produced every three hours. The area of coverage is determined by military priorities and availability of computer resources, but is generally limited to the northern hemisphere. The 3DNEPH has been archived since 1 March 1974 at Asheville. Approximately 120 tapes of 3DNEPH data are produced each month.

While the 3DNEPH potentially could be used for cloud parameterization research, in actuality it has received very little use outside the Air Force. There have been only three serious inquiries at Asheville on the 3DNEPH which have obtained sample tapes. These inquiries were from GFDL, NCAR, and NASA's climate program. None of them however have made any extensive orders of data.

There are several problems with the 3DNEPH which limit its usefulness for cloud parameterization studies. One, the data sources are not specified on the resultant data tapes. All available data are used in the 3DNEPH including radiosonde data which has inferred cloud cover by a temperature-humidity-cloud parameterization technique. Cloud parameterization studies

which try to relate relative humidity data to clouds require an independent measure of clouds. Because the sources of the cloud information are not recorded, the 3DNEPH analysis could be contaminated with radiosonde data in the regions where they are available making independent comparisons of clouds and relative humidity impossible. Another problem is the lack of published verification of the 3DNEPH. It is difficult for an outside scientist to verify the 3DNEPH since it uses all sources of currently available cloud data. The verification is very important because much of the basis of the 3DNEPH satellite processing is empirical relations. The techniques for deriving fractional cloud cover, cloud height, and cloud thickness from the satellite data potentially could not be accurate enough for scientific purposes and would require extensive verification. The cloud amount is determined with a clear/overcast assumption for each picture sample. Shenk and Salomonson (1972) have shown that this type of procedure can lead to serious errors if the cloud area is less than 100 times the field of view of the sensor. Hence the 3DNEPH potential could have cloud amount errors in regions of broken and small clouds. The cloud height determination is made using a black body assumption which would cause erroneous measurements of cirrus heights because of emissivity problems. Cloud thickness is determined by the variance of the IR data around the level of the cloud height. This method requires a broken cloud field to work at all and completely ignores the variations in cloud temperature due to emissivity variations and small clouds filling only part of the field of view of the infrared sensor.

The other currently available cloud measurement product which might be used for cloud parameterization studies is the retrievals of the atmospheric sounders. In the sounding retrieval processing, cloud height and cloud amount are byproducts (Smith and Woolf, 1976). The assumption has been made that

the clouds are at the same height in the processing area. This area is approximately 120 x 280 km. The sounding retrievals for the Data Systems Test (DST) periods are available using these techniques. NCAR is presently starting the evaluation of the usefulness of this cloud amount and cloud height information for cloud parameterization studies.

B. Tropical and GATE Research Groups

The GATE researchers are concentrating on the interactions between cumulus convection and the synoptic scale flow field. These research programs are tied closely to the needs of the general circulation models for better cumulus cloud parameterization techniques. For these studies detailed analyses of convective activity are required. All measurements of the vertical transports of heat, moisture, and momentum that are being made from GATE data must be related to the cumulus convective activity since convection can cause large changes in these transports.

The GATE workshop (Charlottesville meeting, January, 1977) has specified a strong need for a uniform description of the state of the convection. At the present time the convective state is being described independently by individual researchers. The data sources used for describing the state of the convection are satellite images, radar, photographic pictures from ships, and radiosonde profiles. Radar, radiosonde, and ship sky cover pictures are limited in the area that they can cover. The satellite coverage is not limited and can be extremely valuable for studying the relationship between convection and synoptic scale motions. Most GATE researchers do not have access to digital satellite data and therefore can not make quantitative measurements. Hence a cloud measurement analysis for the GATE periods of interest would greatly help the GATE research programs.

For GATE studies analyses of the state of convection in the entire GATE

area are needed. The important parameters are the stage of the convection (growth or decay), the depth of penetration, and the amount of area covered by convective cells. In most cases these quantities can be measured from the satellite data. Some problems will exist in areas of deep convection because of cirrus anvils covering the lower cloud fields. Similarly, inactive cloud layers will have to be distinguished from convectively active cells. It is desirable that these statistics be made for grid scales no larger than 30 km. Such resolution will provide information on a scale small enough to be useful to boundary layer and point location studies. This grid resolution is comparable to that provided by other observing systems. These detailed analyses need not be made for a long time period. Most research is being concentrated on phase 3 data with a few other studies being made on the latter part of phase 2. This period consists of only 35 to 40 days in total.

If the effects of convection can be understood in relation to the satellite measurements, then the satellite data can be used to determine the total area affected by convection and thus the total effect of the convection on the large-scale motion field. Empirical descriptors of this type of relationship have already been made with satellite and rainfall data. Using the detailed studies of GATE it may be possible to correlate satellite cloud measurements with latent heat release. The manner in which latent heat is released in the atmosphere, and the amount of vertical mixing, also may be correlated with the satellite measurements. Such relationships between satellite measurements and atmospheric processes could be used for studying large areas over long time periods to collect the large data sets needed for developing parameterzation schemes for global numerical models.

C. Pilot and Aviation Groups

Clouds influence flight operations. The groups which are most affected by clouds are small aircraft pilots, military operations, and overseas commercial flights.

1. Small aircraft flight forecasts

Many small aircraft pilots are restricted to flight patterns where visibility is not obscured by clouds. These visual flight rules (VFR) severely impact the majority of private pilots without instrument ratings. (The VFR pilots are required to fly below clouds unless the cloud field is scattered so that ascent and descent can be made between clouds.) Flight forecasts including cloud cover information are prepared by NOAA and distributed by the FAA.

The information for the cloud description in the flight forecast briefing comes from two main sources, the surface weather depiction facsimile chart and the experimental satellite cloud analysis chart. The surface weather depiction chart is based on surface observations of clouds report. The experimental satellite cloud analysis is produced by NESS from the hard copy satellite image. A NESS analyst outlines the major cloud features, annotates them as to cloud type, cover, growth patterns and measures the height using the infrared temperature from the MMIPS (Cooley, 1976). The experimental satellite cloud analysis chart is currently made once per day. This analysis is useful for cloud top flight requirements and compliments the surface weather depiction which views the clouds from the bottom. Flight Service forecasters are finding the satellite analysis product useful (Bittner, 1977, private communication).

2. Military Operations

The military requires cloud information for several types of missions.

Cloud information is required for the programming of reconnaissance satellites. Missile target selection decisions require cloud information. Flight operations which require visibility such as mid-air refueling also require cloud information. Cloud data are by the military in flight path fuel optimization to infer winds over data sparse regions.

To meet these needs, the Air Force has developed the 3DNEPH described previously, and a cloud forecast model which uses the 3DNEPH as input data. The 3DNEPH uses all available cloud data for inputs and is continually being expanded as new data sources become available. The area of coverage is limited to those areas with military reconnaissance, target selection, or flight requirements which are generally in the northern hemisphere.

D. Forecast Groups

An objective cloud analysis was produced by NOAA, NESS on an experimental basis (DeCotiis and Conlan, 1971) from NOAA-1 polar orbiter data. There was not much demand for this type of analysis in the NMC operations so the cloud analysis never became an operational product. The techniques were transferred to the Air Force and became part of the 3DNEPH.

With the advent of improved satellite capabilities, interest within NOAA for cloud analysis has revived. The experimental cloud analysis for aviation briefings is one example. Another is the subjective moisture analysis of the eastern N. Pacific (170°E - West Coast) and the Gulf of Mexico. This moisture analysis is done with VTPR channel 7 water vapor sensor and the satellite imagery. From the cloud patterns, ten different moisture profiles are inferred. This information is operationally entered into the LFM as bogus ship reports.

Another product which requires cloud information is fog dissipation forecasting. One of the key parameters of fog dissipation forecasting

is the depth of the fog layer. Also the knowledge of the presence of clouds above the fog layer is required to compute the amount of solar radiation available to burn off the fog. NMC is presently using the experimental satellite cloud analysis for this fog forecasting, though it is not aimed specifically toward fog forecasting.

Still another forecast problem which requires cloud information is convection forecasting. For most mid-latitude precipitation to occur, the tops must be below freezing to provide the ice nuclei to start the precipitation process. Vincent Oliver of NESS has been experimenting with radical enhancement techniques which outline critical temperature areas on SMS/GOES infrared images. This technique also has been applied to severe convection to outline very deep cells. This technique has been developed to be applied to the image sectors going to the forecast offices. NESS is also investigating the development of a cloud top height analysis which would be comparable to radar top information.

The forecast problems which require cloud data boil down to requiring quantitative information on cloud height, cloud thickness, cloud type, or cloud temperature. This information is available in the experimental satellite cloud analysis which is transmitted to forecast offices on the facsimile circuit. Like all facsimile products the forecaster does not get the analysis until several hours after the observation time. The experimental satellite cloud analysis and the surface weather depiction appear to satisfy those operational requirements which are met via the facsimile circuit. However, there is a need for quantitative cloud measurements with a short lead time. Fog forecasting and severe storm forecasting are examples of this need. The forecaster needs to view a sequence of satellite images, select the interesting areas, ask for quantitative measurements of cloud parameters, and receive

immediate answers. This capability is currently available on the McIDAS at Wisconsin and potentially on the MMIPS at NESS. When the AFOS becomes operational, the data base required for this type of cloud analysis will be available at the forecast offices along with the sections of the satellite images. Some additional hardware and software development is required, however, to provide the forecaster with real time quantitative cloud information.

E. Mesoscale Forecasting Research

Mesoscale forecasting research is centered in two main areas. One is to develop quanlitative tools to aid the forecaster making a short-range forecast. The other is to develop quantitative tools to make measurements which can be used to initialize mesoscale models. Satellite data impact mesoscale research because the space-time resolution of the satellites observations is closer to that required to describe the weather phenomena that are most other types of weather data. Research on development of qualitative, quasi-quantitative techniques have shown that data from images of cloud fields can be used to locate the areas of initial convergence which trigger severe storms (Purdom, 1976), fine tune the local mesoscale forecast (Scotfield, 1976), and measure the severity of the instability by measuring the growth rate of the anvil (Sikdar et al., 1970). However these techniques have not made their full impact on the operation forecasts because of the present problems of transmission, display, and inability to make simple measurements from the satellite images at the forecast offices. As these problems are overcome, the impact of geostationary satellite data on qualitative mesoscale forecasts should increase in the near future.

Research on quantitative measurements of satellite images for mesoscale model initialization is progressing, but at a slower rate than the

qualitative research, Houghton and Wilson (1976) have demonstrated the ability to measure mesoscale wind fields, measure convergence and infer realistic vertical motion fields. Kreitzberg (1976) has developed a mesoscale model which uses cloud images to aid in the model initialization and has stated that an operational mesoscale forecast system using satellite inputs could become operational within 5 years. Development of geostationary sounders will influence the development of the ultimate operational mesoscale forecast system.

One initialization mesoscale model parameter which could be measured directly from the cloud fields is the vertical motion field. The growth and decay of clouds is caused by vertical motions. By measuring the changes in the cloud field and using a knowledge of the wind field advecting the clouds (which also could be measured from the cloud field), a vertical motion field could be determined. However, research on this type of cloud analysis has not yet been started.

F. Cloud Wind Measurements

Aside from techniques to measure cloud displacements for wind purposes, cloud analysis techniques are required to measure the height and thickness of the cloud being tracked. The nature of cloud tracking requires that the height and thickness be measured for each cloud tracer. The thickness is required in addition to the height because studies such as Hasler et al. (1976) have shown that some clouds, such as cumulus, move with the speed of the wind at their base.

Measurements of cloud heights from cloud top temperature is made difficult by varying cloud emissivity. During night time hours, only the infrared images are available. Because many of the cirrus tracers are near cloud edges or cloud fragments, the cloud emissivity becomes a crucial factor

in the height measurement. If there were two infrared channels, the emissivity could be computed using the techniques developed for sounder retrievals (Smith and Woolf, 1976), but on the current generation of geostationary satellites only one channel is available. Hence the only technique which is presently available for determining the temperature of a thin cloud element is to make a subjective judgment of what constitutes a cloud field ensemble where all the clouds are approximately at the same level, measure a temperature near the coldest center of the ensemble where the emissivity should be closest to unity, and assign that temperature/height to all the clouds tracked in that ensemble. This method was developed by Les Hubert of NESS and has been used in a similar manner at the University of Wisconsin for infrared-only tracking.

When visible data are available, this can provide information on cloud thickness which can be used to infer the infrared emissivity. The cloud height system developed at Wisconsin by Mosher (1974) uses the visible data to help correct the infrared data for non-unity emissivity problems. An evaluation of this technique was undertaken. The data set of Joanne Simpson of aircraft 3-D measurements of clouds in the GATE area was used for ground truth. The results of this evaluation are:

1. The cloud height system readily can identify the clouds which are blackbody and make corresponding height measurements. The heights of the deep convecting cells agreed to within the error limits of the 3-D measurements. The 3-D measurements of the lower cumulus were of the height of the highest towers while the satellite measurements were of the average height of the cloud. Because of the differences in the thing measured, the height measurements of low cumuli made from satellite data were

lower than 3-D measurements. The thickness plot of the satellite data showed a strong resemblance to the major features of the aircraft photographs. The thickness of the small cumuli was underestimated by about 20% as the theory of finite cloud scattering would suggest (McKee and Cox, 1974).

2. If the assumptions of the cloud model used in the scattering calculations (single layer, horizontally homogeneous) were fulfilled, the emissivity correction worked and raised the cirrus cloud height to within the measurement error of the 3-D measurements.
3. If there were multiple layer cloud fields with the upper layer being a broken thin layer such as altocumulus or cirrus over lower thicker clouds such as cumulus, then the cloud height system gave erratic results in the measurement of both cloud layers.
4. The original cloud height system has emissivities calculated assuming ice spheres. To obtain more accurate emissivities, the visible calibration was modified slightly using empirical data. Using the emissivity calculations of Liou (1974) with ice cylinders rather than spheres has resulted in much more realistic emissivity measurements without any empirical modifications of the visible calibration.
5. The verification data base using the one GATE data set was not considered an adequate statistical verification. A data base of aircraft reports of cloud tops and cloud bases and airport observations of cloud bases appears to be the most extensive data base possible for a large variety of cloud situations.

Programming of a system which will extract this information from a high speed data line, file it, display the conventional reports on top of the satellite image, and file comparisons with satellite measurements has almost been completed.

G. Summary and Recommendations

1. Climate Modeling Community

The needs of the various user groups is quite varied. The climate modeling community has the most pressing needs and also the most stringent accuracy requirements. These modeling requirements are reflected in stated GARP requirements. The modeling community requires detailed cloud measurements to assist in development of more refined cloud parameterization techniques. In addition, cloud climatologies are required to verify the performance of models. Presently available cloud measurement products are not sufficiently accurate to meet the parameterization needs. The presently available climatologies of total cloud cover without height discrimination are not sufficient to meet the verification of the modeling community.

The detailed cloud measurement effort should be carried out in a coordinated manner with an effort on cloud parameterization. The cloud measurements will generate a large volume of data. Only those data which actually are required by the modeling group should be processed. The cloud climatology could be produced by averaging a long period of detailed measurements, but this is a very costly approach. A more cost effective approach would be a simple system which segregates the image data into levels and cloud types and performs running averages. At the end of an average period (1 month or 1 year) the detailed measurements would be obtained from the averaged data.

2. GATE Research Community

The detailed cloud measurement requirements of the GATE community are very similar to the requirements of the cloud parameterization effort. The area coverage requirement is modest and the time period requirement is for only a few weeks of data. Hence, if the cloud parameterization groups could use the GATE area to perform some detailed cloud measurements, the spin off of the effort would provide the GATE research community with a very useful data set for convective adjustment research.

3. Aviation Community

The needs of the aviation community for cloud information have been recognized and both the Air Force and NOAA have acted upon these needs. The Air Force produces the 3-Dimensional Nephananlysis (3DNEPH) every three hours to meet their cloud information needs. NOAA produces weather depiction fax charts based on surface observations of clouds and has initiated an experimental satellite cloud analysis fax chart. The initial reaction to the NOAA/NESS satellite cloud analysis has been favorable.

The Air Force has maintained a continuing developmental attitude toward the 3DNEPH, so any technique developments in cloud measurements could ultimately be incorporated into the 3DNEPH. The NOAA/NESS satellite cloud analysis is a useful and cost effective approach for the present needs of NESS and NWS. It should be expanded to include more periods during the day.

4. Forecast Community

The most pressing forecast needs for cloud information is for short time mesoscale forecasts of fog and convective storms. The analysis techniques of determining cloud heights, thickness, growth rates, etc. are presently at hand. However, a new generation of hardware is necessary

to provide the forecast offices with real time access to the quantitative satellite data.

5. Mesoscale Forecast Research

Real time access to satellite images and the ability to make simple measurements from these images is required for qualitative forecasting. Quantitative forecasting, however, requires input data for models. Techniques to determine the mesoscale distribution of water need to be developed. Extension of current efforts at producing bogus moisture sounding data from cloud images and moisture sensors needs to be done, probably by using VAS data. Techniques to measure the mesoscale wind fields need further development. Tracking clouds can produce horizontal wind fields. Measurements of the growth and dissipation of clouds could provide vertical wind measurements, but the techniques have not yet been developed.

6. Cloud Tracked Wind Groups

The weakest part of present cloud tracking technology is the height determination. When only infrared data is available, subjective judgment is required to assign heights to individual clouds in a field because of emissivity ambiguities. The most reasonable solution to this problem would be to include a second window channel infrared sensor with a different frequency response on the geostationary satellite, and use the techniques developed by the sounding groups to get cloud altitude.

Techniques to obtain cloud heights and cloud thickness using existing visible and infrared sensors show promise and efforts should be made to continue their development and verification. The measurement of cloud thickness using visible images appears promising and could aid in the problem of height assignment for clouds which move with the wind at their base.

III. Precipitation Estimation

The following classes of potential users of precipitation data have been contacted:

1. GCM and climate modeling groups.
2. Agricultural crop prediction groups.
3. River water management and flood forecasting.

Each of these general areas requires routine precipitation measurements on a global basis or in remote areas that are not sampled adequately with rain gauges. A satellite rain estimation system could benefit both researchers and operational forecasters in each of the three groups. In this section the needs of each group will be discussed. The presently available methods of rainfall estimation that could be used for a global precipitation monitoring system will then be discussed.

A. User Requirements

1) Numerical Modelers

Rainfall is an important result of convective cloud circulations since it represents the amount of latent heat released to the atmosphere. The vertical circulations in the clouds cause the latent heating, and also redistribute mass, energy, and momentum between vertical layers. Thus, the measurement of rainfall represents two quantities that are important to the modelers: 1) the amount of heating that has occurred, and 2) the intensity of the vertical mass exchanges. The latent heating is a directly quantifiable measurement, while the vertical mass circulations must be inferred from rainfall measurements.

There have been many models developed to describe cloud circulation. The most notable are Arakawa and Schubert (1974) and Kreitzberg (1976). These models all attempt to describe the vertical mass circulations inside and

outside the clouds. The heating/cooling and moistening/drying are calculated from budget equations using the mass circulations. These models are used as sub-grid parameterizations in the CGM's to account for convective circulations.

The vertical mass circulations of convective cloud systems are difficult to measure. Programs such as GATE have been required to obtain these measurements. However, it is not possible to make GATE type measurements on a global scale. Therefore, other data sources are needed to verify model operation. Satellite rainfall estimates can provide this type of information.

The rainfall estimates would be used along with the cloud census data for model parameterization studies. Thus, the same basic format as stated in the cloud census section of this report is needed. A climatology of rainfall over both land and ocean is needed for general verification. In addition, detailed measurements of precipitation with high space and time resolution are required for regional studies associated with model development. The present observing networks cannot satisfy these needs. Raingauge networks are very sparse in many areas. Tropical areas and oceanic areas have little or no coverage. Climatologies based on these data are very poor because of the sampling problems. A satellite based observing system is definitely required.

2) The agricultural community

The need for grain crop forecasting has increased strongly in recent years. Currently crop forecasts are made by the Center for Climatic and Environmental Assessment (Division of NOAA, Columbia, MO), and several private consulting firms. These groups are all involved in forecasts of world crop yields for prediction of the international grain market. Both government and private

corporations are using this information for trading purposes and government policy decisions.

Rainfall is an essential input to all models or forecast schemes. Data are needed in the underdeveloped countries of South America, Africa, and Asia because of the lack of good meteorological networks in most of those countries. In addition, data are needed from the Soviet Union and China. Satellite measurements have been made experimentally in those areas (Follansbee, 1976) with reasonably successful results. In addition, satellite data are being used over North America to account for deficiencies of the present raingauge networks (E. Merrit, Earthsat Corp., 1976). Raingauge networks often are considered inadequate for sampling of isolated convective storms. A remote system from satellites could be very useful in providing good spacial measurements to augment raingauge networks. The problem of rain gauge sampling will be discussed more extensively in the next section.

In crop prediction, the rainfall measurements are used to derive available soil moisture for plant use. Soil moisture is usually calculated from hydrological budgets using rainfall, evaporation, and stream runoff. Crop models are run continuously during the year, even in the non-growing seasons, so that soil moisture levels are known adequately. Both winter and summer precipitation measurements are needed. Satellite measurements of radiation could be used to advantage because of the effect of radiation on evaporation.

Even without using crop growing models, some forecast information has been derived from satellites by looking for the existence of precipitation at selected critical times in the growing season. For example, the grain crop on the Indian sub-continent critically depends on the arrival of the

monsoon rains. This feature can be easily identified on satellite pictures.

The sampling time and space scales required for crop forecasting are slightly different from those required by the numerical modelers. High spatial resolution is desired while high time resolution is not. A spatial resolution of 50 x 50 miles is needed over the United States because this is the common grid resolution used in crop prediction models (Earthsat Corp. Report, 1976). Total rainfall volumes for each day will satisfy their requirements.

3) The Hydrological Community

Hydrologists require information on a short time scale for flash flood prediction, and a longer time scale for water resource management. These two requirements are quite different.

Flood forecasts require rapid dissemination of rainfall data (1-2 hours), mostly for small river basins. The accuracy of the measurements is not as important as the simple identification of heavy rainfall rates in the river basin. Raingauge networks are often not installed in sufficient density to locate storms. The use of radar for quantitative precipitation measurements is just beginning. The radar data has to be digitized and calibrated. Use of radar precipitation data will undoubtedly increase as NOAA converts its radar stations to digital formats for AFOS.

Flash floods occur when a large volume of rain falls on a limited area. The system causing the flooding can be either a single thunderstorm complex such as the Big Thompson and Rapid City floods or a large storm system such as Hurricane Agnes. Frequently the intense thunderstorm flooding occurs in mountainous regions. This limits the ability of radar to observe the rain producing regions of the storm, making precipitation measurements for flood

forecasting difficult. The monitoring of large storm systems such as hurricanes requires the use of several radar installations at different locations. In the regions of overlap the curvature of the earth prevents radar observations of the lower portions of the clouds. During Hurricane Agnes in central Pennsylvania a significant amount of rainfall was produced in the lower portions of the cloud, and was missed by the radar (National Advisory Committee on the Agnes Floods, 1972). Hurricanes also present radar range limitation problems when the storm is first approaching landfall. Because of these limitiations of radar precipitation measurements, the National Hurricane Center is developing satellite techniques for measuring rainfall and predicting the storm's flood potential.

The other hydrological interest is in the area of water management. These groups require longer time period measurements and accuracies of the measurements become more important. Rainfall measurements are used for hydrological budget studies for water resource planning and for river flood prediction. The river flood potential in river basins depends on the ability of the basin to absorb water. Knowledge of previous precipitation and soil water content is extremely important in river flood prediction.

A large effort has been made by NOAA to measure the winter snow accumulations in watersheds. The satellite pictorial techniques are most successful in mountainous regions where the altitude of snow cover or area of snow cover depict the available water. In areas of lesser orographic relief, these measurements become more difficult because snow depth cannot be sampled from pictorial data. Winter precipitation measurements can provide information for the prediction of the available river water at spring runoff.

B. Presently Available Techniques for Precipitation Measurement

1) Rainfall Estimation Using Satellite Images

Satellite rainfall measurements have been made by several institutions.

The geostationary satellite data have been used by the University of Wisconsin, the National Hurricane and Experimental Meteorology Laboratory (NHEML) of NOAA, Colorado State University, NOAA/NESS and NASA/Goddard. Polar orbiting satellite imagery data have been used by NOAA/NESS, the University of Bristol (England), and the University of Hawaii. The techniques are comprised of two general types: 1) those using the expansion of the cirrus anvil, and 2) those using cloud area correlations.

The needs for rainfall data and the availability of the particular type of satellite data have, in the past, dictated the method used by each institution. These methods will be summarized below. A discussion on how each method could be expanded to a globally operational system to satisfy the general needs previously stated will be given with the method descriptions. The utility of ground based measurement systems will be discussed.

a) Cirrus anvil expansion method (Geostationary Satellites)

Data from geostationary satellites have made it possible to monitor the cirrus anvil growth over deep convective clouds (Sikdar and Suomi, 1971). Correlations of rain volumes from convective clouds with the anvil growth rate have been made at Wisconsin (Sikdar, 1972), NHEML (Griffith and Woodley, 1976), and at Colorado State (Negri, et al., 1976).

The most extensive research on the relationship between anvil growth and precipitation has been made jointly by Wisconsin and NHEML. This research has been primarily on convective clouds over south Florida and over the tropical Atlantic Ocean (GATE area). An empirical relationship between the rain volume from the storm and the cirrus anvil growth has been developed (see Figure 1). This relationship incorporates the stage in the cloud's lifecycle as well as the anvil growth rate.

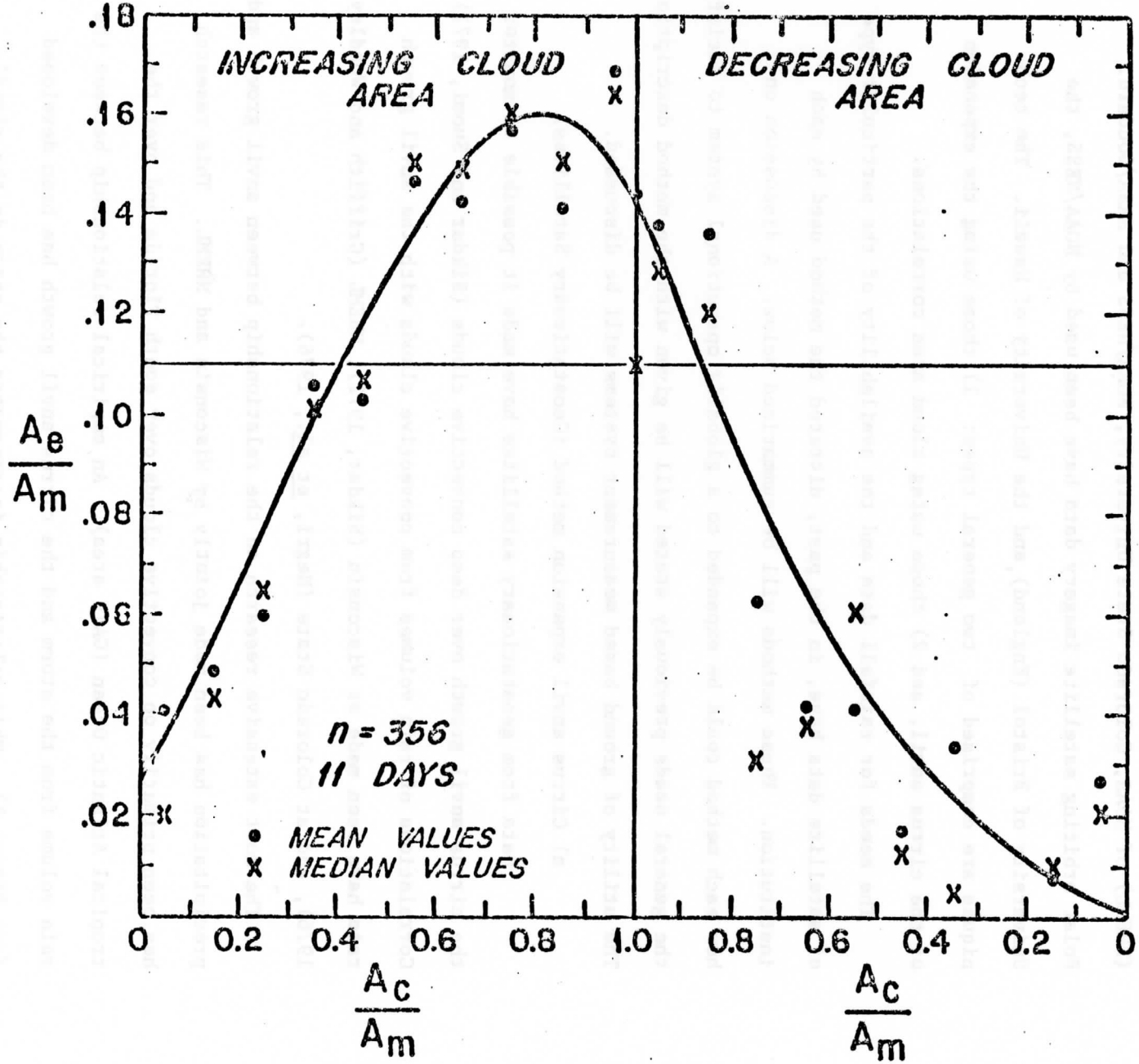

Figure 1: Cloud area on satellite pictures (A_c), maximum cloud area (A_m), and radar echo area (A_e) for tropical convective clouds. The rain volume is directly related to the echo area. From Griffiths et al., 1977.

A similar method also is used by NOAA/NESS for precipitation measurements over the United States and other land areas (R. Scofield, NESS). This method is intended for use by field forecasters who do not have digital data. Hard copy pictures are used, and rainfall rates determined by visual inspection of the pictures. This system employs in a subjective manner the same basic concepts as used by Wisconsin and NHEML.

The anvil expansion technique is based on identifying convectively active clouds. Clouds with tops colder than a threshhold temperature of -20°C for NHEML or -32°C for NESS, and that exhibit rapidly expanding anvils, are identified as rain clouds. The NESS technique separates areas of convectively inactive anvil from the active convective cores for deriving the horizontal details of the precipitation under the anvil. This technique can be applied to very small areas.

Comparisons with ground based measurements have shown that the satellite measurements can be accurate to a factor of 1.5 of the ground truth (Griffith et al., 1976, D. Martin personal communication). (Accuracies are usually expressed as the ratio of satellite over ground truth or vice versa, depending on which value is larger.) Researchers suspect that some inaccuracy occurs because low level rain clouds are not included. In the tropics substantial amounts of rainfall can come from clouds that do not reach the freezing level. The effect of these clouds is being studied currently.

Mid-latitude verifications of the Wisconsin-NHEML system have not been made yet. It is suspected that this relationship is accurate only for tropical convection. The extension of the Wisconsin-NHEML system to other geographic areas will require testing of the nomogram of Figure 1 and possibly new curves for geographic differences.

NHEML has developed an automated objective analysis scheme for applying the expanding anvil technique. This is the only existing automated satellite rainfall measurement system. It has been applied with reasonable success to a variety of situations, hurricanes, Florida cumulus clouds, and GATE area convective systems. Their best success has been with Florida cumulus clouds where the clouds appear as separate well defined objects on the satellite pictures. Reasonable results have been obtained with hurricane measurements, though the ground data used for comparisons are sparse and seldom considered reliable.

To apply the automated technique to GATE data the resolution of the satellite pictures has to be reduced to make computing over the larger area feasible. The data are reduced to statistics on a resolution size of approximately 40 x 40 km ($1/3^{o}$ squares). This implies that cloud clusters are being tracked by the program and not individual Cb's. It is not clear at this time what the impact of this scale change will be on the measurements. Verification of the measurements with ground truth data currently is being attempted, and a final assessment is not available.

It is concluded, from the research done at Wisconsin and NHEML, that it would be possible to obtain rainfall measurements at a time resolution of 1 hour. These measurements can satisfy FGGE and numerical modeling requirements. For global measurements, however, the technique will have to be expanded to higher latitudes. Only a small amount of work has been done on mid-latitude cyclone situations by NESS, Stanford Research Institute (Davis and Wiegman, 1973), and Colorado (Negri et al., 1976). These studies have indicated that the large cirrus canopies which occur over these weather systems make the identification of convective cells more difficult. Skilled operators on a man-computer system could be used for quality control and segregation of convective from non-convective clouds. There do not appear to

be any major obstacles to extending rainfall techniques to higher latitudes.

An operational system developed for FGGE would satisfy agricultural requirements at the same time. Higher horizontal resolutions would be required over the United States. However, the largest need for data is in the undeveloped countries of South America and Asia. These needs could be satisfied, provided that geostationary satellite data are taken continuously and disseminated directly to a rainfall measurement system. Large delays in time will reduce the usefulness of the measurements. The present GOES satellites can cover both North and South America. Future plans call for coverage of the Asian areas by satellites operated by other nations. If a rapid and reliable data exchange is not made between countries, the agricultural utility of the measurements will be limited.

The geostationary satellite data can be of benefit in making flash flood predictions. These measurements are needed for identification of large raining convective systems in watersheds of high flood potential. A man-computer system could be used for the cloud identification. Once a severe convective storm is identified, rainfall calculations could be made from anvil expansion relationships. River runoff and flood potential could be predicted from simplified watershed models. Griffith and Woodley (1977) have applied their rainfall system to the Big Thompson flood of 1976 and have shown that the reasonable rainfall measurements could be made in a real-time format. A system of this type could be used to cover many river basins from one central forecast area.

b) Cloud coverage correlations (Polar Satellites)

Rainfall has been related to the amount of time an area is covered by precipitating clouds. This has been done by three groups: NOAA/NESS (Follansbee, 1976), the University of Hawaii (Kilovsky and Romage, 1976), and Barrett (1975), using polar orbiting satellites. In addition, Gruber (1973),

Merrit (1976), and Craig (1975) have applied similar techniques to geostationary data. In all of these methods convective clouds are delineated subjectively by operators at 6 or 12 hour intervals. Geometric shapes were fitted to the cloud systems and moved with time to determine the amount of time an area was covered by the convective systems (Follansbee, 1976; and Kilovsk and Ramage, 1976). Linear correlations between cloud cover and rainfall were made (see Figure 2). These relationships are stated as being accurate within a factor of 2 for monthly averages.

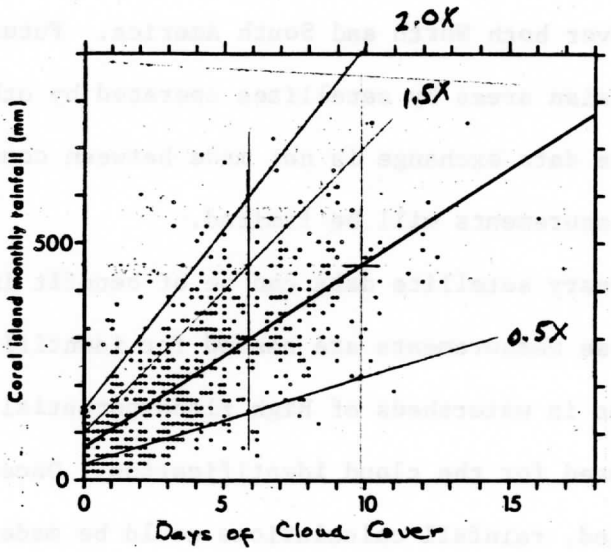

Figure 2: Rainfall-Cloud cover correlation given by Kilonsky and Ramage (1976) for the Tropical Pacific Ocean.

Follansbee (1976) has modified the technique to incorporate the climatic monthly precipitation for the study area. He has calculated the 12 hour precipitation (P_{12}) by: $P_{12} = 0.0075\ DP_n$ where (P_n) is the monthly normal, and (D) the duration of precipitating cloud cover. This refinement essentially is a measure of climatic anomalies.

Gruber (1973) has modified the simple duration of precipitating cloud cover correlation with rainfall to include the amount of precipitate moisture available for rainfall.

It is apparent that cloud cover correlations are more applicable to weekly or monthly precipitation than to daily precipitation. The value of a simple method of this type is that it can be applied to polar orbiting satellites and would be easy to automate. The accuracy and time resolution that can be obtained from this method are definitely not as good as can be obtained with the anvil expansion technique. However, the advantage of the polar system is the uniform global coverage that it can provide at a low cost. The system does not depend on obtaining data from foreign countries as the geostationary data will for a large portion of the globe.

The polar satellite data can be used only for global rainfall climatologies and for agricultural studies in other countries. None of the other needs could be satisfied with this system.

To develop an operational system of this type there are three areas that require study: 1) diurnal variability and the effects of sampling over long time intervals (3, 6, or 12 hours), 2) geographic and regional variance in the cloud cover-rainfall relationships, and 3) objective methods to distinguish precipitating from non-precipitating clouds. Areas one and three can be studied using the high time resolution data from ground based measurements and geostationary satellite data. The geographic anomalies require use of polar orbit data in many areas. Corrections for geographic variations could be applied to the measurements after they are made. For development of an operational system the criteria for recognizing precipitating clouds needs to be established first.

2) Rainfall Estimation Using Satellite Microwave Sensors

Rainfall measurements have been made from microwave data taken from the Nimbus satellites (Rao, Abbott, and Theon, 1976; and Adler and Rogers, 1976). These measurements have been confined to areas over oceans because of the variable emissivities of land surfaces. As a result of the geographic confinement of these measurements there are few data available for ground truth comparisons. Accuracies for these measurements are estimated as being in the vicinity of a factor of 2.

Microwave data could be useful for developing rainfall climatologies. This system essentially identifies the location of raining cloud systems. These measurements are similar to the other polar imaging systems discussed in the last section because they both are flown on polar orbiting satellites. However, the microwave sensors provide more detail to these measurements because rainfall rates are determined directly. Interpolation of the rainfall rates between satellite orbits is not always accurate because of the short lifecycles of the convective clouds and diurnal changes in convective activity. Averaging of measurements over time should improve the quality of the rain volumes derived. This was done by Rao, et al. (1976). Microwave data appear to be more applicable to climatological studies than for daily measurements.

The lack of measurements over land eliminates the use of these data for agricultural and hydrological purposes. Savage (1976) has discussed the possibility of making land measurements, but plans for such a system have not been made yet.

The main value of these measurements would be for latent heat release studies. There data could be used for rainfall climatologies for

numerical modeling studies. Trial measurements of the latent heat release in one hurricane have been made by Adler and Rogers (1976). This study has shown that the microwave data have some utility for hurricane studies. They also could be utilized to forecast flood potential of hurricanes. This type of forecast is being considered by NHEML (Griffith and Woodley, 1977).

3) Ground Based Measurements

Studies by Woodley et al. (1974) and Huff (1971) have shown that extremely high density raingauge networks are needed for sampling convective storms. For an accuracy of a factor of 2 on a daily basis, a raingauge density of 12 mi^2/gauge would be needed (see Figure 3). Such a density is not economically feasible to maintain except over small areas for experimental purposes. The present weather network has gauges spaced over 50 miles apart. Thus, convective rains are poorly sampled with the present network. More accurate rain volume measurements can be obtained only by time averaging of the gauge data for monthly or seasonal periods.

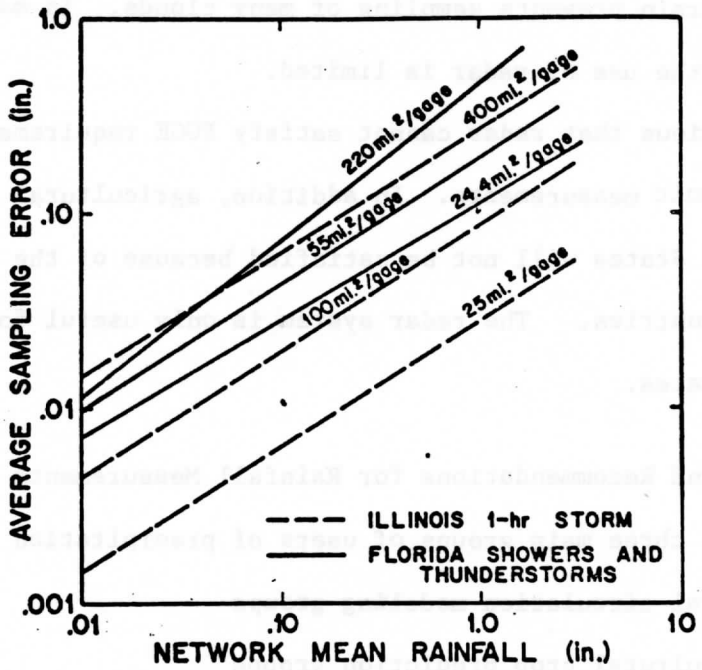

Figure 3: Average sampling error versus network mean rainfall.

Radar measurements have been made in a few selected areas for more accurate measurements (National Severe Storms Lab., OK; McGill University, Canada; and NHEML, Miami). However, these measurements are not easily obtained. Calibrations of the system with raingauge data have to be made on a daily basis for reliable measurements. Changes in atmospheric refractivity, non-uniform beam filling by the precipitation, and anomalous propagation of echoes cause uncertainties in the measurements. Digitized radar data is required for computer processing of precipitation measurements. Woodley et al. (1974) have shown that the calibrated radar system is by far the most accurate rainfall system if calibrations are done properly.

A system of calibrated radars could be used to meet rainfall requirements in most agricultural areas. Such a system could be made by upgrading the present weather radar facilities to provide digital output, establishing calibration procedures, and providing minicomputers to process the radar data.

Radar measurements are difficult to make in mountainous areas (Peck, 1975). The rough terrain prevents sampling of many clouds. In many areas where flash floods occur the use of radar is limited.

It is obvious that radar cannot satisfy FGGE requirements because of the need for oceanic measurements. In addition, agricultural requirements outside of the United States will not be satisfied because of the lack of radar systems in foreign countries. The radar system is only useful for selected areas of the United States.

C. Summary and Recommendations for Rainfall Measurements

There are three main groups of users of precipitation data:

1) General circulation modeling groups

2) Agricultural crop prediction groups

3) Flood forecasters and water management groups.

The general circulation modeling groups are concerned mainly with latent heat release. Their requirements are reflected in the GARP data requirements of precipitation. The agricultural crop predictions require global land data but with high spatial resolution. The flood forecasters require high time resolution over limited land regions. Systems which can provide precipitation data include raingauge networks, radar, satellite microwave sensors, and satellite visual and infrared images. All the systems are only accurate to within a factor of 2. Each of the systems has special strengths, but each also has some weakness. Hence, no one system is ideal for meeting all the user requirements. The general circulation modeling requirements could be satisfied with a special data set, such as FGGE, but the other users require an ongoing operational system. The ultimate operational system will probably be a composite of several systems.

The best system for FGGE would be a composite of polar orbiter microwave measurements over ocean areas and once per day images inferring rainfall over land and ocean areas. The image processing should be done over ocean areas to relate the two systems and to aid in the identification and measurement of deep convective regions which present problems for the microwave sensors. Both systems should be benchmarked against geostationary measurements of precipitation, using the expanding anvil techniques and raingauges where available.

In the composite data set, the source of information for each precipitation measurement needs to be kept with the data. Since each system has limitations and potential biases, the user of the data should be made aware of any limitations and be able to sort out measurements which could cause problems.

The best system for agricultural crop prediction is the polar orbiting image technique with benchmarks provided by geostationary expanding anvil data and raingauge data. The best system for flash flood forecasters is digitized radar supplemented with geostationary data in mountainous regions and for hurricanes. The best system for hydrological and water management groups with high accuracy requirements is a raingauge-digital radar cooperative approach. The raingauges would be used to calibrate the radar, and the radar would be used to extend the coverage of the raingauges. Satellite image data can be used to extend the coverage into mountainous regions with poor radar coverage.

All the systems for precipitation measurement require further development. The radar system requires the conversion of the present radar network to digital outputs. This is gradually being done by NWS as part of the AFOS implementation plan. The calibration procedures need to be developed, as do the data processing techniques. The system for determining precipitation from polar orbiter images requires further technique development efforts to distinguish objectively between precipitating and non-precipitating clouds, to develop transfer equations for different geographic regions, to include diurnal effects, and to establish ongoing verification procedures. The system for determining precipitation from geostationary images requires development efforts to extend the technique to mid latitudes, to identify precipitation from stratus clouds, and to measure precipitation from small clouds in the tropics. The microwave systems require verification over the oceans and sensor development to include multi-channel response with polarized sensors for measurements over land.

REFERENCES

Adler, R.F., and E.B. Rodgers, 1976: Satellite-Observed Latent Heat Release in a Tropical Cyclone, Goddard Space Flight Center Report, X-911-76-151, Greenbelt, MD. 24 pp.

Arakawa, Akio, 1975: Modeling Clouds and Cloud Processes for Use in Climate Models, in The Physical Basis of Climate and Climate Modeling, GARP Publications Series No. 16, World Meteorological Organization, pp. 183-197.

Bryson, Reid A., and Gerald J. Dittberner, 1976: A Non-Equilibrium Model of Hemispheric Mean Surface Temperature, Journal Atmospheric Sciences, 33, #11, 2094-2106.

Budyko, M.I. 1969: The Effect of Solar Variations on the Climate of the Earth, Tellus, 21, 611-619.

Clapp, P.F. 1964: Global Cloud Cover for Seasons Using TIROS Nephanalysis, Monthly Weather Review, 92, 495-507.

Coburn, Allen R., 1971: Improved Three Dimensional Nephanalysis Model, AFGWC Technical Memorandum 71-2, Air Force Global Weather Center, Air Weather Service, Offutt AFB, Nebraska, 72 pp.

Cooley, Duane S., January 30, 1976: Experimental Satellite Cloud Analysis Chart, Technical Procedures Bulletin No. 157, Technical Procedures Branch, Meteorological Services Division, NWS.

Davis, P. A., and E. J. Wiegman, 1973: Application of Satellite Imagery to Estimates of Precipitation over Northwestern Montana. Stanford Research Institute, Atmospheric Science Lab., October, 39 p.

DeCotiis, A.G. and E. Conlan, 1971: Cloud Information in Three Spatial Dimensions Using IR Thermal Imagery and Vertical Temperature Profile Data, Proceedings of the Seventh International Symposium on Remote Sensing of Environment at Willow Run Laboratories at the University of Michigan.

Follansbee, W.A., 1974: Estimation of Average Daily Rainfall from Satellite Cloud Photographs, NOAA Tech. Memo, NESS 44, 39 pp.

Follansbee, W.A., 1976: Estimation of Daily Precipitation Over China and the USSR Using Satellite Imagery. NOAA Tech Memo. NESS 81, Washington, D.C., 30 pp.

Griffith, C.G., W.L. Woodley, D.W. Martin, and J. Stout, 1977: Rain Estimation from Geosynchronous Satellite Imagery, Part I. Visible Studies, Submitted to J. Appl. Meteor.

Gruber, A., 1973: Estimating Rainfall in Regions of Active Convection, J. Appl. Meteor. 12: 110-118.

Hasler, A.F., W. Shenk, and W. Skillman, 1976: Wind Estimates from Cloud Motions: Phase I of an in situ Aircraft Verification Experiment, J. of Applied Meteor., 15, #1, 10-15.

Huff, F.A., 1971: Distribution Hourly Precipitation in Illinois, Circ. 105, Illinois State Water Survey, Urbana, IL, 23 pp.

Kasahara, A. and W.M. Washington, 1971: General Circulation Experiments with a Six Layer NCAR Model, Including Orography, Cloudiness, and Surface Temperature, Calculation, J. Atmos. Sci., 28: 657-701.

Kilonsky, B.J., and C.S. Ramage, 1976: A Technique for Estimating Tropical Open-Ocean Rainfall from Satellite Observations.

Kreitzberg, Carl W., 1976: Interactive Applications of Satellite Observations and Mesoscale Numerical Models, Bul. American Meteor. Soc., 57, #6, pp. 679-685, June, 1976.

Liou, Kuo-Nan, 1974: On the Radiative Properties of Cirrus in the Window Region and Their Influence on Remote Sensing of the Atmosphere, Journ. Atmospher. Sci., 21, #2, 522-532.

Manabe, S., D.G. Hahn, and J.L. Holloway, Jr., 1974: The Seasonal Variation of the Tropical Circulation as Simulated by a Global Model of the Atmosphere, Journ. Atmospher. Sci., 31, #1, 43-83.

McKee, Thomas B. and Stephen K. Cox, 1974: Scattering of Visible Radiation by Finite Clouds, Jour. Atmosph. Sci., 31, #7, 1885-1892.

Merritt, E., 1976: Earthsat Spring Wheat System Test 1975. Final Report to NASA/Johnson Space Flight Center, NASA-CR-147711, 591 pp.

Miller, Donald B. and Robert G. Feddes, 1971: Global Atlas of Relative Cloud Cover, 1967-1970, U.S. Department of Commerce and U.S. Air Force, Washington, D.C., Sept. 1971, 237 pp.

National Advisory Committee on Oceans and Atmospheres, Nov. 22, 1972: A Report for the Administrator of NOAA, The Agnes Flood, A Post-Audit of the Effectiveness of the Storm and Flood Warning System of the National Oceanic and Atmospheric Administration, Washington, D.C.

Negri, A.J., D.W. Reynolds, and R.A. Maddox, 1976: Measurements of Cumulonimbus Clouds Using Quantitative Satellite and Radar Data. 7th Conference on Aerospace and Aeronautical Meteorology and Symposium on Remote Sensing from Satellites, Melbourne, FL, November 16-19.

Peck, E.L., 1975: Precipitation Research. Reviews of Geophys. and Space Sci., Vol. 13 No. 3, 431-433 pp.

Purdom, James F.W., 1976: Some Uses of High Resolution GOES Imagery in the Mesoscale Forecasting of Convection and its Behavior, Sixth Conference on Weather Forecasting and Analysis, Albany, NY, Amer. Meteorol. Soc., 57, #6, pp. 679-685, June, 1976.

Rao, M.S.V., W.V. Abbott, and J.S. Theon, 1976: Satellite-Derived Global Oceanic Rainfall Atlas (1973 and 1974), Goddard Space Flight Center, Report X-911-76-116, Greenbelt, MD.

Sadler, James C. and Barry E. Harris, 1970: The Mean Tropospheric Circulation and Cloudiness over Southeast Asia and Neighboring Areas, Scientific Report No. 1, Hawaii Institute of Geophysics, University of Hawaii, 37 pp.

Savage, R.C., 1976: The Transfer of Thermal Microwaves Through Hydrometeors. Ph.D. Thesis, University of Wisconsin-Madison, Madison, WI. 147 pp.

Schneider, Stephen H., 1972: Cloudiness As a Global Climate Feedback Mechanism: The Effects of the Radiation and Surface Temperature of Variations in Cloudiness, J. Atmos. Sci., 29, #8, 1413-1422.

Schutz, C. and W.L. Gates, 1971: Global Climatic Data for Surface, 800 mb: January, R-915-ARPA, The Rand Corporation, Santa Monica, CA, 173 pp.

Scofield, Roderick A., Nowcasting: Fine Tuning the Local Forecast, Sixth Conference on Weather Forecasting and Analysis, Albany, NY, Amer. Meteorol. Soc., pp. 268-272.

Scofield, R.A., 1976: Satellite Pictures Used for Locating the Rainfall Associated with a Convective System Over Texas. Sixth Conference on Weather Forecasting and Analysis, Albany, NY, May 10-14.

Sellers, William, 1973. A New Global Climate Model, Journ. Appl. Meteorol., 12, #12, 241-254.

Shenk, W.E. and V.V. Salomanson, 1972: A Simulation Study Exploring the Effects of Sensor Spatial Resolution on Estimates of Cloud Cover From Satellites, Journ. Appl. Meteorol., 11, 214-220.

Sikdar, D.N., 1972: ATS-3 Observed Cloud Brightness Field Related to a Meso-Synoptic Scale Rainfall Pattern, Tellus, 24, 400-413.

Sikdar, D.N., V.E. Suomi, and C.E. Anderson, Convective Transport of Mass and Energy in Severe Storms Over the United States ... An Estimate From a Geostationary Attitude, Tellus, 22, pp. 521-532, 1970.

Smith, W.L. and H.M. Woolf, 1976: The Use of Eigenvectors of Statistical Convenience Matrices for Interpreting Satellite Soundings Radiometer Observations, Journ. Atmosph. Sci., 33, #7, 1127-1140.

Somerville, R.C.J., P.H. Stone, M. Halem, J.E. Hansen, J.S. Hogan, L.M. Druyan, G. Russell, A.A. Lacis, W.J. Quirk, and J. Tenenbaum, 1974: The GISS Model of the Global Atmosphere, J. Atmosph. Sci., 31, #1, 84-117

Telegadas, Kosta and Julius London, 1954: A Physical Model of the Northern Hemisphere Troposphere for Winter and Summer, New York University Final Report on A.F. Cambridge Research Center Contract AF 19 (122)-165, pp. 55.

Van Loon, H., 1972: Cloudiness and Precipitation in the Southern Hemisphere, in Meteorology of the Southern Hemisphere, Meteorological Monograms, 13, #35, Am. Met. Soc., Boston, MS, pp. 101-111.

Woodley, W.L., A. Olsen, A. Herndon, V. Wiggert, 1974: Optimizing the Measurement of Convective Rainfall in Florida. NOAA Tech. Memo ERL WMPO-18, Boulder, CO, 99 pp.

Reprinted from JOURNAL OF APPLIED METEOROLOGY, Vol. 18, No. 12, December 1979
American Meteorological Society
Printed in U. S. A.

An Application of a Geostationary Satellite Rain Estimation Technique to an Extratropical Area

DONALD P. WYLIE

JOURNAL OF APPLIED METEOROLOGY VOLUME 18

An Application of a Geostationary Satellite Rain Estimation Technique to an Extratropical Area

DONALD P. WYLIE

Space Science and Engineering Center, University of Wisconsin, Madison 53706

(Manuscript received 18 September 1978, in final form 20 July 1979)

ABSTRACT

The use of geostationary satellite data for estimating precipitation in non-tropical areas was explored with data taken in Montreal, Canada. The previous studies using geostationary images for rain estimation have concentrated primarily on tropical clouds (Griffith *et al.*, 1978; Stout, *et al.*, 1979). The intent of this study was to evaluate the applicability of using these data and techniques in other geographical areas. The Montreal area provided a wide range of weather situations common to midlatitudes for which the techniques could be tested. Because of the many variables in this area (different cloud types, moisture availability, temperature vertical structure and others) the rain rates of the cloud areas varied. Large differences in rain rates between the days studies in Montreal were found. The Montreal data also had rain rates that were considerably smaller than found in the tropical studies.

To explain these differences the environments of the clouds were investigated using sounding data. By applying a cumulus model (Simpson and Wiggert, 1969) to the soundings most of the daily differences in rain rates were explained. The large differences between the tropical studies and Montreal also were described by the model. It is proposed that future rain estimation schemes combine satellite image with sounding data through a cloud model to form a technique applicable to a wide variety of weather situations and geographical areas.

1. Introduction

The use of satellite data for estimating precipitation has gained attention in recent years because of the need for rainfall information in many areas of the world where weather observations are sparse or nonexistent. Studies of tropical cumulus convection have encouraged the development of techniques using geostationary satellite data (Griffith *et al.*, 1978; Stout *et al.*, 1979; hereafter referred to as Griffith or Stout). Intense efforts using these data were made for the Atlantic Tropical Experiment (GATE, 1974) of the Global Atmospheric Research Program (GARP). Other satellite rain estimation techniques for sampling large oceanic areas have been developed using microwave sensors (Rao and Theon, 1977). Similar precipitation and latent heat release data will be needed on a global scale for the First GARP Global Experiment (FGGE) scheduled for the calendar year 1979.

Outside of the atmospheric research community the need for rainfall information is also very strong. Agricultural grain crop forecasters have sought precipitation data in many of the undeveloped countries of South America and Asia where weather observation networks are very poor (Merritt, 1976). Hydrologists have sought the same information in sparsely populated areas for river basin studies (Barrett, 1976). Many of the needs for satellite-derived precipitation estimates have been in the continental areas of the world and several attempts have been made to satisfy these needs.

Early efforts at estimating precipitation from satellite images have correlated weekly or monthly precipitation to the length of time a station was covered by convective clouds (Follansbee, 1974; Kilonsky and Ramage, 1976). These studies have used polar orbiting satellite images taken twice per day for determining cloud cover and assigned constant rainfall rates to the cloud areas. Refinements to the techniques have used climatological rain rates with the satellite-measured cloud areas for estimating seasonal precipitation accumulations (Follansbee, 1976). Satellite data also have been used to extend coverage between raingages (Barrett, 1976).

Geostationary satellites have provided time sequences of images from which cirrus anvil expansions can be measured as proposed by Sikdar (1972). These measurements have been used by Griffith and Stout on tropical cumulonimbus and by Scofield and Oliver (1977) on air mass thunderstorms over the southern United States. Because of the success of these studies and the needs for rain information in many nontropical areas of the world a test of using geostationary images outside of the tropics was made.

0021-8952/79/121640-09$06.25

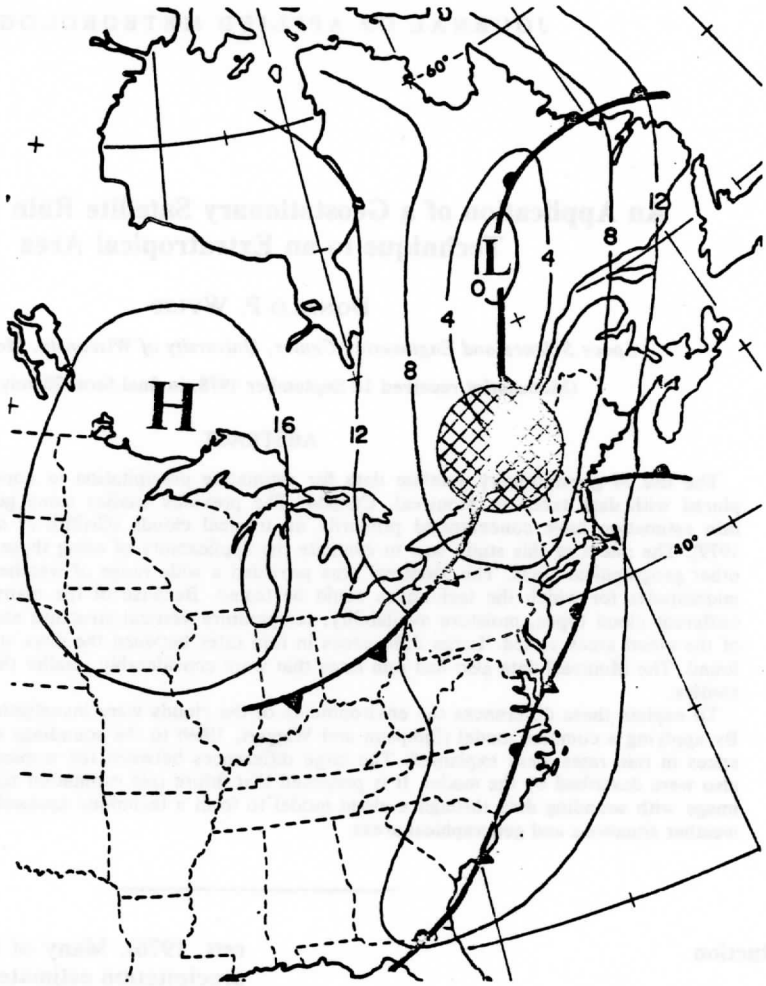

FIG. 1. Surface analysis for 1800 GMT (1300 LST), 2 June 1977, of eastern Canada. Shaded areas indicate precipitation. The circle indicates the area covered by the radar.

This paper will describe the study made on data from Montreal, Quebec, Canada. Images from the Eastern Geostationary Orbiting Satellite (GOES-E) were used for testing the feasibility of estimating rain over a midlatitude continental area. The results obtained in Canada will be compared to the tropical data obtained by Stout, to show the similarities and differences between the application of satellite data to the two different geographical areas.

2. Data used

GOES-E images were archived at one-half hour intervals by the University of Wisconsin-Madison. Visible images (0.7 μm wavelength) and infrared images (11.5 μm) were recorded at spacial resolutions of 2.8 and 5.6 km. The geographical position of the earth in the image was determined from landmark measurements. These satellite images were compared to radar images of the same area.

Rainfall rates under the clouds were measured by the 10.0 cm weather radar of McGill University, Montreal, which covered a 200 km radius circle centered on Montreal (Fig. 1). The method of determining rainfall rate is described by Hodge and Austin (1977). This method basically used a nominal Z-R relationship and then corrected it for bias errors based on the 24 h accumulations of 150 gages in the area. The initial relationship between radar reflectivity (Z, mm^6 m^{-3}) and rain rate (R, mm h^{-1}) of $Z = 200\,R^{1.6}$ was used. Radar-derived rain totals over each gage were calculated and compared to the accumulations measured by the gages. The bias errors then were removed by adjusting the Z-R relationship based on the gage totals and recalculating the rainfall rates.

The rainfall rates were averaged over 4 km × 4 km boxes in the horizontal. Scans at multiple altitudes were used to average the rain rates over 1 km in the

TABLE 1. Summary of the data used in the geostationary satellite rain estimation study.

Date	Time period studied (LST)	Satellite data type	Location	Cloud cover (%)
4, 6 Sep 74	0930–1530	Visible	GATE	56
	0330–2000	IR		64
1 Jun 77	1230–1530	Visible	Montreal	44
		IR		33
2 Jun 77	1200–1500	Visible	Montreal	67
		IR		28
29 Jun 77	0800–1330	Visible	Montreal	26
		IR		25
16 Sep 77	1000–1430	Visible	Montreal	60
		IR		98
20 Sep 77	1030–1430	Visible	Montreal	NA*
		IR		51
26 Sep 77	1000–1330	Visible	Montreal	30
		IR		83

* NA, not available.

vertical centered at 3 km above the earth's surface. These data formed a constant altitude projection of rainfall rate which was then remapped to the projection of the satellite image.

3. The types of weather studied

A total of six days when precipitation occurred in Montreal were studied (Table 1). Three of the days in June represented the type of precipitation found in the summer months over eastern Canada. A warm air mass typically covered most of the area, while a cold front advanced from the northwest (Fig. 1). Cumulonimbus clouds (Cb) developed in the warm air and were clearly visible on the satellite images (Fig. 2). East of the front Cb's were easily identified by being isolated or in lines parallel to the low-level wind direction. More widespread cloud cover and precipitation occurred near the cold front making individual cloud identification more difficult. Cirrus from the convective cells also covered the area masking the appearance of the cells on the satellite image.

Three days in September 1977 were studied which represented the type of precipitation found in the fall and winter. On these days the Cb cells were not easily distinguished (Fig. 3). A massive cloud area encompassed most of the radar's viewing area and precipitation was widespread under the cloud cover.

4. The measurement of rainfall rates

The amount of cloud cover in the viewing area of the radar was measured on each of the satellite images taken at one-half hour intervals during the time periods shown in Table 1. Threshold levels of brightness (visible images) and temperature (infrared) were used to define the cloud areas on the digital images. The amount of image area above the threshold brightness or colder than the threshold temperature were digitally summed by the computer.

For comparisons of the cloud cover found in Montreal to the GATE studies it was necessary to

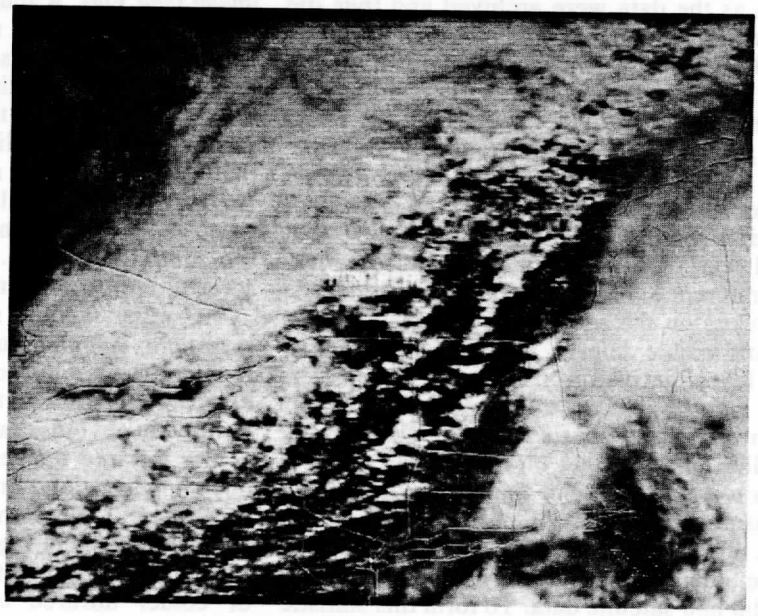

FIG. 2. GOES-E satellite image of eastern Canada, centered on Montreal, 2 June 1977.

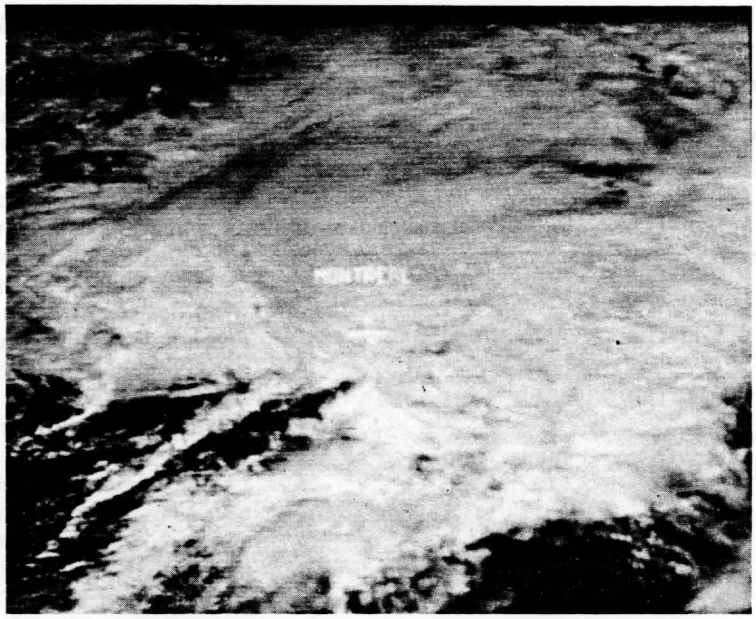

FIG. 3. As in Fig. 2 except for 26 September 1977.

correct the brightness levels of the images. The angle of the sun illuminating the clouds varied both with latitude and the time of day in which each image was taken. A different satellite also was used for the studies of Griffith and Stout. These conditions produced differences in the brightnesses of the clouds between the two geographical areas (GATE and Montreal) and variations in brightnesses between the different days studied in Montreal. These variances were seen only in the visible images. The infrared sensor was routinely calibrated by NOAA as the data were archived and thus did not require any extra processing.

To produce a visible image independent of sun angle and sensor changes, the visible brightness was converted to an optical thickness of the cloud using a plane-parallel, homogenous, multiple-scattering model (Mosher, 1975). The brightest cloud on each image was used as a reference for the radiative scattering model by assuming that this cloud was of a nearly infinite optical thickness. A reference was needed to calibrate the visible sensors on the satellites. All measurements of areas on visible images were made using the threshold levels derived from the multiple-scattering model and the reference calibrations.

To form a statistical basis for estimating rainfall from satellite images, data on the rainfall rates of the clouds were needed. For these data the McGill radar measurements were compared to the satellite images. A rain rate statistic for the cloud areas seen on the satellite images was derived from a combination of radar and satellite data. To form this statistic the total amount of rain falling within 200 km of Montreal was derived by integrating the radar-measured rain rates over the radar's viewing area. This represented a volumetric water flux into the area. The volumetric rain rate then was divided by the amount of cloud cover measured by the satellite over the same area. The cloud-cover measurement was made using the threshold of optical thickness or infrared temperature as previously discussed. This produced a new rain rate statistic that was a function of the threshold used on the satellite image (see Figs. 4 and 5).

The radar-satellite rainfall rates were averaged over the time periods shown in Table 1 for each day. Because satellite images produced cloud areas that were larger than the rain areas seen on the radar, the radar-satellite rainfall rates were smaller than the rainfall rates measured by the radar alone. Lovejoy and Austin (1979) found the satellite cloud areas to be approximately four times larger than the radar rain areas. Thus the combined radar-satellite rain rates were smaller by the same ratio.

The radar-satellite rainfall rates varied with the threshold levels of optical thickness or infrared temperature used because the cloud areas measured were sensitive to the thresholds used. It is intuitively obvious that higher optical thicknesses or colder infrared temperature thresholds would produce smaller cloud area measurements which also was the situation found in these data. The rain rate statistics shown in Figs. 4 and 5 depict this relationship by increasing with increased optical thickness or colder infrared temperature. The volumetric

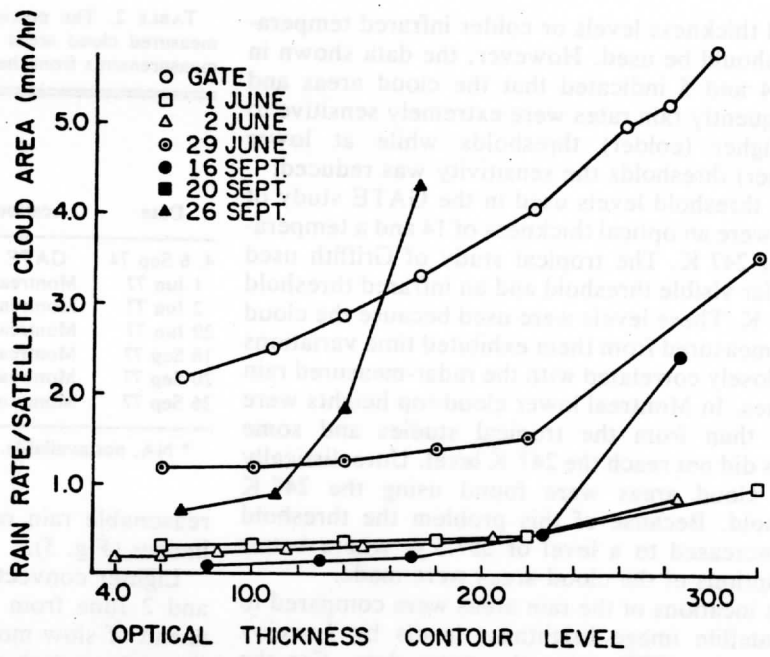

FIG. 4. Rainfall rates for the cloud areas measured on the visible satellite images expressed as a function of the brightness threshold used to define cloud area. Rainfall rates were derived using McGill radar measurements of rain volumes combined with satellite measurements of cloud areas. See text Section 4 for description.

water fluxes into the area were not affected because they were independently measured by the radar and thus the changes shown in Figs. 4 and 5 represent cloud area changes alone.

The objective of any satellite-based rain estimation scheme is to choose threshold levels that define convective cloud areas and eliminate non-convective clouds and land forms. Therefore the higher

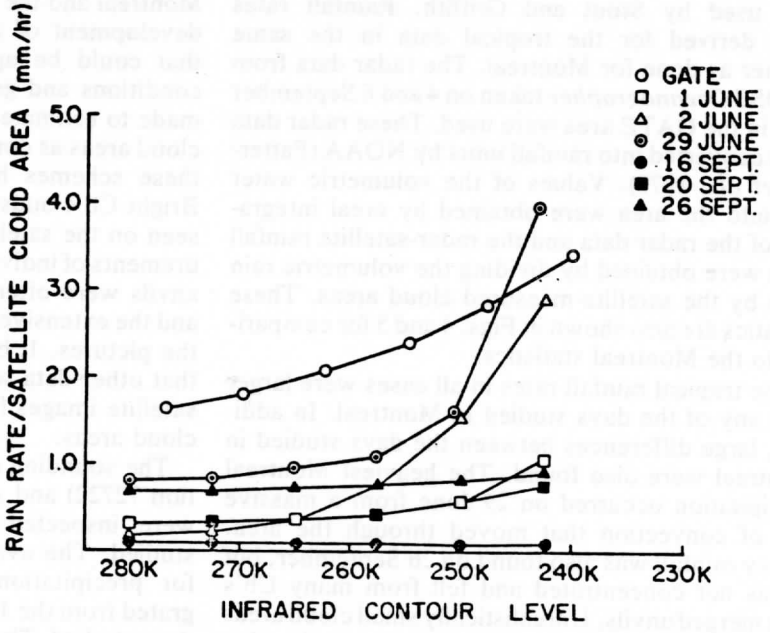

FIG. 5. Rainfall rates for the cloud areas measured on the infrared satellite images expressed as a function of the infrared temperature used to define the cloud areas. Rainfall rates were derived using the combination of McGill radar rain volumes and satellite cloud areas. See text.

optical thickness levels or colder infrared temperatures should be used. However, the data shown in Figs. 4 and 5 indicated that the cloud areas and consequently rain rates were extremely sensitive to the higher (colder) thresholds while at lower (warmer) thresholds the sensitivity was reduced.

The threshold levels used in the GATE study of Stout were an optical thickness of 14 and a temperature of 247 K. The tropical study of Griffith used a similar visible threshold and an infrared threshold of 253 K. These levels were used because the cloud areas measured from them exhibited time variations that closely correlated with the radar-measured rain volumes. In Montreal lower cloud-top heights were found than from the tropical studies and some clouds did not reach the 247 K level. Unrealistically small cloud areas were found using the 247 K threshold. Because of this problem the threshold was increased to a level of 257.5 K where better descriptions of the cloud areas were made.

The locations of the rain areas were compared to the satellite image brightness levels by Lovejoy and Austin (1977) using the same data. For the thresholds used the rain areas were located within an accuracy of 40 km. In all cases the satellite cloud areas defined by the thresholds were larger than the rain areas and the rain areas were contained inside them. for further details on the locations of the rainfall see Lovejoy and Austin (1979).

5. The variability of rainfall rates

The Montreal data were compared to the tropical data used by Stout and Griffith. Rainfall rates were derived for the tropical data in the same manner as done for Montreal. The radar data from the OSS *Oceanographer* taken on 4 and 6 September 1974 in the GATE area were used. These radar data were converted into rainfall units by NOAA (Patterson *et al.*, 1979). Values of the volumetric water flux into the area were obtained by areal integration of the radar data and the radar-satellite rainfall rates were obtained by dividing the volumetric rain rates by the satellite-measured cloud areas. These statistics are also shown in Figs. 4 and 5 for comparison to the Montreal statistics.

The tropical rainfall rates in all cases were larger than any of the days studied in Montreal. In addition, large differences between the days studied in Montreal were also found. The heaviest Montreal precipitation occurred on 29 June from a massive line of convection that moved through the area. Heavy rainfall was also found on 26 September, but it was not concentrated and fell from many Cb's with merged anvils. Unrealistically small cloud areas were measured on the visible images on this day but not on the infrared images. The small cloud areas produced the unrealistically large rainfall rates for the higher optical thicknesses (Fig. 4) while more reasonable rain rates were found for the infrared images (Fig. 5).

TABLE 2. The precipitation rates (mm h^{-1}) of the satellite-measured cloud areas and the precipitable water vapor (mm) measurements from the soundings in the area.

Date	Location	Rain rates over the satellite cloud areas: Visible (τ = 14 [illegible])	Rain rates over the satellite cloud areas: IR (257.5 K)	Sounding integrated precipitable water
4, 6 Sep 74	GATE	2.8	2.2	54
1 Jun 77	Montreal	0.3	0.4	27
2 Jun 77	Montreal	0.2	0.9	22
29 Jun 77	Montreal	1.2	1.0	38
16 Sep 77	Montreal	0.1	0.1	22
20 Sep 77	Montreal	NA*	0.4	27
26 Sep 77	Montreal	2.4	0.9	27

* NA, not available.

Lighter convective precipitation was found on 1 and 2 June from isolated Cb's in the warm areas ahead of slow moving cold fronts that approached the area on each of the two days. On both days the rapidly expanding anvils from Cb's were seen on the satellite images, but the rainfall rates from these clouds remained small when compared to 29 June and 26 September.

Light precipitation rates also were found on 16 and 20 September. These days were dominated by extensive areas of stratus clouds which yielded very small precipitation amounts.

The large day-to-day variations in rainfall rates found in this study and the large differences between Montreal and the tropics presented a problem to the development of a general rain estimation scheme that could be applied to a range of convection conditions and geographical areas. Attempts were made to estimate rainfall rates from the changes in cloud areas as done by Griffith and Stout. However, these schemes had little success on these data. Bright Cb clouds with expanding anvils were often seen on the satellite images but quantitative measurements of individual anvil areas were difficult. The anvils were often merged into large cloud masses and the extensive stratus cloud cover often obscured the pictures. It became apparent during this study that other data would be needed in addition to the satellite images for estimating the rain rates of the cloud areas.

The sounding data from Maniwaki, Quebec (station 72722) and Albany, New York (station 72518) were inspected for changes between the days studied. The available water vapor measurements for precipitation (precipitable water) were integrated from the 1200 GMT soundings for each of the days studied. The precipitable water vapor measurements are shown in Table 2 along with the rainfall rates derived from the cloud areas. These measurements are compared to the precipitable water vapor

TABLE 3. Comparison between GATE and Montreal rain rates measured from satellite-derived cloud areas, sounding precipitable water vapor and the output of the cumulus model. See text for an explanation of the model.

Date	Location	Ratio of rain rates Montreal/GATE		Ratio of precipitable water vapor Montreal/GATE	Ratio of model output for 2 km bubble Montreal/GATE
		Visible	IR		
4, 6 Sep 74	GATE	1.0	1.0	1.0	1.0
1 Jun 77	Montreal	0.1	0.2	0.5	0.3
2 Jun 77	Montreal	0.1	0.4	0.4	0.3
29 Jun 77	Montreal	0.4	0.5	0.7	0.5
16 Sep 77	Montreal	0.05	0.05	0.4	0.0
20 Sep 77	Montreal	NA*	0.2	0.5	0.0
26 Sep 77	Montreal	0.6	0.4	0.5	0.3

* NA, not available.

measurements made in GATE on the days that the cloud data of Stout were obtained (OSS *Oceanographer* soundings on 4 and 6 September 1974).

The precipitable water vapor measurements in general showed the same differences between the tropics (GATE) and Montreal as the rainfall rates measured from the satellite and radar data. The precipitable water and rain rates measured are shown in Table 3 as ratios of the GATE measurements. The Montreal precipitable water values were from 0.4 to 0.7 of GATE. The highest Montreal values were found on 20 June which also was the day of the highest rainfall rates.

On the days of lighter precipitation (1 and 2 June, 16 and 20 September) the precipitable water measurements did not depict the low rainfall rates. On those days the precipitable water measurements were 0.4–0.5 of GATE while the rainfall rates were smaller (from 0.05 to 0.4 of GATE). Because of this problem it was necessary to consider the stability of the cloud environments in addition to the available water vapor.

6. The use of a cumulus model

The one-dimensional model developed by Simpson and Wiggert (1969) for cloud seeding experiments was applied to the days studied here. The model was run on the morning soundings from Maniwaki, Albany and the *Oceanographer* that were used to measure the precipitable water. The model simulated cloud growth by using an ascending bubble. This model was used here because it included highly detailed descriptions of the cloud physics processes in the development of precipitation.

A convective bubble of 2 km radius was raised in the model for each sounding. The bubbles were started from an altitude where free buoyant ascent could be made. This varied from 50 mb above the surface in the GATE soundings to 200 mb on 26 September in Montreal. The Montreal area soundings were often stable in the lower layers and free ascent did not occur unless the bubbles were started at the top of the convectively stable layer.

The intention of using a model was to interpret the effects of different cloud environments. The precipitation output from the bubble (model output) could not be used as a direct prediction of rainfall rate for cloud areas by itself. This output represented only one bubble ascent while in reality a cloud system is composed of many bubbles and the numbers and rates of generation of the bubbles cannot be predicted from sounding data.

The relative differences in precipitation rates of the clouds between the days studied were estimated by comparing the model output for the bubble ascents made from the soundings. This was done by expressing the model output precipitation as a ratio of the GATE soundings. These ratios are shown in Table 3 for comparison to the daily variations in rainfall rates that were measured using the combined radar and satellite data.

It is apparent that the model more closely approximated the differences between precipitation rates in GATE and in Montreal than the precipitable water. The best results were obtained on the Montreal days where large precipitation rates occurred, 29 June and 26 September. Better predictions of precipitation rates than the precipitable water measurement also were made for the other days. On the lightest precipitation days (16 and 20 September) the model predicted little or no precipitation, although precipitable water amounts were present at the same levels as found on the June days. For the September days the stability of the soundings greatly limited the ascent distance of the model bubble. Convective instability was found only in very shallow layers on the soundings and thus the model indicated no precipitation.

7. Method of estimating rainfall using satellite and soundings

Using the model output and the satellite cloud-cover measurements, estimates of rainfall for the Montreal area were made to demonstrate the feasibility of a combined technique. The rates of precipitation for each of the Montreal days were

estimated from the model output and GATE measurements of rain rates for satellite-derived cloud areas. The rainfall rates (R_m) were estimated by multiplying the model output ratios (r) shown in Table 3 by the average GATE rain rates (R_g) shown in Table 2, i.e.,

$$R_m = rR_g. \quad (1)$$

On days where the model predicted no precipitation a minimum rain rate of 0.1 mm h^{-1} was used. The GATE data were used as a baseline because this was part of the data set used by both Griffith and Stout in developing their rain estimation schemes.

The total accumulated precipitation (P_t) for the viewing area of the McGill radar was estimated by applying the rain rates from (1) to the satellite-measured cloud areas (A_c) for each image and summing over the time periods studied (N observations):

$$P_t = R_m A_c. \quad (2)$$

It should be realized that this estimation scheme was made using the GATE data, the satellite cloud area measurements over Montreal, and the cumulus model. This scheme was independent of the Montreal radar data and thus it could be tested using the Montreal radar as the "ground truth" measurement. The accuracies of estimating precipitation have been expressed by Griffith as an error ratio statistic of the measured to the estimated or vice versa. The ratio has been calculated so that it is always greater than unity. A large ratio indicated a large over prediction or underprediction while a ratio of 1.0 indicated a perfect prediction. These error factors were calculated for the estimation scheme and are shown in Table 4.

For the six days studied in Montreal the best estimates of rainfall were made on the June days where summer convective systems were present. The best results were on the day when one large system dominated, 29 June. For the fall days the accuracy of the estimation scheme decreased. The extremely heavy precipitation on 26 September was not predicted accurately because the model estimated a low rainfall rate based on the soundings. On 16 and 20 September the model predicted no rainfall and the nominal rain rate of 0.1 mm h^{-1} had to be assumed. The soundings were stable on those days thus halting the rise of the bubble in the model.

8. Summary and conclusions

The errors shown in Table 4 are slightly larger than the errors reported by Griffith for the tropical applications of a satellite technique. However, it should be realized that the Montreal area presented a wide variety of convective conditions, and rain estimation in this area was considerably more difficult than in the tropics. With the use of sounding data through the model it was possible to build a combined satellite-model technique that showed skill.

To encompass all geographical areas and seasons of the year a more sophisticated model is needed. The model used here was designed for cumulus clouds which occurred in warm air masses, hence reasonable success was obtained for the summer days studied. For the fall days studied the model was not applicable because of the different cloud types and cloud environmental conditions; consequently, rainfall rates had to be assumed. The model also did not consider the dynamics of the wind field or any other mesoscale dynamics which affected the clouds. However the results of this study indicate that a combined satellite-model rain estimation technique could be developed at least for the summer season and the accuracy of such a technique would be approximately an error factor of 2.0 for 3 h rainfall accumulations.

Acknowledgments. The author is extremely grateful for the advice and comments given by F. Mosher, G. Austin and S. Lovejoy in the course of this study. The author is also grateful to V. Wiggert of NOAA/NHEML for providing the cumulus model. The help of D. Martin, J. Stout and C. Lo in the course of this work was deeply appreciated.

TABLE 4. The measured and predicted rainfall accumulations for the McGill radar area over the time periods indicated.

Date	Time periods studied (LST)	Radar measured accumulated precipitation (10^7 m^3)	Predicted precipitation (10^7 m^3)		Error ratio	
			Visible	IR	Visible	IR
1 Jun 77	1230–1530	7.4	17.9	10.4	2.4	1.4
2 Jun 77	1200–1500	8.8	27.1	8.9	3.1	1.0
29 Jun 77	0800–1330	26.5	32.1	24.6	1.2	1.1
16 Sep 77	1000–1430	7.2	4.4	7.0	1.6	1.0
20 Sep 77	1030–1430	14.6	NA*	3.2	NA*	4.6
26 Sep 77	1000–1330	40.3	14.1	30.8	2.8	1.3
Average error ratio					2.2	1.7

* NA, not available.

This study was funded by NASA Contract NAS5-23462.

REFERENCES

Barrett, E. C., 1976: Satellite data in mapping rainfall for solution of associated problems in regions of sparse conventional observations. *Remote Sensing of the Terrestrial Environment*, Wright & Sons Ltd, Clifton, Bristol, U.K.

Follansbee, W. A., 1974: Estimation of average daily rainfall from satellite cloud photographs. NOAA Tech. Memo. NESS 44, Washington, DC, 39 pp.

——, 1976: Estimation of daily precipitation over China and the USSR using satellite imagery. NOAA Tech. Memo. NESS 81, Washington, DC, 30 pp.

Griffith, C. E., W. L. Woodley, P. G. Grube, D. W. Martin, J. Stout and D. N. Sikdar, 1978: Rain estimation from geostationary satellite imagery-visible and infrared studies. *Mon. Wea. Rev.*, **106**, 1153–1171.

Hodge, D. B., and G. L. Austin, 1977: The calibration of weather radar using radiometers for an attenuation study. *Radio Sci.*, **12**, 293–298.

Kilonsky, B. J. and C. S. Ramage, 1976: A technique for estimating tropical open-ocean rainfall from satellite observations. *J. Appl. Meteor.* **15**, 972–975.

Lovejoy, S., and G. L. Austin, 1979: The delineation of rain areas from visible and IR satellite data for GATE and mid-latitudes. *Atmosphere-Oceans*, **20**, 79–92.

Merritt, E., 1976: Earthsat spring wheat system test 1975. Final Report to NASA/Johnson Space Flight Center, NASA-CR-147711, 591 pp.

Mosher, F., 1975, Appendix to: D. W. Martin, J. Stout, and D. N. Sikdar, 1975: GATE area rain estimation from satellite images. Report, NOAA Grant 04-5-158-47, Space Science and Engineering Center, University of Wisconsin-Madison.

Patterson, V. L., M. D. Hudlow, P. J. Pytlowany, F. P. Richards, and J. D. Hoff, 1979: GATE radar rainfall processing system. NOAA Tech. Memo. EDIS 26, Washington, DC, 34 pp.

Rao, M. S. V., and J. Sm Theon, 1977: New features of global climatology revealed by satellite-derived oceanic rainfall maps. *Bull. Amer. Meteor. Soc.*, **58**, 1285–1288.

Scofield, R. A., and V. J. Oliver, 1977: A scheme for estimating convective rainfall from satellite imagery. NOAA Tech. Memo. NESS 86, 47 pp.

Sikdar, D. N., 1972: ATS-3 observed cloud brightness field related to a mesosynoptic scale rainfall pattern. *J. Appl. Meteor.* **11**, 241–220.

Simpson, J., and V. Wiggert, 1969: Models of precipitating cumulus towers. *Mon. Wea. Rev.*, **97**, 471–489.

Stout, J., D. W. Martin and D. N. Sikdar, 1979: Estimating GATE rainfall from geostationary satellite images. *Mon. Wea. Rev.*, **107**, 585–598.

SMALL SCALE CONVECTION:
AN EXPERIMENT IN CLOUD ADVECTION

SANJAY S. LIMAYE

Introduction

Recently there has been an increased interest in the use of digital satellite images in atmospheric studies. In particular, cloud motion determination and cloud evolution have received attention. Cloud growth has been related to rainfall (Griffith, et al., 1978; Stout et al., 1979) and thunderstorm intensity (Adler and Fenn, 1979). The basic technique in these studies is the measurement of cloud area as a function of time. The process of delineating the area of any given cloud as a function of time is complicated by the fact that clouds more in addition to growing. Manually identifying and following clouds for the purpose of measuring growth rates is frequently a tedious and laborious task. If the task is automated, such as by Griffith et al., 1978, only large convective can be identified, followed and delineated. It is only possible to manually measure small convective systems areas or to delineate the individual convective cells within a larger cloud system. Small convective systems do produce rain and are especially important at the beginning sates of severe weather. It would be desirable to automate the measurement cloud growth rates for all sizes of clouds. This task could be easier if one viewed the cloud evolution in a quasi-Lagrangian frame--not by following clouds, but by moving the clouds in time according to their measured motion. A side benefit of this exercise would be to shed light on the cloud motions themselves and their interpretation as winds.

Procedure

Given a satellite image and a wind field, calculating cloud advection is a straightforward process. In the present case, the wind field was actually the

cloud motions themselves for the time that the satellite images was taken. Thus, there is no ambiguity in answering the question "How are the clouds moving?"

Conceptually the problem is simple. A satellite image (F) at an initial time (t_0) is given that shows the cloud tracers. The cloud motions obtained from tracer clouds using a triplet of images with the first image of which is the image F_0. Knowing the speed and direction of individual clouds, one can predict the positions of clouds at any other time ($t_i + t_0 + \Delta\tau$) provided $\Delta\tau$ is small enough such that the wind field can be assumed to be constant. A forecast satellite image showing the predicted positions of clouds can thus be constructed.

The construction of forecast image showing the advectively predicted cloud field pixel by pixel requires that the cloud motions be available pixel by Pixel. The cloud vectors obtained from following tracer clouds are not available on such a fine pixel by pixel scale due to the sparsity of tracer clouds and the fact that tracer clouds are larger than one image sample. In fact, experience during the Global Atmospheric Research Program (GARP), Global Atlantic Tropical Experiment (GATE), as wellas during the Data Systems Tests has shown that the density of cloud tracer winds over a given area is quite variable. Therefore it is reasonable to objectively analyze the cloud tracer winds over the area of interest with as small a grid spacing as possible. The speed and direction of the cloud motion at a given image sample can be calculated by a two dimensional interpolation scheme from the nearest four grid point values of the zonal and meridional components of motion:

$$u(x,y) = u(x_0,y_0) + \frac{\partial u}{\partial x}\,\delta x + \frac{\partial u}{\partial y}\,\delta y + \ldots$$

$$v(x,y) = v(x_0,y_0) + \frac{\partial v}{\partial x}\,\delta x + \frac{\partial v}{\partial y}\,\delta y + \ldots$$

In practice, only the first order terms need to be retained if the image resolution is about one tenth of grid spacing. The objective analysis on a tight grid and the sub-grid scale interpolation will thus retain the shear and deformation components of the wind field along with the rotational and translational parts.

To compare the forecast image with the actual image both must have the same geometrical relationships. The geographical coordinates of latitude and longitude (λ_0,ϕ_0) of a given image pixel in the satellite coordinates of line are elements (ℓ,e). The zonal (u) and meridional (v) components of the observed cloud motion are then determined for a given pixel as described above. If the time interval between the forecast image and the initial image is $\Delta\tau$, the cloud that would be advected to the point $\lambda_i,\phi i$ at time t_i by:

$$\lambda_i = \lambda_0 - \Delta\tau u/R \cos(\phi_0)$$

$$\phi_i = \phi_0 - \Delta\tau v/R$$

where R is radius of earth and $\Delta\tau$ is time interval and u and v are the zonal and meridional components of the wind at the pixel being advected.

Once the cloud location in earth coordiantes at the forecast time t_i has been determined it is necessary to transfer digital brightness count back into satellite coordiantes. This requires the inverse naviation transform that converts (Λ_i,ϕ_i) at time t_i to the satellite image coordinates (ℓ_i,e_i) valid for time t_i. Repeating this procedure for every sample along every scan in the output area results in the desired forecast cloud cover image.

An example:

An image segment covering the GATE area on day 261 of 1974 was chosen for the experiment. The cloud motions were obtained from full resolution visible

images. The low level cloud motion vectors from 1330 GMT were objectively analyzed by the WIND*SRI program with a grid spacing of 0.25 degree in both latitude and longitude. The 1315 and 1330 GMT images are shown in Figure 1 at full resolution. Figure 2 shows the measured cloud vectors with a subjectively determined streamline analysis superposed on the wind field. Figure 3 shows the objectively analyzed field used in the cloud advection computations.

The forecast image shown in Figure 4 was constructed by moving the clouds seen in the first image in the sequence (1315 GMT) by 15 minutes so as to facilitate a direct comparison with the iamge obtained at 1330 GMT. The point by point difference between the forecast image and the actual image is shown in Figure 5. If the two images were identical, the difference image would be perfectly black. As is obvious from Figure 5, there are considerable differences between the actual image and the advected image.

This is not too suprising. After all, the clouds are not permanent entities; in addition to moving, they grow and decay. The question then arises: "Are the differences between the actual image and the advected image only due to cloud evolution?" If it can be ascertained that the objective analysis of original cloud motions is valid such that one may interpolate the motions within the grid, the answer would be a definite yes. In the present case, however, the answer is somewhat ambiguous. The streamline analysis shows that there are several regions of confluence. The meteorological processes in these regions are causing the evolution of clouds. The apparent difference in the two iamges could be related to this reason. In the present scheme the clouds can only be advected, they cannot be "created" or "destroyed" digitally.

A second and perhaps the major source of difference is the use of objective analysis of cloud winds. The navigation is resolution limited. For 15 minute intervals at full image resolution the uncertainty in the measured vectors is about 1.1 m s^{-1}. Given that the fastest cloud vectors are about 6 m s^{-1}, this amounts to about a 15-20% uncertainty in the derived wind field.

REFERENCES

Adler, Robert F., and Douglas D. Fenn, 1979. Thunderstorm intensity as determined from satellite data. J. Appl. Meteor., 18, 502-517.

Griffith, C. E., W. L. Woodley, P. G. Grube, D. W. Martin, J. Stout and D. N. Sikdar, 1978. Rain Estimation from geostationary satellite imagery--visible and infrared studies. Mon. Wea. Rev., 106, 1153-1171.

Stout, John E., D. W. Martin and D. N. Sikdar, 1979. Estimating GATE rainfall with geosynchronous satellite images. Mon. Wea. Rev., 107, 585-598.

LIST OF FIGURES

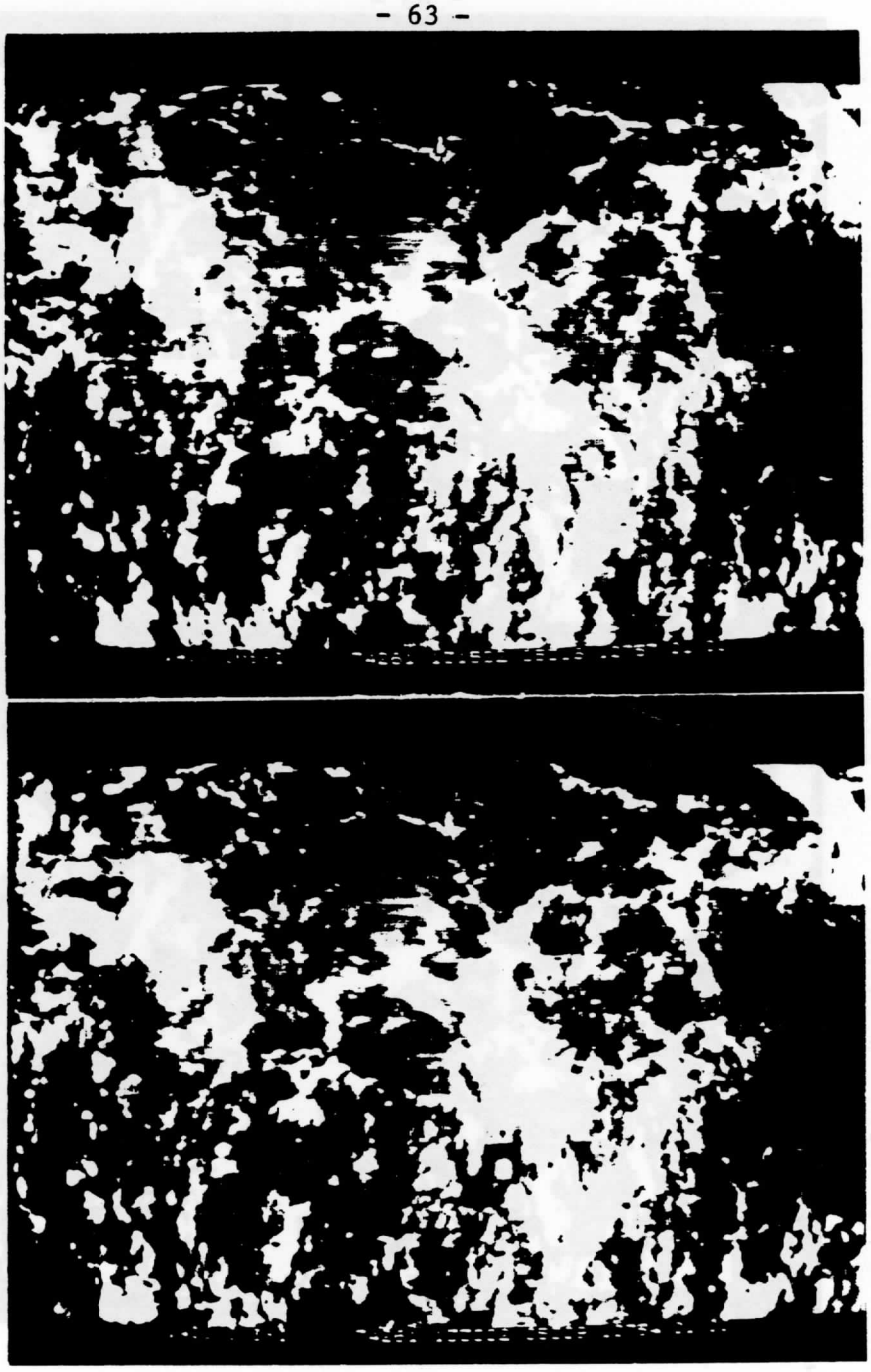

Figure 1

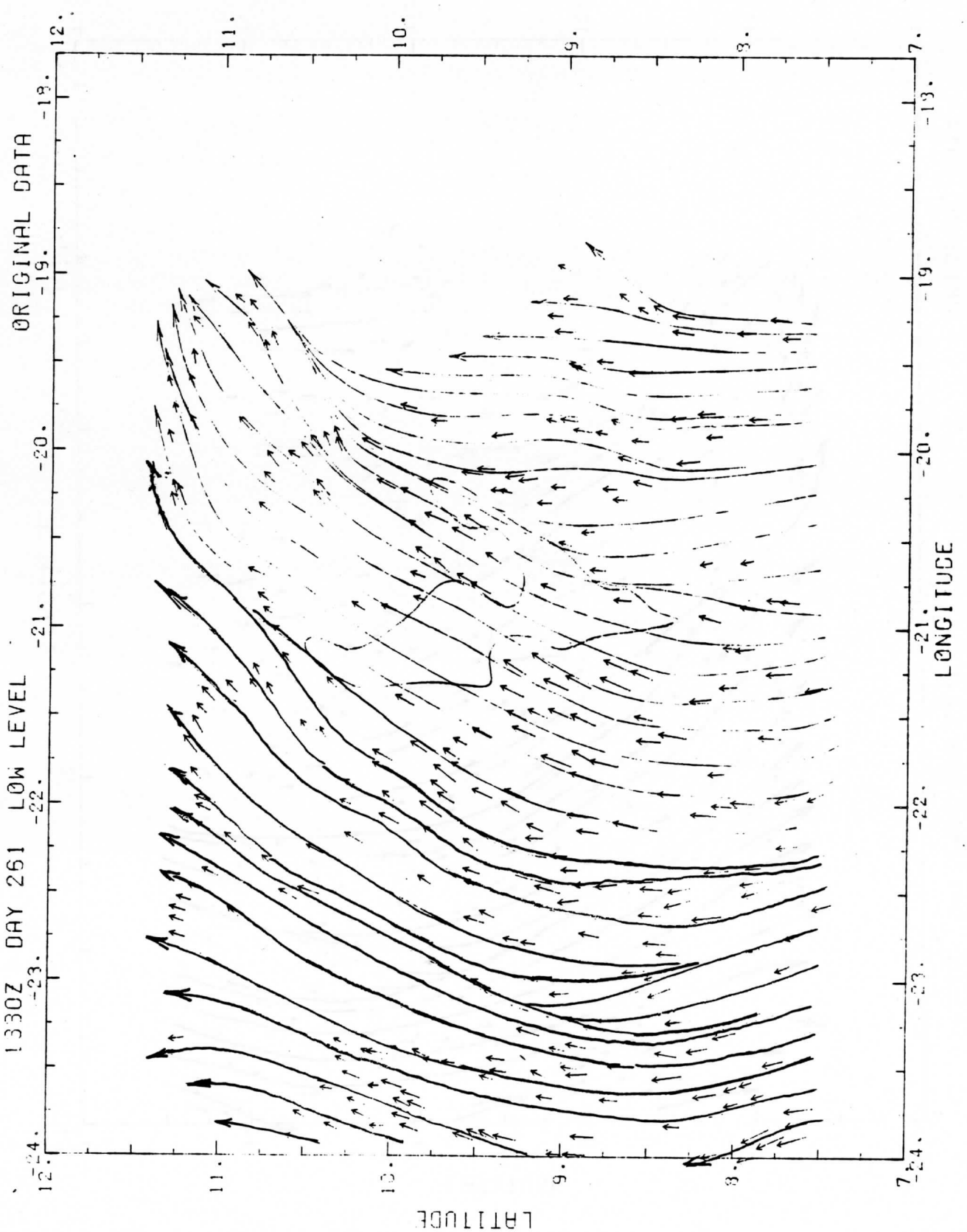
ORIGINAL DATA
1330Z DAY 261 LOW LEVEL
LONGITUDE
LATITUDE
12.
11.
10.
9.
8.
7.
-18.
-19.
-20.
-21.
-22.
-23.
-24.

Figure 2

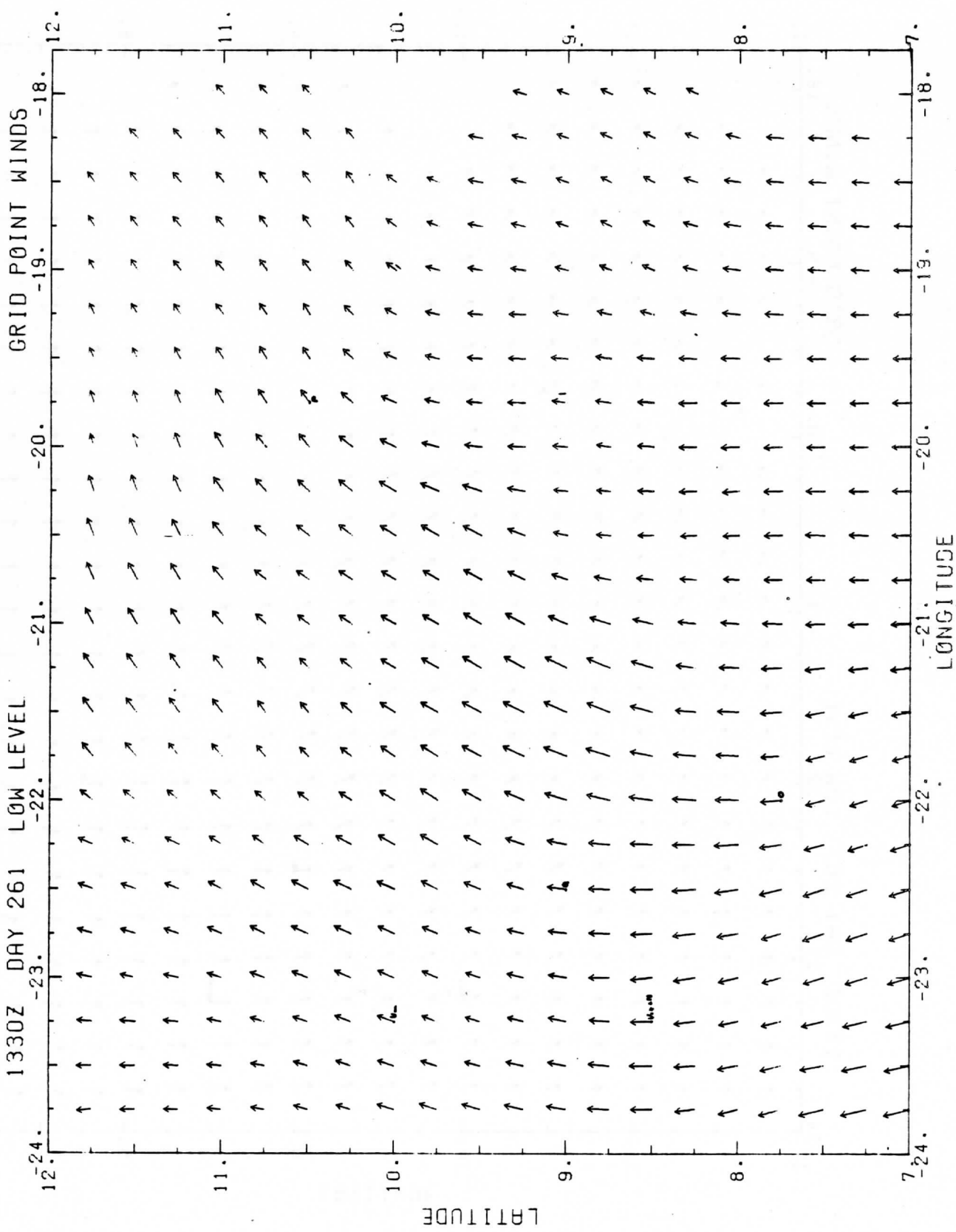
1330Z DAY 261 LØW LEVEL
GRID PØINT WINDS
LATITUDE
LØNGITUDE
12.
11.
10.
9.
8.
7.
-18.
-19.
-20.
-21.
-22.
-23.
-24.

Figure 3

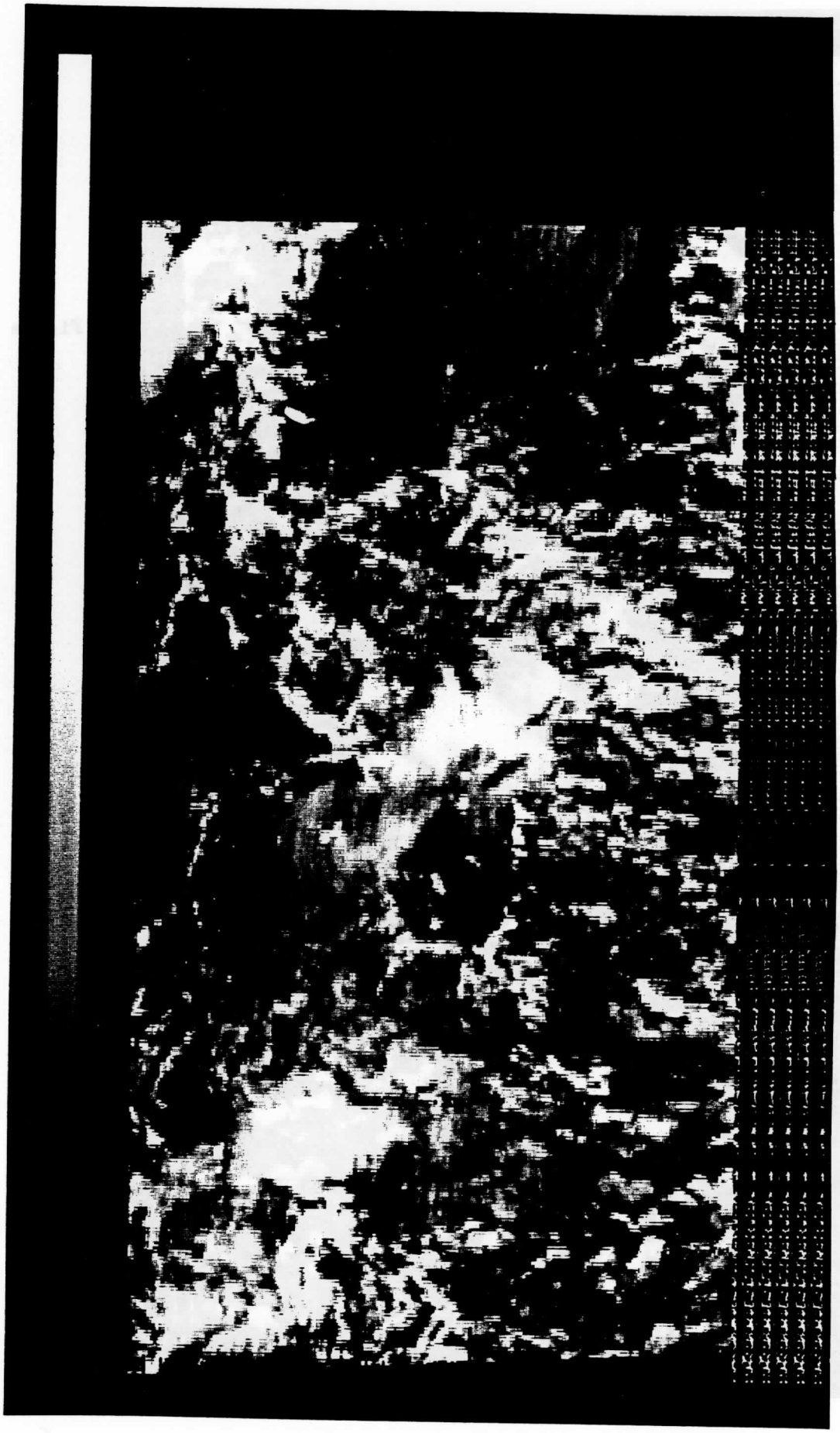

Figure 4

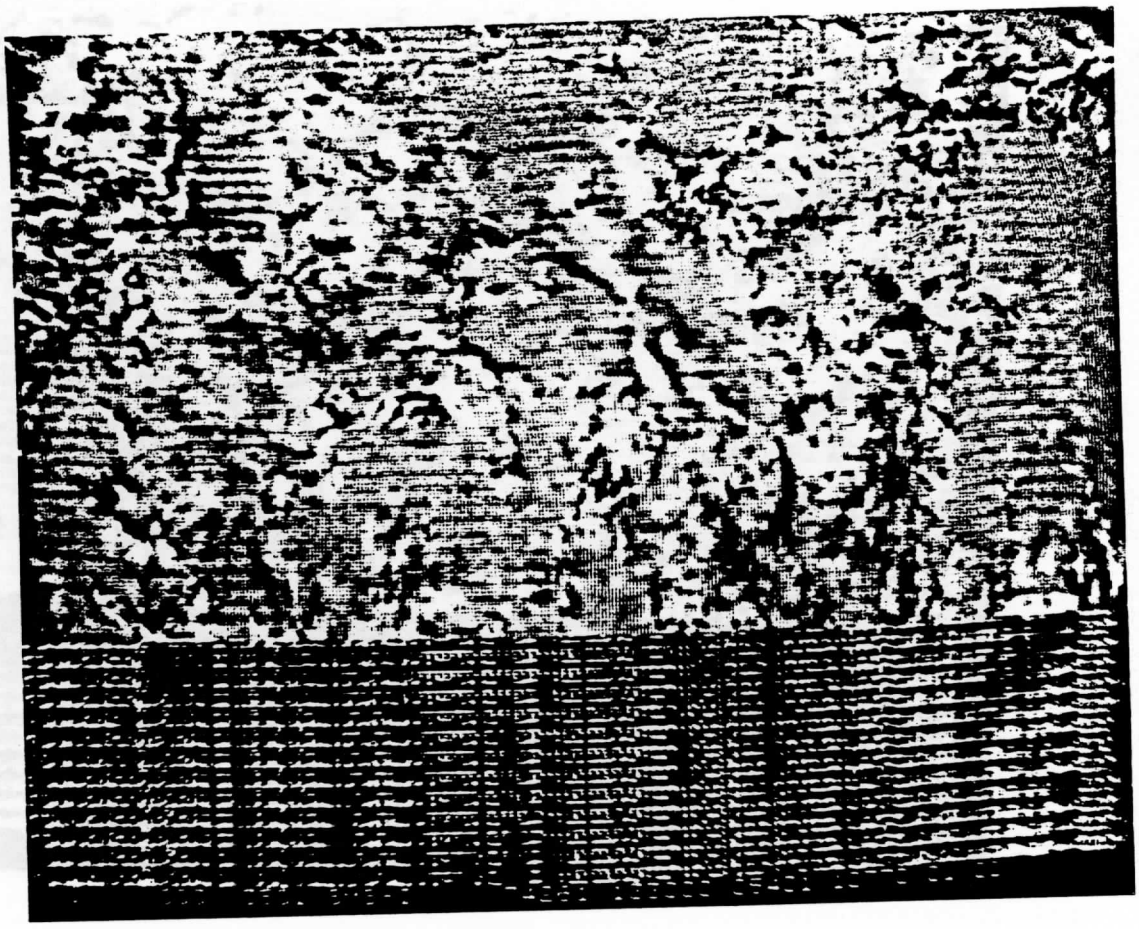

Figure 5

Visible Flux Variations Across Finite Clouds

Frederick R. Mosher

Space Science and Engineering Center
University of Wisconsin-Madison
1225 West Dayton Street
Madison, Wisconsin 53706

January 1979

VISIBLE FLUX VARIATIONS ACROSS FINITE CLOUDS

Frederick Ray Mosher

Under the supervision of Professor Verner E. Suomi

A new radiative transfer model has been developed to handle visible flux variations across and within finite clouds of varying shapes. The model was developed to investigate the parameters which influence the brightness patterns observed on satellite images. The model, called the "building block model," determines flux distributions by joining small cubes, whose radiative transfer characteristics have been determined with a previous Monte Carlo simulation, to form larger clouds. The interactions between the cubes are solved by using iterative techniques. The method has much of the versatility of Monte Carlo models to handle a large variety of cloud shapes, as well as the speed of the analytical finite cloud models.

Simulations with the model show that the fluxes coming from all external regions of finite cubic clouds, including the center regions, departed significantly from the plane-parallel results. Investigations into the effects of regions of liquid water concentrations near the cloud top showed the inhomogeneity appeared as a bright region for the overhead sun, but had very little effect at large solar zenith angles. For the overhead sun case, when the region of liquid water concentration was placed beneath the cloud top, the bright spot was not nearly as noticeable. When the concentration was more than an optical thicknesses of 25 (about 1 km) below the top, the bright spot completely

disappeared.

Simulations with a tower on top of a cubic cloud showed the tower to appear darker than the main body of the cloud for the overhead sun, but to appear brighter than the main body of the cloud when the sun was near the horizon. Clouds shaped like cylinders, truncated spheres, inverted parabaloids, and cubes were approximated by assemblies of cubic elements. Each of these shapes showed a different relationship of albedo and solar zenith angle. Clouds simulated by assemblies of cubic elements matched aircraft flux measurements better when the overall cloud shape resembled the observed cloud shape than when the cubic elements were assembled into a simple 'box' shape of equivalent dimensions.

Approved: _____
Verner E. Suomi

Date: 1-12-79

1. Introduction

The theoretical development of radiative transfer is not yet sufficiently sophisticated to adequately treat the problem of visible light scattering in naturally occurring clouds. Interpretation of satellite cloud images in particular has been hampered by the deficiencies of radiative transfer theories. Meteorological satellites have made available on a routine basis high resolution visible images of clouds. These images are used to make subjective judgments about meteorological features (Anderson, et al., 1974). Much of the development of these qualitative uses of satellite data has been based on intuitive interpretation of the visible cloud images. An underlying explanation of what causes the brightness variations of clouds is needed.

The development of quantitative meteorological measurements from visible satellite images has depended heavily on empirically derived relationships. Rainfall estimation efforts by Follensbee (1976), Barrett (1975), Sikdar (1972), and Griffith et al. (1978) have been empirically oriented, as have cloud thickness efforts of Griffith and Woodley (1973) and Kaveney et al. (1977). Improvements in these quantitative measurement techniques require a firmer foundation of visible light scattering in clouds.

Most of the theoretical work dealing with cloud scattering of light has dealt with plane-parallel homogeneous clouds. These theoretical clouds are flat on the top and bottom and extend out to infinity

in the horizontal direction. Results of Hansen (1971b), Twomey et al. (1967), and others have shown that the scattered light is related to the cloud thickness. As the cloud gets thicker, the reflected brightness increases toward an asymptotic limit. When the cloud is a kilometer or so thick, the cloud has very nearly reached its full brightness limit. From these theoretical plane-parallel results one would expect clouds thicker than a kilometer to be very bright and to have a uniform brightness. Digital satellite visible images show a large variability of brightness with any given cloud. Griffith and Woodley (1973) and Reynolds and Vonder Haar (1973) showed a relationship between cloud height (thickness) and satellite observed brightness for convective clouds in the range of 3 to 15 kilometers. Plane-parallel theory will not explain this observed relationship.

The theoretical treatment of clouds with finite horizontal domain has been done using Monte Carlo techniques by Busygin et al. (1973) for cylinder, parabaloid, and sphere clouds, and by McKee and Cox (1974) for cubic clouds. They showed that light is scattered out the sides of the clouds resulting in a decrease in brightness of the top surface as compared to plane-parallel results. McKee and Cox (1976) have argued that the brightness-height (thickness) relationship observed by Griffith and Woodley (1973) could be due to increased cloud width rather than increased cloud thickness. Davies (1976, 1978b) has shown that the height to width ratio of cuboidal clouds is important in determining the amount of light scattered in a given direction. Reynolds et al. (1978) have shown from satellite data that the height to width ratio effect

predicted by cuboidal cloud models agrees with observed cloud brightnesses. As the clouds of a given thickness got wider, they became brighter. Aida (1977) has shown that the spacing between finite cubes in an array can also influence the reflected brightness of the cloud.

The evidence is starting to mount that the horizontal as well as the vertical dimension is important in scattering of light from clouds. Realistic clouds are not smooth geometric figures. They have texture in addition to their finite geometry. The question of cloud top texture for semi-infinite clouds has been investigated by Weinman and Swarztrauber (1968) for sinusoidal variations of cloud top texture, and by Van Blerkom (1971), Wendling (1977), and Davies (1976) for square wave striations. They have shown for an overhead sun, the presence of cloud top texture decreases the upward scattered light. McKee and Klehr (1978) showed that with the sun overhead, a turret on top of a cubic cloud would appear darker than the parent cubic cloud.

The above studies of finite clouds used Monte Carlo simulations for the radiative transfer of the visible light in clouds. While the Monte Carlo technique is well suited to studies with finite geometric boundaries, it requires large amounts of computer time. A Monte Carlo model can require hours of CPU time. Hence, while Monte Carlo simulations are useful for studying the effects of different geometries, they are not practical for applications of operational problems of radiative transfer because of the excessive computer time required.

Because of the computer costs of Monte Carlo simulations, models which will run faster are being developed. Barkstrom and Arduini

(1976) have treated a cylindrical cloud geometry using a diffusion equation applied to the transfer of radiation within a homogeneous cloud. Davies (1976) has developed an analytical model using the Eddington approximation to the radiative transfer equation applied to homogeneous cuboidal clouds. Davies (1978a) has used his analytical model to investigate the spatial variations of intensity and flux across the finite cuboidal cloud. The main problem with the analytical models is that they are constrained to a limited number of homogeneous geometric shapes. The problems of cloud top texture, liquid water inhomogeneities, etc., cannot be handled by the existing analytical models.

In this paper a new radiative transfer model will be developed which can treat the problems of cloud top texture and liquid water inhomogeneities for finite clouds in addition to treating the problem of flux variations across the top of finite clouds. Section 2 develops the model. Section 3 contains an error analysis and shows comparisons with other models. Section 4 shows results of the model. Questions of flux variations across finite clouds are investigated. Comparisons between the finite cloud and the plane-parallel results are made. The model is used to show the effects of liquid water inhomogeneities, cloud top towers, and cloud shape. Section 5 contains the discussions and conclusions.

2. Building Block Finite Cloud Model

This section describes a new approach to the finite cloud multiple scatter simulation problem. This approach is a geometric one and is conceptually similar to a three-dimensional doubling or adding method. It avoids the exorbitant costs which repeated applications of a Monte Carlo model require and also avoids many of the constraints of the existing analytical finite cloud models. The cloud scattering model consists of an array of building block cubes stacked together. The starting element of this model is a small cube whose radiative scattering characteristics have been determined from a Monte Carlo model. An input flux illuminates one of the faces of the cube. The Monte Carlo model is then used to determine the flux (energy/unit area) exiting each of the six faces of the cuboid. For flux entering the top of the cube the fraction exiting the top will be designated as the transfer function T; the fraction exiting the bottom will be designated B; and the fraction exiting each side will be designated S. Figure 1 illustrates this initial cubic transfer function for the case where the flux enters the top of the cube. Naturally, such a transfer function also serves for flux entering the sides or bottom. Because of the symmetry of the cube, the light coming in a side and going out the top has the same transfer function as light coming in the top and going out a side.

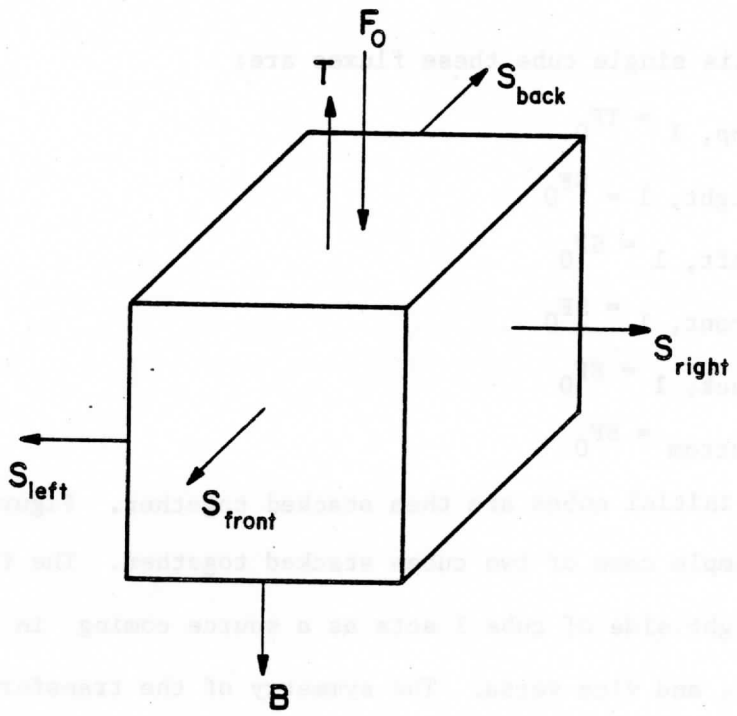

Fig. 1. The initial cubic transfer function is determined from a Monte Carlo simulation. The simulation has flux entering one face of the cuboid and being scattered out the six faces of the cube.

The fluxes coming out of the various faces of cube 1 are:

$$
\begin{aligned}
&F_0 = \text{input flux} \\
&F_{\text{top, 1}} = \text{flux coming out of top of cube 1} \\
&F_{\text{right, 1}} = \text{flux coming out of right side of cube 1} \\
&F_{\text{left, 1}} = \text{flux coming out of left side of cube 1} \\
&F_{\text{front, 1}} = \text{flux coming out of front side of cube 1} \\
&F_{\text{back, 1}} = \text{flux coming out of back side of cube 1} \\
&F_{\text{bottom, 1}} = \text{flux coming out of bottom of cube 1.}
\end{aligned}
\tag{3.1}
$$

For this single cube these fluxes are:

$$
\begin{aligned}
F_{top,\ 1} &= TF_0 \\
F_{right,\ 1} &= SF_0 \\
F_{left,\ 1} &= SF_0 \\
F_{front,\ 1} &= SF_0 \\
F_{back,\ 1} &= SF_0 \\
S_{bottom} &= BF_0
\end{aligned}
\qquad (3.2)
$$

These initial cubes are then stacked together. Figure 2 illustrates the simple case of two cubes stacked together. The flux coming out of the right side of cube 1 acts as a source coming in the left side of cube 2, and vice versa. The symmetry of the transfer function can be

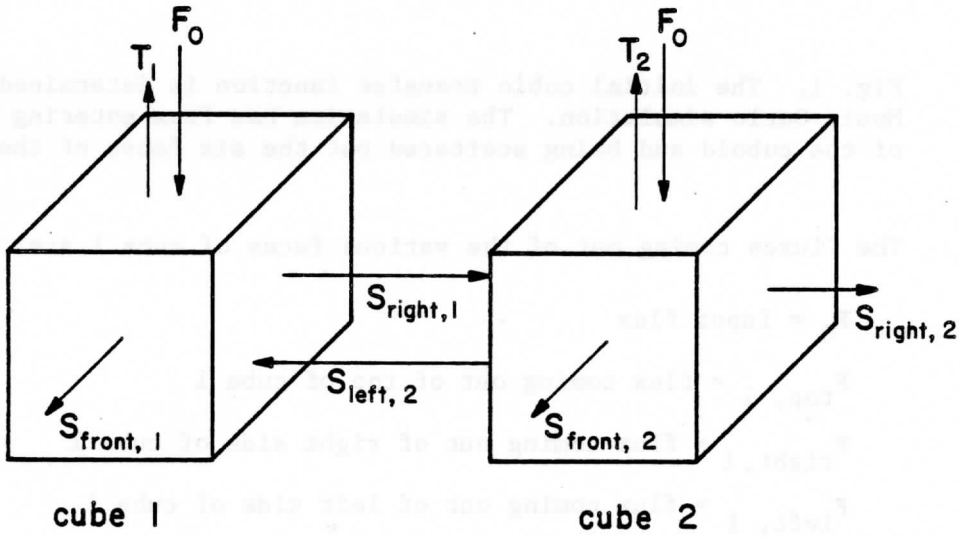

Fig. 2. The simplest case of the building block model is when two cubes are stacked together. The flux coming out the left side of cube 2 acts as a source as it enters the right side of cube 1, and vice versa. The fluxes from the cubes form a set of coupled, linear, simultaneous equations which can be solved by algebraic means.

applied to flux coming in the sides. The total fluxes coming out of each face of the cube are given by:

Cube 1		Cube 2	
$F_{top,\ 1} = TF_0 + SF_{left,\ 2}$		$F_{top,\ 2} = TF_0 + SF_{right,\ 1}$	
$F_{right,\ 1} = SF_0 + TF_{left,\ 2}$		$F_{right,\ 2} = SF_0 + BF_{right,\ 1}$	
$F_{left,\ 1} = SF_0 + BF_{left,\ 2}$		$F_{left,\ 2} = SF_0 + TF_{right,\ 1}$	
$F_{front,\ 1} = SF_0 + SF_{left,\ 2}$	(3.3)	$F_{front,\ 2} = SF_0 + SF_{right,\ 1}$	(3.4)
$F_{back,\ 1} = SF_0 + SF_{left,\ 2}$		$F_{back,\ 2} = SF_0 + SF_{right,\ 1}$	
$S_{bottom,\ 1} = BF_0 + SF_{left,\ 2}$		$S_{bottom,\ 2} = BF_0 + SF_{right,\ 1}$	

These coupled, linear, simultaneous equations can be solved with algebraic or iterative methods.

By stacking a large number of cubes together, larger clouds can be constructed. Each cube has six faces, with six output fluxes and six input fluxes from adjacent cubes. Let I_{top} be the flux input to the top of the cube (which is output from the bottom of the cube above it); I_{right} can be the input flux into the right face, etc. The output fluxes from the cube are then:

$$F_{top} = TI_{top} + BI_{bottom} + SI_{right} + SI_{left} + SI_{front} + SI_{back} \quad (3.5)$$

$$F_{right} = SI_{top} + SI_{bottom} + TI_{right} + BI_{left} + SI_{front} + SI_{back} \quad (3.6)$$

$$F_{left} = SI_{top} + SI_{bottom} + BI_{right} + TI_{left} + SI_{front} + SI_{back} \quad (3.7)$$

$$F_{front} = SI_{top} + SI_{bottom} + SI_{right} + SI_{left} + TI_{front} + BI_{back} \quad (3.8)$$

$$F_{back} = SI_{top} + SI_{bottom} + SI_{right} + SI_{left} + BI_{front} + TI_{back} \quad (3.9)$$

$$F_{bottom} = BI_{top} + TI_{bottom} + SI_{right} + SI_{left} + SI_{front} + SI_{back} \quad (3.10)$$

Hence, there are six equations with six unknowns for each cube. T, B, and S are the known transfer functions for the top, bottom, and side obtained from the original Monte Carlo simulation. The output fluxes from interior cubes are the input fluxes for their neighboring cubes. If there are N cubes, then there are 6N linear equations with 6N unknowns. By specifying the fluxes at the exterior boundaries of the building block cloud, the equations can be solved using algebraic or iterative techniques.

An iterative approach to solve the linear simultaneous equations was used because familiar matrix methods for inverting the resultant matrix equation, such as Gaussian elimination, are very expensive and/or very cumbersome as the number of cubes increases. For instance, a cubic cloud constructed from an array 15 x 15 x 15 smaller cubes will have 3,375 cubes and 20,250 equations with 20,250 unknowns. An iterative approach for solving this type of system of equations is commonly used by researchers numerically solving elliptic partial differential equations. For the case where the system of equations are nonlinear, a variation of this approach, using Newton's method, is outlined by Greenspan (1974). If the equations are rewritten as:

$$f(I_1, I_2 \ldots I_6, F_i) = I_1 a + I_2 b + I_3 c + I_4 d + I_5 e + I_6 f - F_i \qquad (3.11)$$

with a, b,...f being the appropriate transfer function, I_i, $I_2 \ldots I_6$ being the input fluxes, and F_i the output flux across the ith face, then Newton's method can be used to find where $f(I_1, I_2 \ldots, F_i) = 0$ for all coupled equations.

Newton's method for a single equation is the well known iterative formula:

$$x^{n+1} = x^n - \frac{f(x^n)}{f'(x^n)} \tag{3.12}$$

where the superscript n is the iteration cycle. The system of equations becomes:

$$x_1^{n+1} = x_1^n - \frac{f(x_1^n,\ x_2^n \ldots x_m^n)}{\frac{\partial f(x_1^n,\ x_2^n \ldots x_m^n)}{\partial x_1}}$$

$$x_2^{n+1} = x_2^n - \frac{f(x_1^{n+1},\ x_2^n \ldots x_m^n)}{\frac{\partial f(x_1^{n+1},\ x_2^n \ldots x_m^n)}{\partial x_2}} \tag{3.13}$$

$$\vdots$$

$$x_m^{n+1} = x_m^n - \frac{f(x_1^{n+1},\ x_2^{n+1} \ldots x_m^n)}{\frac{\partial f(x_1^{n+1},\ x_2^{n+1} \ldots x_m^n)}{\partial x_m}}$$

Note that for x_2, the value of x_1^{n+1} is used in the Newton evaluation of x_2^{n+1}, so the newly generated value is utilized as fast as it is generated. This usage accelerates the convergence rate.

In the system of equations for the finite clouds, the input fluxes at the boundaries are specified. The input fluxes of any internal cube face are the output fluxes of adjacent cubes. Hence, only the output fluxes need to be solved for. For the equation 3.11

the $\partial f/\partial F_i = -1$. The iteration formula is then:

$$F_i^{n+1} = F_i^n + f(I_1, I_2 \ldots I_6, F_i) \qquad (3.14)$$

The initial guess of the output fluxes across internal faces is zero. The iteration continues until all the output fluxes are in radiative equilibrium and approaching a limiting value. The radiative equilibrium is specified as the total input flux being equal to the total output flux to within 10^{-5} for all cubes. The approaching limiting value is specified when the most rapidily changing flux is within 10^{-4} of its previous iterative value. The computation time required to solve the system of equations is quite small. For cubic clouds made up of 10 x 10 x 10 smaller cubes the computation time required in a UNIVAC 1110 computer was on the order of 30 seconds. Hence, the computation time required of this building block approach is in the seconds to minutes range which is typical of the analytical finite cloud methods as opposed to the minutes to hours required for many of the Monte Carlo simulations.

Figures 3a, b, and c show the fluxes coming out of the top, bottom, and front side faces of a cube with optical dimensions 100. The bigger cube was constructed from an array of 10 x 10 x 10 smaller cubes with optical dimension 10. The transfer functions for the smaller cube are obtained from the Monte Carlo tabulations in Appendix E of Davies (1976). The sun is overhead and the phase function is strongly peaked in the forward direction so as to match the Deirmendjian (1969) phase function for the C1 cloud at .45 microns. The input flux to the cubes is 1.

TOP FACE OF CLOUD

.299	.394	.429	.443	.448	.448	.443	.429	.394	.299
.394	.534	.589	.613	.622	.622	.613	.589	.534	.394
.429	.589	.656	.686	.697	.697	.686	.656	.589	.429
.443	.613	.686	.719	.732	.732	.719	.686	.613	.443
.448	.622	.697	.732	.745	.745	.732	.697	.622	.448
.448	.622	.697	.732	.745	.745	.732	.697	.622	.448
.443	.613	.686	.719	.732	.732	.719	.686	.613	.443
.429	.589	.656	.686	.697	.697	.686	.656	.589	.429
.394	.534	.589	.613	.622	.622	.613	.589	.534	.394
.299	.394	.429	.443	.448	.448	.443	.429	.394	.299

AVERAGE FLUX ACROSS THIS FACE= .570330

$\tau_y = 100$ (vertical) $\tau_x = 100$ (horizontal)

Fig. 3a. Example of the results of the building block model. The flux variation across the top of a cube of optical dimension 100 x 100 x 100 is shown. The input flux has 1 with an overhead sun. The illustrated cube was constructed from 10 x 10 x 10 smaller building blocks of optical dimension 10.

BOTTOM FACE OF CLOUD

.002	.003	.004	.005	.005	.005	.005	.004	.003	.002
.003	.006	.008	.009	.010	.010	.009	.008	.006	.003
.004	.008	.011	.013	.014	.014	.013	.011	.008	.004
.005	.009	.013	.015	.016	.016	.015	.013	.009	.005
.005	.010	.014	.016	.018	.018	.016	.014	.010	.005
.005	.010	.014	.016	.018	.018	.016	.014	.010	.005
.005	.009	.013	.015	.016	.016	.015	.013	.009	.005
.004	.008	.011	.013	.014	.014	.013	.011	.008	.004
.003	.006	.008	.009	.010	.010	.009	.008	.006	.003
.002	.003	.004	.005	.005	.005	.005	.004	.003	.002

AVERAGE FLUX ACROSS THIS FACE= .009047

$\tau_y = 100$ (vertical) $\tau_x = 100$ (horizontal)

Fig. 3b. Same as Fig. 3a except this illustrates the flux variation coming out of the bottom of the cube.

FRONT FACE OF CLOUD

.348	.445	.481	.495	.500	.500	.495	.481	.445	.348
.151	.224	.260	.277	.284	.284	.277	.260	.224	.151
.075	.122	.151	.166	.173	.173	.167	.151	.123	.075
.042	.072	.092	.104	.110	.110	.104	.092	.072	.042
.025	.044	.058	.067	.071	.071	.067	.058	.044	.025
.015	.028	.037	.043	.046	.046	.043	.037	.028	.015
.010	.017	.024	.028	.030	.030	.028	.024	.018	.010
.006	.011	.015	.018	.019	.019	.018	.015	.011	.006
.003	.006	.009	.010	.011	.011	.010	.009	.006	.003
.002	.003	.004	.005	.005	.005	.005	.004	.003	.002

AVERAGE FLUX ACROSS THIS FACE= .104882

$\tau_z = 100$ (vertical) $\tau_x = 100$ (horizontal)

Fig. 3c. Same as Fig. 3a except this illustrates the flux variation coming out the side of the cube.

The figures illustrate that there is a flux variation across the top and sides due to the light leaking out the sides. While the strongest variation across the top is nearest the edges, there is still a noticeable variation in the interior regions of the cloud top.

The non-vertical incidence of light was handled by the building block model by decomposing the incident flux into vertical and horizontal components, and applying these fluxes normal to the top and side faces. The incident flux was still kept at 1. However, because of the finite vertical extent of the cloud the cloud intercepts greater than unit flux. For the non-vertical incidence of light, the input flux on the top surface was $\cos \Theta_o$/unit area and the flux on the side surface was $\sin \Theta_o$/unit area with Θ_o being the solar zenith angle. This convention was adopted because this is a situation which would be observed by a satellite or an airplane viewing a naturally occurring cloud.

3. Error Analysis

The building block model has three main sources of errors. One is the limited number of allowable angles within the model. The flux is modeled normal to the six faces of the cube, so only six directions are allowed in this configuration of the model. For a symmetric geometry case, this reduces down to three directions (the light coming out of the top, side, and bottom). For a strong anisotropic scattering situation, this limited angular representation can cause errors. For the case where the light enters the top of the cube, the model assumes that the light coming out the sides has the energy equally distributed. That means an equal amount of the energy is going up as is going down. For strong anisotropic scattering, this is not the case. In the tabulated results of McKee and Cox (1974) and Davies (1976) for the energy coming out of the sides, more goes down than up. Since the model assumes an equal amount going up as down, the model therefore overestimates the amount of radiation going up because of the limited directional resolution.

The second major error source in the building block model is caused by the discrete representation of gradients. The model assumes that the energy is uniformly distributed across each face of the cube. A brightness gradient is built up by having a number of cubes along the gradient representing the gradient in a stepwise fashion. This discrete representation of a continuous variable can cause errors. In the case of the overhead sun, there is a vertical gradient of flux through the cloud which the building block model samples at a discrete

number of points. Within each cube the top should be brighter than the bottom because of the vertical gradient, but the model assumes an average flux across the cube. If the gradient is linear across the cube this assumption causes no problem. However, even with a non-linear gradient the model still distributes the energy in a linear fashion. With a vertical gradient the model brings the energy further down than is the case. As a result the model underestimates the amount of radiation exiting from the top.

The third major error source comes from decomposing the non-vertical incident flux into vertical and horizontal components, and applying these fluxes normal to the top and side faces. Phenomena such as the incident beam passing through a corner and showing up on the shadowed faces are not represented well by the decomposition arrangement of the building block model.

3.1 Plane Parallel Error Analysis

An attempt was made at quantifying the expected errors of the building block model. The building block model was reconfigured in a plane parallel homogeneous model by having cyclic boundary conditions on the sides of the model. Any energy coming out the right side of the model re-entered on the left side. Likewise, any energy coming out the front re-entered the rear. The purpose of reconfiguring the building block model into a plane parallel model was to gain a quantitative insight into the errors caused by limited number of angles and the discrete representation of gradients in a simple one-dimensional framework. Since the three-dimensional building block model

decomposes the oblique incident flux into normal vertical and horizontal components, the one-dimensional analysis was done for normal incident flux. The model was run for various combinations of optical thickness cubes and number of cubes in the vertical column. The model was run first with an isotropic phase function to investigate the errors due to the discrete nature of the model. Then an anisotropic phase function was used to investigate the errors due to the strong forward scattering phase function peak. The initial transfer functions for the cubes were obtained from the appendix of Davies (1976) for both the isotropic and anisotropic phase functions, as were the plane parallel results.

Figure 4 shows the percent error $\left(\frac{\text{building block-plane parallel}}{\text{building block}}\right)*100$ of the building block model configured as a plane parallel model for an isotropic phase function.

The horizontal axis is the initial optical thickness of the cube used to build up the cloud. The vertical axis is the number of cubes used in the vertical column. The numbers and contours on the figure are the percent error associated with this configuration of building blocks. Positive errors indicate that the building block model overestimated the upward flux as compared to the rigorous plane parallel results. The figure shows that the errors in the discrete formulation of the radiative transfer for isotropic scattering are generally less than 10 percent. The worst cases are for the single cubes which must model the flux gradient with a single discrete step. The errors are reduced when more cubes are used to model the gradient through the

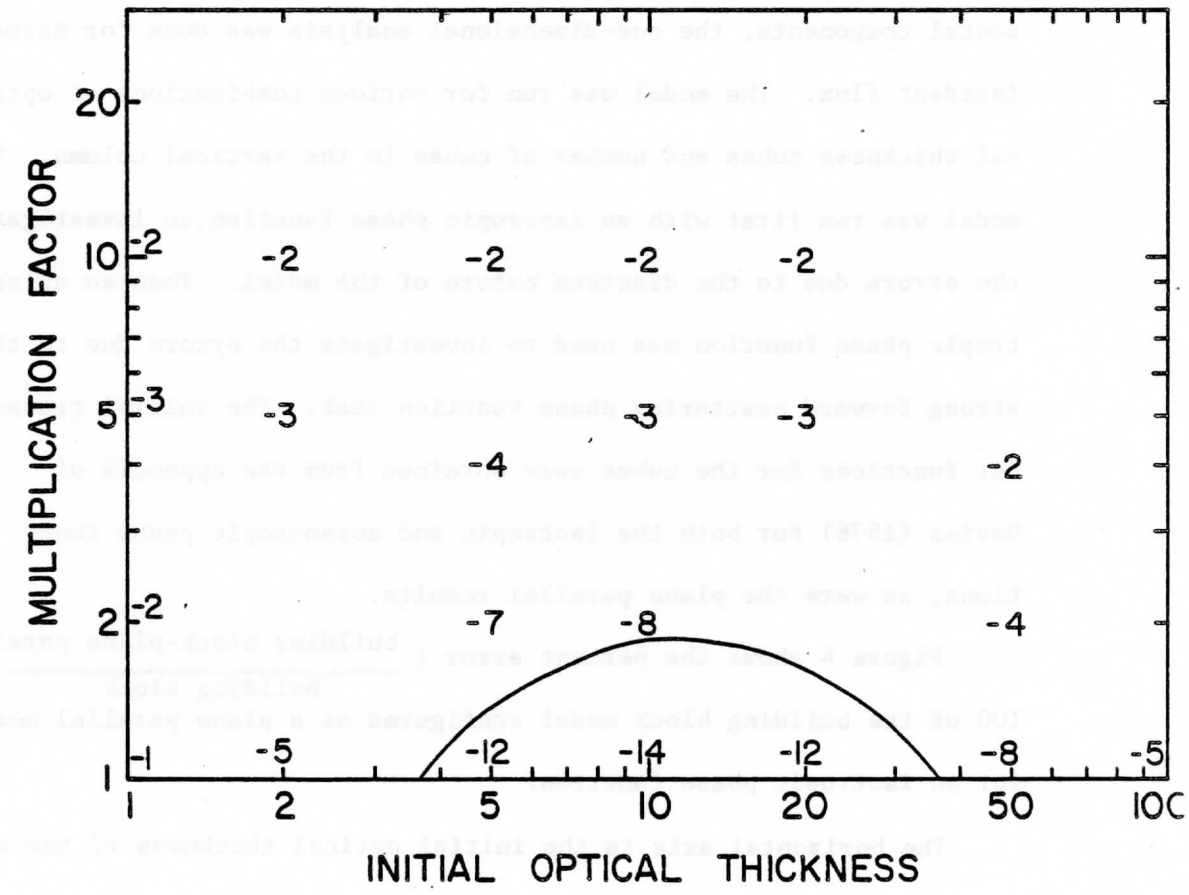

Fig. 4. Error analysis of the building block model reconfigured to compute reflected plane-parallel flux with normal incident flux with an isotropic phase function. The absissa is the initial size of the cube used in the model. The axis of the ordinates is the number of cubes in a vertical column in the model. The contours are the percent error

$$\frac{(\text{building block} - \text{plane parallel})}{\text{building block}} \times 100$$

associated with this configuration. Positive values indicate that the building block model overestimated the upward flux.

cloud.

Figure 5 shows the percent error for an anisotropic phase function with an asymmetry factor of g = .855 used in the building block model configured as a plane parallel model. The figure shows that the anisotropic character of small cubes can cause significant errors in overestimating the reflected flux. The errors can be reduced by increasing the number of cubes. This has the effect of making a larger optical path which will have more multiple scattering to reduce the anisotropic nature of the scattering. The total optical depth of the cloud must be between 15 and 30 before the error drops below the 10% level. Hence the building block model is not appropriate for clouds smaller than optical dimensions 15 to 30. When the individual building block cube size becomes quite large, such as 50 to 100 optical dimensions, then the model underestimates the upward flux because of the discrete gradient representation of the model. This underestimation discrete gradient problem is not as severe a problem as the overestimation anisotropic problem of the smaller cubes.

Figure 5 contains both the discrete gradient and the anisotropic errors, while Figure 4 contains only the discrete gradient errors. The difference between the two figures will give an estimate of the errors associated with the anisotropic scattering in the model. Figure 6 shows the percent error due to the anisotropic scatter [% error Figure 5 - % error Figure 4] in the building block model.

The percent errors of Figures 4, 5, and 6 can be used to define some bounds of the errors expected from finite cloud simulations.

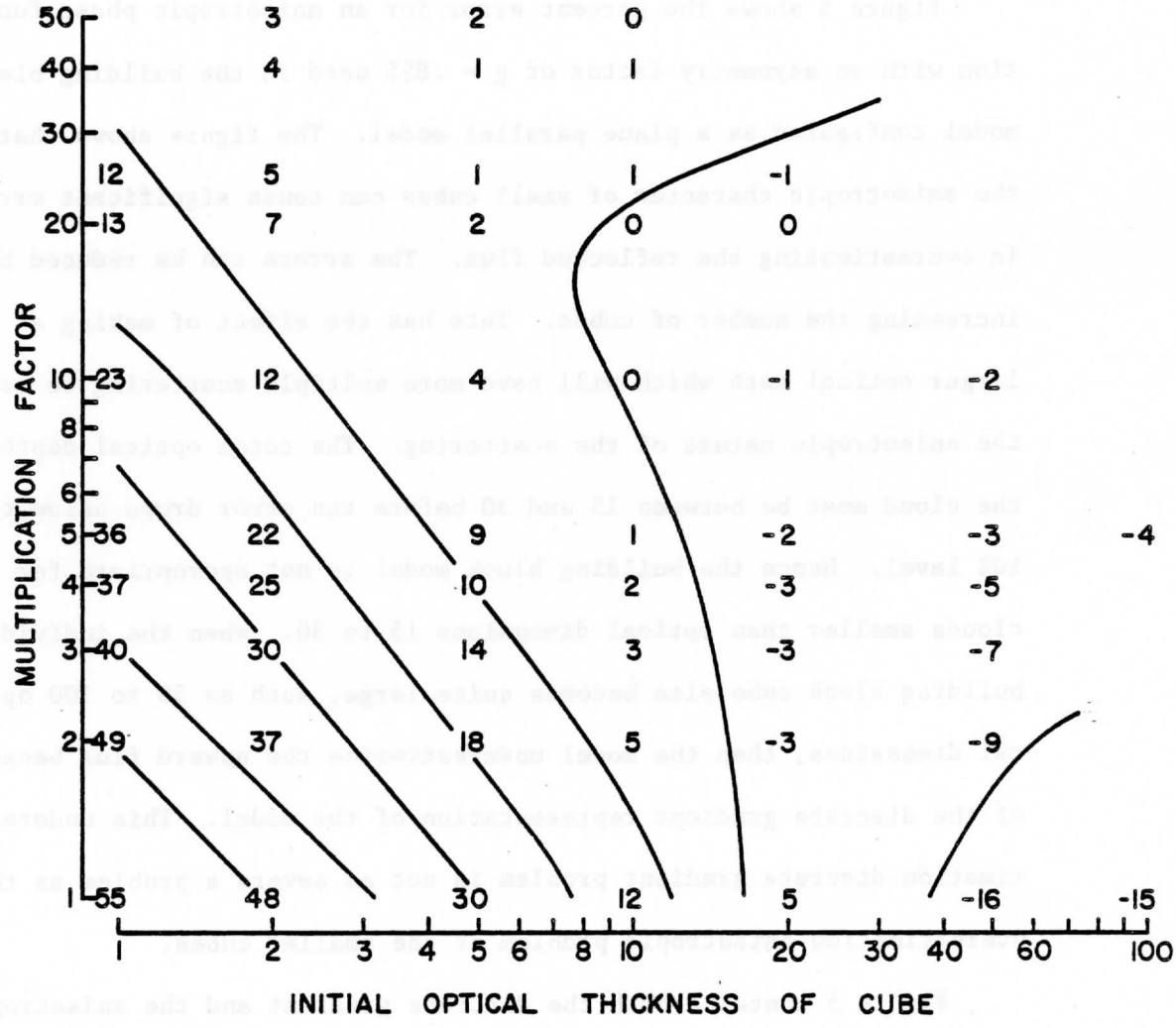

Fig. 5. Error analysis of the building block model reconfigured to compute plane parallel fluxes with an anisotropic phase function typical of visible light scattering in water clouds.

The bottom of Figure 5 shows the error associated with a plane parallel simulation using a single cube thickness. The entire vertical gradient needs to be represented within the single cube. This then represents an extreme case of the error which could be expected for a single cube. Calculations which use more than a single cube to represent a gradient should have less error than this extreme for each individual cube.

An example is the cube of 100 optical dimensions of Figure 3 which was made of 10 x 10 x 10 cubes of optical dimension 10. The curves of Figure 5 indicate that the average flux out of each face should have an error approaching 0% (using the figure for the multiplication factor of 10) while each individual cube might be off by as much as 12% (using the figure for the multiplication of 1). Figure 6 shows that any individual cube which has a strong anisotropic nature (such as an edge or corner cube near the sunlit side) could have an error of up to 26%. Figure 4 shows that any individual cube which is in an isotropic region with a strong flux gradient (such as near a nonilluminated edge of a large cloud) could expect errors up to -14%.

3.2 Comparison of Building Block Model with Monte Carlo Models of Cuboidal Clouds

Comparisons of the results of the building block model with the results of the Monte Carlo Models of Davies (1976) and McKee and Cox (1974) have been made. The building block model was configured as a 10 x 10 x 10 cube. Hence a building block of final optical dimension

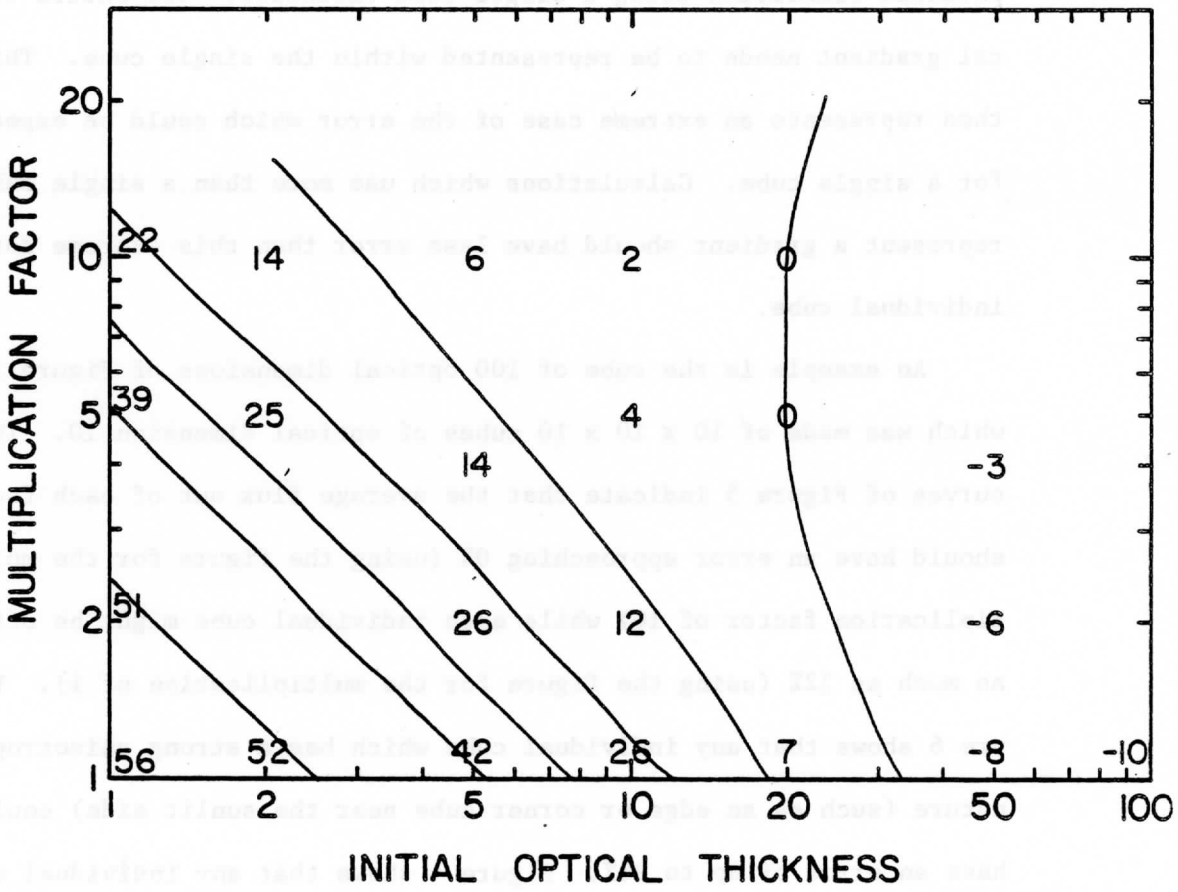

Fig. 6. Difference between Fig. 4 and 5 showing the percent error due to the anisotropic scatter.

20 was constructed out of cubes of optical dimension 2; one of final dimension of 100 was constructed from cubes of dimension 10, etc. The transfer functions used in the building block model were obtained from Appendix E of Davies (1976) for anisotropic scattering. The fluxes across the top of the building block model were averaged together to obtain a quantity for comparison with the Monte Carlo Models.

Comparisons of the building block model with the results of McKee and Cox (1974) show good qualitative agreement of trends but not precise quantitative agreement. Figures 7a, b, and c show the results of McKee and Cox (1974) and the building block model for the fraction of the light incident on the top and side faces which exit the top, bottom, and sides of the cubic cloud. For the overhead sun, the building block model has slightly less light coming out of the sides and more coming out of the top as compared to McKee and Cox (1974). The basic trends are quite similar, however. For the case where the solar zenith angle is 60° the sides of the building block model have more light coming out than McKee and Cox, while the bottom has less. The curves, however, again agree in shape and trends. The building block model in a 10 x 10 x 10 cube configuration was compared with the Monte Carlo results of Davies (1976) for the average flux coming out the top of cubes in the optical thickness range of 5 to 200. Davies (1976) normalized the cube's projected area for incident light to be equal to unity. The building block results were divided by $(\cos \Theta_o + \sin \Theta_o)$ for comparison with Davies' work. Table 1 lists the average flux coming out of the top of cubes for the Monte Carlo (MC) model of Davies

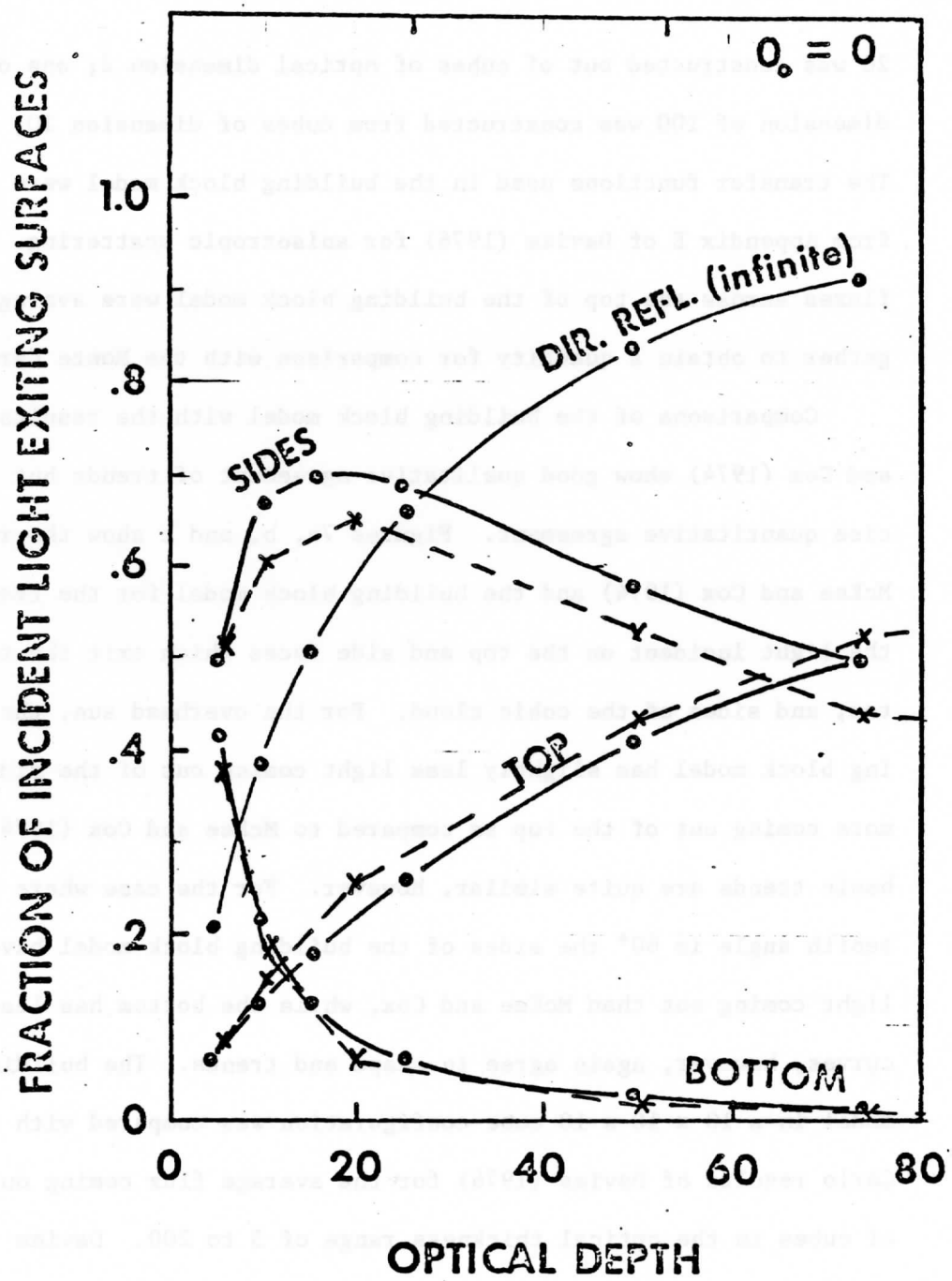

Fig. 7a. Comparison of the fraction of the incident light which exits the top, bottom, and sides of cubic clouds as a function of optical depth for the results of the building block model (dashed lines) and for the results of McKee and Cox (1974) (solid lines). The solar zenith angle is equal to zero degrees.

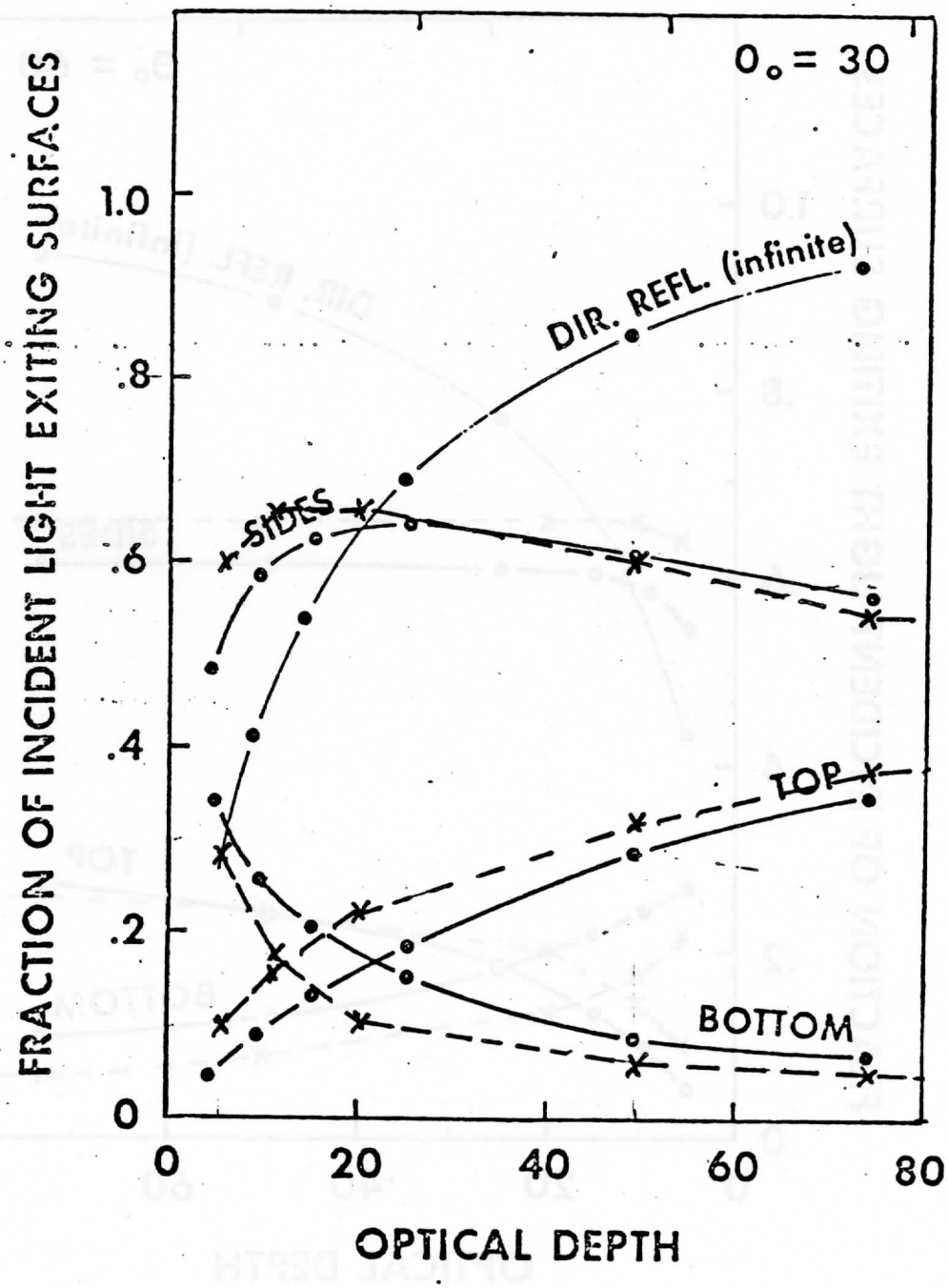

Fig. 7b. Same as Figure 7a, except for a solar zenith angle of 30°.

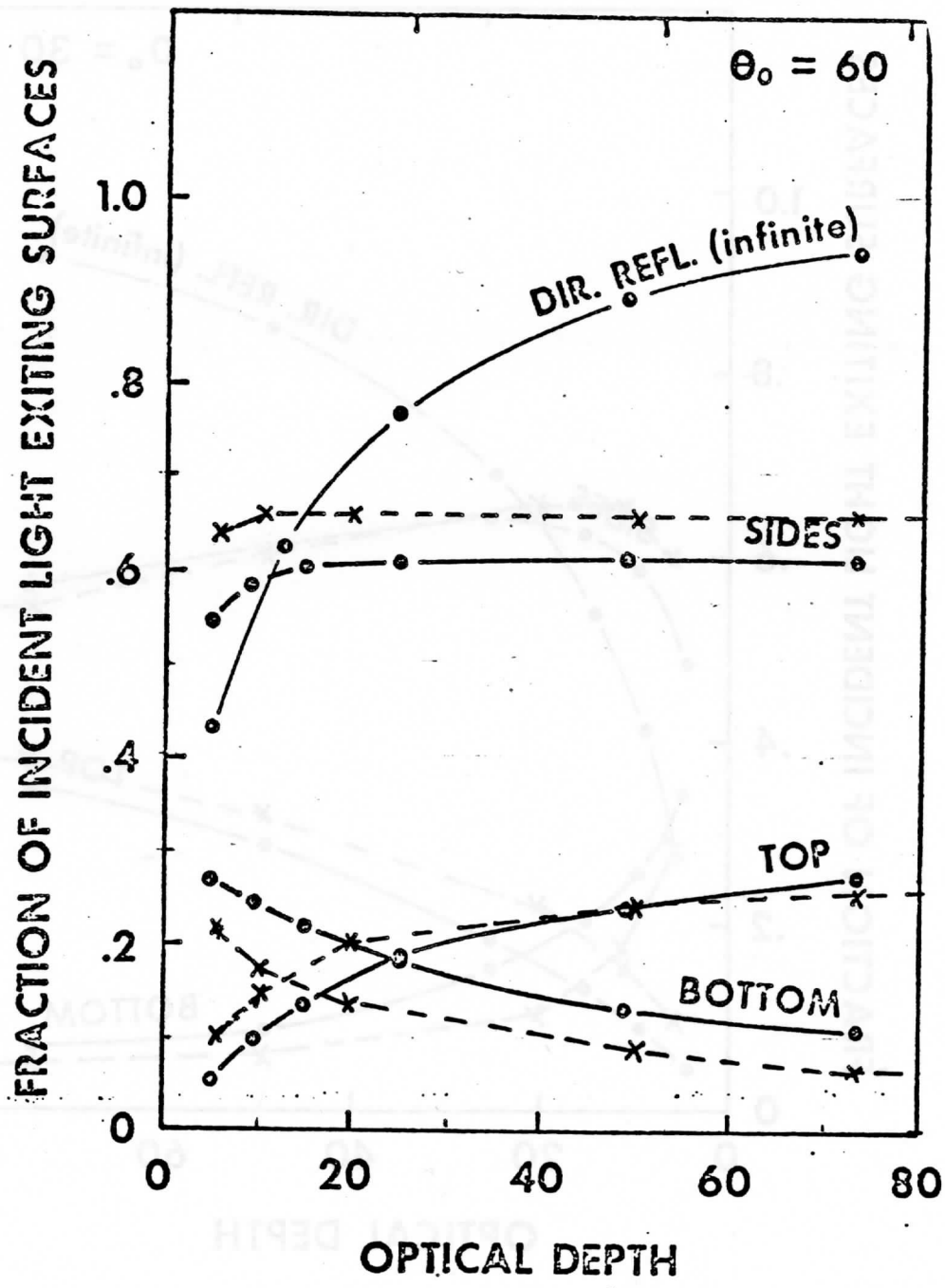

Fig. 7c. Same as Figure 7a, except for a solar zenith angle of 60°.

Table 1

Average flux across the top cubes

τ	θ	MC	FA	$\frac{BB}{\cos\theta + \sin\theta}$	% error FA	% error BB
5	0°	.0711	.0182	.0843	-291	+16
10	0°	.1277	.0842	.1579	-52	+19
20	0°	.2251	.1978	.2655	-14	+15
50	0°	.4088	.4003	.4457	-2	+8
100	0°	.5625	.5602	.5703	-.4	+1.4
200	0°	.6990	.6988	.6667	-.03	-4.8
5	60°	.0618	.0892	.1148	+31	+46
10	60°	.1079	.1446	.1617	+25	+33
20	60°	.1718	.2013	.2023	+15	+15
50	60°	.2450	.2617	.2478	+6.4	+1.1
100	60°	.2899	.2960	.2752	+2.1	-5.3
200	60°	.3175	.3211	.2959	+1.1	-7.3

(1976), the finite analytic (FA) model of Davies (1976), and the building block (BB) results, and the percent error of each model as compared to the Monte Carlo model. The table shows the building block model has errors which are generally comparable in magnitude to the finite analytical model for cubes with optical dimensions less than 100. For larger cubes, the finite analytic model's errors tend toward zero, while building block model errors remain finite. For the overhead sun, the building block errors are consistent with the error analysis of Figure 5. For optical thickness less than 100, the building block model overestimated the flux out the top, while for larger clouds, it underestimated the flux. The errors of the smaller cubes are larger than the larger cubes. For a solar zenith angle of 60° the errors increase slightly and are somewhat larger than would be expected from the error analysis of Figure 5. The additional error would be due to the decomposition of the incident beam into top and side normal components.

Davies (unpublished results) has run Monte Carlo simulations of a 100 x 100 x 50 cube which show the flux variation across the various faces of the cube. These results of Davies can be used to verify the accuracy of the building block model's flux variations across the cube. Figure 8a shows the flux across the top surface of the Monte Carlo simulation for an overhead sun. Figure 8b shows the same thing for the building block model in a 10 x 10 x 5 configuration with each building block being a cube of optical thickness 10. Figure 8c shows the percent difference, $(\frac{BB-MC}{BB})*100$, between the two models at each

grid point. The error level in the Monte Carlo model ranged from 1 to 3%. The building block model had differences of 4 to 7% near the edges, and generally less than 3% in the interior regions. These error numbers are slightly smaller than the error estimates of Figure 5. The cloud side of the Monte Carlo simulation for an overhead sun is shown in Figure 9a. The vertical spacing between grid points is optical thickness 5 with a horizontal spacing of 10. The Figure 9a shows that the brightest part of the side is not next to the illuminated top, but rather an optical thickness 5 down from the top. The single scatter component of the light coming out the sides would be largest next to the illuminated top, but the multiple scatter component becomes appreciable after traveling a distance into the cloud. The brightest part of the side being displaced slightly down from the top would be due to the buildup of the multiple scatter component of the scattered light. Figure 9b shows the side of the building block model for the overhead sun case. The spacing between grid points is optical thickness 10. The building block model has the brightest part of the side being right next to the top edge. Figure 9c shows a graph of the center grid points from top to bottom for the sides of the two models. The figure shows that while the building block model does a reasonably good job of depicting the brightness variation down the side of the cube, it does not capture the sense of the variation near the very top. This illustrates the model's problem in handling the anisotropic scattering of stronly peaked phase functions. Near the illuminated top, the multiple scattering has not yet smoothed

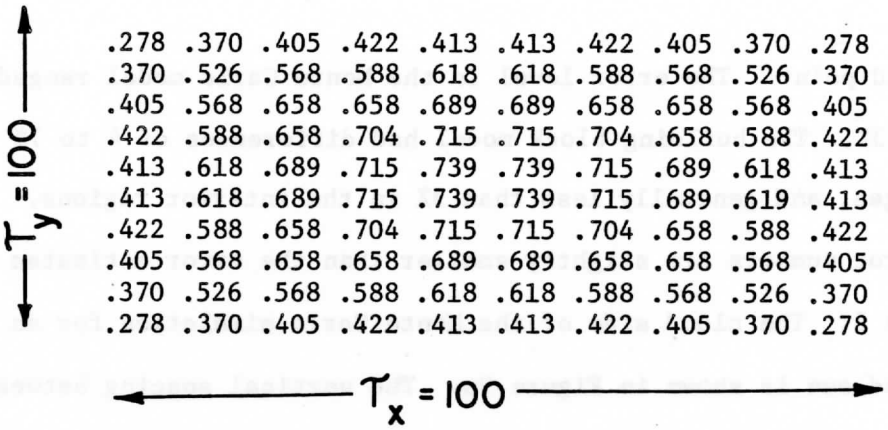

Fig. 8a. Monte Carlo simulation of the flux variation across the top of a cuboid with optical thickness dimensions 100 x 100 x 50 high for an overhead sun.

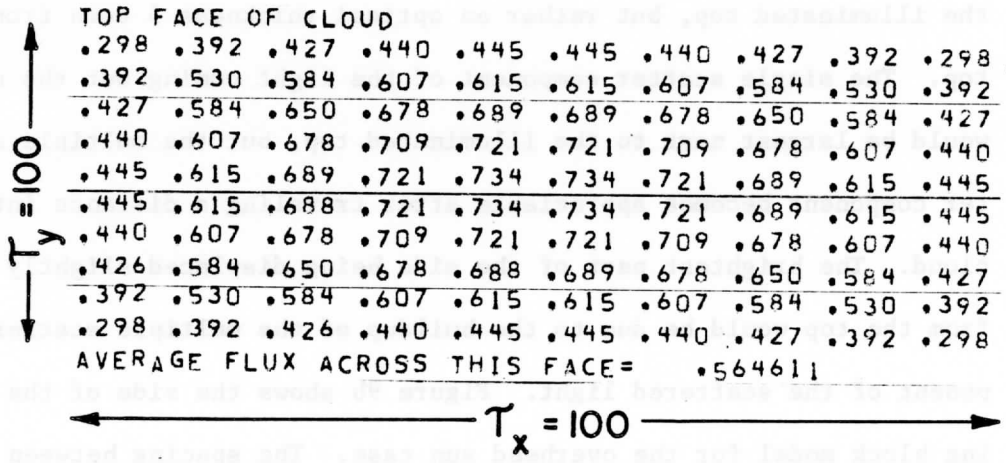

Fig. 8b. Building block simulation of the same cuboid as fig. 8a.

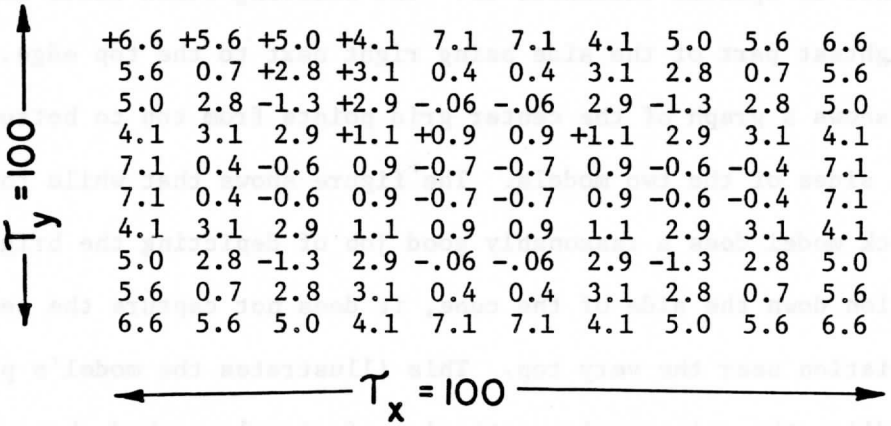

Fig. 8c. Percent difference between the Monte Carlo simulation of 8a and the building block simulation of 8b.

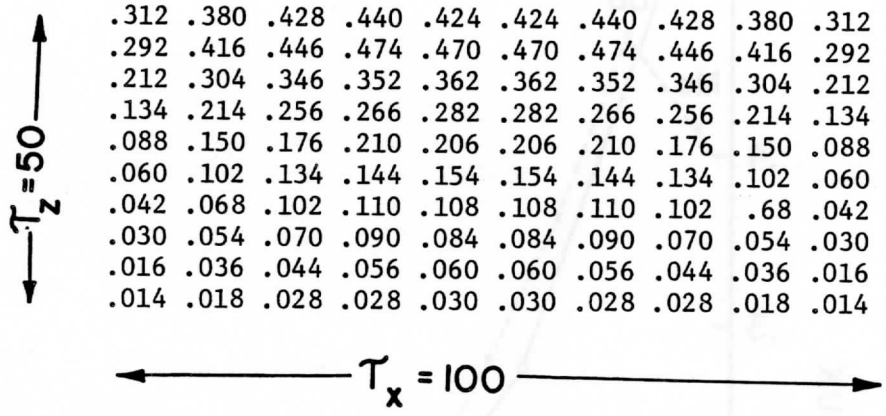

Fig. 9a. Monte Carlo simulation of the flux variation across the side of a cuboid with optical thickness dimensions of 100 x 100 x 50 high for an overhead sun. The vertical spacing between grid points is optical thickness 5 while the horizontal spacing is 10.

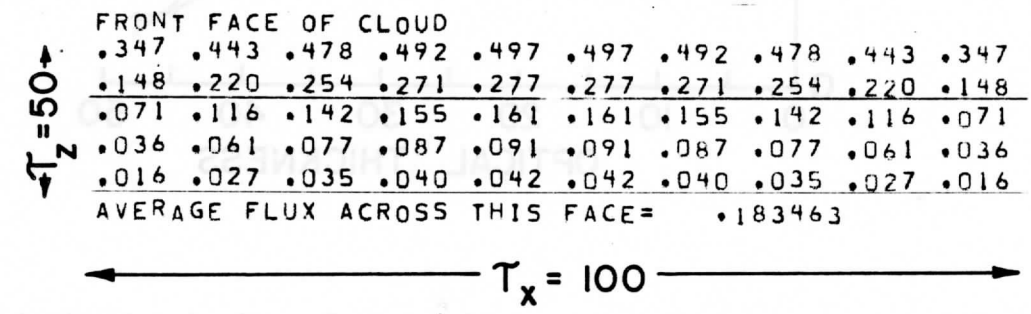

Fig. 9b. Building block simulation of the flux variation across the side of the same cuboid as fig. 9a. The vertical and horizontal grid spacing is optical thickness 10.

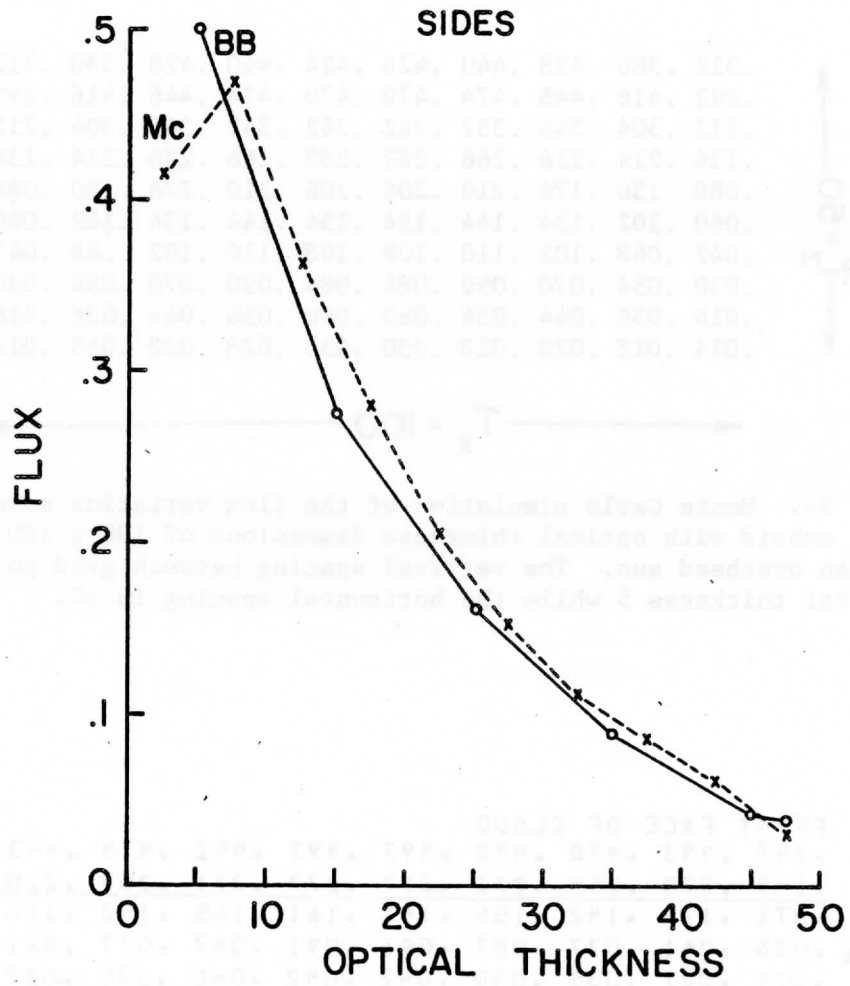

Fig. 9c. Graph of the center grid points from the top to the bottom for the side of the cuboid of figures 9a and 9b. The Monte Carlo results of fig. 9a are dashed and the building block results of 9b are the solid curve.

out the phase function sufficiently for the building block model to accurately portray the brightness variation of the side near the cube's top. Figure 9d shows the percentage error of the building block model side grid points as compared to the Monte Carlo model. The higher resolution Monte Carlo results were averaged together to match the resolution of the building block model. The percentage errors are generally comparable with the prediction of Figure 5 except for the second row which is slightly worse than the predicted errors. These errors are within the limits predicted by Figure 6 for forward scatter errors.

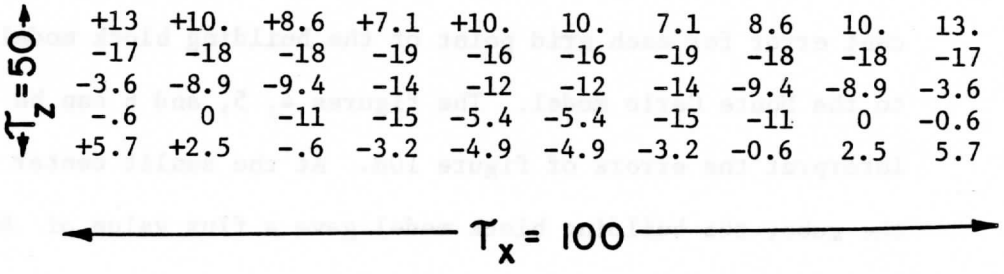

Fig. 9d. Percent difference $\left[\left(\frac{BB - MC}{BB}\right) \times 100\right]$ between the Monte-Carlo simulation and the building block simulation for the flux variation across the side of a 100 x 100 x 50 high cuboid with an overhead sun.

The Monte Carlo model was also run for a solar zenith angle of 60°. Figure 10a shows the Monte Carlo results for the cloud top with the sun on the left. The Monte Carlo results in the figure have been multiplied by the projected area scaling factor to agree with the convention of the building block model of unit input flux. The spacing between grid points is optical thickness 10. The brightest part of the cloud top is displaced in slightly from the edge of the cloud as was the case for the cloud side in the overhead sun case of Figure 9a. Figure 10b shows the building block results for the same geometry. Figure 10c shows a flux cross section across the top of the cloud for the two models. The building block model does not handle the sunlit edge very well because of the highly anisotropic nature of the scattering there. The center and edge portions of the building block model are dimmer than Monte Carlo results. Figure 10d shows the percent error for each grid point of the building block model as compared to the Monte Carlo model. The figures 4, 5, and 6 can be used to interpret the errors of figure 10d. At the sunlit center top edge of the cube, the building block model gave a flux value of .641 in figure 10b. Since this is a region of high anisotropic scattering, figure 6 can be used for error estimation. For a single cube of optical thickness 10, figure 6 predicts a overestimation of 26% of the flux normal to that surface, or .167 for the top surface. The sunlit side surface of this cube had a flux value of .623 (not shown on the illustration) which would also be 26% (a flux value of .162) too high for the component normal to that surface. Using the cube's transfer

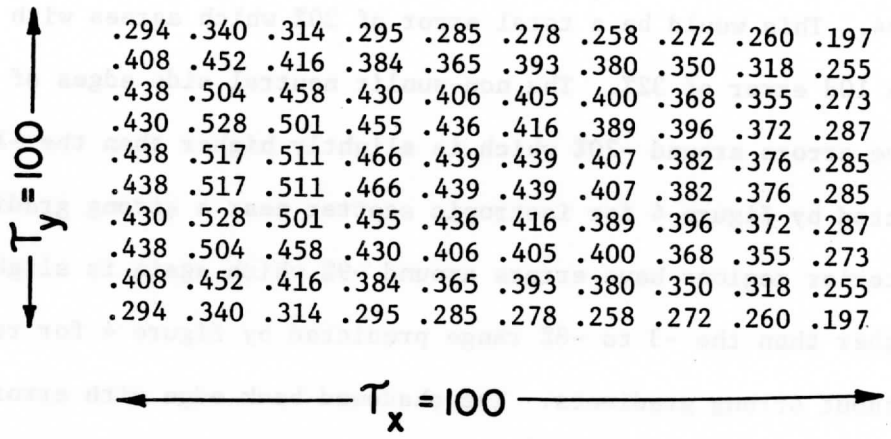

Fig. 10a. Monte Carlo simulation of the flux variation across the top of a cuboid 100 x 100 x 50 high for a solar zenith angle of 60 degrees with unit flux input. The sun is coming in from the left.

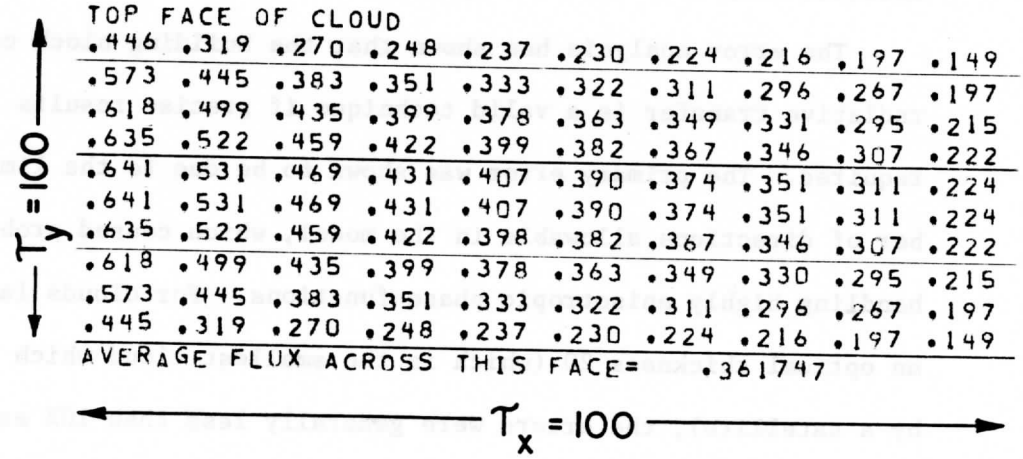

Fig. 10b. Building block model simulation of the flux variation across the top of a cuboid 100 x 100 x 50 for a solar zenith angle of 60 degrees with unit flux input. The sun is coming in from the left.

function, the overestimate of .162 on the side would result in an additional excess flux of .027 on the top, or a total excess flux of .194. This would be a total error of 30% which agrees with the figure 10d error of 32%. The non-sunlit neutral side edges of the cube have errors around -20% which is slightly higher than the -14% predicted by figure 4 for isotropic scatter near a strong gradient. The interior regions have errors around -9% which again is slightly higher than the -3 to -8% range predicted by figure 4 for regions without strong gradients. The shadowed back edge with errors approaching -30% is poorly predicted by figure 4. An additional error of -16% above what was predicted by figure 4 was noted. This additional error would be due to the model convention of splitting the incident beam into normal components.

The error analysis has shown that the building block concept of radiative transfer is a valid technique if precise results are not required. The primary error was shown to be due to the limited number of directions allowable in the model, which caused problems with handling highly anisotropic phase functions. For clouds larger than an optical thickness 20 (which is the smallest cloud which can be seen by a satellite), the errors were generally less than 10% except near the edges where anisotropic and gradient effects would be the greatest. The errors at the edges can be as large as 30%. Figures 4, 5, and 6 give appropriate estimates of expected errors in the building block model for various size cubes and combinations of cubes.

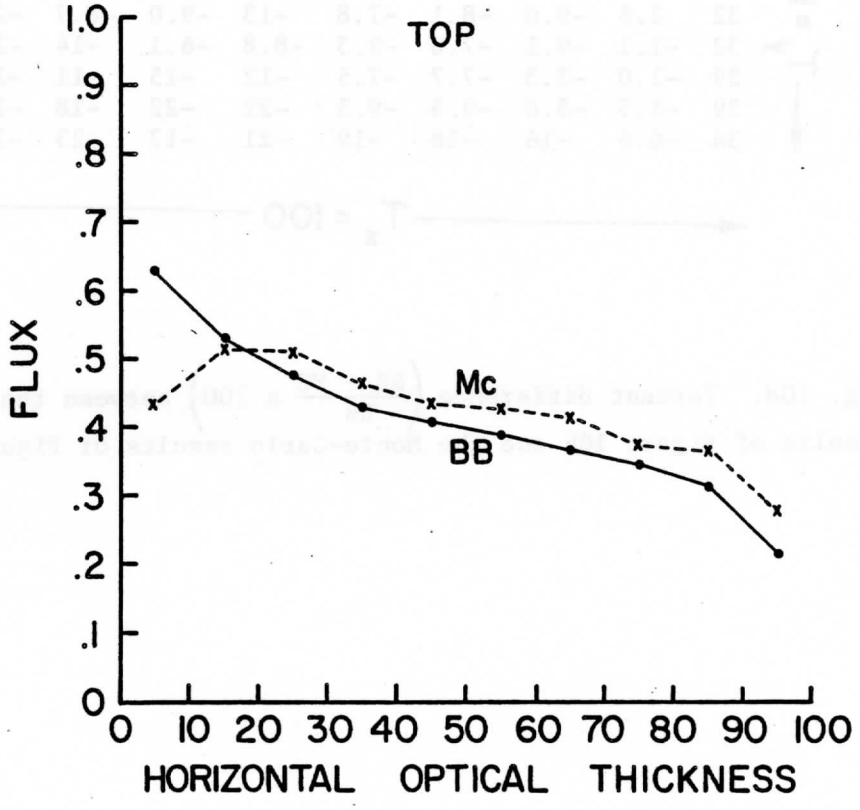

Fig. 10c. Cross section of the flux variation across the top of the figures 10a and 10b going from the sunlit left side to the shadowed side through the center of the cuboid. The Monte Carlo results are dashed and the building block results are solid.

$\tau_y = 100$									
	34	-6.6	-16	-18	-19	-21	-17	-23	-30	-31
	29	-1.5	-8.6	-9.3	-9.5	-22	-22	-18	-19	-29
	29	-1.0	-5.3	-7.7	-7.5	-12	-15	-11	-20	-27
	32	-1.1	-9.1	-7.8	-9.3	-8.8	-6.1	-14	-21	-30
	32	+2.6	-9.0	-8.1	-7.8	-13	-9.0	-8.7	-21	-27
	32	2.6	-9.0	-8.1	-7.8	-13	-9.0	-8.7	-21	-27
	32	-1.1	-9.1	-7.8	-9.3	-8.8	-6.1	-14	-21	-30
	29	-1.0	-5.3	-7.7	-7.5	-12	-15	-11	-20	-27
	29	-1.5	-8.6	-9.3	-9.5	-22	-22	-18	-19	-29
	34	-6.6	-16	-18	-19	-21	-17	-23	-30	-31

$\tau_x = 100$

Fig. 10d. Percent difference $\left(\frac{BB - MC}{BB} \times 100\right)$ between the building block results of Figure 10b and the Monte-Carlo results of Figure 10a.

4. Building Block Model Results

The building block model has been used to investigate the flux variations across cloud tops which are caused by cloud geometry and cloud composition. The purpose of this investigation is to help form a basis for the interpretation of brightness variations observed in satellite images of clouds. The implicit assumption made in this investigation is that the patterns of variation in intensity across clouds would be related to the patterns of variations of flux across clouds. A discussion on the validity of this assumption is contained in section 4.3.

4.1 Flux Variations Across Homogeneous Cubic Cloud Tops

The building block model has been used to investigate the variations of flux across cubic clouds. Figures 3a, b, and c illustrate the variations of flux coming from the top, bottom, and front side of a cubic cloud with optical dimensions of 100 for an overhead sun. The geostationary satellites mainly look down on clouds, so the flux variation across the top is the quantity of most interest. Figures 11a, b, c, and d illustrate the flux across the top face of a cubic cloud with optical dimensions of 100 for solar zenith angles of 0°, 27°, 54° and 81°.

Figures 12a and b show the flux variations across the center of cubes 100 and 500 optical thickness for these four sun angles. The cross sections in Figures 12a and b go through the center of the cube. For the overhead sun case, the figures show that the center of the

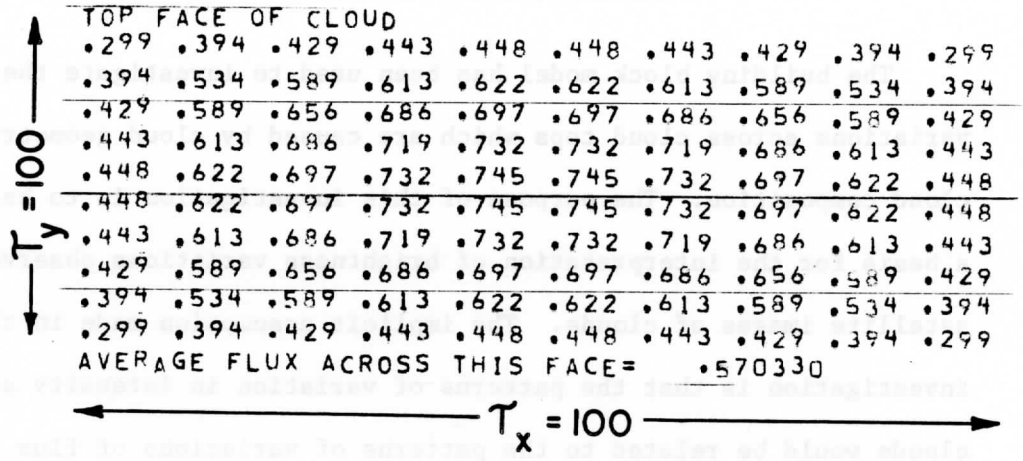

Fig. 11a. Flux variation across the top of a cubic cloud of optical dimension 100. The input flux was 1; the solar zenith angle 0 degrees.

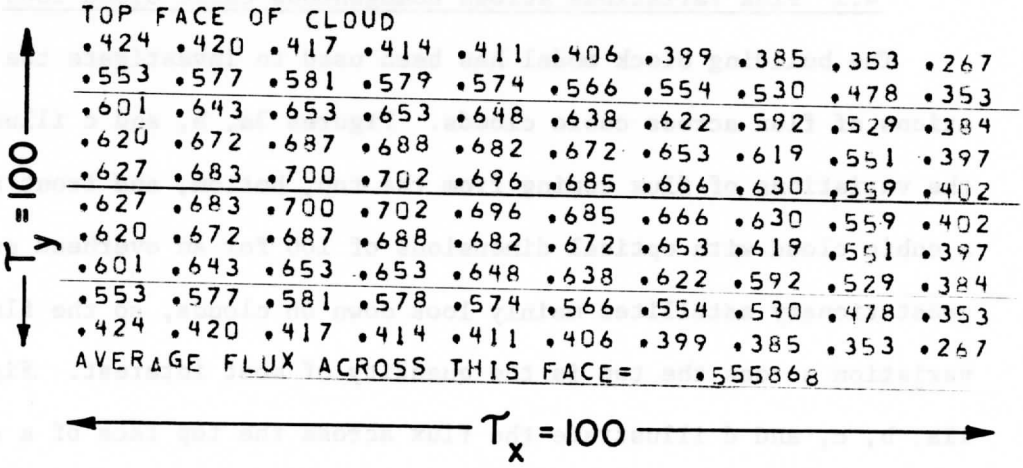

Fig. 11b. Same as figure 11a, except the solar zenith angle is 27 degrees. The sun is on the left hand side of the cube.

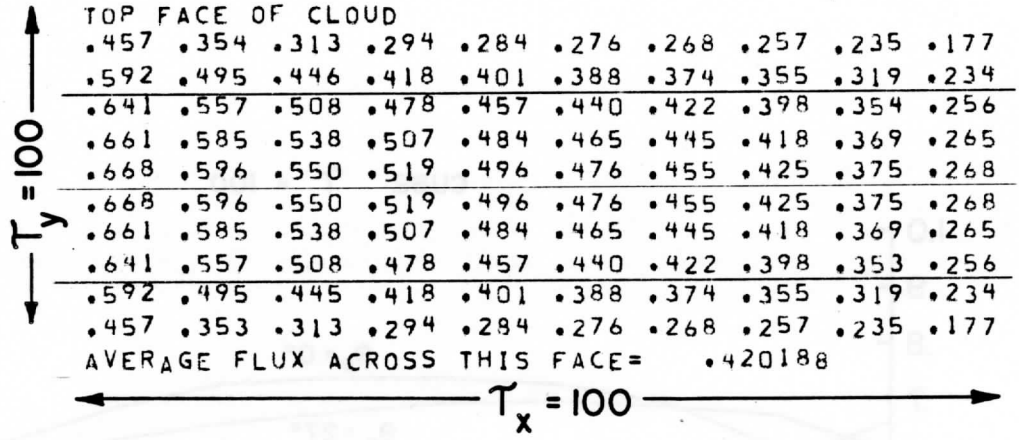

Fig. 11c. Same as figure 11b, except the solar zenith angle is 54 degrees.

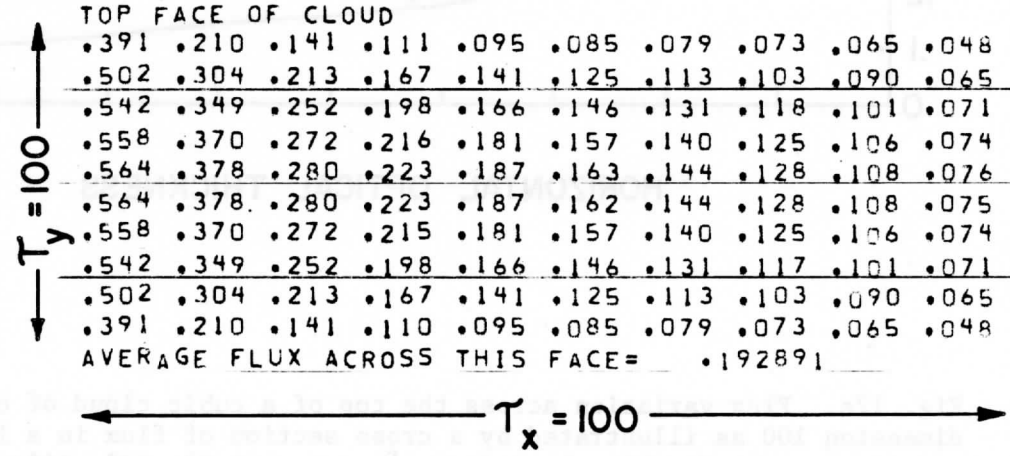

Fig. 11d. Same as figure 11b, except the solar zenith angle is 81 degrees.

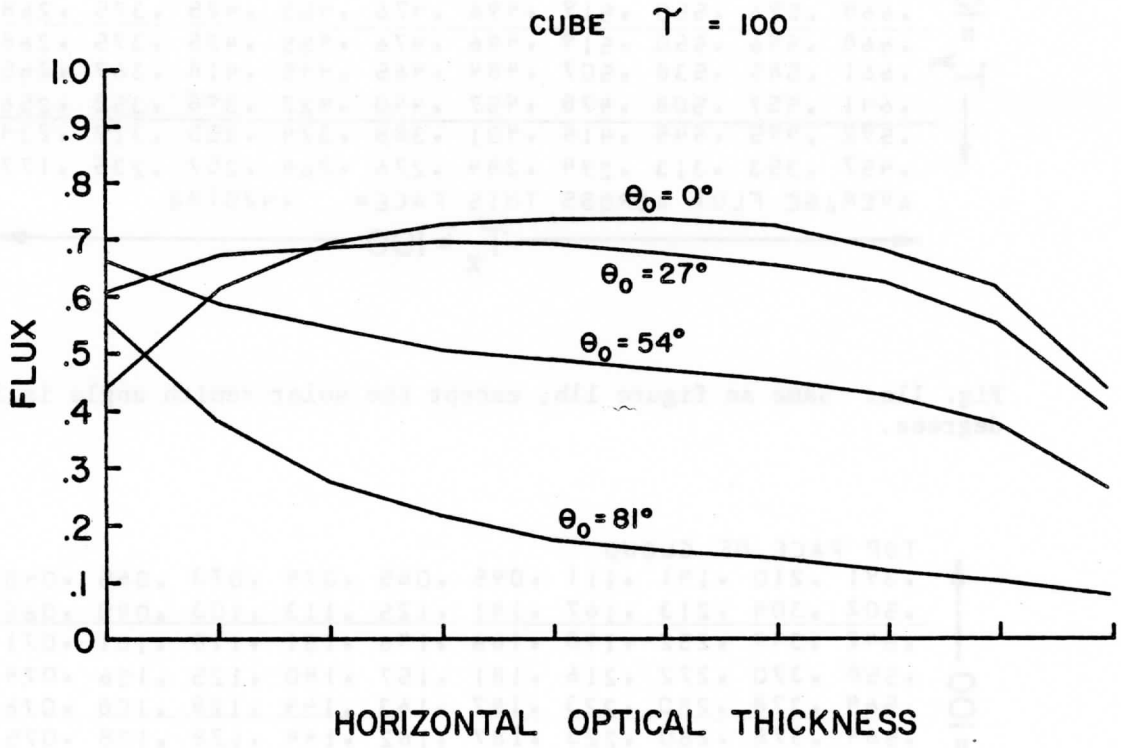

Fig. 12a. Flux variation across the top of a cubic cloud of optical dimension 100 as illustrated by a cross section of flux in a line across the top of cubic cloud for sun angles of 0°, 27°, 54°, and 81°. The sun is on the left hand side of the cube.

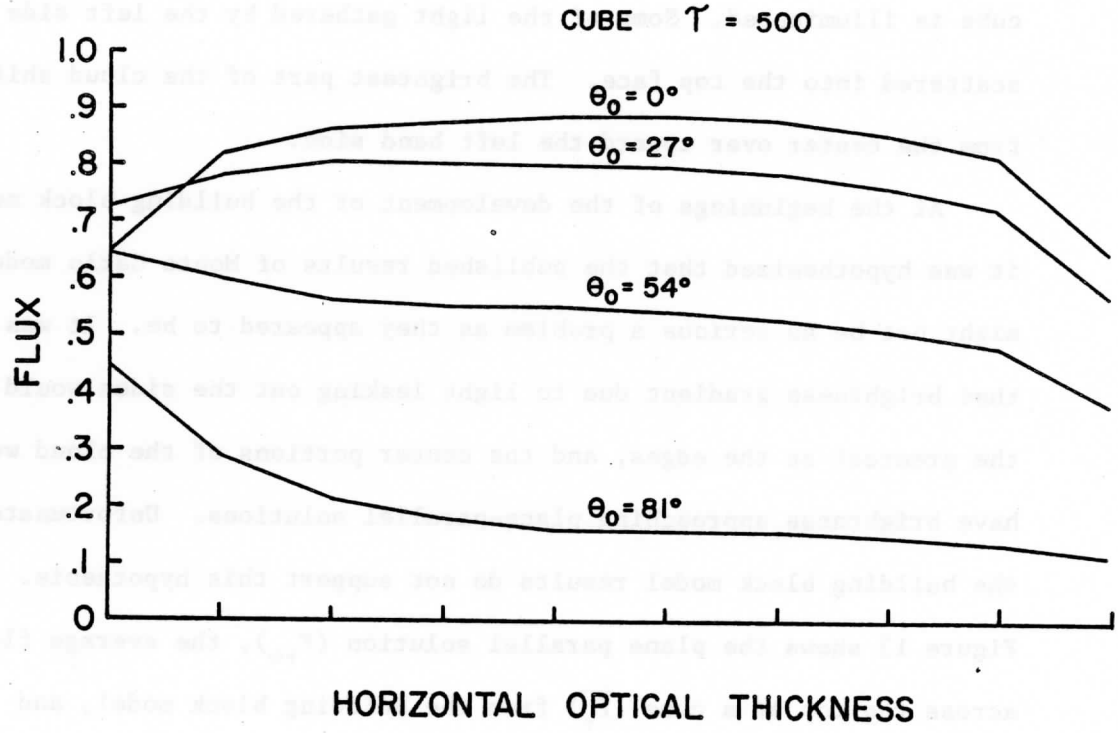

Fig. 12b. Same as 12a, except for a cube of optical dimension 500.

cloud is the brightest. There is a rather sharp gradient of flux at the boundaries and a reasonably uniform flux across the interior portions of the cloud. As the sun goes down, the left hand side of the cube is illuminated. Some of the light gathered by the left side is scattered into the top face. The brightest part of the cloud shifts from the center over toward the left hand side.

At the beginnings of the development of the building block model it was hypothesized that the published results of Monte Carlo models might not be as serious a problem as they appeared to be. It was hoped that brightness gradient due to light leaking out the sides would be the greatest at the edges, and the center portions of the cloud would have brightness approaching plane-parallel solutions. Unfortunately the building block model results do not support this hypothesis. Figure 13 shows the plane parallel solution ($F_{\uparrow\infty}$), the average flux across the top of a cube ($\overline{F_{\uparrow}}$) from the building block model, and the maximum flux on the top face ($F_{\uparrow max}$) as a function of optical thickness for the cube with an overhead sun. The figure shows that for small clouds the maximum flux is still significantly less than the plane-parallel solution. For larger clouds the brightest part of the cloud comes closer to the plane-parallel solution than the average flux would indicate, but is still significantly different from the plane-parallel solution so as to cause errors if plane-parallel theory is applied.

As the solar zenith angle increases the sides collect incident solar flux in addition to the top. In the works of McKee and Cox

(1974) and Davies (1976), the quantity being determined was not flux per se, but rather the fraction of the incident light exiting each surface. This quantity has been termed "fractional irradiance" by Davies (1978b) and "albedo" by Busygin et al.(1973). The fractional irradiance is a function of both the outgoing flux and the input projected area which equals (Top Area) x cos Θ_o + (Illuminated Side Area) x sin Θ_o. For a broken cloud deck at large solar zenith angles, the entire solar beam can be intercepted by clouds even though there are holes between clouds. Hence, for theoretical cubic cloud results which are to be compared with real clouds, the fractional irradiance or average albedo ($\overline{A}$) is not as meaningful as the average upward flux ($\overline{F}_{\uparrow}$) from the top. Figure 14 shows the upward flux from top surface as a function of optical thickness for the plane-parallel solution ($F_{\uparrow\infty}$), the average albedo ($\overline{A}$) from cubes, the average flux upwards from cubic tops ($\overline{F}_{\uparrow}$),and the maximum flux from the cube top ($F_{\uparrow max}$) for a solar zenith angle of 27°. The graph is similar to Figure 13 with the overhead sun, in that the plane-parallel solution is larger than the finite cloud solutions. However, by using the average albedo ($\overline{A}$) rather than the average flux ($\overline{F}_{\uparrow}$), the magnitude of the error is exaggerated somewhat.

As the solar zenith angle increases the sides collect more and more solar energy. At 45° the side receives the same energy as the top. Figure 15 is the same as Figure 14 except the sun is now 45°. While the average flux from the top is less than the plane-parallel solution, the brightest part of the cloud now very closely approxi-

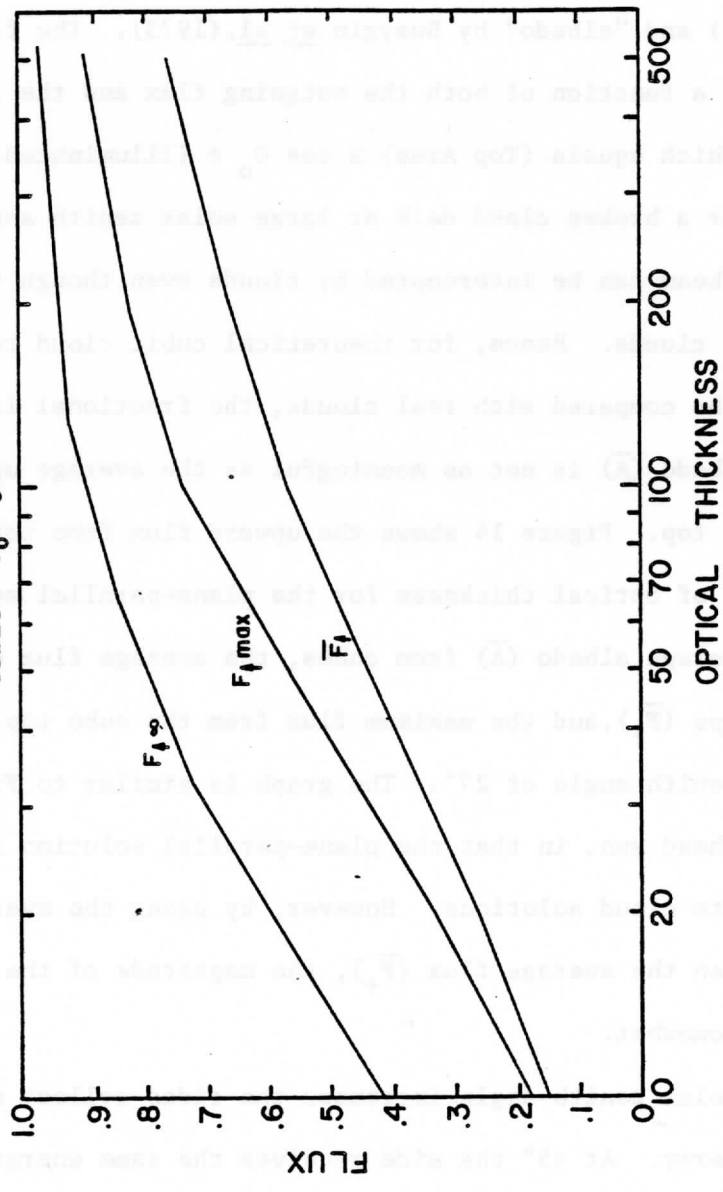

Fig. 13. Comparison of the plane parallel flux computation ($F_{\uparrow\infty}$) as a function of optical thickness with average flux coming out of the top of a cubic cloud ($\overline{F_\uparrow}$) and the maximum flux ($F_{\uparrow max}$) coming from any point of the cubic cloud top. The solar input was unity with a solar zenith angle of 0 degrees.

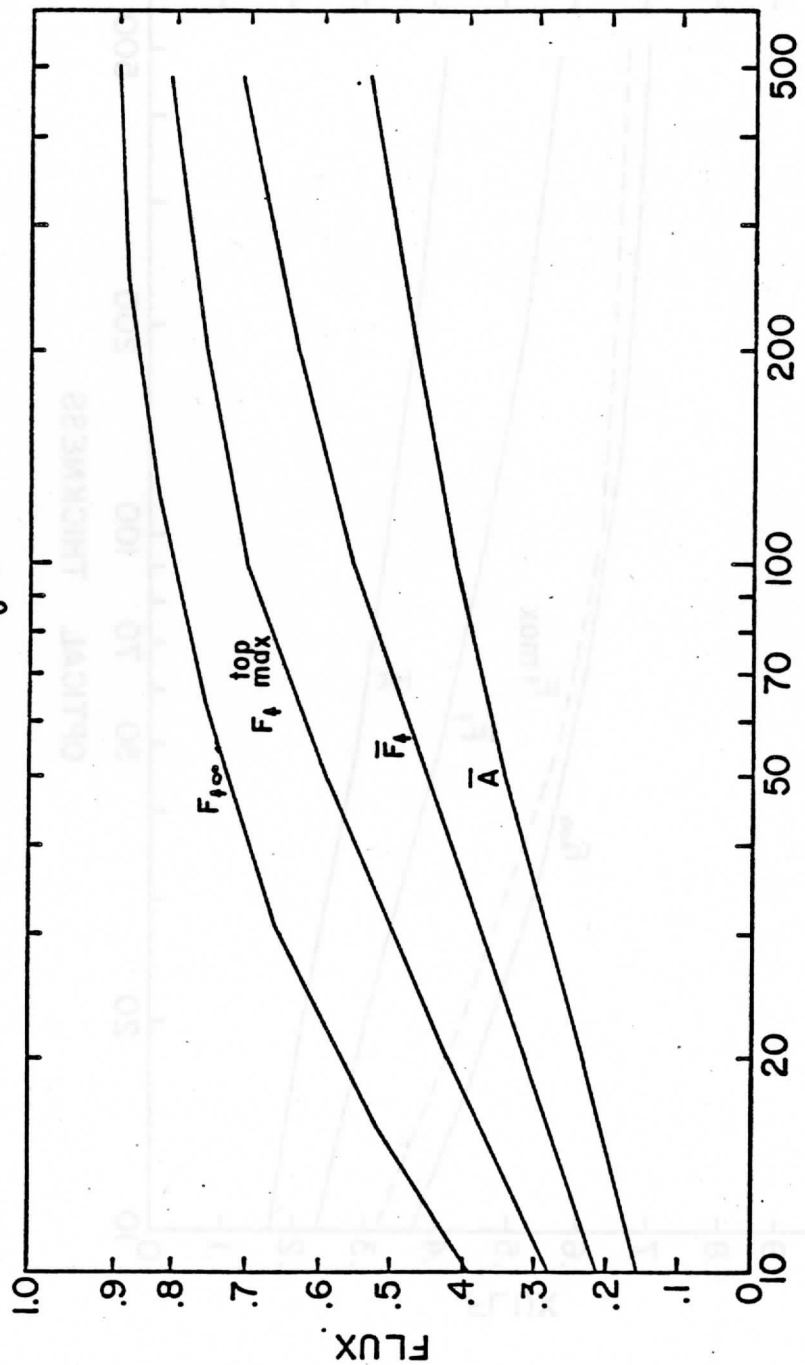

Fig. 14. Same as fig. 13 except for the addition of the average albedo ($\bar{A}$) (which is the quantity determined by researchers who use a normalized projected area) for a solar zenith angle of 27 degrees.

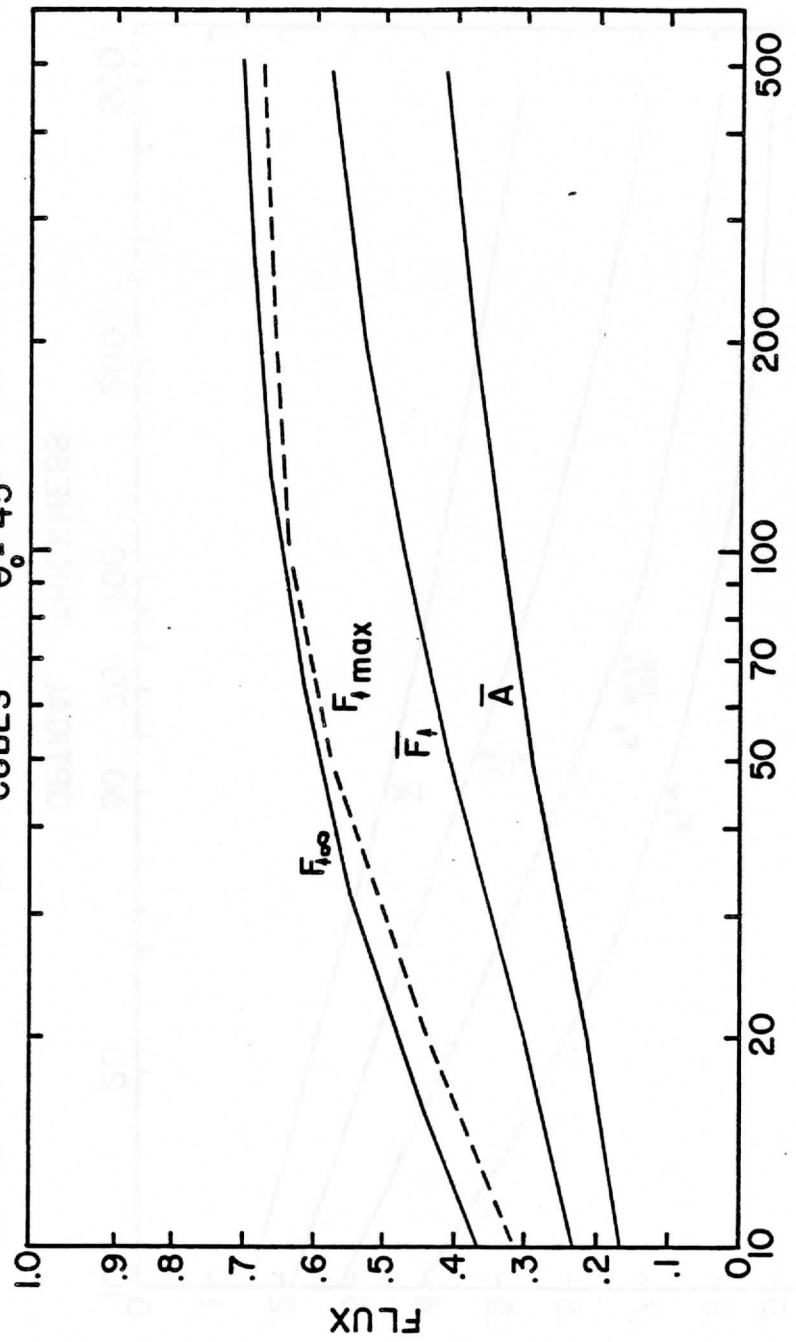

Fig. 15. Same as fig. 14 except the solar zenith angle is 45 degrees.

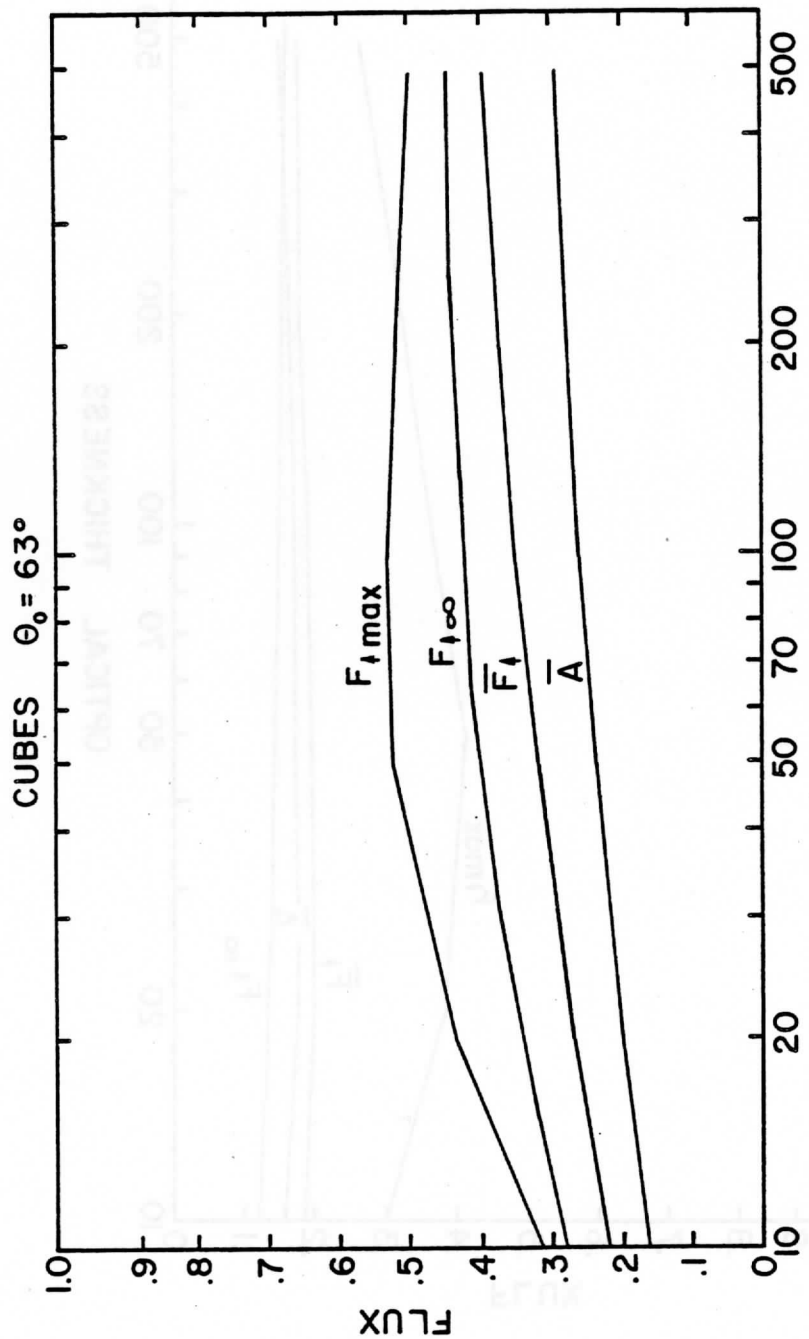

Fig. 16. Same as fig. 14 except the solar zenith angle is 63 degrees. The maximum flux is greater than the plane parallel solution because light which is captured by the illuminated side is scattered into the top of the cube.

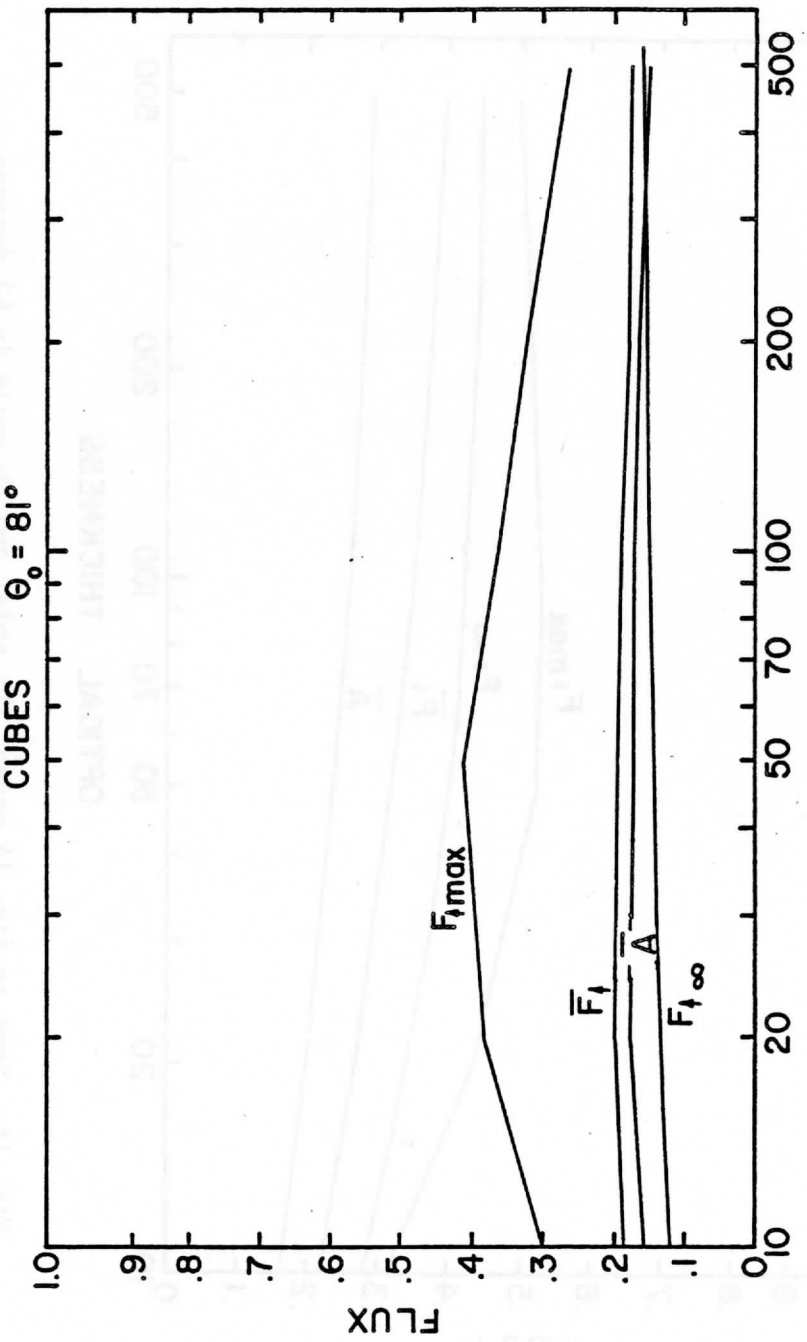

Fig. 17. Same as fig. 14 except the solar zenith angle is 81 degrees.

mates the plane-parallel solution. The brightest part of the cloud has been shifted over toward the sunlit side. Since the error analysis of the preceding section showed the building block next to the edges to be in error, the brightest part in this discussion is the brightest part not on an edge.

As the solar zenith angle increases beyond 45° the side now receives more energy than the top. The brightest part of the top is now near the left hand sunlit side because the light being captured by the side is being scattered toward the top. Figure 16 shows the same as Figure 14 except the solar zenith angle is now 63°. The average flux and albedo are still less than the plane-parallel solution, but the brightest part of the cloud has flux well in excess of the plane-parallel solution.

As the solar zenith angle continues to increase, the brightest part of the cloud continues to be much larger than the plane-parallel solution. Figure 17 is the same as Figure 14 except the solar zenith angle is now 81°. Here the plane-parallel solution is the dimmest, with the average flux and albedo of the cubes being fairly close to the plane-parallel solution. However, the brightest part of the cube (the left hand sunlit side) is considerably brighter than the plane-parallel solution.

Fluxes from cubic clouds depart significantly from plane-parallel theory, as Figures 13-17 have shown. This departure is a function of both cloud size and solar zenith angle. To illustrate the magnitude of the error in using plane-parallel theory, the following figures

will show the ratio of the plane-parallel flux to the finite cloud flux as a function of sun angle. The plane parallel values were obtained from the plane parallel model of Hansen (1971a). Figure 18 shows the ratio of the plane-parallel flux to the average flux from the finite cloud top for different size cubes. The values used to construct this figure are contained in Table 2. Figure 19 shows the ratio of the plane-parallel solution to the flux at the center of the top surface as a function of sun angle. Table 3 contains the values of these curves. These curves are similar to Figure 18 except that they are flatter for the larger cubes, showing less of a sun angle dependence. Figure 20 shows the flux at the point on the top which is near the shadowed side. The point is one grid point in from the shadowed side along the center axis (sunlit to shadowed) of the cubic cloud. Table 4 contains the values used to construct the graphs. Here the departures from plane-parallel theory are larger than the other figures, but the dependence of the departures on sun angle is very small except for the very smallest cubes.

There are two parts to the finite cloud problem as related to departures from plane-parallel theory. One is the loss of light from the sides of the finite cloud. The other is the gain of light from the sunlit side. Figure 18, the average flux, contains both of these factors. Figure 19, the center flux, shows that the effects of the loss through the sides is most pronounced for small cubic clouds of optical dimensions 20 or less. For the larger cubes the departures from plane-parallel theory are on the order of 10 to 30 percent and

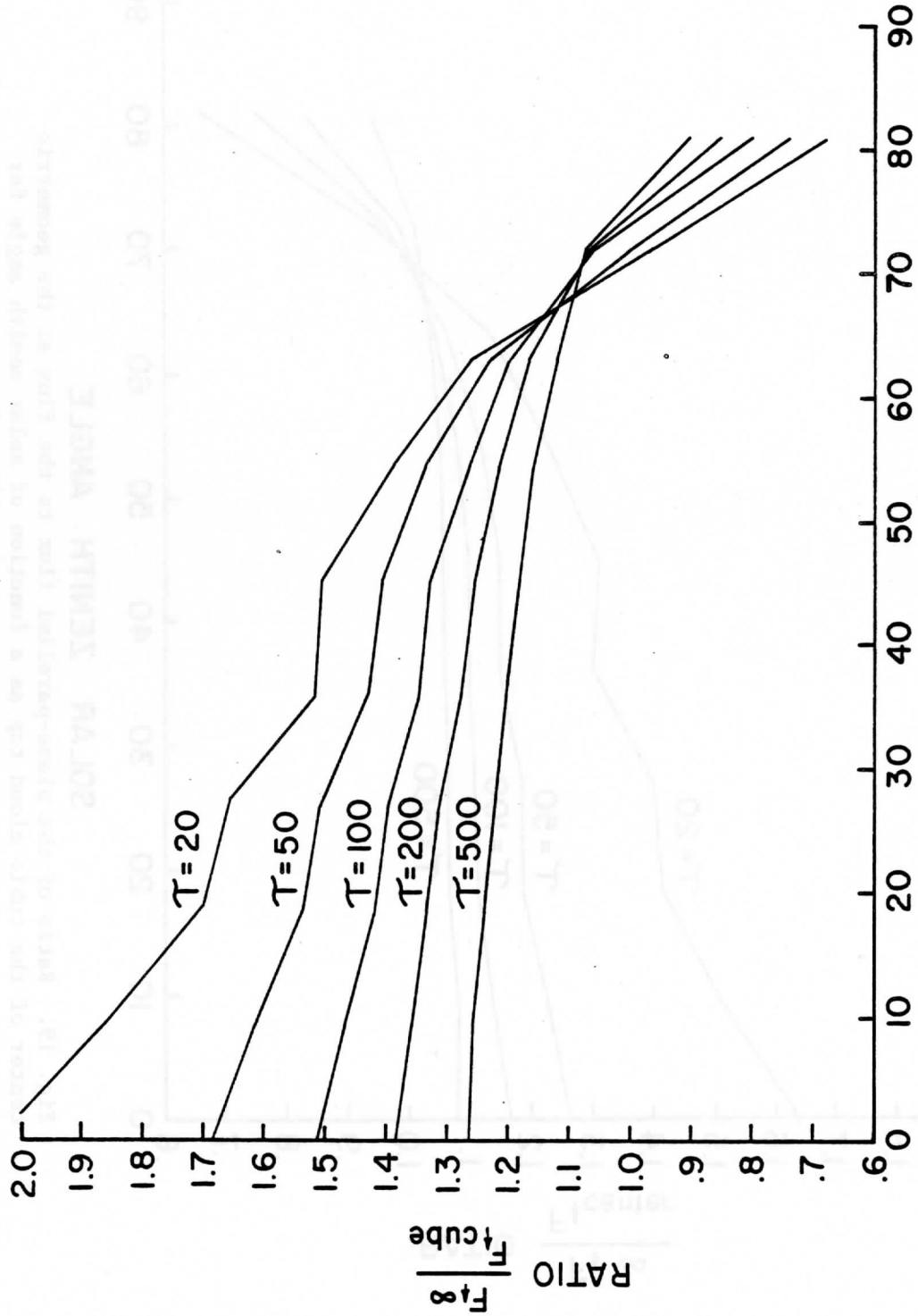

Fig. 18. Ratio of the plane-parallel flux to the average flux from the top of cubic clouds as a function of solar zenith angle for cubes of optical dimension 20, 50, 100, 200, and 500.

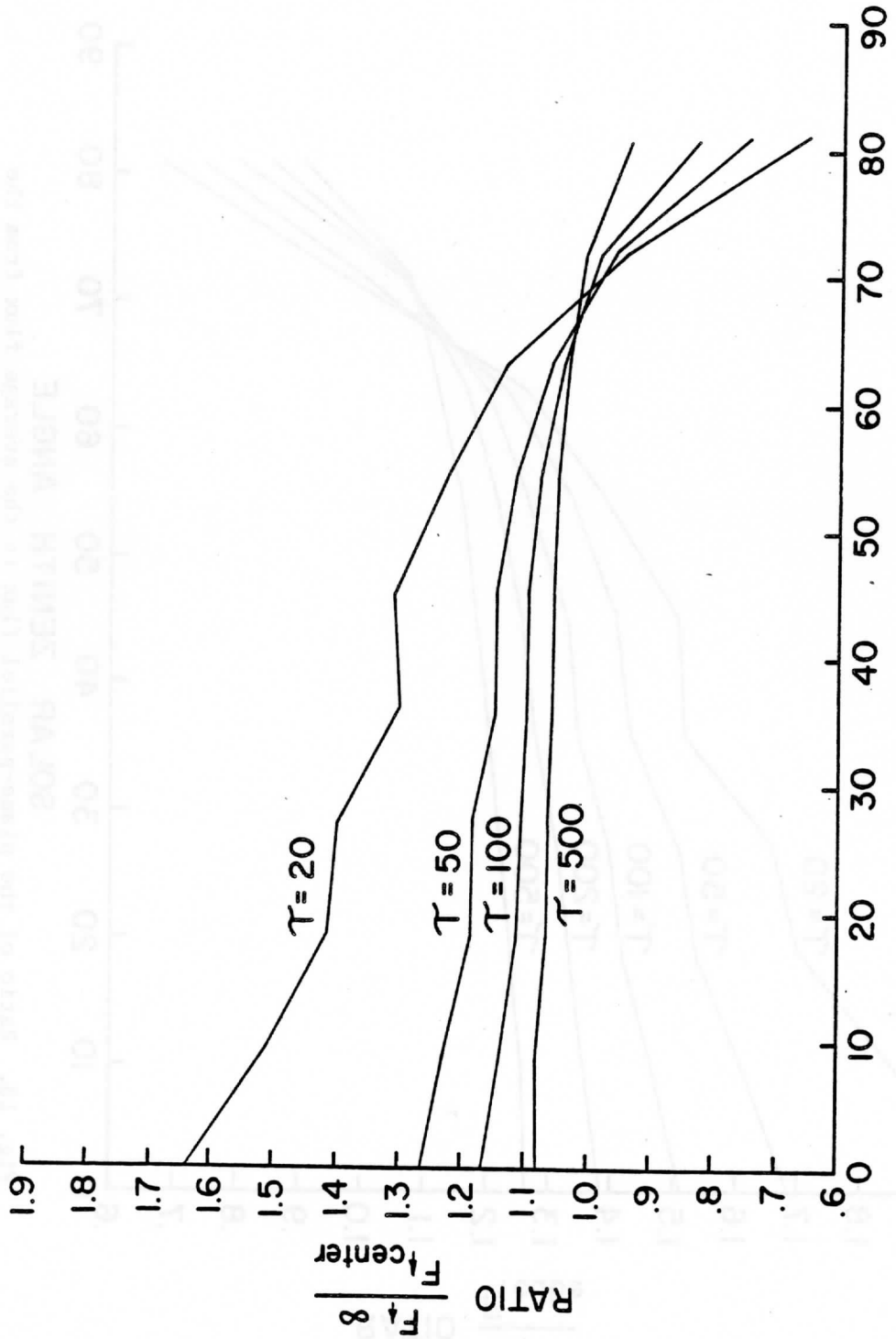

Fig. 19. Ratio of the plane-parallel flux to the flux at the geometric center of the cubic cloud top as a function of solar zenith angle for cubes of optical dimension 20, 50, 100, and 500.

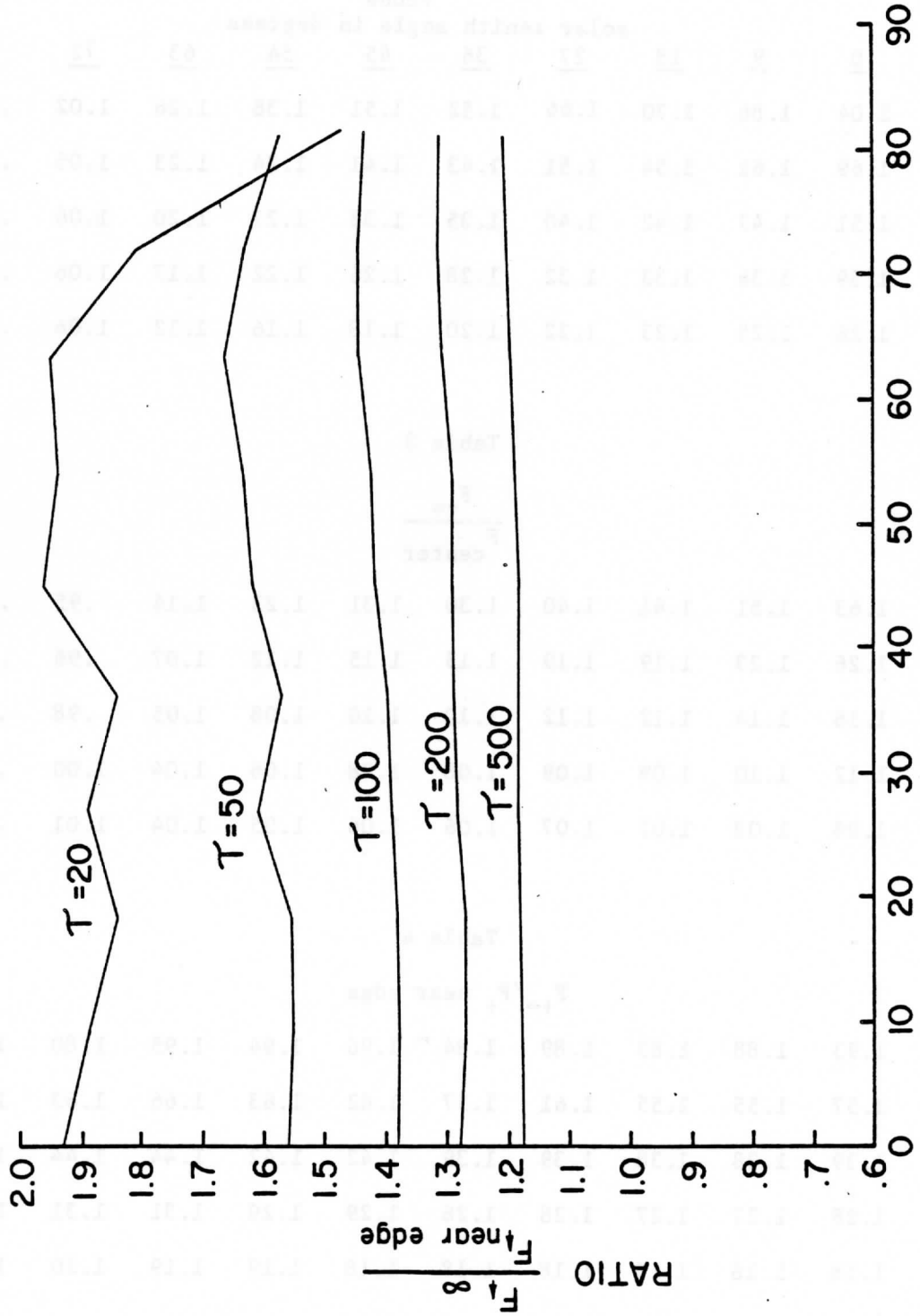

Fig. 20. Ratio of the plane-parallel flux to the flux at the top right hand point next to the shadowed side of the cube as a function of solar zenith angle for cubes of optical dimension 20, 50, 100, 200, and 500.

Table 2

ratio $\frac{F_{\uparrow\infty}}{F_{\uparrow cube}}$

	solar zenith angle in degrees									
τ	0	9	18	27	36	45	54	63	72	81
20	2.04	1.86	1.70	1.66	1.52	1.51	1.38	1.26	1.02	.68
50	1.69	1.61	1.54	1.51	1.43	1.41	1.34	1.23	1.05	.74
100	1.51	1.47	1.42	1.40	1.35	1.33	1.27	1.20	1.06	.80
200	1.39	1.36	1.33	1.32	1.28	1.26	1.22	1.17	1.06	.85
500	1.26	1.25	1.23	1.22	1.20	1.18	1.16	1.12	1.06	.90

Table 3

$\frac{F_{\uparrow\infty}}{F_{center}}$

20	1.63	1.51	1.41	1.40	1.30	1.31	1.23	1.14	.95	.66
50	1.26	1.23	1.19	1.19	1.15	1.15	1.12	1.07	.96	.75
100	1.16	1.14	1.12	1.12	1.10	1.10	1.08	1.05	.98	.83
200	1.12	1.10	1.09	1.09	1.08	1.08	1.06	1.04	1.00	.89
500	1.08	1.08	1.07	1.07	1.06	1.06	1.05	1.04	1.01	.94

Table 4

$F_{\uparrow\infty}/F_{\uparrow}$ near edge

20	1.93	1.88	1.83	1.89	1.84	1.96	1.94	1.95	1.80	1.47
50	1.57	1.55	1.55	1.61	1.57	1.62	1.63	1.66	1.63	1.56
100	1.39	1.38	1.38	1.39	1.39	1.42	1.42	1.44	1.44	1.43
200	1.28	1.27	1.27	1.28	1.28	1.29	1.29	1.31	1.31	1.31
500	1.18	1.18	1.18	1.18	1.18	1.18	1.19	1.19	1.20	1.21

are reasonably independent of sun angle. Hence, for these larger cubes, the center value is reasonably "insulated" from the effects of the sides. For this "insulation" to occur, the center value needs to be at least an optical thickness of 25 away from the edge. The larger the distance from the edge, the better the insulation value. Figure 20, the flux at the point near the top center edge away from the sunlit side, shows the effects of "insulation" of light gain from the sunlit side, but not of the light loss from the exposed edge. For optical thicknesses of 50 and greater there is almost no dependence on sun angle. Hence, here also, the edge has been "insulated" from the effect of the sun for optical thicknesses of 25 or greater.

The brightest part of the cubic cloud tops is near the center of the cube for small solar zenith angles. As the solar zenith angle increases the side captures more light which "leaks" to the top surface, which causes the brightest part of the cloud to be displaced toward the sunlit side. To examine the departure of the flux from the brightest part of the cubic cloud from plane-parallel theory, Figure 21 shows the ratio of the plane-parallel flux to the flux of the brightest part of the cube which is not an edge. Table 5 contains the data for this curve. This figure shows that for solar zenith angles of 0° to 35°, the departure from plane-parallel theory is primarily a function of cube size. At solar zenith angles of greater than 35° the ratio is more a function of solar zenith angle than of size.

The curves in Figure 21 can be used to explain some of the observed discrepancies in trying to apply plane-parallel theory to natu-

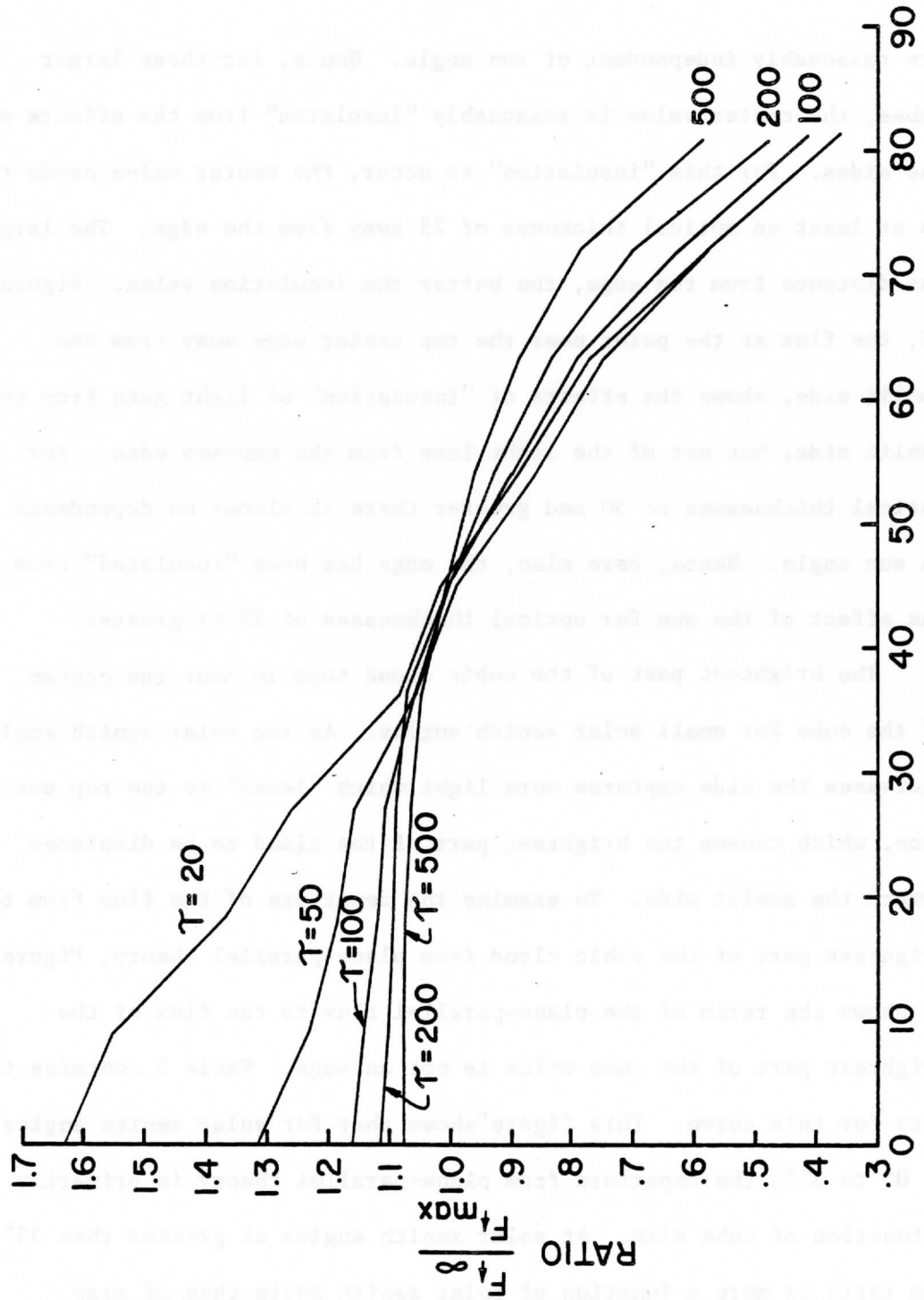

Fig. 21. Ratio of the plane-parallel flux to the flux at the brightest point on the cubic cloud top not on an edge as a function of solar zenith angle for cubes of optical dimensions 20, 50, 100, 200, and 500.

Table 5

$$\frac{F_{\uparrow\infty}}{F_{\uparrow max}}$$

	solar zenith angle in degrees									
τ	0	9	18	27	36	45	54	63	72	81
20	1.63	1.55	1.37	1.26	1.09	1.03	.89	.77	.58	.36
50	1.31	1.23	1.19	1.16	1.06	.98	.87	.75	.58	.36
100	1.16	1.14	1.12	1.11	1.06	.99	.89	.79	.63	.41
200	1.12	1.10	1.09	1.09	1.06	1.00	.93	.84	.70	.48
500	1.08	1.08	1.07	1.06	1.05	1.01	.96	.89	.79	.59

rally occurring clouds. As part of an attempt to obtain a relative calibration for the SMS satellite, Mosher (1974) used the fact that for plane-parallel theory, the curve of intensity vs. optical thickness obtains a limiting value for very thick clouds with optical thicknesses larger than 100. The brightest parts of cloud clusters in the GATE area were assumed to have reached this limiting maximum intensity. The cloud clusters were picked because of the deep convection extending throughout the region and the relatively large horizontal extent of this deep cloud mass. It was assumed that these extensive cloud clusters would approximate the plane-parallel assumption. The factor alpha (α) was defined as the intensity times a constant of a plane-parallel cloud of optical thickness 512 (I_{512}) under the same solar and viewing angles as the measured cloud, divided by the measured maximum squared six bit intensity of the SMS-1 satellite data on the cloud cluster. If all the assumptions of the plane-parallel theory were met, then this factor alpha should be a constant and yield information on the satellite calibration. However, when alpha was measured as a function of sun angle, it showed a marked dependence on sun angle. Figure 22 shows the measured data of alpha vs. sun angle for day 248 of 1974 of the GATE region. The solid curve is the prediction of the ratio of the plane-parallel flux to the brightest part of a cube of optical dimension 500 scaled to be equal to .8 at a solar zenith angle of zero. The predictions of the finite cubic cloud appear to agree quite well with the measured data from real clouds.

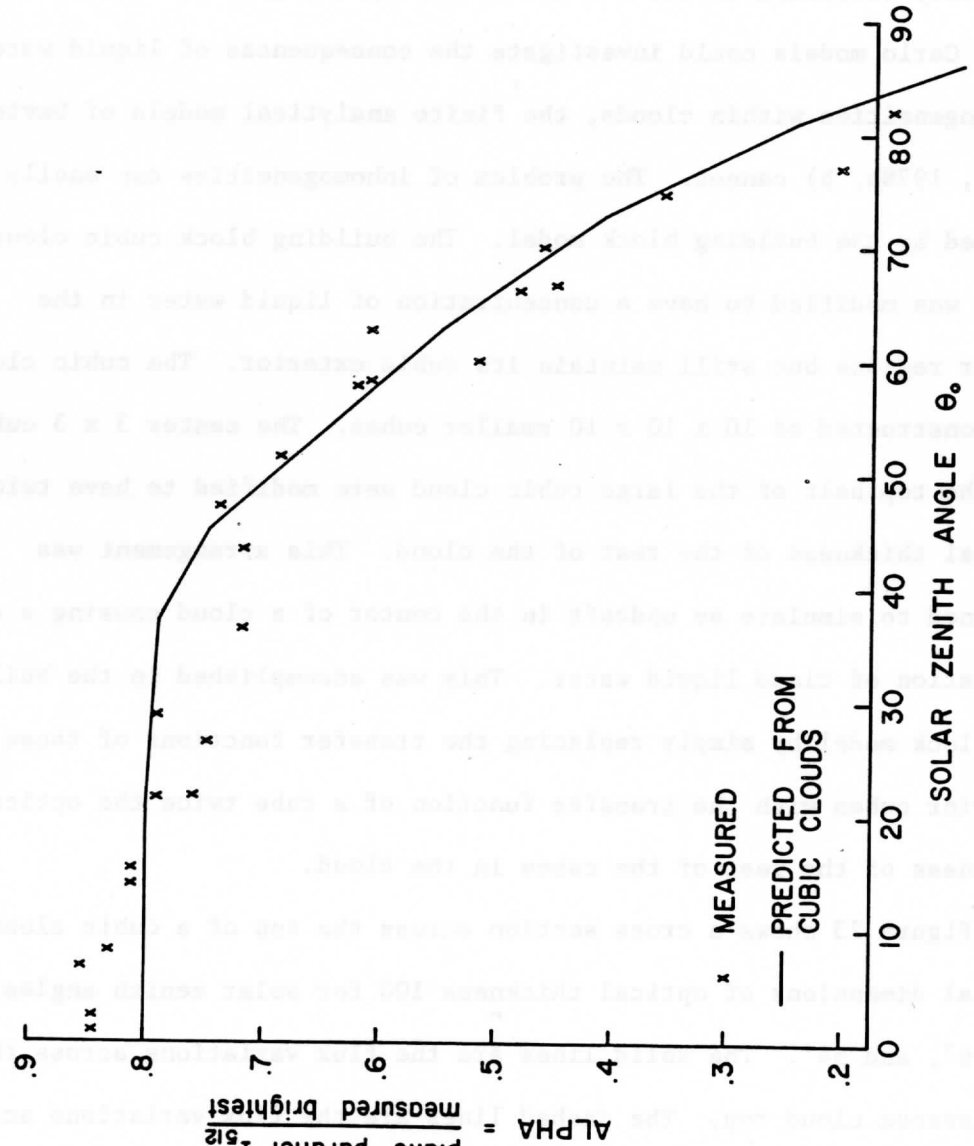

Fig. 22. Ratio of the plane-parallel intensity solution for a cloud of optical thickness 512 to the measured maximum scaled brightness of the SMS satellite data of a cloud cluster as a function of solar zenith angle. The crosses were measured values, and the solid line is the curve predicted from cubic cloud flux calculations of a cube with optical dimensions 500.

4.2 Flux Variations Across Inhomogeneous Cubic Cloud Tops

The development of the finite cloud properties so far has assumed that the finite cloud is homogeneous throughout its volume. However, naturally occurring clouds are not necessary homogeneous. While Monte Carlo models could investigate the consequences of liquid water inhomogeneities within clouds, the finite analytical models of Davies (1976, 1978a, b) cannot. The problem of inhomogeneities can easily be handled by the building block model. The building block cubic cloud model was modified to have a concentration of liquid water in the center regions but still maintain its cubic exterior. The cubic cloud was constructed of 10 x 10 x 10 smaller cubes. The center 3 x 3 cubes for the top half of the large cubic cloud were modified to have twice the optical thickness of the rest of the cloud. This arrangement was designed to simulate an updraft in the center of a cloud causing a concentration of cloud liquid water. This was accomplished in the building block model by simply replacing the transfer functions of those interior cubes with the transfer function of a cube twice the optical thickness of the rest of the cubes in the cloud.

Figure 23 shows a cross section across the top of a cubic cloud of nominal dimensions of optical thickness 100 for solar zenith angles of 0°, 36°, and 54°. The solid lines are the flux variations across the homogeneous cloud top. The dashed lines are the flux variations across the inhomogeneous cloud. The increased optical depth at the center of the cloud causes a localized increase in the flux, but does not noticeably increase the flux outside the region where the concentrations are

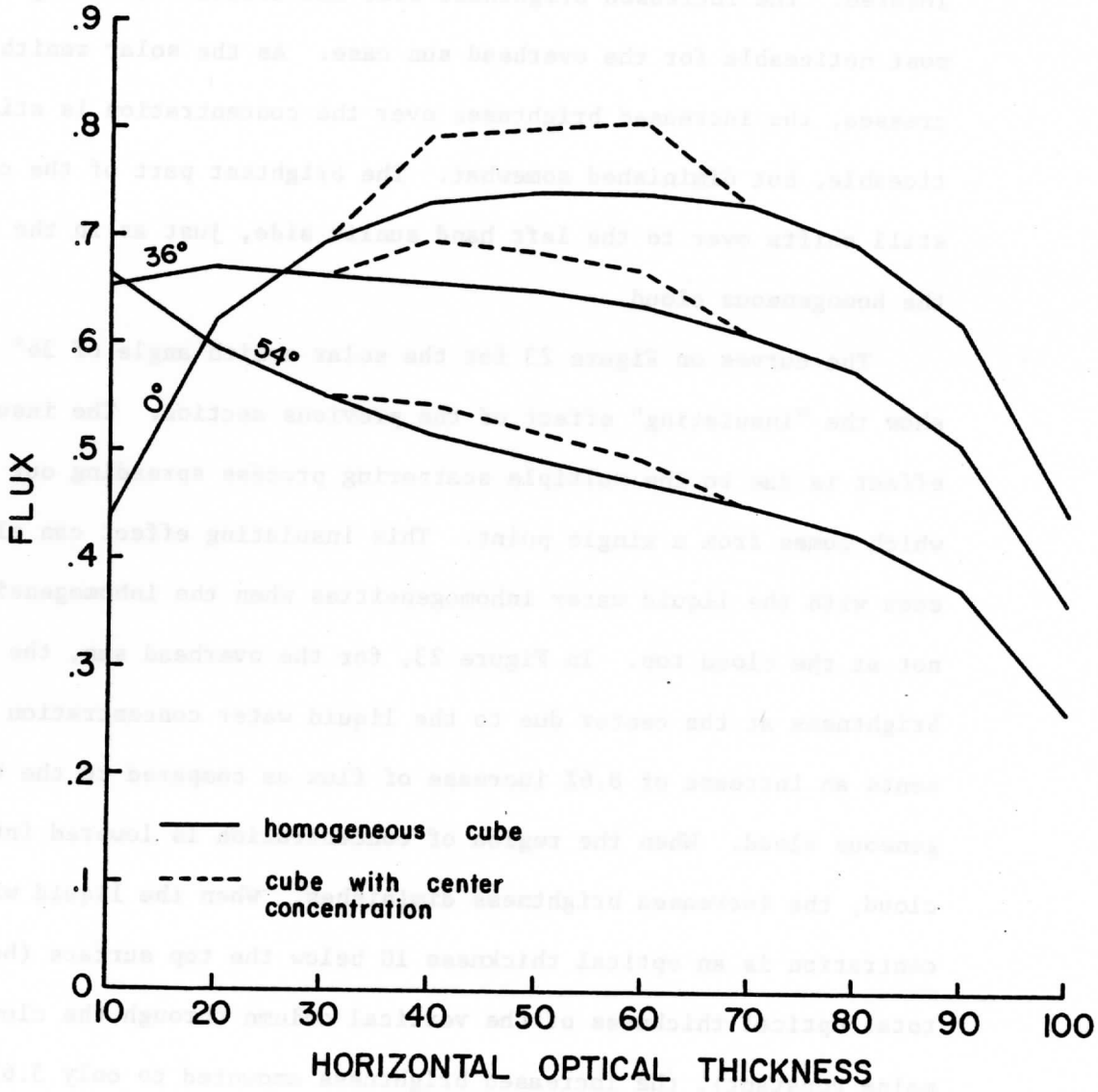

Fig. 23. Cross section of the flux across the top a cubic cloud of optical thickness 100 showing the effect of a liquid water inhomogeneity in the cloud center for three different sun angles. The solid lines are fluxes from homogeneous cubic clouds. The dashed lines are for cubic clouds which have a liquid water inhomogeneity of twice the liquid water of the rest of the cloud for a shaft in the top half of the cloud center.

located. The increased brightness over the concentration region is most noticeable for the overhead sun case. As the solar zenith increases, the increased brightness over the concentration is still noticeable, but diminished somewhat. The brightest part of the cloud still shifts over to the left hand sunlit side, just as in the case of the homogeneous cloud.

The curves on Figure 23 for the solar zenith angle of 36° and 54° show the "insulating" effect of the previous section. The insulating effect is due to the multiple scattering process spreading out the light which comes from a single point. This insulating effect can also be seen with the liquid water inhomogeneities when the inhomogeneity is not at the cloud top. In Figure 23, for the overhead sun, the increased brightness at the center due to the liquid water concentration represents an increase of 8.6% increase of flux as compared to the homogeneous cloud. When the region of concentration is lowered into the cloud, the increased brightness diminishes. When the liquid water concentration is an optical thickness 10 below the top surface (but the total optical thickness of the vertical column through the cloud remains constant), the increased brightness amounted to only 3.6%. When the concentration was lowered to an optical thickness of 20 below the top, the increased brightness was only 1.3%. When the concentration was an optical thickness of 30 below the top, the increased brightness was only 0.5%. The SMS satellite would not be able to detect a change in brightness that small.

4.3 Flux Variation Across Cubic Clouds with a Tower on Top

The building block concept was extended to allow investigations of non-cuboidal shapes which could be constructed from building blocks. The protrusions from the basic cloud present the possibility that light which exits the boundary of one part of the cloud could re-enter the cloud through some other boundary. To account for this recapture, a knowledge of the angular distribution of the light coming out of a surface is required. Since the building block model generates flux, not intensity, this angular distribution must be postulated. The simplest distribution possible is the isotropic distribution where the intensity has no angular dependence. However, Mie theory for single scattering and experimental measurements of clouds, such as Brennan and Bandeen (1970) show that clouds can have anisotropic characteristics. While isotropic scattering cannot be universally applied to clouds, it can be used as an approximation to the intensity distribution for some clouds. For large clouds, the multiple scattering can smooth out much of the directional character of the photon scattering. Appleby and Irvine (1973) showed that after a photon has traveled an optical path length of 25 in a water cloud, it has lost most of its directional characteristics. Brennan and Bandeen (1970) showed that the anisotropic character of stratocumulus clouds was a function of solar zenith angle and viewing angle. Solar zenith angles of over 70° and viewing nadir angles of greater than 50° showed strong anisotropic effects. However, solar zenith angles of 60° or less and nadir angles of 50° or less showed only weak anisotropic effects. Hence for larger clouds with

moderate solar and viewing zenith angles, which are typical of most satellite image applications, the isotropic assumption can be appropriately used as a first guess angular distribution of the intensity coming from a cloud. The isotropic assumption has been used in this study for both the recapture of light by protrusions, and for relating the flux from the model to intensity measurements such as a satellite would see.

The first non-cuboidal shape investigated was a small tower on top of a larger parent cloud. The fluxes were first computed without any light recapture. This flux distribution was then used as a first guess field for the Newton method iterations when the light recapture was accounted for. For each exposed exterior small cube face, the input flux was determined as the sum of the external flux and all the solid angles of light coming from boundary cube surfaces within sight of the cube surface being processed. For isotropic radiation from a flat surface, flux input from the unit area i^{th} cube into the unit area j^{th} cube face can be approximated (Hottel and Sarofim, 1967) by:

$$F_{ij} = \frac{1}{\pi} \frac{\cos \beta \cos \delta F_i}{(r_{ij})^2}$$

with $\cos \beta$ = cosine of angle exit vector to the normal i^{th} face

$\cos \delta$ = cosine of angle entrance vector to the normal j^{th} face

r_{ij} = distance between the two faces

F_i = the flux coming out of the i^{th} cube face.

The model included shadows. The position of shadows was computed and the solar input flux was set to zero for these cube surfaces. If the shadow covered a part of a cube, the surface was considered completely in shadow if more than 50% of the surface area was covered. Likewise, if less than 50% of the area was in shadow, the surface was considered to be shadow free.

The results of the building block model of a cube with a tower on top were compared with the Monte Carlo results of McKee and Klehr (1978). McKee and Klehr used a basic main cloud of x, y dimensions, of optical thickness equal to 120, a Z dimension thickness of 60, an overhead sun, and Deirmendjian's (1969) C-1 phase function. A variety of different shaped turrets were placed on top of the main cloud. Table 6 lists from the results the fraction of the incident light coming out of the main cloud and tower tops and sides of McKee and Klehr (MK) and of the building block (BB) for a turret which becomes progressively taller. The building block model used initial cubes of optical thickness 20 whose transfer functions were obtained from Davies (1976) for the asymmetry factor g = .855. As the tower becomes taller more light exits the tower sides and it becomes progressively darker. Figure 24a shows the results of McKee and Klehr (dashed lines) and the building block model (solid lines) for the percent of the incident coming out of the top of the parent cloud and of the tower, as a function of the height of the tower. Figure 24b shows the same thing for the sides of the cloud and tower. The building block model follows the trends of the Monte Carlo model tower results quite nicely, lending confidence

Table 6

	z	x,y	% incident	Fraction of total light: top MK	top BB	sides MK	sides BB	bot MK	bot BB
 cld	60	120	100	.631	.604	.330	.339	.039	.057
 tur	20	40	11.1	.060	.054	.069	.073		
cld	60	120	88.9	.490	.442	.332	.358	.050	.065
 tur	40	40	11.1	.049	.046	.106	.108		
cld	60	120	88.9	.464	.420	.332	.363	.049	.063
 tur	80	40	11.1	.043	.040	.139	.136		
cld	60	120	88.9	.439	.400	.330	.361	.049	.062

Table 6. Comparison of the fraction of the incident light which comes out the top, sides, and bottom of a cuboidal cloud with a turret on top as a function of the height of the turret. The Monte Carlo results of McKee and Klehr (1978) (MK) and the results of the building block model (BB) are shown for an overhead sun.

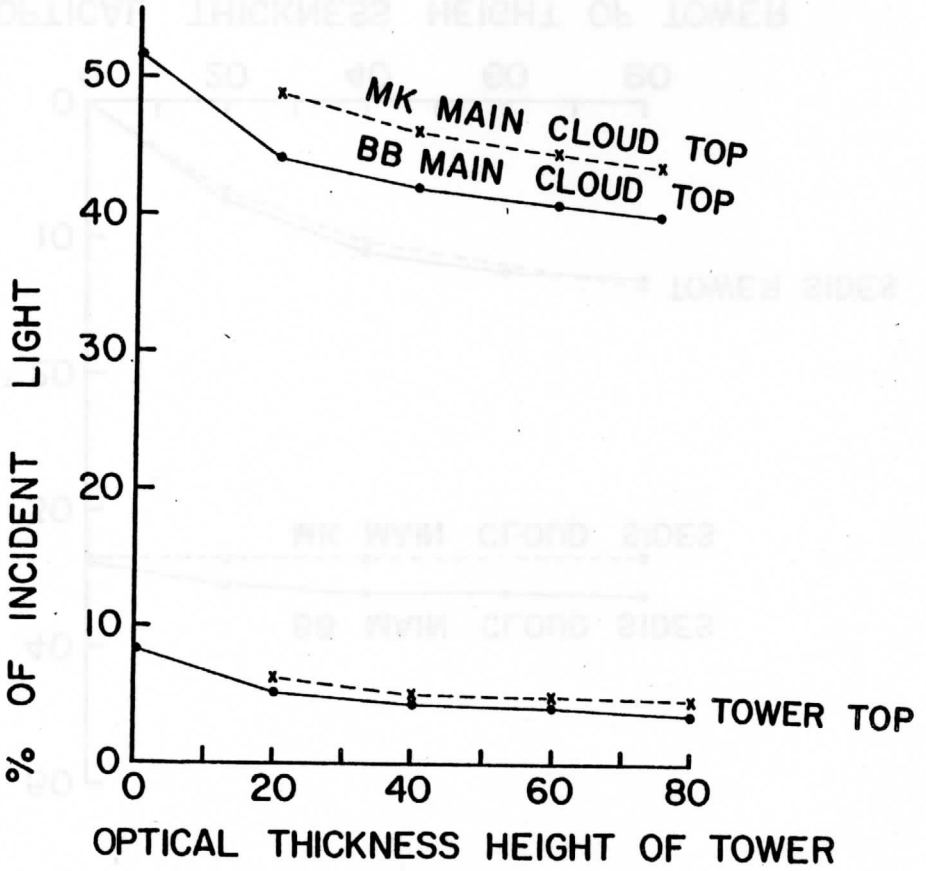

Fig. 24a. Comparison of the building block results (solid curves) with the Monte Carlo results of McKee and Klehr (1978) (dashed curves) for the percent of the incident light exiting the cloud and the tower tops as a function of the height of the tower. The main cuboid has optical thickness dimensions of 120 x 120 x 60 high. The tower has horizontal dimensions of 40. The sun is overhead.

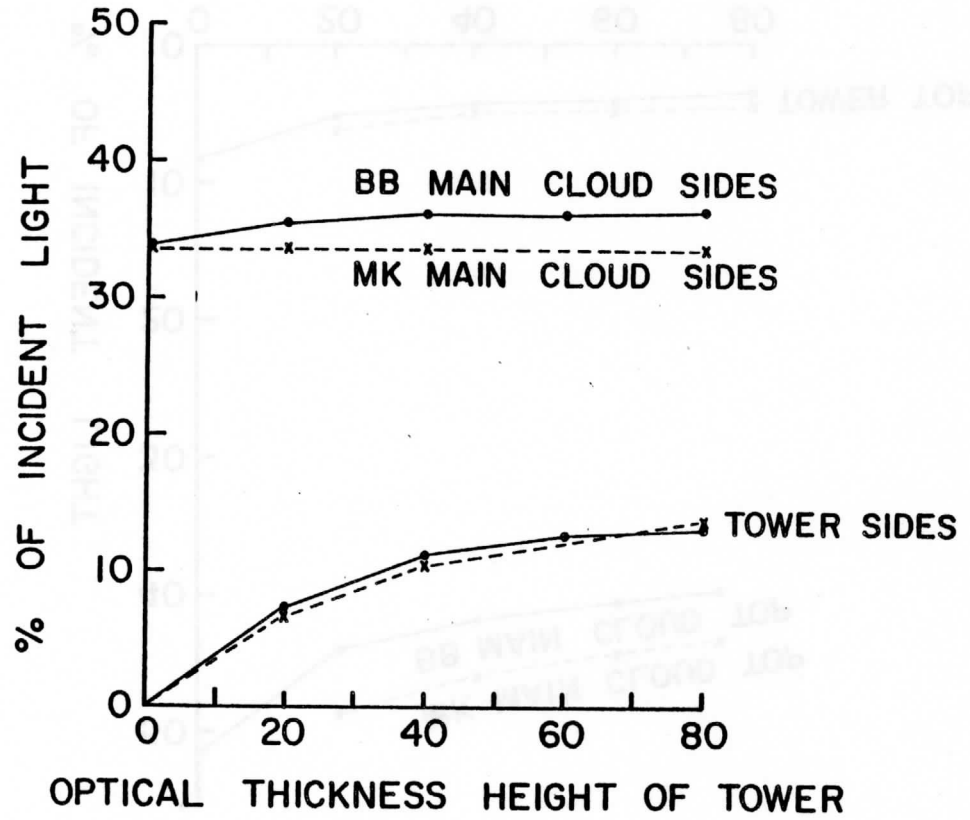

Fig. 24b. Same as fig. 24a except for the percent of the incidental light exiting the sides of the main cloud and the tower as a function of tower height.

in the ability of the building block model's ability to handle non-standard geometric cloud configurations which involve light recapture.

In order to investigate the effects of sun angle on the scattering of light from a tower, the building block model was used with a tower geometry of the basic 10 x 10 x 10 cube construction of the previous sections, but with an additional 3 x 3 x 2 high tower on top of the basic cube. All the cubes, including those in the tower, have the same liquid water content, so the cloud is a homogeneous cloud. Figure 25 shows this construction for small building blocks of optical thickness 10. Hence the big cube underneath the tower has optical dimensions of 100 x 100 x 100 and the tower has optical dimensions of 30 x 30 x 20 high. The figure is for an overhead sun and shows the fluxes coming out of the top surfaces. The tower is the area inside the box drawn in the figure. This figure can be compared with Figure 3a which shows the same cloud, but without the tower. As can be seen from the figure, the tower appears darker than the base cloud. Figure 26 shows a cross section across the cloud top through the center of the tower. The dashed line is the cloud with the tower. The solid line is the cloud without the tower. This shows the cloud with the tower on it to be darker than the cloud without the tower, even outside the immediate tower vicinity. The center of the tower is relatively brighter than the edges of the tower. The fraction of the incident light exiting the cloud top without the tower was 57%, but was only 55% with the tower. These results of the tower appearing darker and the total albedo of the

TOP FACE OF CLOUD

.301	.397	.433	.447	.452	.452	.447	.433	.398	.301
.397	.538	.595	.619	.626	.625	.617	.595	.539	.398
.433	.595	.663	.690	.694	.692	.682	.660	.595	.434
.447	.619	.690	.712	.689	.680	.675	.678	.616	.448
.452	.626	.694	.689	.427	.477	.416	.653	.617	.451
.452	.625	.692	.680	.477	.540	.466	.644	.615	.451
.447	.617	.682	.675	.416	.466	.406	.640	.608	.446
.433	.595	.660	.678	.653	.644	.640	.648	.592	.433
.398	.539	.595	.616	.617	.615	.608	.592	.539	.399
.301	.398	.434	.448	.451	.451	.446	.433	.399	.302

$\tau_y = 100$

$\tau_x = 100$

Fig. 25. The flux variation across the top of a cubic cloud of optical dimensions 100 with a 30 x 30 x 20 tower on top of the parent cubic cloud. The position of the tower is shown by the box in the figure. The sun is overhead. The tower appears darker than the parent cloud because of light leaking out the sides of the small tower.

top decreasing with the addition of the tower are consistent with the results of the Monte Carlo simulations of McKee and Klehr (1978).

At first glance these results appear to contradict intuition. The portion of the cloud with the tower is thicker, so why shouldn't it be brighter than the rest of the cloud? The answer to this deals with the finite shape of the tower. Without the tower all the incoming sunlight hitting the area of the tower would hit the top of the base cloud and contribute to the general multiple scattering taking place. However, when the tower is added some of the light which hits the top of the tower is scattered out the sides of the tower. Some of the light coming out the tower sides is recaptured by the top of the base cloud, but over half of the light from the tower sides is lost in directions which cannot be recaptured. Hence the addition of the tower represents a net loss of input energy to the cloud system.

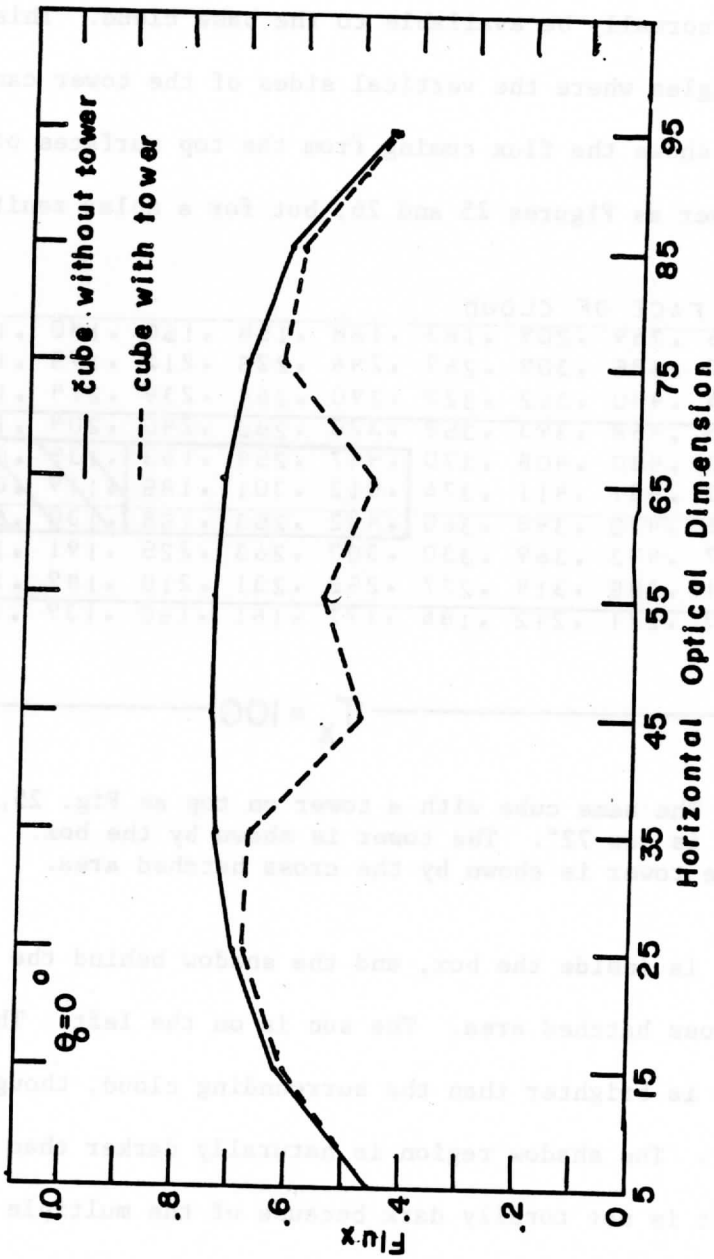

Fig. 26. Cross section of flux variation across the cloud top through the center of the tower. The solid line is the cubic cloud without the tower and the dashed line is the cloud with the tower on top. The sun is overhead. The parent cloud ia a cube 100 x 100 x 100. The tower has optional dimensions 30 x 30 x 20.

If the tower is to appear bright, it must capture light which would not normally be available to the base cloud. This possible for low sun angles where the vertical sides of the tower can capture light. Figure 27 shows the flux coming from the top surfaces of the same cube with a tower as Figures 25 and 26, but for a solar zenith angle of 72°.

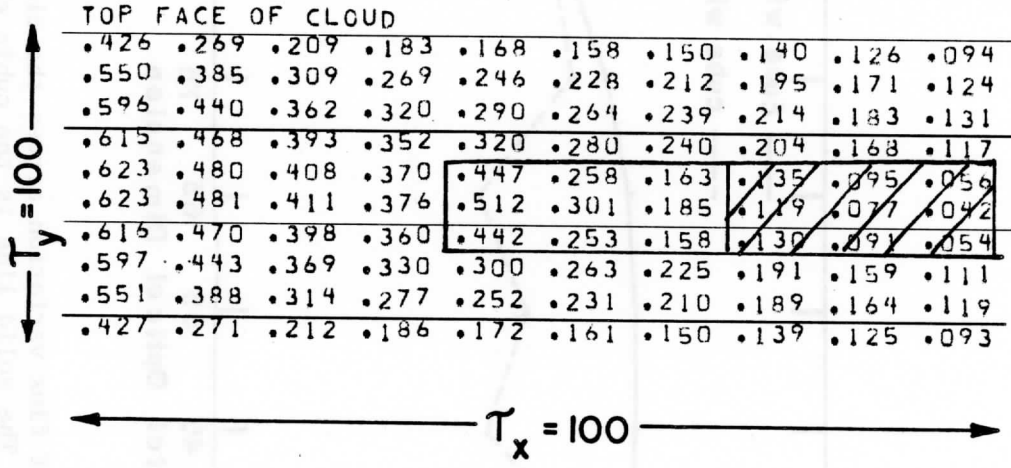

Fig. 27. The same cube with a tower on top as Fig. 25, except that the sun angle is now 72°. The tower is shown by the box. The shadow behind the tower is shown by the cross hatched area.

The tower is inside the box, and the shadow behind the tower is shown by the cross hatched area. The sun is on the left. The left side of the tower is brighter than the surrounding cloud, though the right side is darker. The shadow region is naturally darker than the surrounding cloud, but is not totally dark because of the multiple scattered light coming out of the base cloud's interior. Figure 28 shows the same cross section across the cloud top as Figure 26, but the solar zenith angle is now 72°. The dashed line is for the case with the tower addition. On the left side of the tower, the flux coming out of the base cube is

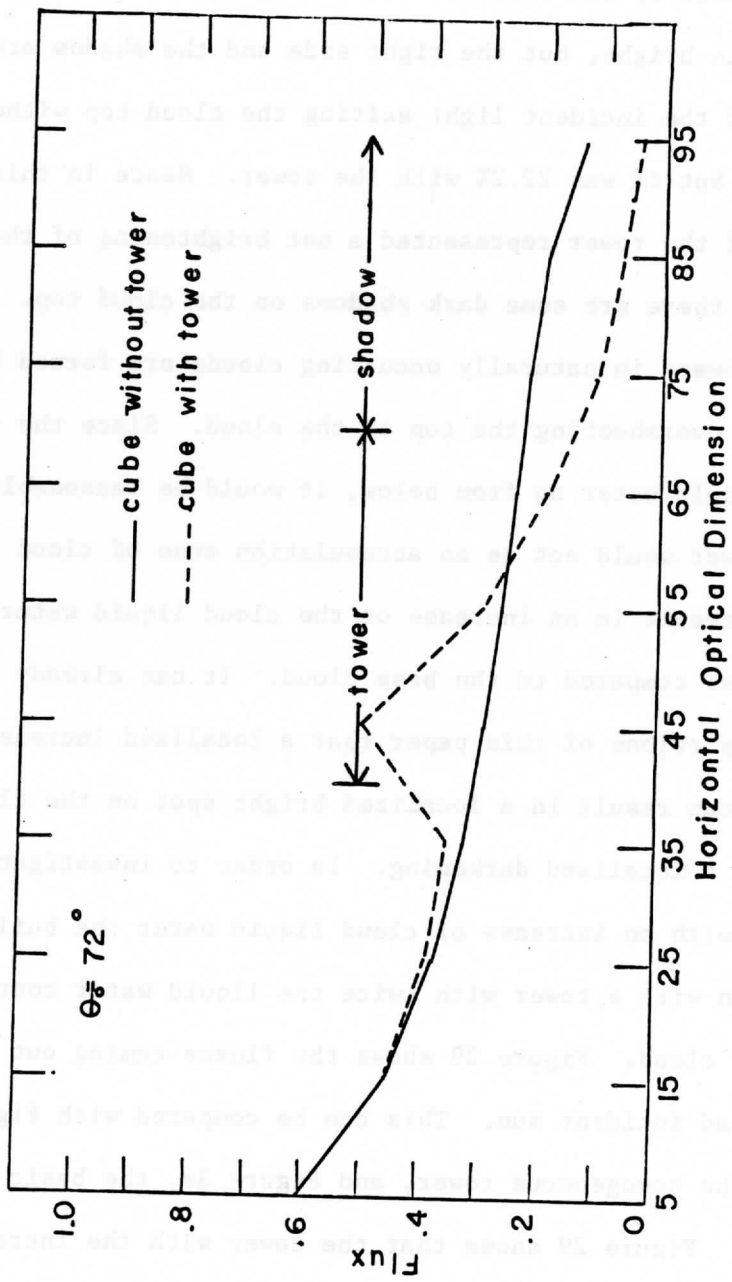

Fig. 28. The same cross section across the top of the tower as fig. 26, except that the solar zenith angle is now 72°. The dashed line represents the flux from the cloud with the tower. The position of the tower and its shadow are indicated.

approximately the same as without the tower. The left side of the tower is bright, but the right side and the shadow are dark. The fraction of the incident light exiting the cloud top without the tower was 21.9%, but it was 22.2% with the tower. Hence in this case, the addition of the tower represented a net brightening of the cloud top even though there are some dark shadows on the cloud top.

Towers in naturally occurring clouds are formed by vigorous updrafts overshooting the top of the cloud. Since the updraft is bringing liquid water up from below, it would be reasonable to expect that the tower would act as an accumulation zone of cloud droplets. This would result in an increase of the cloud liquid water content of the tower as compared to the base cloud. It has already been shown in previous portions of this paper that a localized increase of cloud liquid water can result in a localized bright spot on the cloud. The tower causes a localized darkening. In order to investigate the effect of a tower with an increase of cloud liquid water the building block model was run with a tower with twice the liquid water content of the rest of the cloud. Figure 29 shows the fluxes coming out of the top for an overhead incident sun. This can be compared with Figure 25, the cloud with the homogeneous tower, and Figure 3a, the basic cloud without the tower. Figure 29 shows that the tower with the increased liquid water content has a greater flux coming out of the tower than does the homogeneous tower of Figure 25. The increased liquid water tower has a center flux which is approximately the same as the surrounding cloud, but the edges of the tower are still darker. This results in what

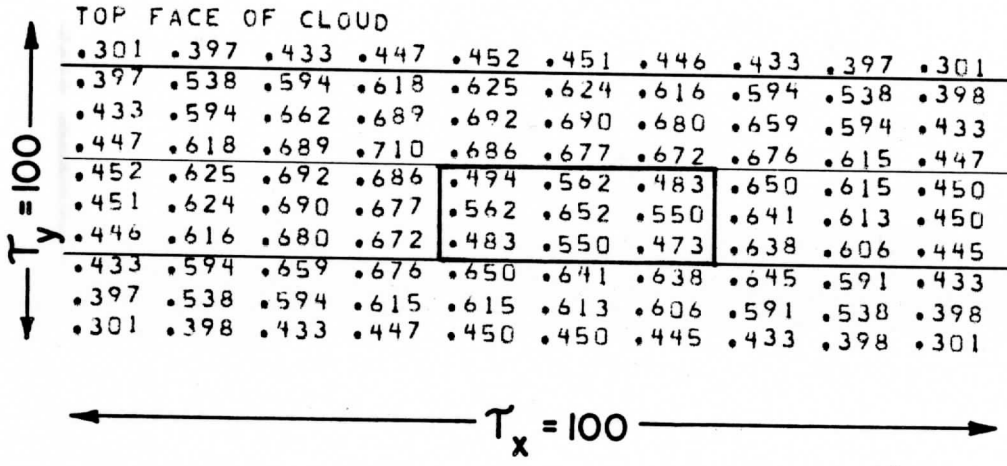

Fig. 29. The flux variation across the top of a cubic cloud with a tower on top. The tower has twice the liquid water content of the rest of the parent cloud. The geometric configuration is the same as fig. 27 with an overhead sun.

would appear to be a dark ring around the tower. The sun angle was then changed to 72° with the increased liquid water tower. The increased liquid water tower was slightly brighter than the homogeneous tower, but not significantly so.

The results of the theoretical simulations of towers show dark rings around towers for an overhead sun. These results can be seen in naturally occurring clouds. Figure 30a shows a picture (from Black, 1978) of tropical cyclone Lottie taken by Sky Lab astronauts on December 8, 1973 at 23:43:30 GMT. The sun was located at 18.5°S latitude, 176.0°E longitude. The photograph was overexposed by 3 f stops. The relative brightness features of the storm were made visible in Figure 30b by photographic enhancement, using high contrast film. The sun was almost directly overhead ($\theta_o < 10°$) in this photograph, so the darker portions of the enhanced photograph are probably <u>not</u> shadows. Figure

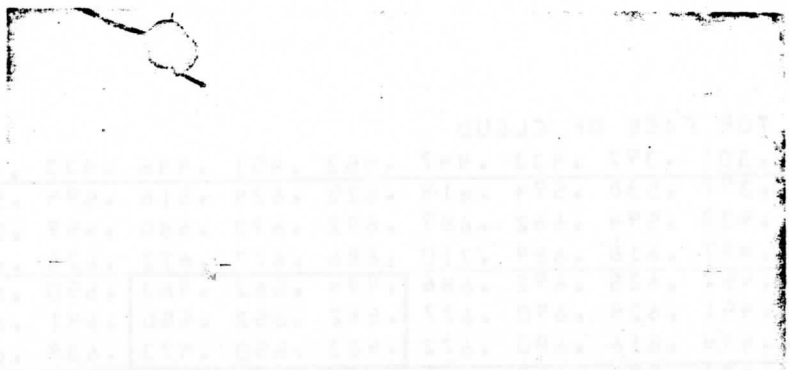

Fig. 30a. Photograph of Tropical Cyclone Lottie taken by sky lab astronauts on December 8, 1973 at 23:43:30 GMT. The storm was located at 18.5°S latitude, 176.0°E longitude. The photograph of the storm was overexposed by 3 f stops.

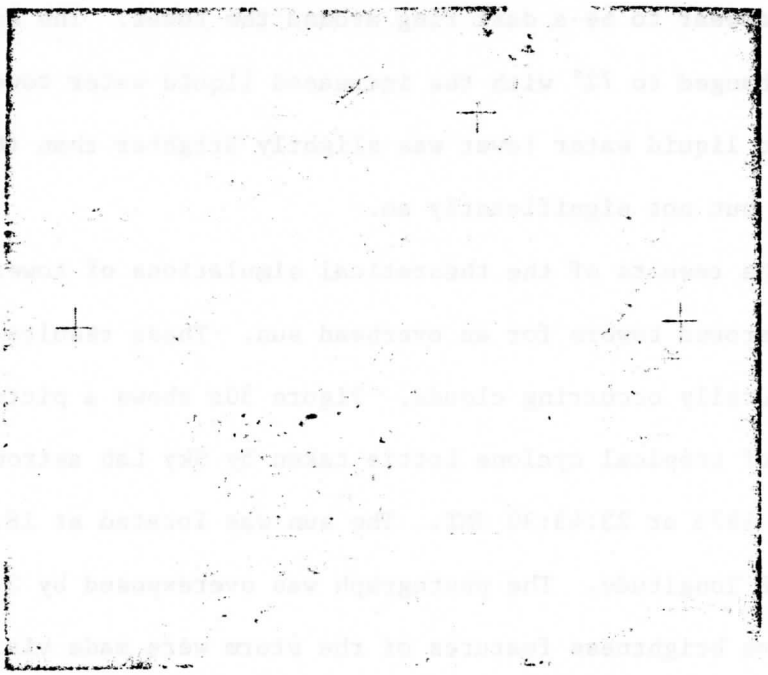

Fig. 30b. The same photograph as fig. 30a, but the relative brightness variations have been made more visible by photographic enhancement using high contrast film.

30c shows an enlargement of the southwest eyewall region. Here many overshooting towers appear as relative dark spots.(the Sky Lab

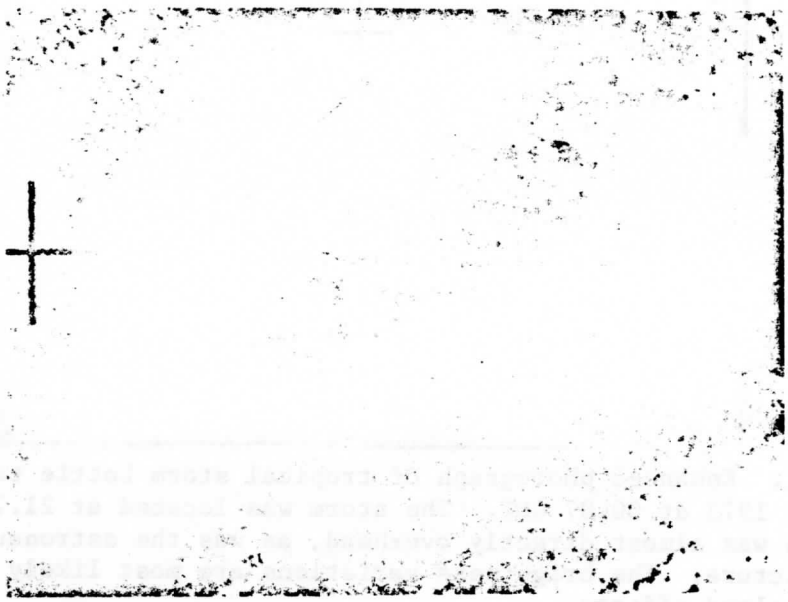

Fig. 30c. An enlargement of the southwest eyewall region of fig.30b. The solar zenith angle was less than 10°, so the dark features cannot have been shadows. The dark spots appear to be overshooting towers above the parent cloud system.

overflow tropical cyclone Lottie again on December 11, 1973 at 00.07 GMT). The storm was located at 21.7°S, 175.3°W.

Figure 31 shows a vertical enhanced photograph of the storm. The sun was again almost directly overhead (θ_o<5°) so shadows would not be possible with this geometry. The photograph shows detailed texture with relative bright and dark features on top of the storm which give it a boiling appearance. These brightness patterns are probably due to the finite geometry of the structure of the overshooting convective towers within the storm.

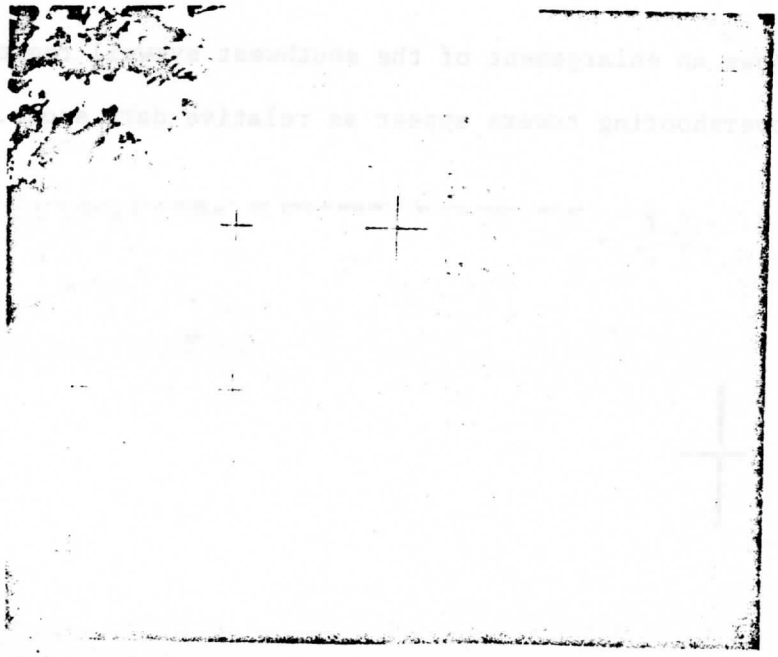

Fig. 31. Enhanced photograph of tropical storm Lottie taken on December 11, 1973 at 00.07 GMT. The storm was located at 21.7°S, 175.3°W. The sun was almost directly overhead, as was the astronaut who took this picture. The brightness variations are most likely caused by finite cloud effects.

4.4 Effects of Cloud Shape

The previous section showed that cloud top texture (such as an overshooting turret) can affect the light being scattered by a cloud. Cloud shape can also affect the scattered light. Busygin et al. (1973) showed that the relationship of cloud albedo to solar zenith angle depended on cloud shape for cylinders, spheres, and inverted parabaloids. Most of Busygin's results were for reasonably small clouds with optical depths of approximately 14.

The building block model was configured to simulate the approximate shapes used by Busygin of cylinders, spheres, and inverted parabaloids with constant height to maximum width dimensions. Since the building block model does not handle the forward scatter of light very well for

the size cloud used by Busygin, a study of the effects of cloud shape was done using clouds with heights of optical thickness 110. The size of the initial building block cube was 10, with the geometric shapes being approximated by the pile of building blocks. Shadows were considered with the convention that if over half a surface of a building block was covered by shadow, the entire block was considered in the shadow. The total albedo of the cloud being defined as: the scattered flux out the top of the figure x the top area + one-half the flux out the sides x the sides area; the quantity being divided by the normal input flux on the top x the top area + the normal input flux on the sides x the input side area.

Figure 32 shows the relationship of the total albedo to the solar zenith angle for the various shapes and plane parallel. The cube shape has the greatest albedo variation while the parabaloid has very little albedo variation. The albedo difference between shapes is greatest for the overhead sun, which is consistent with the previous section on the effects of turrets. For the overhead sun the cube had the highest albedo. It also had the maximum dimension at the cloud top. As the cloud top dimension decreased between the different shapes, the albedo also decreased. The inverted parabaloid had the smallest cloud top dimension, and it had the lowest albedo. As the solar zenith angle increased, the albedo of the different shapes tended toward a common trend. The trends of the albedos of the different shapes are more closely related to each other than they are to the trends of the plane-parallel solution.

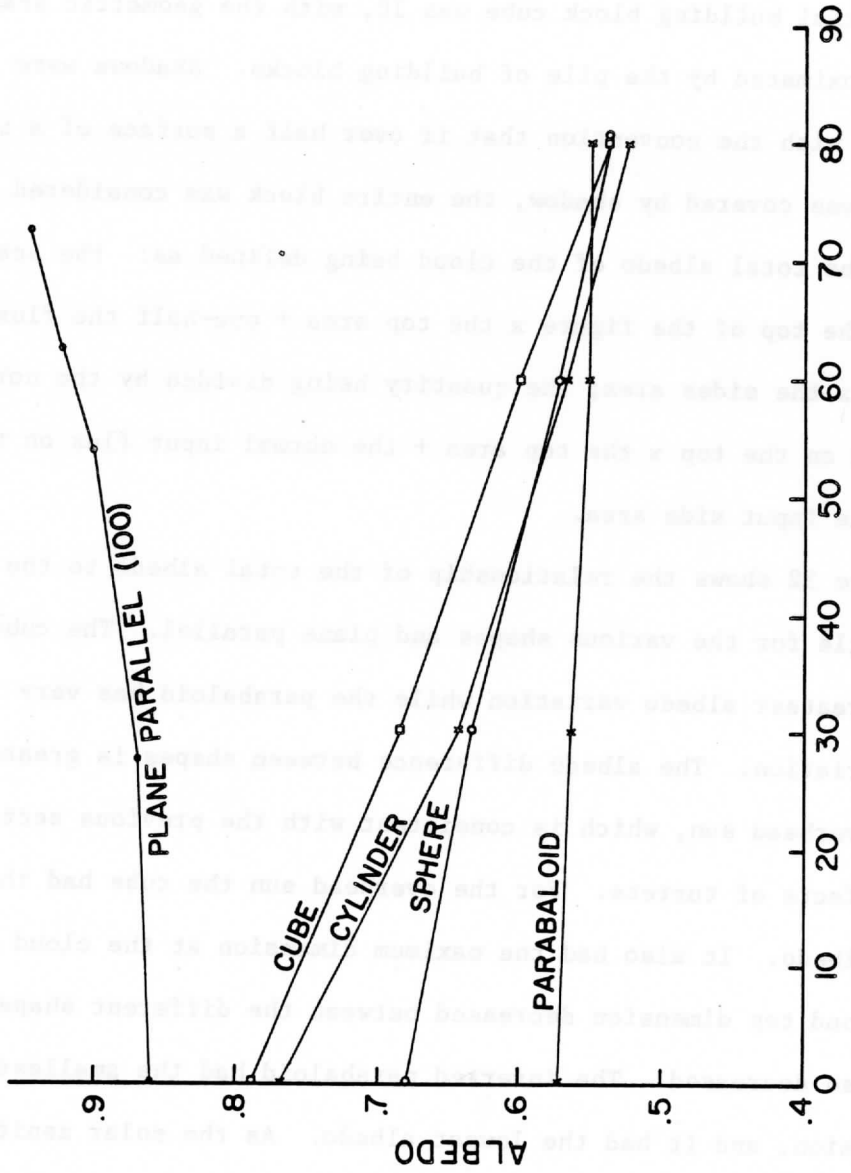

Fig. 32. Cloud albedo as a function of solar zenith angles for cloud shapes of a cube, cylinder, sphere with truncated bottom, an inverted parabaloid, and the plane-parallel solution. The cloud shapes were approximated using building blocks. The cloud height equaled the maximum width of optical thickness 110 for all the cloud shapes.

The trends of curve for the cube of Figure 32 agree with the albedo analysis of Davies (1976). However, the trends of the other curves do not agree with Busygin et al.(1973). The clouds of Busygin et al. were much smaller than the ones used in this study. The smaller clouds would have more single scatter characteristics, which could explain some of the differences noted. Investigation of these differences are worthy of future study.

4.5 Simulation of Naturally Occurring Clouds

The study of the effects of cloud shape also included an investigation into the ability of the building block model to simulate light scattering in naturally occurring cumulus clouds. The data set chosen for investigation was day 261 (September 18), 1974 in the GATE area off the coast of Africa.

On day 261 a group of aircraft made a coordinated box flight pattern around an area on developing cumulus convection. Included in this array of aircraft was a C-130 flying at 5.48 km and a DC-6 flying at 1.13 km. The cloud bases on this day were reported at .6 km and .88 km. The DC-6 was flying through the clouds near the cloud bases. It was equipped with upward and downward looking visible radiometers, a liquid water probe, and a down looking 8-11 micron radiometer, in addition to other meteorological sensors. The C-130, flying above the DC-6, had among its instrument configuration side looking cameras which were suitable for photogrammetric mapping of cloud geometries. In addition to the aircraft instrumentation, the SMS-1 geostationary satellite recorded the visible radiances reflected from the clouds. The SMS-1

spatial resolution was approximately .8 km.

Figures 33a and b show the "candidate cloud" selected for the investigation. The cloud was near the corner of the box flight pattern, so the aircraft was able to view the cloud from two different orientations. Figure 33a shows the candidate cloud looking west, and Figure 33b shows the candidate cloud looking north. The cloud was large enough for the satellite to distinguish, yet was small enough so the aircraft could conveniently view the cloud.

The dimensions of the candidate cloud were determined using photogrammetry similar to the method described by Holle (1978). A sequence of the C-130 aircraft side looking camera images were used. The three-dimensional orientation and speed of the C-130 were recorded as part of the flight instrumentation recording. Knowing the speed of the aircraft and the time interval between images, a base line distance was established. Measuring the angles to points on the cloud and knowing the airplane height and orientation along with the base line distance, provides the photogrammetric information required to determine the three-dimensional geometry of the candidate cloud. The cloud was 26 km long and was 1.0 to 1.6 km high above its base. The measurements of the small side of the cloud showed the cloud to be 5.9 to 5.5 km wide at the base and 1.7 to 1.6 km wide at the top of the towers.

The satellite view of the candidate cloud is shown by Figure 34. The arrow on the image points to the candidate cloud. Figure 35 shows the digital satellite brightness values of the candidate cloud contours of every 25 counts have been drawn on the figure. The values of the

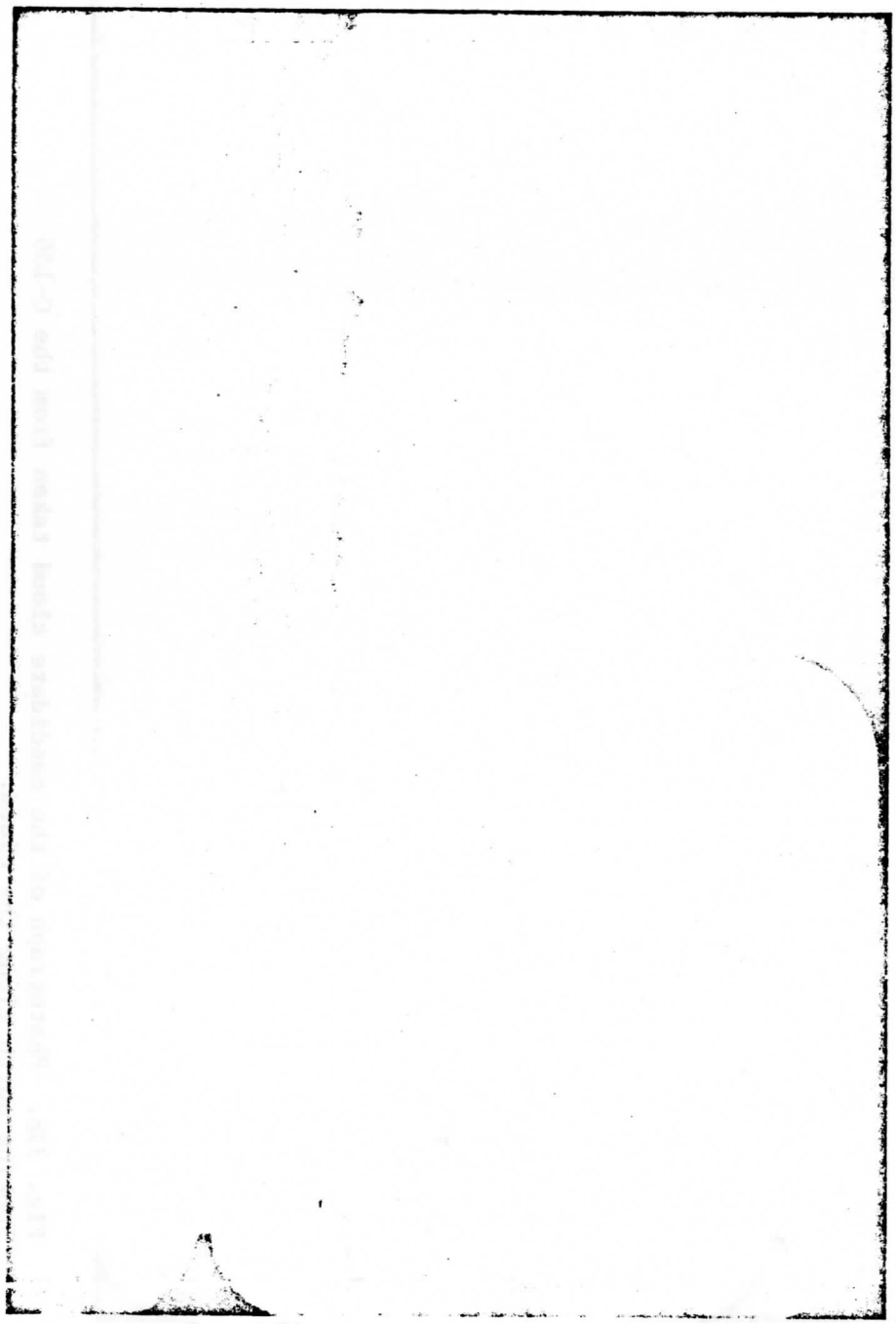

Fig. 33a. Photograph of the "candidate cloud" taken from the C-130 flying at 5.5 km on September 18, 1974 in the GATE area. The photograph is looking west. A series of these side looking camera photographs were used to perform a photogrammetric mapping of the external dimensions of the "candidate cloud."

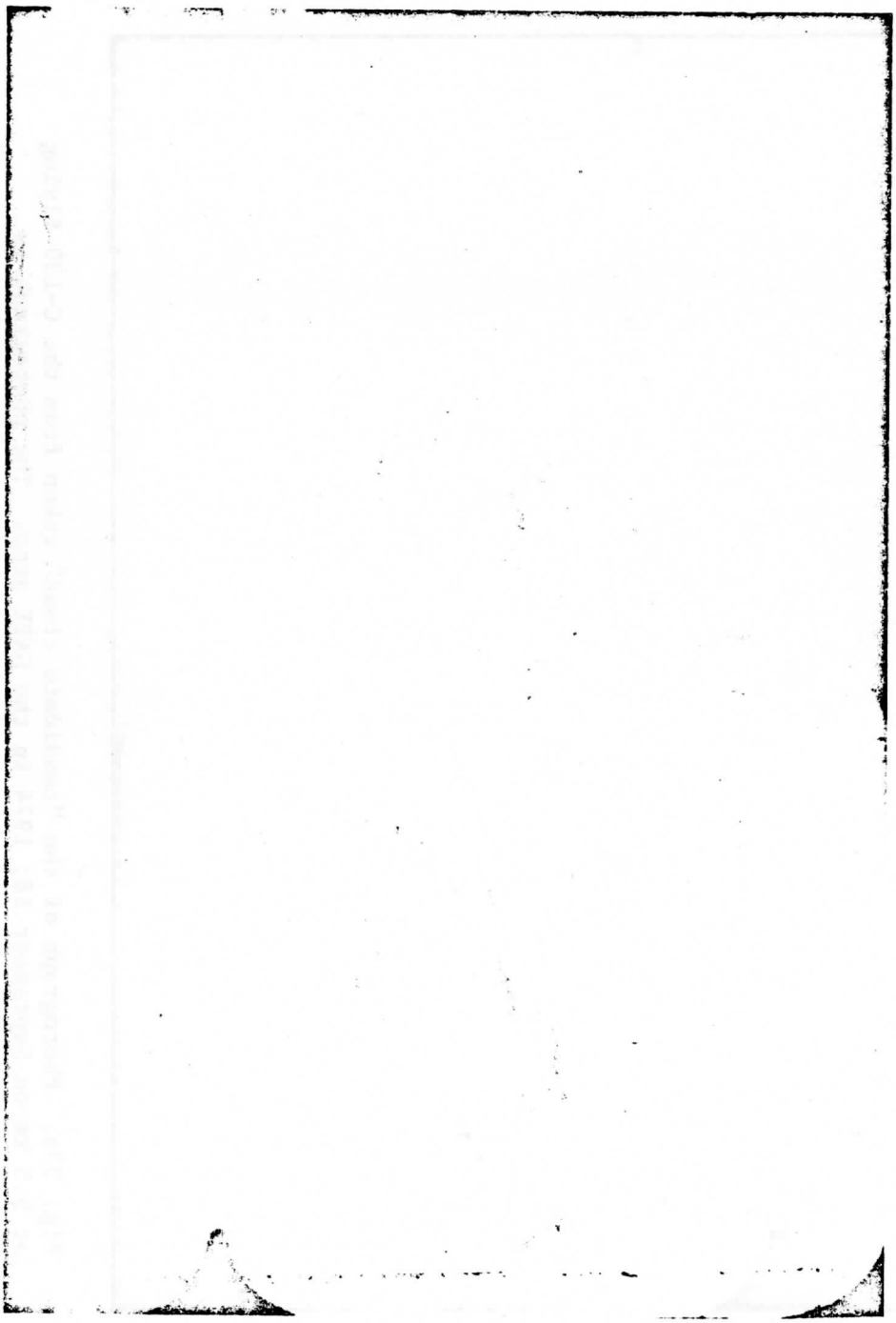

Fig. 33b. Photograph of the candidate cloud taken from the C-130 looking north along the cloud.

cloud center are in the range of 180-190 with several small regions of counts greater than 200. Each of the pixels is approximately .8 km wide. The cloud appears to be tilted along a NE-SW line because of the computer printer having different spacing for lines and elements. The solar zenith angle at the time of this data was 13°, and the azimuth direction to the sun lies fairly close to the long axis of the cloud.

The DC-6 flew through the southern portion of the candidate cloud at an elevation of 1.13 km. There was a discrepancy of 6 km between the satellite determined longitude, and the DC-6 determined position of cloud entry. No north-south discrepancy could be determined with the available data. The approximate aircraft flight path is shown on Figure 35 by the heavy line on the satellite data. The photogrammetric measurements made from the C-130 show the cloud to be approximately 1.2 to 1.4 km thick at this point of airplane entry. Figure 36 shows a trace of the up and down visible flux recorded by the DC-6 as it flows through the candidate cloud. Eppley pyranometers with spectral range .3 to 3 microns were used for these measurements. Cloud liquid water was sensed by a Johnson Williams hot wire flowmeter. The portion of the cloud where liquid water was sensed is noted on Figure 36. The amount of liquid water sensed was .1 gm/m^3. The DC-6 was equipped with Barnes PRT-5 IR radiometer operating in the 9.5 to 11.5 micron window range. The radiometer was pointing down in order to measure sea surface temperature. Since the sea surface temperature is fairly constant and cloud droplets affect the window radiation, this radiometer can be used to determine when the DC-6 had cloud elements beneath it.

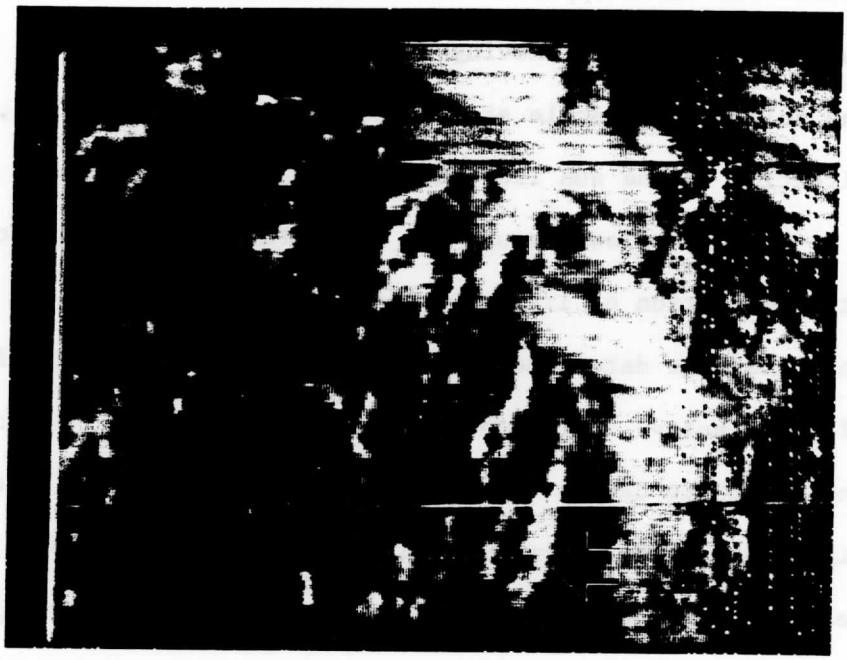

Fig. 34. The SMS-1 satellite view of the candidate cloud at 1400Z on September 18, 1974. The arrow points to the point on the candidate cloud where the DC-6 flew through the cloud. The cloud is located at 8.55°N, 21.20°W. Zenith angle is 13°, with the sun shining along the long axis of the candidate. The image shows an area approximately 500 km wide.

Fig. 34. The SMS-1 satellite view of the candidate cloud at 1400Z on September 18, 1974. The arrow points to the point on the candidate cloud where the DC-6 flew through the cloud. The cloud is located at 8.55°N, 21.20°W. Zenith angle is 13°, with the sun shining along the long axis of the candidate. The image shows an area approximately 500 km wide.

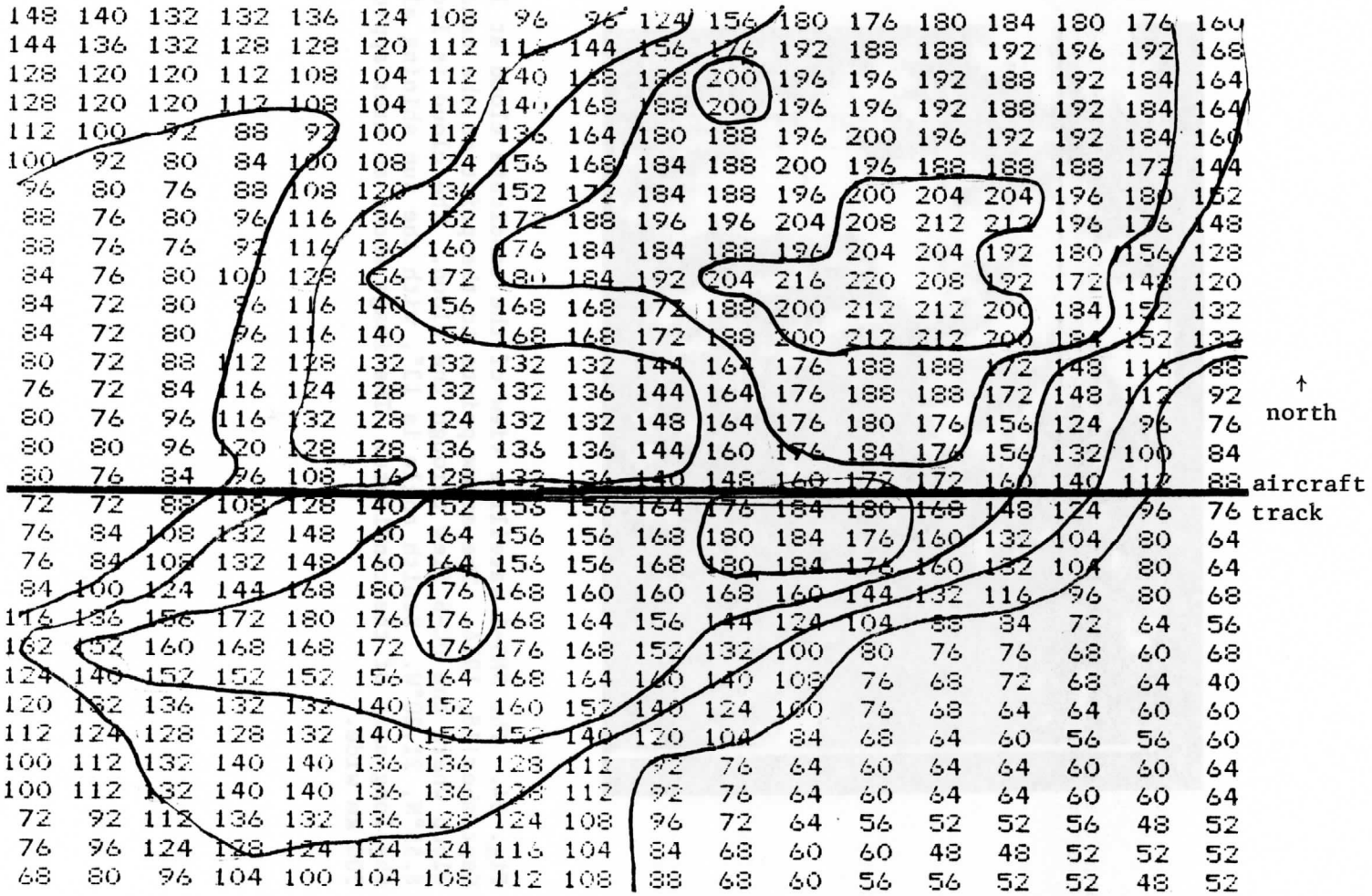

Fig. 35. The digital brightness values of the SMS-1 image of the candidate cloud. The brightness values have been contoured every 25 counts. Each data point is .8 km wide.

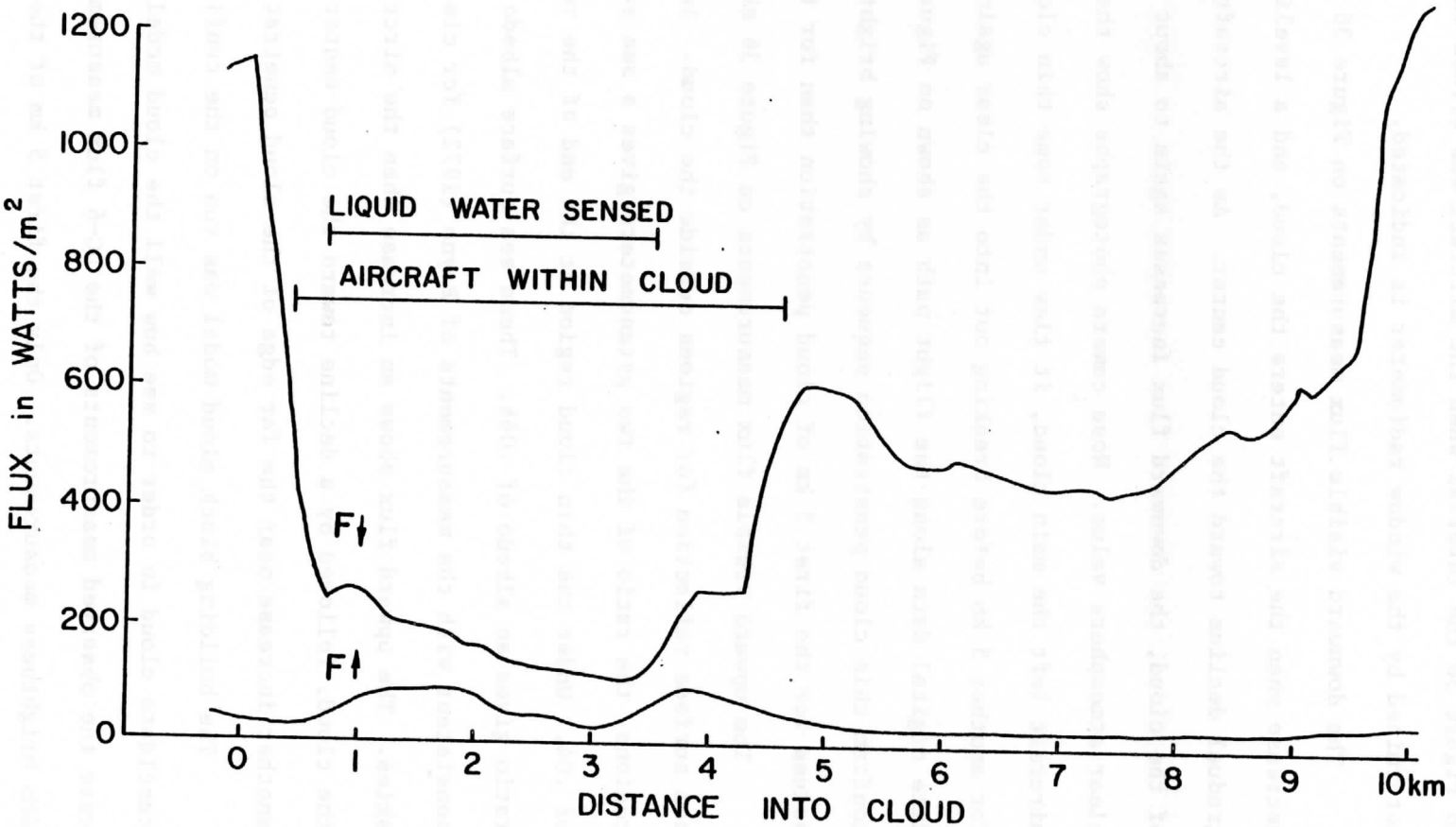

Fig. 36. Traces of the up and down welling flux measurements made by the Eppley pyranometers on the DC-6 as it flew through the candidate cloud. The time when cloud liquid water was sensed is indicated. The time when the aircraft was flying within the cloud as determined by deviations of sensed sea surface temperature is shown also on the figure.

On Figure 36 the interval when the aircraft was within the cloud as determined by the window radiometer is indicated.

The downward visible flux measurements on Figure 36 shows a marked decrease when the aircraft enters the cloud, and a leveling off with a gradual decline toward the cloud center. As the aircraft nears the edge of the cloud, the downward flux increases again to about half of the clear atmosphere value. Nose camera photographs show that after the aircraft left the main cloud, it flew under some thin cloud elements for another 5 km before breaking out into the clear again. The satellite digital data along the flight path as shown on Figure 35 tends to confirm this cloud penetration sequence by showing brighter cloud values for the first 5 km of cloud penetration than for the last 5 km.

The upward visible flux measurements on Figure 36 shows the dark sea surface reflection for regions outside the cloud. In the clear regions, the ratio of the two pyranometers gives a sea surface albedo of .04. Under the thin cloud region at the end of the record, the ratio gives an albedo of .066. These sea surface albedo values are consistent with the measurements of Payne (1972) for clear and cloudy skies. The upward flux shows an increase when the aircraft first enters the cloud, followed by a decline toward the cloud center, and then another increase near the far edge of the cloud penetration.

The building block cloud model was run on the configuration of the candidate cloud in order to see how well the cloud model could replicate the observed measurements of the DC-6 flux measurements and the SMS brightness measurements. Only the first 5 km of the cloud, when

the aircraft was actually in the cloud, was considered in the cloud modeling effort. The sea surface albedo was considered by having the flux into the bottom of the cloud to be the flux out of the bottom, times the sea surface albedo. The flux incident on the cloud side from the sea surface was 1/2 the incident vertical flux down times the sea surface albedo. A sea surface albedo of .06 was used in the cloud model runs. A solar zenith angle of 0° was used. The optical dimensions used were determined from the measured liquid water content (.1 g/m^3) and an assumed average droplet radius which gave an extinction coefficient of approximately 40 km^{-1}. The cloud width of 5 km then converts into an optical width of 200. The cloud thickness of 1.4 km converts to an optical depth of 56, so an optical depth of 60 was used in the model.

The building block model determines only flux distributions, while the satellite measures only intensity. If one makes the assumption that the flux distribution is related to the intensity distribution, then the building block flux results can be applied to simulate satellite intensity patterns. The satellite brightness values from the cloud model were determined, assuming that the light leaving the cloud top was isotropic. The SMS sensor was designed with a square root digitization scheme. For an isotropic source the sensed intensity can be represented by:

$$I = 245 * (F)^{1/2}$$

with F being the output flux at any given point on the cloud top. The maximum intensity value of 245 was obtained from the SMS-1 calibration work of Smith and Loranger (1977).

The initial geometry tried was a cuboid of optical dimensions 200 x 200 x 60. It was constructed of 10 x 10 x 6 cuboids with each cuboid's optical dimensions being 20 x 20 x 10. The simulated satellite brightness values are shown in Figure 37. Each simulated pixel has a spatial resolution of .5 km.

151	164	169	172	173	173	172	169	164	151
164	180	188	191	192	192	191	188	180	164
169	188	196	200	202	202	200	196	188	169
172	191	200	205	206	206	205	200	191	172
173	192	202	206	208	208	206	202	192	173
173	192	202	206	208	208	206	202	192	173
172	191	200	205	206	206	205	200	191	172
169	188	196	200	202	202	200	196	188	169
164	180	188	191	192	192	191	188	180	164
151	164	169	172	173	173	172	169	164	151

Fig. 37. The simulated satellite sensed brightness values for a cuboidal cloud with dimensions comparable to the candidate cloud. Each simulated pixel has a spatial resolution of .5 km. This can be compared with the actually observed brightness values of fig. 35.

The interior fluxes, however, differed from those observed by the DC-6. Figure 38 shows the simulated interior fluxes which were between levels 5 and 6 of the cloud model. (The aircraft was approximately 5/6 of the way down the cloud.) The solar flux input to the cloud was specified as 1200 watts/m^2, which was the value measured by the DC-6 in the clear portions of the flight. The simulated downward flux shows a sharp drop from outside to inside the cloud, but after the cloud boundary is

passed the interior downward flux increases toward the cloud's center where a relative maximum is reached. The upward flux gradually increases until a maximum is reached at the cloud center. The cause of this relative maximum at the cloud center is because of the square shape of the simulated cloud. The cloud top is a source of radiation and the sides and bottom are effective sinks of radiation. The radiation diffuses down from the top and out the sides and bottom. Since the sides are sinks the fluxes must be a minimum near the boundary sinks, which implies that the center would appear as a relative maximum. The observed cloud fluxes had a relative minimum near the cloud center.

The model results just described were for monochromatic visible light with no absorption by the cloud. The total solar spectrum measured by the aircraft pyranometers has some absorption in the near infrared wavelengths. While absorption was not considered in the model, absorption should not change the relative maximum in the cloud center of the cubic cloud. The top is the source of the radiation. The amount of absorption is a function of the distance from the source. For a cube, the distance from the top source of the center is approximately the same as for the edges for any given vertical level of the cube. The absorption should not greatly affect the horizontal patterns of flux distribution of a cubic cloud. Hence it would appear that a cubic geometry is not sufficient to model the radiation patterns of realistic clouds.

Since a cubic geometry does not appear to model cumulus clouds

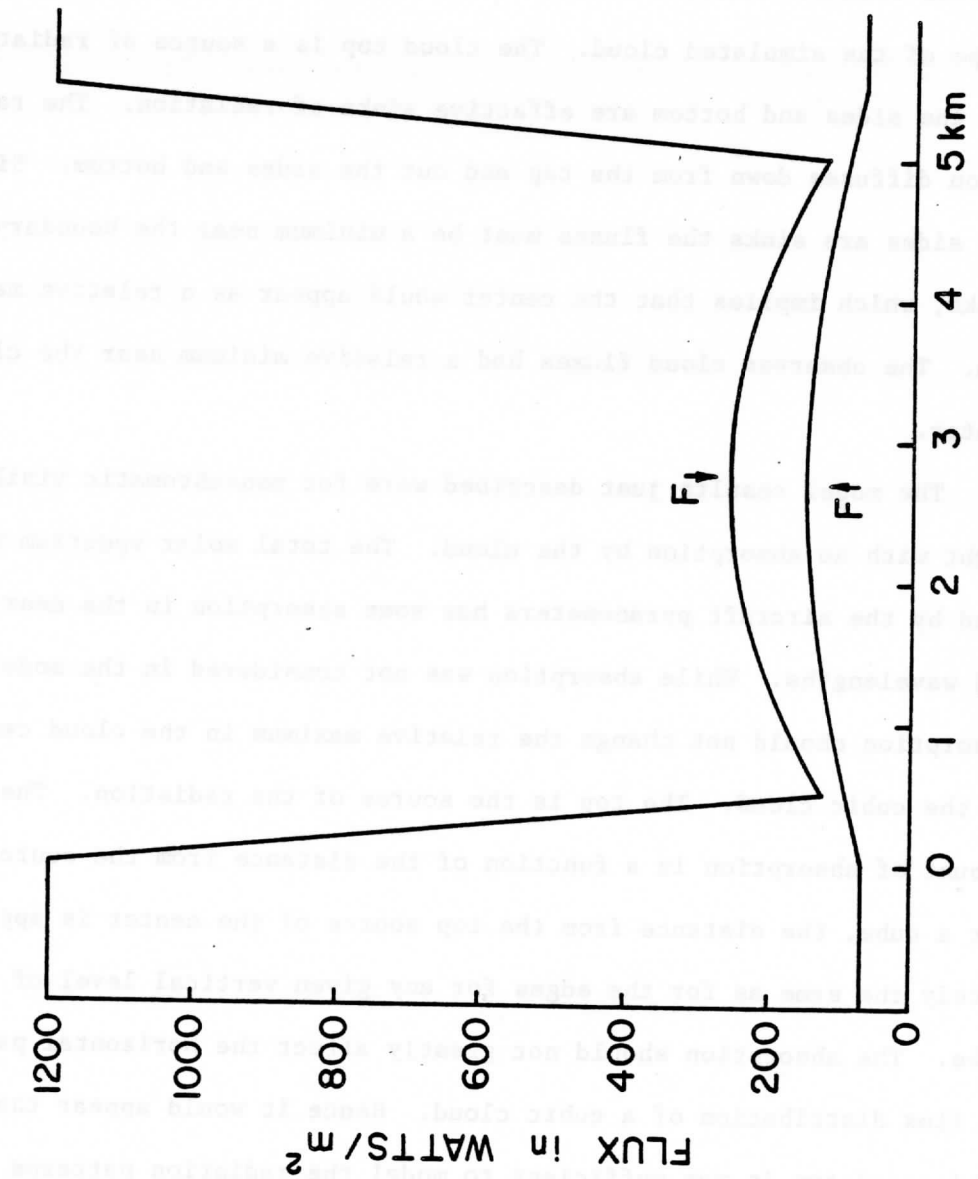

Fig. 38. The simulated interior aircraft flux measurements for a cuboidal cloud. The simulated cuboidal fluxes do not model the observed interior fluxes of fig. 36 very well.

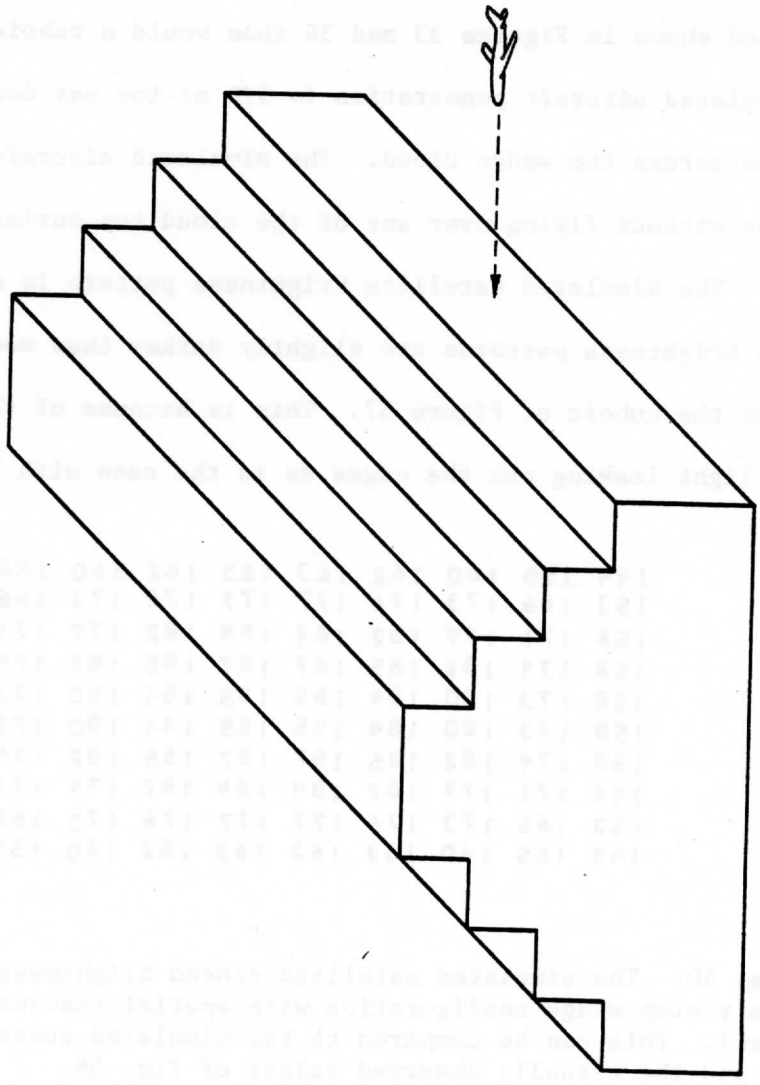

Fig. 39. Illustration of the stair step wedge geometric configuration used to attempt a more realistic simulation of the cumulus cloud visible radiative transfer problem.

correctly, a stair step wedge geometry was tried. The stair step wedge configuration used is shown in Figure 39. The bottom dimensions of the wedge are 200 x 200 and the wedge cloud has an optical thickness of 60 at the center. It was felt that this geometric configuration would more realistically approach the geometric configuration of the cloud shown in Figures 33 and 34 than would a cuboidal shape. The simulated aircraft penetration is 5/6 of the way down the cloud, and goes across the wedge cloud. The simulated aircraft enters the cloud side without flying over any of the cloud top surfaces.

The simulated satellite brightness pattern is shown in Figure 40. The brightness patterns are slightly darker than would be the case with the cuboid of Figure 37. This is because of the increased chance of light leaking out the edges as in the case with the tower geometry

144	155	160	162	163	163	162	160	155	144
153	166	173	176	177	177	176	173	166	153
156	171	179	182	184	184	182	179	171	156
158	174	182	185	187	187	185	182	174	158
158	173	180	184	185	185	184	180	173	158
158	173	180	184	185	185	184	180	173	158
158	174	182	185	187	187	185	182	174	158
156	171	179	182	184	184	182	179	171	156
153	166	173	176	177	177	176	173	166	153
144	155	160	162	163	163	162	160	155	144

Fig. 40. The simulated satellite sensed brightness values for the stair step wedge configuration with spatial resolution of .5 km/ pixel. This can be compared to the simulated cuboidal values of fig. 37 and the actually observed values of fig. 36.

of the previous section. The brightness pattern of the wedge cloud is fairly uniform across the cloud top. Figure 41 shows a satellite

brightness cross section across the observed satellite image of the candidate to cloud, the cuboid cloud top, and the wedge cloud top. The wedge cloud is dimmer than the cubic cloud, but it still has the same general pattern as the cubic cloud. Both show a resemblance to the observed brightness pattern.

The main difference between the cubic and wedge clouds is in the simulated aircraft penetration. Figure 42 shows the simulated cloud interior flux measurements for the wedge cloud. The downward flux shows a relative minimum at the cloud center, though the minimum is brighter than observed fluxes. The decrease of downward flux at the cloud edges is not as sharp in the simulated data as in the observed data. The simulated upward flux shows a sharp increase at the cloud edge with a gradual decline until a relative minimum is reached at the cloud center. The general trend of the simulated upward and downward agree quite nicely with the observed fluxes. The reason the simulated fluxes of the wedge cloud reach a minimum at the center is because light can enter the cloud at the top of each stair step. Each stair step thus acts as a source of radiation along the cloud sides. The cloud edges are sources, so there can be a relative maximum near the cloud side.

While the pattern of flux measurements on the DC-6 showed the characteristic localized minimum at the center for cumulus cloud penetrations, one cloud penetration was found which showed a maximum well within the cloud where there was abundant liquid water. Figure 43 shows the trace of the pyranometers for this cloud penetration.

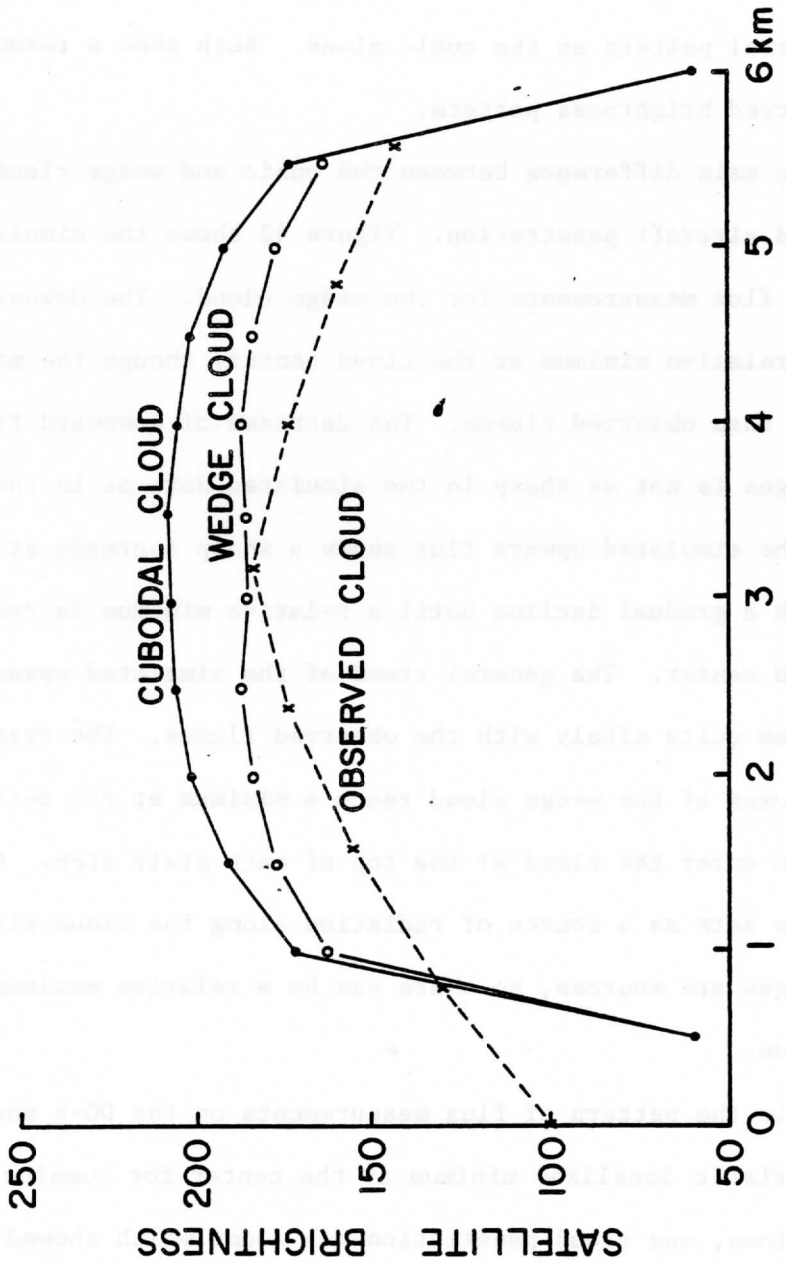

Fig. 41. Cross section of the satellite brightness variations across the observed candidate cloud, the simulated cuboidal cloud, and the simulated stair step wedge cloud.

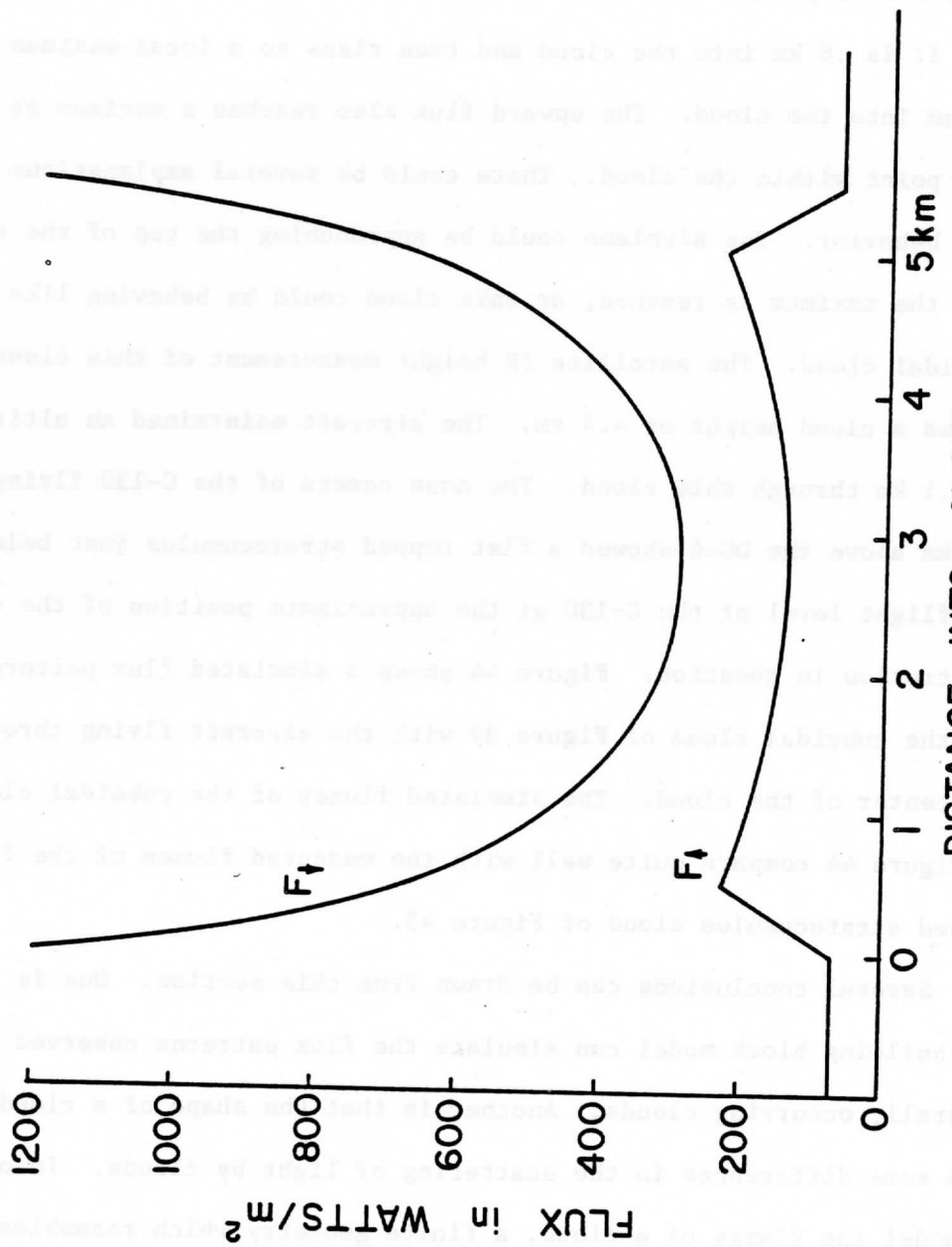

Fig. 42. The simulated interior aircraft flux measurements for the stair step wedge cloud. The wedge geometry simulated fluxes compare quite well with the measured fluxes of fig. 36.

The liquid water is plotted at the bottom of the graph. Note that the vertical scale of flux of this figure is half of the scale of the previous plots. The downward flux reaches a localized minimum when it is .6 km into the cloud and then rises to a local maximum at 3.7 km into the cloud. The upward flux also reaches a maximum at this point within the cloud. There could be several explanations for this behavior. The airplane could be approaching the top of the cloud when the maximum is reached, or this cloud could be behaving like a cuboidal cloud. The satellite IR height measurement of this cloud showed a cloud height of 4.4 km. The aircraft maintained an altitude of 1.1 km through this cloud. The nose camera of the C-130 flying at 5.5 km above the DC-6 showed a flat topped stratocumulus just below the flight level of the C-130 at the approximate position of the cloud penetration in question. Figure 44 shows a simulated flux pattern for the cuboidal cloud of Figure 39 with the aircraft flying through the center of the cloud. The simulated fluxes of the cuboidal cloud of Figure 44 compare quite well with the measured fluxes of the flat topped stratocumulus cloud of Figure 43.

Several conclusions can be drawn from this section. One is that the building block model can simulate the flux patterns observed in naturally occurring clouds. Another is that the shape of a cloud does make some differences in the scattering of light by clouds. In order to model the fluxes of a cloud, a finite geometry which resembles the the cloud in question is required. A simple cuboidal shape is not generally sufficient to model many naturally occurring clouds.

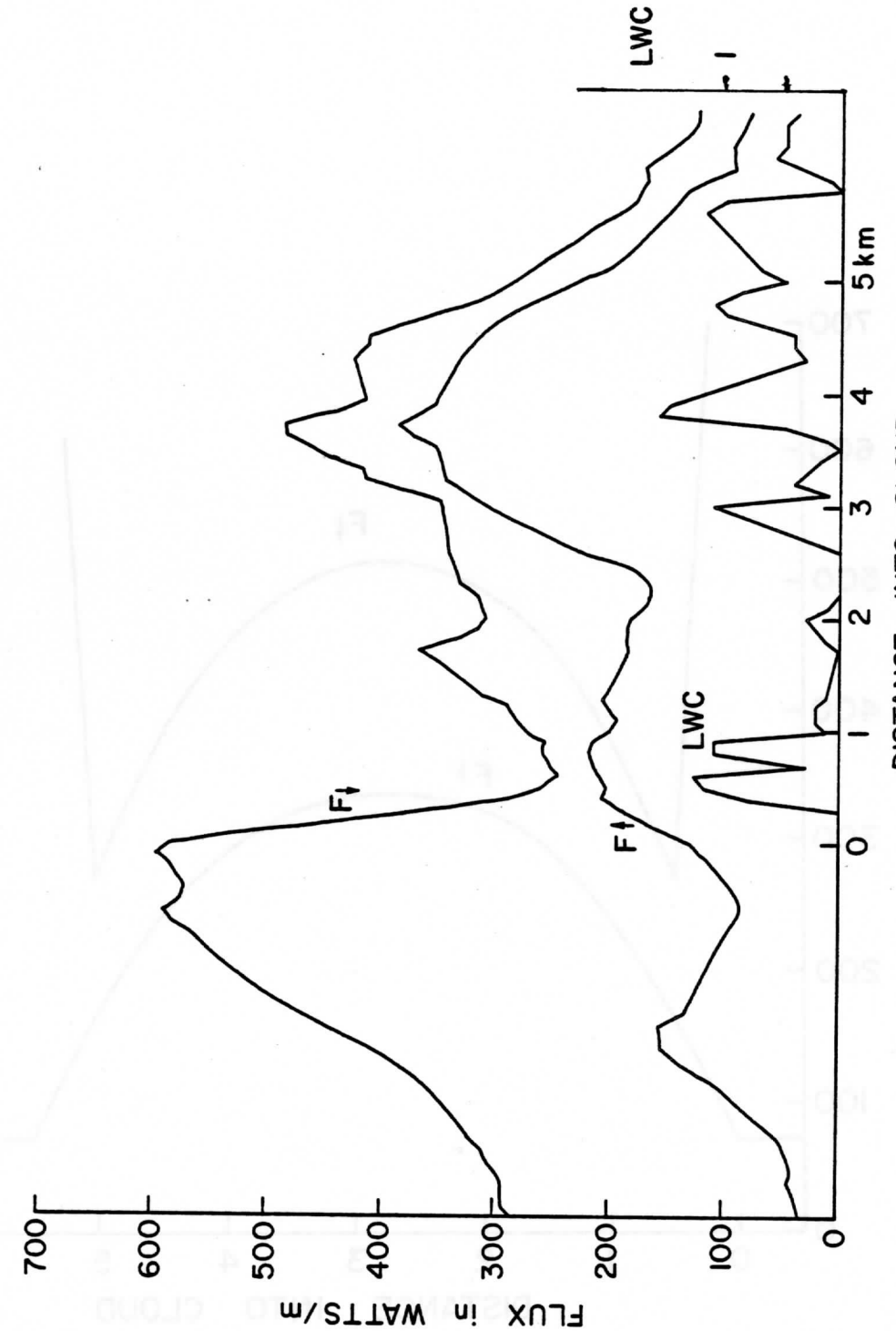

Fig. 43. Trace of the DC-6 pyranometers as it flew through a flat topped stratocumulus cloud. The up and down welling visible fluxes both reach a maximum near the center of the cloud. This is in contrast to the minimum in the center observed in cumulus cloud penetrations.

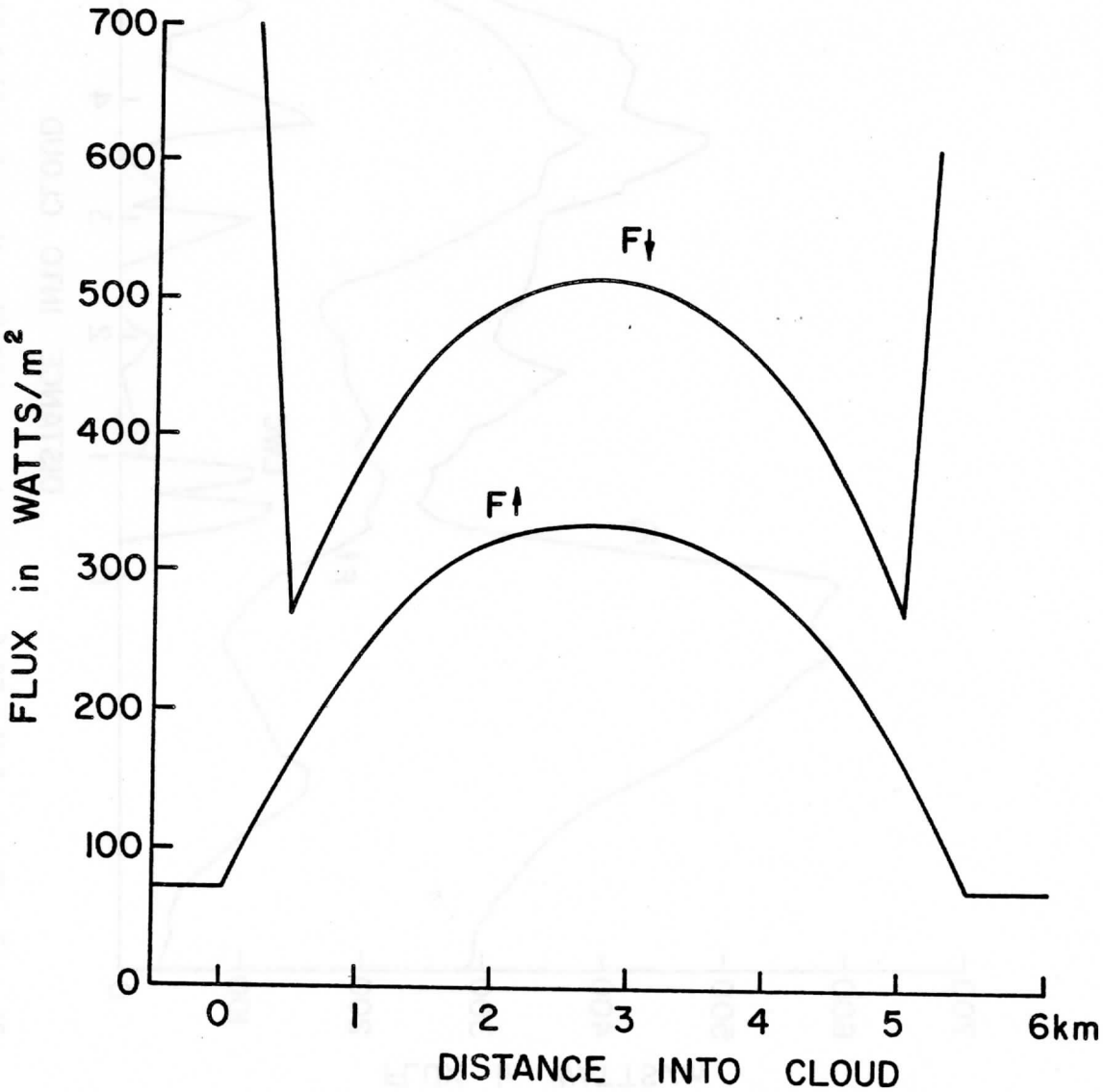

Fig. 44. Simulated flux measurements of a flat topped cuboidal cloud with the aircraft flying through the center of the cloud. The simulation can be compared to the observed measurements of fig. 43.

5. Summary and Conclusions

The theoretical treatment of the three-dimensional visible light scattering in clouds is currently of great interest in the scientific community. Two basic approaches to the finite cloud problem have been developed. The first has been the Monte-Carlo simulation approach, which has been that of Busygin et al. (1973), McKee and Cox (1974, 1976), Davies (1976, 1978b), Aida (1977), and Davis et al. (1978). The Monte-Carlo simulations can handle a large variety of cloud geometries and structures. The Monte-Carlo simulations can be quite accurate, but they are very time consuming computer runs.

The second approach has been to solve the radiative transfer, using analytical solutions, such as the work of Barkstrom and Arduini (1976), and Davies (1976, 1978a, b). These approaches are fast and generally reliable, but they are constrained to work on only a few homogeneous geometric shapes.

In this study a hybrid approach to the finite cloud problem has been developed which combines the versatility of the Monte-Carlo models to handle different cloud geometries with the speed of the analytical methods. This hybrid approach, which has been called the building block model, determines cloud flux distributions by joining small cuboids, whose radiative transfer characteristics have previously been determined with a Monte-Carlo simulation, to form larger clouds. The flux distribution across and within cloud forms which can be constructed from a "pile of building blocks" can be

handled by this approach with speed and accuracy which is generally comparable with analytic finite cloud approaches.

The cloud scattering model developed in this study is the simplest three-dimensional model which is possible, using this hybrid approach. The model was configured to allow the transfer of energy normal to the six sides of the building blocks. For a symmetric scattering case, such as an overhead sun, this reduces to three allowable directions: up, down, and sideways. The error analysis shows that this simple approach can correctly distribute the energy throughout the cloud with errors generally less than 10% except when strong forward scatter affects the distribution of energy such as near sunlit cloud edges where errors of over 30% are possible. If these forward scatter effects are to be treated correctly the model would have to be expanded to include a larger number of angular transfer functions.

The model has been used to investigate some of the finite cloud effects which can be associated with cloud brightness patterns observed by satellites. For homogeneous cube-shaped clouds with optical dimensions of 100, the model showed a flux variation across the cloud with sharp gradients near the edges and a reasonably uniform flux pattern across the top center regions of the cloud. As the sun was shifted toward the side of the cloud, the brightest part of the cloud top shifted toward the sunlit side. The model was also used to investigate the possibility of developing correction factors for applying plane parallel solutions to finite cloud situations. The model showed that the center portions of a finite cloud show the most

consistent correction factors because the center is farthest from the edge effects. However, even the center values of the cloud departed significantly from plane parallel solutions so that care must be taken in applying plane parallel solutions to any part of a cloud.

The model was used to investigate the effects of liquid water inhomogeneities within a cubic cloud of optical dimension 100. A concentration of liquid water at the cloud top (but still maintaining a flat top) will affect the scattered light by showing up as a bright spot for the overhead sun case. For large solar zenith angles the liquid water inhomogeneity had very little effect on the scattered light. When the liquid water concentration was placed lower down into the cloud, the bright spot diminished rapidly. When the liquid water concentration was an optical thickness 25 (about a kilometer) below the cloud top, the bright spot completely disappeared.

The model was also used to investigate the effects of cloud structure. For an overhead sun a cloud top turret appeared darker than the parent cloud. When the sun was near the horizon, the turrets appeared as bright spots. Cloud shapes such as approximate cylinders, truncated spheres, inverted parabaloids, and cubes all showed varying albedo relationships to solar zenith angle. The figures with the smaller cloud top dimension (even though the maximum dimensions were the same) showed lower albedos for the overhead sun. For larger solar zenith angles, the albedos of the different shapes showed a greater similarity than for the overhead sun. Attempts at trying to model aircraft flux measurements of clouds showed that simulations

using geometric shapes which closely resemble the observed shapes gave the best representation of the observed flux patterns.

The results of this study have several scientific implications. One is that the theoretical modeling of naturally occurring clouds is even more difficult than had been suspected. Not only is the fact that the cloud is finite in horizontal dimensions important, but the details of the cloud's external structure and liquid water inhomogeneities near the cloud's surface are also important in the scattering of light from clouds. Another implication of this study is that conventional interpretation of the causes of brightness variations observed on satellite images of clouds needs to be re-examined. For cases with the sun nearly overhead, bright spots on satellite images may well be caused by water concentrations near the cloud top, while darker spots are probably towers. The multiple scattering within the cloud makes it difficult to detect any details caused by the internal structure of the cloud. Hence, internal cores, rain-producing areas, etc., of clouds cannot be distinguished except through the effects of these internal structures on the top 1 km of the cloud. For sun angles near the horizon, the cloud top geometry is more important in producing brightness variations than are water inhomogeneities.

BIBLIOGRAPHY

Aida, Masaru, 1977: Reflection of Solar Radiation from an Array of Cumuli. J. of the Meteor. Society of Japan, 55, 174-181.

Anderson, Ralph K., et al., 1974: Application of Meteorological Satellite Data in Analysis and Forecasting. ESSA Technical Report NESC51. NOAA, U. S. Dept. of Commerce, Washington, D. C.

Appleby, John F., and William M. Irvine, 1973: Path-Length Distribution of Photons Diffusely Reflected from a Semi-Infinite Atmosphere. The Astrophysical Journal, 183, 337-346.

Barkstrom, B. R., and R. F. Arduini, 1976: The Effect of Finite Horizontal Size of Clouds Upon the Visible Albedo of the Earth. Proceedings of the Symposium on Radiation in the Atmosphere, Garmisch-Partenkirchen, FRG, 19-28 August 1976. H. J. Bolle, Ed. Princeton, Science Press, 630 pp.

Barrett, E. C., 1976: Satellite data in mapping rainfall for the solution of associated problems in regions of sparce conventional observations. Remote Sensing of the Terrestial Env., Wright and Sons Ltd., Clifton, Bristol, U.K.

Black, Peter, 1977: Some Aspects of Tropical Storm Structure Revealed by Handhold Camera Photographs from Space: Skylab Explores the Earth, NASA publication, pp. 417-461.

Brennan, B., and W. R. Bandeen, 1970: Anisotropic Reflectance Characteristics of Natural Earth Surfaces. Applied Optics, 9, 405-412.

Busygin, V. P., N. A. Yevstratov, and Ye. M. Feygel'son, 1973: Optical Properties of Cumulus Clouds and Radiant Fluxes from Cumulus Cloud Cover, Atmospheric and Oceanic Physics, Vol. 9, pp. 1142-1151.

Davies, Roger, 1976: The Three-Dimensional Transfer of Solar Radiation in Clouds. Ph.D. Thesis, University of Wisconsin-Madison.

Davies, Roger, 1978: The Spatial Variations in the Visible Radiances from Cloud of Finite Horizontal Extent. Preprints of the Third Conference on Atmospheric Radiation, American Meteorological Society, pp. 202-204.

Davies, R., 1978: The Effect of Finite Geometry on the Three-Dimensional Transfer of Solar Irradiance in Clouds. J. Atmos. Sci., 35, 1712-1725.

Davis, John, Stephen Cox, and Thomas McKee, 1978: Solar absorption in clouds of finite horizontal extent. Preprints to the Third Conference on Atmospheric Radiation at Davis, California. American Meteorological Society. pp. 195-197.

Deirmendjian, D., 1969: Electromagnetic Scattering on Spherical Polydispersions. American Elsevier Publishing Company, Inc., New York, 290 pp.

Follansbee, W. A., 1976: Estimation of Daily Precipitation Over China and the USSR Using Satellite Imagery. NOAA Tech Memo. NESS 81, Washington, D. C. 30 pp.

Griffith, C. G., and W. L. Woodley, 1973: On the Variation with Height of the Top Brightness of Precipitating Convective Clouds, J. Appl. Meteor., 12, 1086-1089.

Griffith, C. G., W. L. Woodley, P. G. Grube, D. W. Martin, J. Stout, and D. N. Sikdar, 1978: Rain Estimation from Geosynchronous Satellite Imagery, Visible and Infrared Studies. Mon. Wea. Rev., 106, 1153-1171.

Greenspan, Donald, 1974: Discrete Numerical Methods in Physics and Engineering. Academic Press, Inc., N. Y., 312 pp.

Hansen, J. E., 1971a: Multiple Scattering of Polarized Light in Planetary Atmospheres, Part I. The Doubling Method. J. Atmos. Sci., 28, 120-125.

Hansen, J. E., 1971b: Multiple Scattering of Polarized Light in Planetary Atmospheres, Part II. Sunlight Reflected by Terrestrial Water Clouds. Journal of the Atmospheric Sciences, 28, 1400-1426.

Holle, R. L., 1978: Photogrammetry of Thunderstorms. To appear in Thunderstorms: A Social, Scientific, and Technological Documentary (E. Kessler, ed.), Norman, University of Oklahoma Press.

Hottel, H. C., and A. F. Sarofim 1967: Radiative Transfer, McGraw Hill, Inc.

Kaveney, W. J., F. G. Feddes, and K. N. Liou 1977: Statistical Inference of Cloud Thickness from NOAA 4 Scanning Radiometer Data. Mon. Wea. Rev., 105, 99-109.

McKee, Thomas B., and Stephen K. Cox, 1974: Scattering of Visible Radiation by Finite Clouds. Journal of the Atmospheric Sciences, 31, 1885-1892.

McKee, T. B., and J. T. Klehr, 1978: Effects of Cloud Shape on Scattered Solar Radiation. Mon. Wea. Rev., 106, 399-404.

Mosher, F. R., 1974: SMS Cloud Heights. Final Report on NASA Contract NAS5-23296.

Payne, Richard E., 1972: Albedo of the Sea Surface. J. Atmos. Sci., 29, 959-970.

Reynolds, David, and Thomas H. Vonder Haar, 1973: A Comparison of Radar-Determined Cloud Height and Reflected Solar Radiance Measured from the Geosynchronous Satellite ATS-3, J. Appl. Meteor., 12, 1082-1085.

Reynolds, David, T. B. McKee, and K. S. Danielson, 1978: Effects of Cloud Size and Cloud Particles on Satellite-Observed Reflected Brightness. J. of Atmos. Sci., 35, 160-164.

Sikdar, D. N., 1972: ATS-3 Observed Cloud Brightness Field Related to a Meso-Synoptic Scale Rainfall Pattern, Tellus, 24, 400-413.

Smith, Eric A., and David Loranger, 1977: Radiometer Calibration of Polar and Geosynchronous Satellite Shortwave Detectors for Albedo Measurements. Preliminary Draft. Atmos. Sci. Dept. Colorado State University.

Twomey, S., H. Jacobowitz, and H. B. Howell, 1967: Light Scattering by Cloud Layers. J. Atmos. Sci., 24, 70-79.

Van Blerkom, D. J., 1971: Diffuse reflection from clouds with horizontal inhomogeneities. Astrophy. J., 166, 235-242.

Weinman, J. A. and P. N. Swarztrauber, 1968: Albedo of a striated medium of isotropically scattering particles. J. Atmos. Sci., 25, 497-501.

Wendling, Peter, 1977: Albedo and reflected radiance of horizontally inhomogeneous clouds. J. Atmos. Sci., 34, 642-650.

TWO DIMENSIONAL FOURIER ANALYSIS OF SATELLITE IMAGES

Sanjay S. Limaye and Donald P. Wylie
Space Science and Engineering Ctr.
University of Wisconsin-Madison
1225 W. Dayton Street
Madison, Wisconsin 53706

1. INTRODUCTION

Since the days of the Applications Technology Satellite I (ATS-I) the number of satellite images of earth from geosynchronous spacecrafts is growing rapidly. The operational satellites GOES I and GOES II are transmitting high resolution visible and IR images on a routine basis. The enormous data collected every day has prompted efforts in gleaning useful information from satellite images more efficiently. Bulk of the effort so far has been concentrated in the area of determining cloud motions and rainfall from deep convective systems. Not much progress has been made in several key problem areas such as cloud typing, cloud cover statistics, image scene interpretaion among others. Some exploratory studies have been done in the past - for example Leese and Epstein (1963) studied the application of two-dimensional spectral analysis to quantification of satellite photographs. Booth (1973) looked the application of Bayesian classifiers in cloud typing. However, the use of such techniques has not been widespread and further research is warranted. This paper describes an attempt to use two-dimensional Discrete Fourier Transform (DFT) to GOES images as a means of specifying the textural and spatial information in the images quantitatively. The use of fast fourier transform makes the procedure comparatively inexpensive.

The two-dimensional Fourier Transform is used to obtain the two-dimentional power spectrum which inherently contains the textural and spatial

information about the clouds that we are seeking.

2. TWO-DIMENSIONAL DISCRETE FOURIER TRANSFORM

The discrete two-dimensional Fourier transform F(u,v) of a two-dimensional array f(x,y) is defined as (Andrews, 1970):

$$F(u,v) = \frac{1}{N^2} \sum_{x=0}^{N-1} \sum_{y=0}^{N-1} f(x,y) \exp\left\{-\frac{2\pi i}{N}(xu + yv)\right\}$$

u and v are called the spatial frequencies and F(u,v) is called the frequency spectrum of f(x,y). The power spectrum of f(x,y) is then $|F(u,v)|^2$. In the case of satellite images the array f(x,y) is real, containing a set of numbers proportional to radiances and hence F(u,v) shows conjugate symmetry. The highest frequency resolved is equal to N/2 cycles, (Nyquist frequency).

The two-dimensional power spectrum thus represents the spatial sizes of the features contained in the transformed area at all frequencies from 1 cycle to N/2 cycles. The strict interpretation of this power spectrum implies periodic patterns in both dimensions beyond the transformed area. Since this is seldom the case, one needs to pay attention to the effect of the finite length of the sample and the finite resolution of the data on the calculated power spectrum. The major effect of the finite resolution is to introduce spurious power at all wave numbers. This aliasing is highest at the highest wave numbers and is low at small wave numbers. The effect of the finite length of the sample introduces another source of error in the spectral power estimates since the larger spatial scales are then not adequately represented in the data. This effect is dominant at low wave numbers although some contamination occurs at high wave numbers also.

The effect of the finite sample can be minimized by (i) removing the mean of the data from the sample, and (ii) smoothing of the spectral estimates by averaging, e.g. with a Hanning filter (Blackman and Tukey, 1958) which is discussed in section 3.1.

The application of the Fourier fast transform to the two-dimensional case reduces the computing time enormously. These techniques have been documented elsewhere quite extensively and will not be discussed here (Rosenfeld and Kak, 1976; Andrews, 1970; Cooley and Tukey, 1963).

3. APPLICATION TO SATELLITE CLOUD PHOTOGRAPHS

Several visible SMS-I image sectors taken during the GARP Atlantic Experiment (GATE) of the Global Atmospheric Research Program (GARP) in the summer of 1974 over the GATE area were selected. The visible images from SMS are formed of 8-bit samples and were retrieved from the Vertical Slant Track Mass Storage Unit (VSTMUS) tapes archived at the Space Science and Engineering Center, University of Wisconsin-Madison. Several problems during the data readout caused some quasi-random shot noise and dropped lines to be present in the images. These images were therefore subjected to a shot noise filter that almost eliminated the noise. These filtered images were then Fourier analyzed and an example is shown in Figure 1. A latitude longitude grid is superposed on the image to indicate the non-uniform geometry.

The strict interpretation of u and v as spatial frequencies in units such as cycles/km require that the original image have uniform geometry. No satellite image meets this requirement, of course, and the images need to be digitally remapped - a much more expensive operation than the transform itself. Fortunately however, the GATE area is quite close to the equator and its east-west extent is only about 6° longitude. For these reasons, it was decided that the image would not be remapped and used as it was.

3.1 Method of Calculation

The calculations were performed on the UNIVAC 1110 computer of the Madison Academic Computing Center (MACC) and the available core allowed an image segment of only 256 x 256 pixels to be transformed at a time. The Fourier transform F(u,v) contains $2N^2$ components, N^2 real and N^2 imaginery. Both the real and complex parts of the transforms were scaled appropriately to an 8-bit integer number and the real and imaginary parts were recorded on computer tape as a digital image.

The raw power spectrum of the image in Figure 1 obtained by squaring and adding the real and imaginery parts of the Fourier Transform is shown in Figure 2. In this power spectrum image the intensity is proportional to the logarithm of the power. It should be mentioned here that the brightness number in the visible SMS images is proportional to the square-root of the sensed radiance. Before applying the Fourier Transform, the image had been converted to a linear radiance scale removing the square-root digitized scale imposed by the sensor. The lowest frequency 0 cyc/pixel is in the center of Figure 2 and the Nyquist frequency can be found at all 4 corners. All four quadrants are symmetrical copies of the same 2-dimensional spectra.

The approach used here is somewhat different from that used by Leese and Epstein (1963) in their study. Until recently, the recommended procedure to obtain the power spectrum has been to compute the auto-covariance function for a given lag and then the power spectrum is then determined by the Fourier Transform of the auto-covariance function (Jenkins and Watt, 1968, Blackman and Tukey, 1958, Otnes and Enochson, 1972). This was done because of the enormous amount of computer time required in the Fourier Transform of a large array. For example, Leese and Epstein obtained the spectral estimates

of a TIROS image in segments of 96 x 96 with a maximum lag of 24; while they did not give the computer time required for this case, they estimated that for an array sixe of 60 x 60 and lag size = 15, the computer time required to obtain the complete spectrum on a IBM 7090 computer would be 9 minutes. In contrast, in the present study the entire power spectrum calculation and creating a digital image of the output for an input image 256 x 256 large using the fast Fourier Transform method took only ~54 seconds on UNIVAC 1110 computer. It is more practical and in no way inferior to obtain the power spectrum estimates directly Fourier Transform (Enochson and Otnes, 1972). Both methods ultimately suffer from the same problems of finite data size and it is necessary to smooth the spectrum.

The spectral images show clustering of power in isolated frequency ranges (Fig. 2). This is characteristic of the trade-wind cumulus cloud patterns which have many groups of clouds. Because these groups do not have one preferred size, no one strong peak in the spectrum was found. The largest spectral estimates (highest power) was found at the ends of the spectrum, the lowest frequencies (center of the image) and the highest frequencies (the corners). This is somewhat different from most other geophysical data which have the highest power at the lowest frequencies and a decrease in power toward the high frequencies--the "red noise" spectra. The spectral images indicate that there are many sharp changes in brightness indicated by the high power at the high frequencies. This is probably from the edges of the clouds where high gradients in brightness occurred. The power at the low end is the result of having several large clouds in the images and large areas without clouds.

3.2 Smoothing of Spectra

The use of a Hann Filter is quite common in spectral analysis. Leese

3.1 Method of Calculation

The calculations were performed on the UNIVAC 1110 computer of the Madison Academic Computing Center (MACC) and the available core allowed an image segment of only 256 x 256 pixels to be transformed at a time. The Fourier transform F(u,v) contains $2N^2$ components, N^2 real and N^2 imaginery. Both the real and complex parts of the transforms were scaled appropriately to an 8-bit integer number and the real and imaginary parts were recorded on computer tape as a digital image.

The raw power spectrum of the image in Figure 1 obtained by squaring and adding the real and imaginery parts of the Fourier Transform is shown in Figure 2. In this power spectrum image the intensity is proportional to the logarithm of the power. It should be mentioned here that the brightness number in the visible SMS images is proportional to the square-root of the sensed radiance. Before applying the Fourier Transform, the image had been converted to a linear radiance scale removing the square-root digitized scale imposed by the sensor. The lowest frequency 0 cyc/pixel is in the center of Figure 2 and the Nyquist frequency can be found at all 4 corners. All four quadrants are symmetrical copies of the same 2-dimensional spectra.

The approach used here is somewhat different from that used by Leese and Epstein (1963) in their study. Until recently, the recommended procedure to obtain the power spectrum has been to compute the auto-covariance function for a given lag and then the power spectrum is then determined by the Fourier Transform of the auto-covariance function (Jenkins and Watt, 1968, Blackman and Tukey, 1958, Otnes and Enochson, 1972). This was done because of the enormous amount of computer time required in the Fourier Transform of a large array. For example, Leese and Epstein obtained the spectral estimates

of a TIROS image in segments of 96 x 96 with a maximum lag of 24; while they did not give the computer time required for this case, they estimated that for an array sixe of 60 x 60 and lag size = 15, the computer time required to obtain the complete spectrum on a IBM 7090 computer would be 9 minutes. In contrast, in the present study the entire power spectrum calculation and creating a digital image of the output for an input image 256 x 256 large using the fast Fourier Transform method took only ~54 seconds on UNIVAC 1110 computer. It is more practical and in no way inferior to obtain the power spectrum estimates directly Fourier Transform (Enochson and Otnes, 1972). Both methods ultimately suffer from the same problems of finite data size and it is necessary to smooth the spectrum.

The spectral images show clustering of power in isolated frequency ranges (Fig. 2). This is characteristic of the trade-wind cumulus cloud patterns which have many groups of clouds. Because these groups do not have one preferred size, no one strong peak in the spectrum was found. The largest spectral estimates (highest power) was found at the ends of the spectrum, the lowest frequencies (center of the image) and the highest frequencies (the corners). This is somewhat different from most other geophysical data which have the highest power at the lowest frequencies and a decrease in power toward the high frequencies--the "red noise" spectra. The spectral images indicate that there are many sharp changes in brightness indicated by the high power at the high frequencies. This is probably from the edges of the clouds where high gradients in brightness occurred. The power at the low end is the result of having several large clouds in the images and large areas without clouds.

3.2 Smoothing of Spectra

The use of a Hann Filter is quite common in spectral analysis. Leese

and Epstein used a two-dimensional 3 x 3 Hann Filter to smooth the spectral estimates. The same filter was used in the present study to correct for leakage between spectral estimates and the effects of finite data sample sizes as previously mentioned.

3.3 Statistical significance

The question of statistical significance of the computed spectral power has been discussed by many authors (see for example Jenkins and Watts, 1968) and it is beyond the scope of this study. There is enough statistical variability in the computed spectrum that for more representative spectral power estimates some averaging either in frequency space or of different spectra could be performed. However, the drawback of smoothing in frequency space is that the frequency resolution would be degraded considerably. Computer limitations generally restrict one to a resolution of about 128 Hz/256 pixels and smoothing of two neighboring samples would reduce it to only 64 Hz/256 pixels. Given that the resolution at sub-point of the SMS/GOES visible images is about 1 km, this amounts to the cloud size determination resolution of about 4 km (4 pixels) on a side.

For climatological purposes the frequency resolution of the power spectrum could be improved by either averging several spectra for the same loca area made from pictures taken at different times, or by taking several sample boxes around the same general area and averaging the spectra from each box. The real limitation of this technique, however, is that only a finite amount of data can be analyzed. Degrading the resolution of the satellite images would allow longer wavelengths of clouds to be represented in the spect at the expense of resolving small scale features.

4. SIMPLE SPECTRAL METHOD

The problem of cloud typing or classification is difficult to do by automated methods. With spectra we can describe the brightness variations of features having the same dimensions. This generally implies somewhat different types of clouds - cirrus and cumulus being two extreme examples. The complete cloud typing problem is more complicated and requires more information than can be obtained from spectra alone. The power spectrum itself can provide some texture information and cloud size information. We seek a simple approach that could be used operationally as discussed below.

Ideally one would wish to perform a Fourier Transform in 3 dimensions - the line and element direction and the level of brightness of the picture element. Most satellite cloud images are 8 bit-sampled images, i.e. 256 gray levels. Thus an image segment 256 lines x 256 elements has $(256)^3$ or 2^{24} bits of data. It is beyond the capabilities of most computers to manipulate this amount of data in core, and peripheral storage areas need to be used requiring a more complicated and input-output bound code. Of course, one need not look at all 256 gray levels since most cloud image analysis at present restricted to 3 or 9 levels (with accompanying uncertainties). A simpler solution then is to preprocess the image of interest to retain only the clouds of interest. This is done by scanning the input image and retaining only those brightness values that fall within a prespecified range. The upper limit for the range is chosen to be 255 (the maximum brightness attainable with 8 bits) so as to prevent occurrence of "black holes" within bright clouds and the lower range is selected at wish according to the type of dominant clouds or degree of convective activity, etc. The output image is thus a binary image with only two brightness levels 0 and 1 delineating cloudy and clear areas.

The power spectrum is then evaluated for the binary image as before. An example of binary images are shown in Figure 3 while the corresponding power spectrum (smoothed) is shown in Figure 4. Only one quadrant of the transform was smoothed with a 3 x 3 Hann Filter. This sequence reflects the evolution of clouds over a three hour period and the changes in the cloud sizes and distribution are clearly reflected in the spectra.

The spectral estimates appear to be more organized. Lines of spectral peaks are weakly evident which indicates some elongation of the cloud features in the original images. A cloud line or elongated cloud would produce an elongated spectral feature with a perpendicular orientation on the spectral image. Some evidence of this type of situation is apparent in Figure 3. For example on the lower left side of the filtered quadrant spectral lines orientated from southwest to northeast are present. Being on the bottom of the quadrant, they are from very low frequencies in the north-south direction, while from mid-range frequencies in the east-west direction. The cloud image appears to have features elongated from north to south with a slight tilt to northeast-southwest which appear to be the probable causes of the spectra produces. Incidently, this orientation, southwest to northeast, roughtly corresponds to the low-level wind direction of the area.

5. CONCLUSIONS

This work has shown that the Fourier Analysis of satellite images through FastFourier Transforms is a useful technique in cloud census work over limited areas. The technique may allow a determination of the basic cloud statistics: cloud size distribution and cloud population. It may be possible to specify the fractional cloud cover due to clouds of certain dimensions and hopefully different types.

Several problems need to be tackled yet. The first one remains the ability

to transform large amounts of data. In the present study the image size was restricted to 256 x 256. It is certainly more desirable to obtain spectral estimates over larger areas. At 1 km. resolution this corresponds to an area roughly 2.5° on each side. Larger spatial scales could be analyzed by degrading the spatial resolution of the data but only at the cost of losing information at the higher frequencies. The restrictions of orthagonality imply somewhat limited applications of this technique in cloud census studies.

The second problem is to establish the statistical reliability of computed spectral power. Further work is necessary to evaluate the extent to which smoothing of spectral estimates is necessary in the frequency domain, and by averaging different samples.

Acknowlegements

This work was performed under NASA Contract NAS5-23462. We thank Dr. A. N. Madiwale and Dr. F. Mosher for their many discussions on this subject.

REFERENCES

Andrews, H.D., 1970: Computer Techniques in Image Processing, Academic Press, New York, 187 pp.

Blackman, R.B., and J.W. Tukey, 1958: The measurement of power spectra from the point of view of Communications Engineering. Dover Publications Inc. New York. 180 pp.

Booth, A.R., 1973: Objective Cloud Type Classification using visual and infrared Satellite Data. Technical note BN768, University of Maryland, College Park, Md.

Cooley, J.W. and J.W. Tukey, 1965: An algorithm for the Machine Calculation of Complex Fourier Series. Math. Comput. (19). 297 pp.

Jenkins, G.M. and D.G. Watts, 1968: Spectral Analysis and its applications. Holden-Day, San Francisco.

Leese, J.A. and E.S. Epstein, 1963: Application of two dimensional spectral analysis to the quantification of satellite cloud photographs. J. App. Meteor. (2), 629-644.

Otnes, R.K., and L. Enochson, 1972: Digital Time Series Analysis. John Wiley & Sons. New York. 467 pp.

Rosenfeld, A. and A.C. Kak, 1976: Digital Picture Processing, Academic Press, New York, 457 pp.

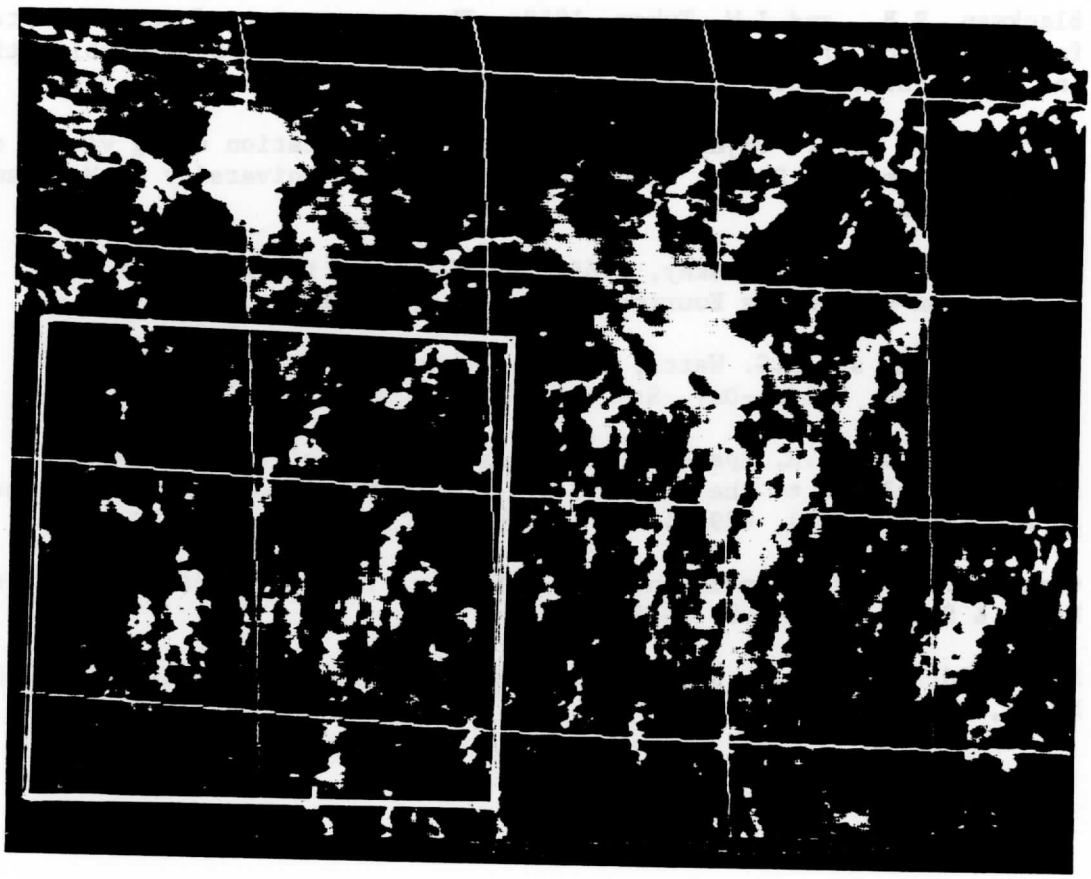

Figure 1: The GOES image of the GATE area taken at 1300 GMT, 18 Sept. 1974. The spectra were calculated from the area inside of the box.

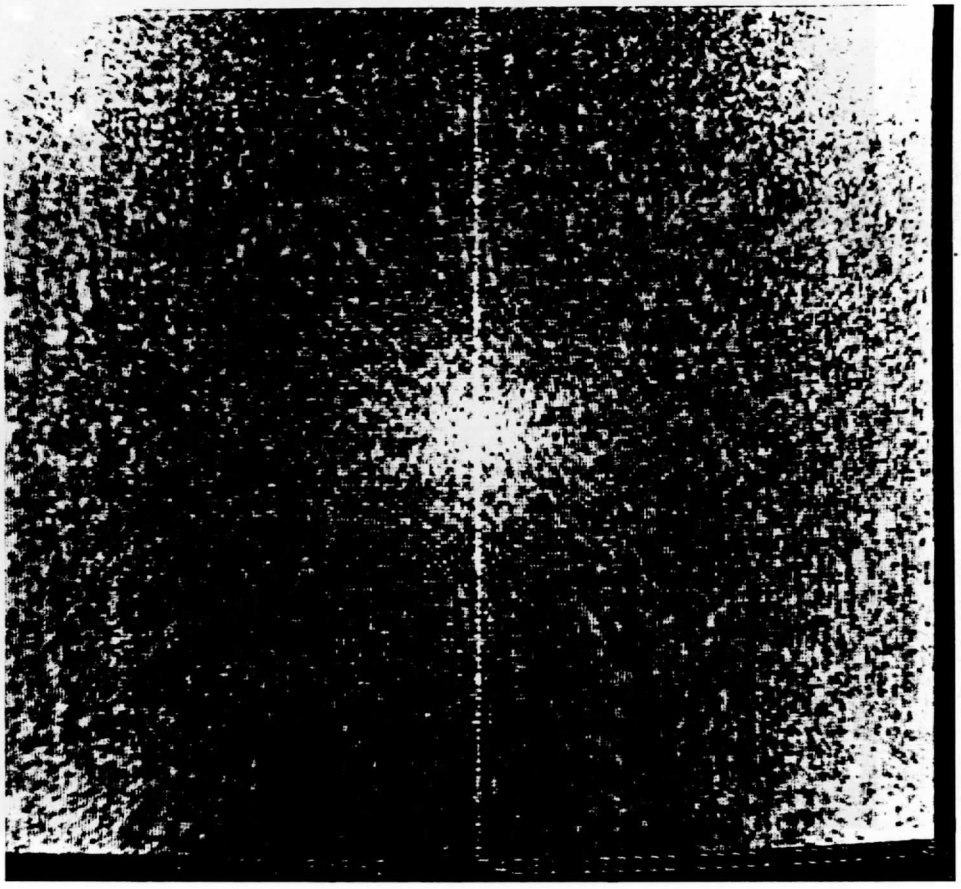

Figure 2: The spectral image from Figure 1. Frequency of 0 cycles/256 pixels is in the center of the image with 128 cyc/256 px at each of the 4 corners. Each quadrant is symetrical around the center. The same spectral estimates are repeated in each of the 4 qudrants.

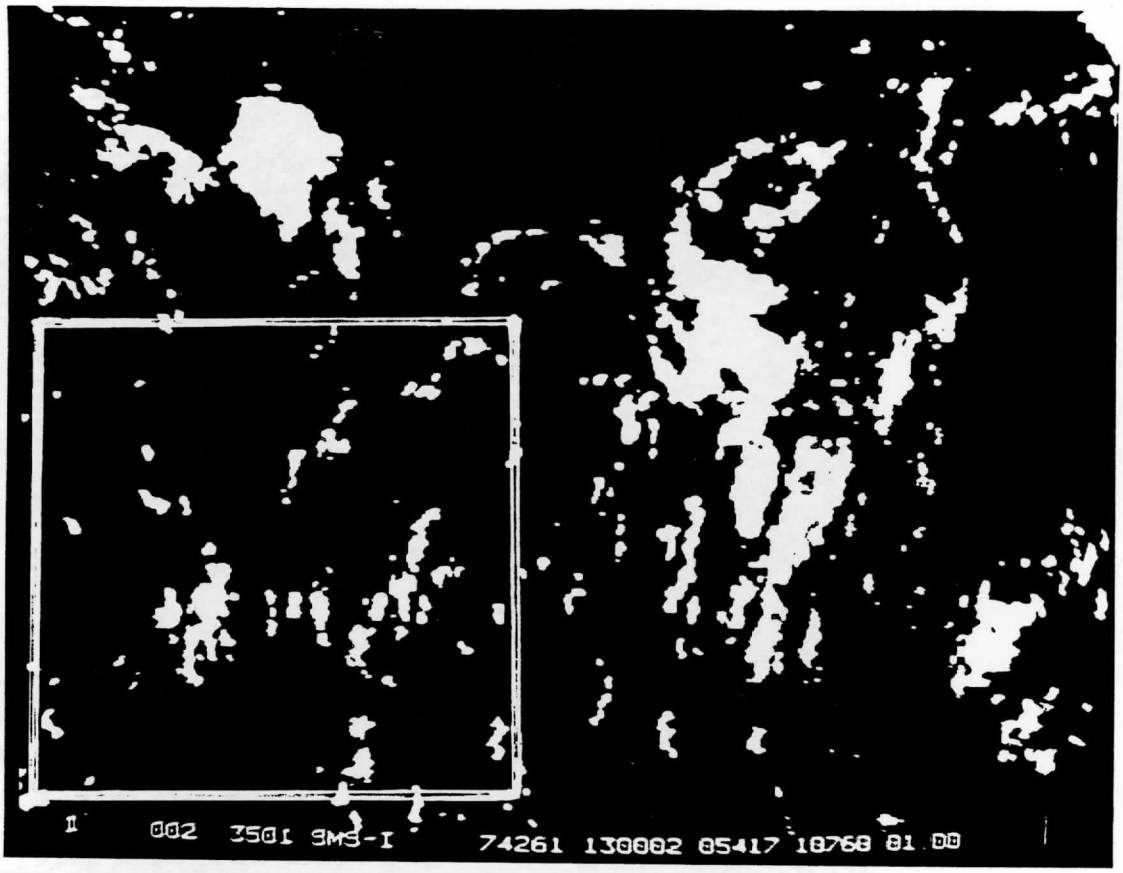

Figure 3: GOES image of the GATE area at 1300 GMT, 18 Sept. 1974 enhanced to a binary black and white scale (only two levels of brightness).

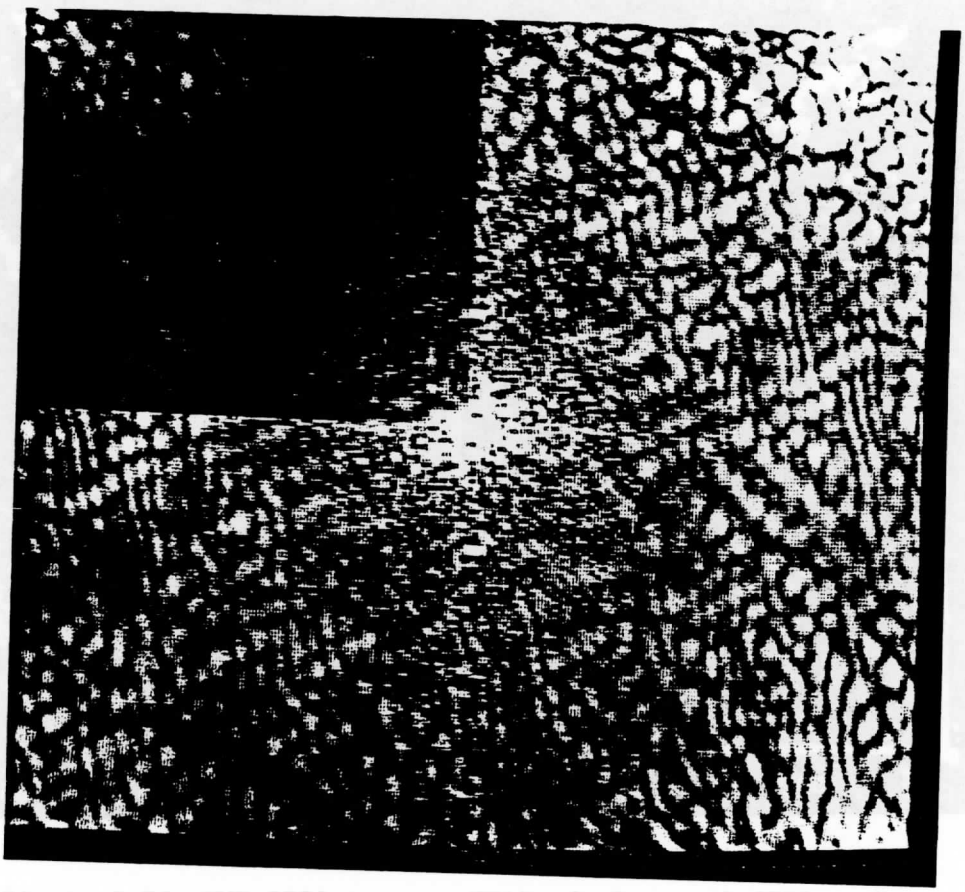

Figure 4: The computed spectral image of the binary satellite image shown in Figure 3. The darker upper left quadrant of the spectral image has been "Hanning Filtered" as described in section 3.2.

Estimating Incoming Solar Radiation from Satellite-Based Observations Using Two-Dimensional Histograms

Vincent D. Condella, Jr.

Space Science and Engineering Center
University of Wisconsin-Madison
1225 West Dayton Street
Madison, Wisconsin 53706

November 1981

Abstract

Visible and infrared digital data from a geostationary satellite are compiled in a 3 x 3 two-dimensional histograms and compared to incoming solar radiation at the earth's surface. Twenty-four histograms from 4 GATE ships were used to derive an empirical formula equating the percentage of points in each histogram box to the percentage of incoming radiation reaching a ship's sensor. An independent set of 24 histograms from the GATE area was used to test the empirical relationship and over two-thirds of the predicted values were within 18% of observed measurements.

I. INTRODUCTION

Since the early days of meteorological history, the daily observations and study of clouds has been a key task for atmospheric scientists. Clouds are often thought of as "the shutters of earth", reflecting incoming shortwave radiation from the sun while emitting longwave radiation to space. Due to this relationship, clouds play an important role in the radiation budget of the troposphere.

One of the main tasks of any synoptic weather station is observing the amounts and types of clouds in the sky for a given time. Conventional observations made from ground-based sites include systematic errors that are due to the location of the station, method of observation, and the experience of the observer (Malberg, 1973). If the total cloud cover (TCC) is defined as the fraction of the surface region directly above which there is a cloud (Hoyt, 1977), then ground-based observations tend to overestimate TCC due to projection problems (Malberg, 1973); i.e. the observer views the sides of clouds instead of recording the fraction of the region above which clouds are located. The classic cloud climatology of Telegadas and London (1954), based on observations from the earth's surface, contains information on average cloud types and their heights as a function of latitude. Some vertical resolution is lost when several cloud layers are present, and visual estimates of medium and high level cloud amounts become conservative. Holle et al. (1977) encountered similar problems when estimating cloudiness from whole-sky pictures taken aboard ships during GATE (Global Atmospheric Research Project Atlantic Tropical Experiment).

The advent of the meteorological satellite in the early 1960's gave scientists a view of clouds from above, and many climatologies of total cloud cover have been done based on analysis of fractional cloud cover within grids on visual images. Clapp (1964) compiled TIROS nephanalysis data to obtain seasonal cloud cover maps; and Malberg (1973) determined total cloud cover over Europe using daytime visible satellite photographs. In the latter case, "the daily degree of cloud cover was estimated from satellite pictures by experienced assistants." This could be interpreted to mean that a cloud was defined as a bright area not classified as snow or ice cover.

Hoyt (1977) found satellite-derived estimates of TCC to be 13 - 16% lower than ground-based observations. Using percent possible sunshine values from sunshine recorders, he discovered sunshine-derived estimates to be similar to satellite estimates. Hoyt points out that nearly all climate modelling and radiation budget work use ground-based estimates of TCC, even though sunshine or satellite-derived estimates offer a "truer" cloud cover.

Since radiation is one of the major forcing functions of the atmosphere's general circulation, and because cloudiness is the most variable factor influencing radiation, accurate and complete cloud cover data is essential to modelling efforts. Individual climate models require different types of cloud information. The models of Budyko (1969), Sellers (1973), and Bryson and Dittberner (1976) maintain a mean effective fractional cloud cover, assuming that global variations of cloud cover over the past century are negligible (Suomi et al., 1977). In a

more complex model, such as the Geophysical Fluid Dynamics Laboratory (GFDL) general circulation model, the annual mean observed cloud distributions are utilized. These distributions vary with latitude and height, but not with longitude or time (Manabe et al., 1974; Suomi et al., 1977).

Schneider (1972) has studied the sensitivity of global climate to variations in cloudiness. He has found that an increase in fractional cloud cover from 50% to 58% could decrease the surface temperature by 2 K. On the other hand, an increase in the effective cloud height from the present value of 5.5 km to 6.1 km may increase the surface temperature by 2 K. It appears evident that detailed cloud measurements are required for cloud parameterization inputs to climate and radiation models.

In order to gain better quantitative estimates of the energy budget of the earth's atmosphere, the effect of clouds on incoming solar radiation needs to be parameterized. Kasten (1977) compared ground-based observations of cloud cover and surface pyrradiometer measurements in order to study the dependence of radiation fluxes on cloud amount. However, the amount of sky covered by clouds does not provide enough information about the effects of cloudiness on incoming solar radiation. The transmission of solar radiation through clouds is highly dependent upon a cloud's size, shape, and microphysical structure (Reynolds et al., 1978; McKee & Klehr, 1978; Mosher, 1979). For example, a surface station reporting 100% overcast may still be receiving 10% of the total possible solar radiation that it would record under clear-sky conditions. If the

overcast consists of high, thin cirriform clouds, a considerably greater percentage of total solar radiation would be received.

Cloud thickness can be just as important as areal coverage in the study of the effects of clouds on incoming solar radiation. The relative brightness of a cloud in a visible (VIS) satellite image is a measure of a cloud's thickness. The brightness-thickness relationship is not a linear one since intensity increases only slightly for large optical thickness values (see Figure 1). Data from the infrared (IR) sensors aboard satellites contain information about cloud top temperatures and other radiative properties. Together, the two channels delineate the characteristics of cloud cover over a region. For example, low VIS and high IR brightness values are usually representative of thin cirrus clouds and minimal attenuation of incoming solar radiation. Maximum attenuation would be expected from thick, towering cumulonimbus clouds signified by bright regions in both VIS and IR satellite images.

In this study, relationships between VIS and IR brightness values were investigated. Bispectral values for limited fields of view were compiled in the form of two-dimensional histograms and compared to surface radiation measurements. In an empirical study, the histograms were used to predict the amount of incoming solar radiation reaching the earth's surface. In this way, it may be possible to see how cloud thickness and height combine to alter incoming solar radiation.

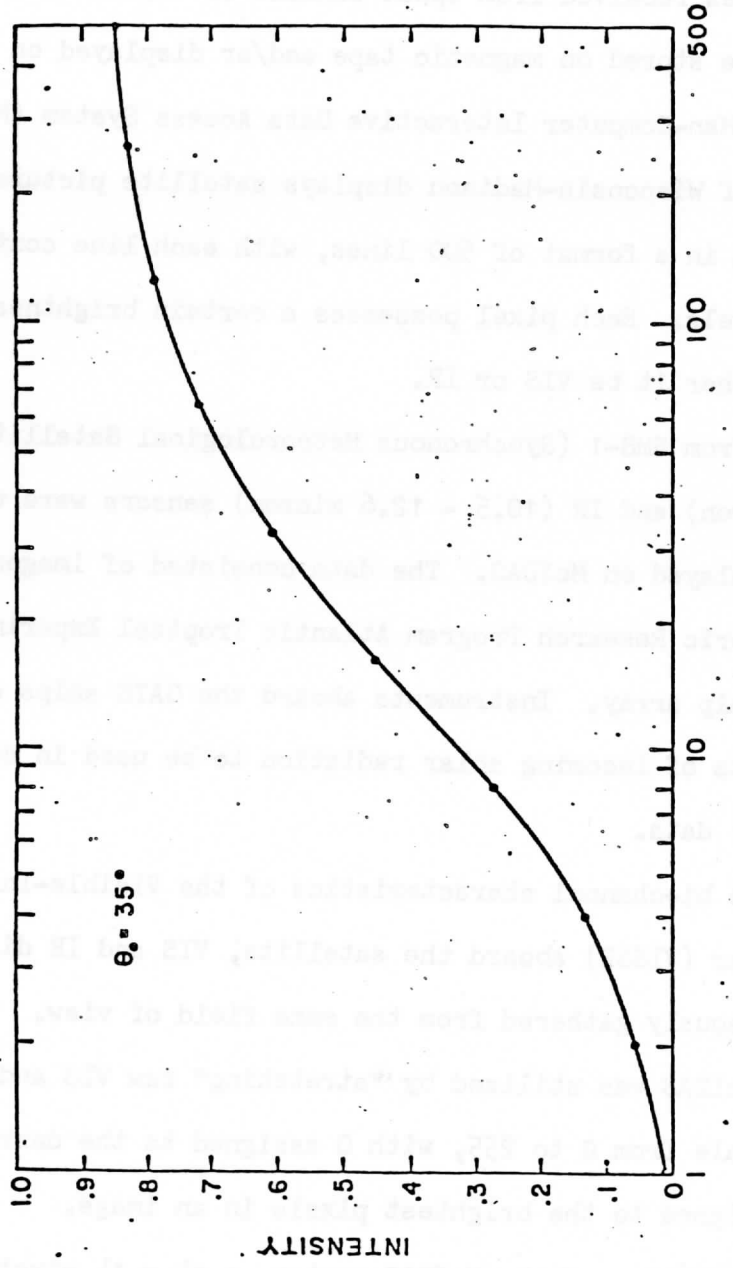

Figure 1: The brightness intensity of clouds in a satellite image as a function of optical thickness for the case of a solar zenith angle of 35 degrees. (from Mosher, 1974)

II. THE DATA

(a) Collection

Satellite images received from space consist of thousands of bits of data which can be stored on magnetic tape and/or displayed on a video screen. The Man-Computer Interactive Data Access System (McIDAS) at the University of Wisconsin-Madison displays satellite pictures on a television screen in a format of 500 lines, with each line containing 672 elements or pixels. Each pixel possesses a certain brightness value from 0 to 255, whether it be VIS or IR.

Digital data from SMS-1 (Synchronous Meteorological Satellite) VIS (0.5 - 0.7 micron) and IR (10.5 - 12.6 micron) sensors were used in this study and displayed on McIDAS. The data consisted of images over the Global Atmospheric Research Program Atlantic Tropical Experiment (GATE) Phase III ship array. Instruments aboard the GATE ships collected copious measurements of incoming solar radiation to be used in conjunction with the SMS-1 data.

Because of the bi-channel characteristics of the Visible-Infrared Spin Scan Radiometer (VISSR) aboard the satellite, VIS and IR digital data were simultaneously gathered from the same field of view. The full dynamic range of McIDAS was utilized by "stretching" raw VIS and IR counts to fit a scale from 0 to 255, with 0 assigned to the darkest pixels and 255 assigned to the brightest pixels in an image.

With the capabilities of the McIDAS system, a 14 x 14 pixel box was centered on a satellite image over the latitude-longitude coordinate of a ship's location. The images had a resolution of one mile and each

box covered 196 square miles of "sky" around a ship. This procedure insured the detection of clouds affecting radiation sensors aboard a ship.

It was imperative that the only pixels included in a histogram were those representing clouds which passed over a ship because these clouds directly attenuated incoming solar radiation. Therefore, cloud motions were estimated by viewing satellite images from one hour before and after the time of study.

(b) Analysis

The 196 VIS and IR digital data points centered over the GATE ship Researcher for 1300 GMT on day 251 of 1974 are shown in Figures 2 & 3. Nearly cloud-free conditions are indicated since all pixels have values in the lower third of the 0 - 255 range. Whole-sky cameras aboard the ship recorded 90% of the sky covered by high, thin clouds (Holle et al., 1977), not easily detected in satellite images.

Figure 4 is an example of a two-dimensional histogram, accompanied by ship measurements of incoming solar radiation every three minutes from 1300 - 1330 GMT, for the data in Figures 2 & 3. The 0 - 255 range of brightness values has been partitioned into thirds for each channel, making it possible for a pixel to be located in one of nine categories. Since all pixels for the Researcher fall into the lower right box in Figure 7 (regardless of cloud motions), a value of 100 is inserted into the box to indicate the percentage of points in that category.

Cloud motions were important for the GATE ship Dallas on this same day. As shown in Figures 5 & 6, VIS brightness values were confined to

69	54	44	44	42	39	37	29	29	29	29	24	24	29
64	61	54	56	49	37	39	42	37	32	29	34	29	29
49	54	56	61	49	39	39	44	39	37	32	32	32	32
37	44	59	64	46	32	29	32	32	29	22	29	24	27
51	71	79	66	44	32	32	32	29	27	29	27	29	29
61	71	79	59	34	27	34	34	32	29	24	29	32	29
56	56	66	54	32	29	32	34	34	34	29	29	27	29
37	34	29	22	27	24	24	27	27	27	29	24	24	27
32	34	27	27	27	27	27	27	29	29	29	32	32	32
27	29	29	29	24	24	24	29	29	29	29	29	32	32
29	32	32	29	29	29	29	29	29	32	32	32	32	34
24	22	19	27	27	24	22	22	19	24	27	24	22	32
29	27	29	29	27	27	24	27	29	27	29	29	24	29

Figure 2: SMS-1 visible brightness values centered over the GATE ship Researcher at 1300 GMT on day 251 of 1974.

40	40	48	48	46	46	36	36	26	26	19	19	15	15
40	40	48	48	46	46	36	36	26	26	19	19	15	15
40	40	48	48	46	46	36	36	26	26	19	19	15	15
40	40	40	40	34	34	23	23	17	17	15	15	15	15
40	40	40	40	34	34	23	23	17	17	15	15	15	15
40	40	40	40	34	34	23	23	17	17	15	15	15	15
40	40	40	40	34	34	23	23	17	17	15	15	15	15
21	21	15	15	13	13	11	11	13	13	15	15	19	19
21	21	15	15	13	13	11	11	13	13	15	15	19	19
21	21	15	15	13	13	11	11	13	13	15	15	19	19
21	21	15	15	13	13	11	11	13	13	15	15	19	19
9	9	9	9	9	9	11	11	13	13	17	17	21	21
9	9	9	9	9	9	11	11	13	13	17	17	21	21

Figure 3: Same as Figure 2 except infrared brightness values.

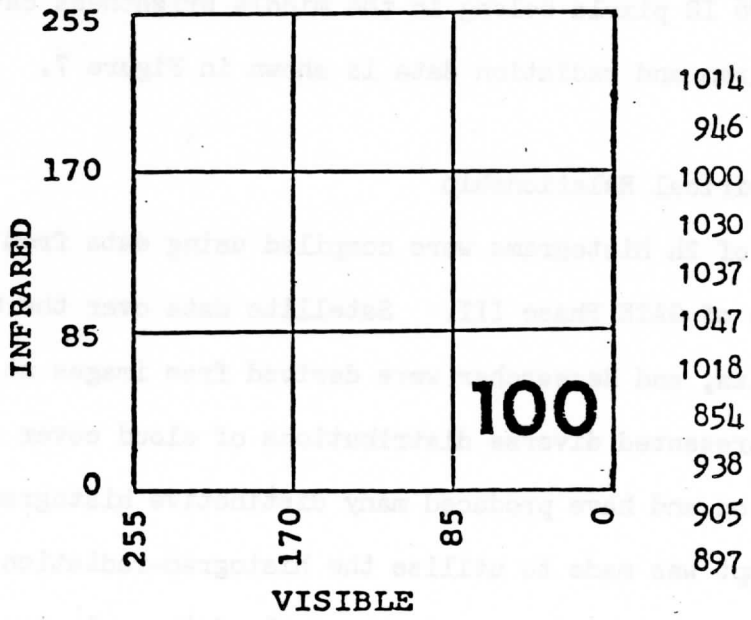

Figure 4: Two-dimensional histogram of satellite data over the GATE ship Researcher for day 251 of 1974 at 1300 GMT, as well as incoming solar radiation values recorded aboard the ship every three minutes from 1300 - 1330 GMT (units of W m^{-2}).

the upper two-thirds of the range while IR values remained mostly in the middle third. Whole-sky photo analysis reported 100% of the sky covered by middle-level clouds (bases between 2 - 8 km), and the clouds were moving approximately south to north. In order to best represent clouds that would pass over the ship and affect incoming solar radiation from 1300 - 1330 GMT, a 28 pixel box of data was chosen south of the ship's location (see Figures 5 & 6). This area included two VIS pixels in the upper third of the brightness range and 26 pixels in the middle range. All 28 IR pixels belong in the middle brightness category. The Dallas histogram and radiation data is shown in Figure 7.

(c) An Empirical Relationship

A total of 24 histograms were compiled using data from 4 ships during 6 days of GATE Phase III. Satellite data over the Oceanographer, Gilliss, Dallas, and Researcher were derived from images at 1300 GMT. This data represented diverse distributions of cloud cover and incoming solar radiation and have produced many distinctive histograms.

An attempt was made to utilize the histogram-radiation relationship in a way that would allow an estimate of cloud transmission to be made from VIS and IR digital brightness values. This was done by relating the percentage of points within a given box in a histogram to the percentage of incoming solar radiation reaching the earth's surface.

When the histogram boxes are lettered as shown in Figure 8, the formula

$$.1(A) + .3(B) + .9(C) + .2(D) + .3(E) + .6(F) + .4(G) + .5(H) + .5(H) + .9(I) = P \qquad (1)$$

143	98	69	81	101	106	91	86	96	113	116	118	108	103
129	107	97	110	126	128	113	107	122	137	134	128	122	118
116	116	126	138	150	150	136	128	148	160	153	138	136	133
118	126	136	148	158	155	145	145	153	153	140	121	123	121
158	165	168	165	155	153	145	123	113	93	86	84	93	108
170	183	178	178	163	150	128	128	126	101	86	91	111	118
171	178	175	175	163	153	140	136	126	117	113	110	118	126
173	173	173	173	163	155	153	143	126	133	140	128	126	133
173	173	173	173	163	155	153	143	126	133	140	128	126	133
153	153	150	150	160	160	145	133	136	148	138	126	118	131
153	165	175	170	178	175	165	148	145	148	138	126	118	133
145	163	173	170	173	175	165	148	128	138	138	131	126	136
128	145	158	155	153	153	148	140	121	113	133	143	150	153
155	165	160	158	165	170	168	150	140	140	153	170	165	165

Figure 5: Same as Figure 2 except for GATE ship Dallas. Shaded region represents an estimate of cloud cover passing over the ship from 1300 - 1330 GMT.

94	94	94	94	94	94	94	94	92	92	86	86	84	84
94	94	94	94	94	94	94	94	92	92	86	86	84	84
94	94	94	94	94	94	94	94	92	92	86	86	84	84
94	94	94	94	94	94	94	94	92	92	86	86	84	84
113	113	109	109	113	113	113	113	107	107	98	98	92	92
113	113	109	109	113	113	113	113	107	107	98	98	92	92
113	113	109	109	113	113	113	113	107	107	98	98	92	92
113	113	109	109	113	113	113	113	107	107	98	98	92	92
134	134	117	117	113	113	109	109	103	103	98	98	94	94
134	134	117	117	113	113	109	109	103	103	98	98	94	94
134	134	117	117	113	113	109	109	103	103	98	98	94	94
134	134	117	117	113	113	109	109	103	103	98	98	94	94
98	98	94	94	96	96	96	96	96	96	94	94	94	94
98	98	94	94	96	96	96	96	96	96	94	94	94	94

Figure 6: Same as Figure 5 except infrared brightness values.

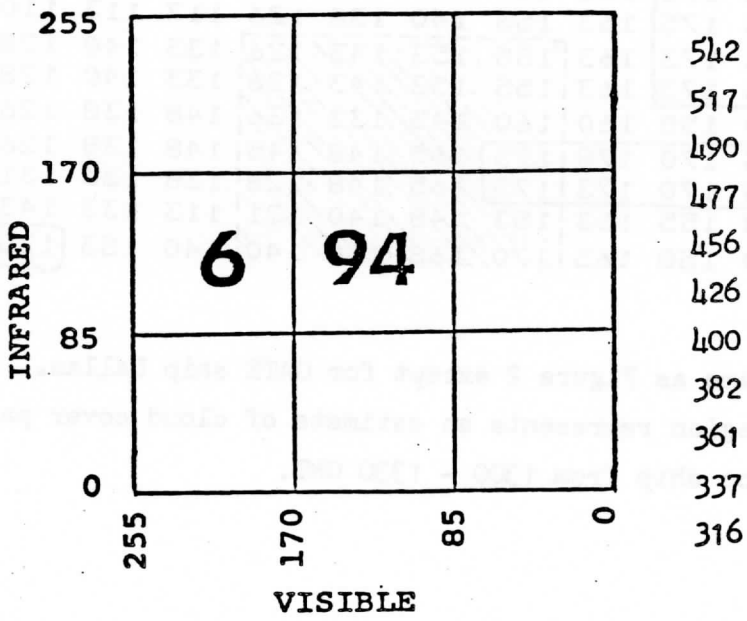

Figure 7: Same as Figure 4 except for the GATE ship Dallas.

equates the percentage of points within a given box to the percent of possible incoming solar radiation at the earth's surface (P). When the percentage of points is entered as a number between 0 - 100 for the appropriately lettered box, the result P will also be a number between 0 - 100.

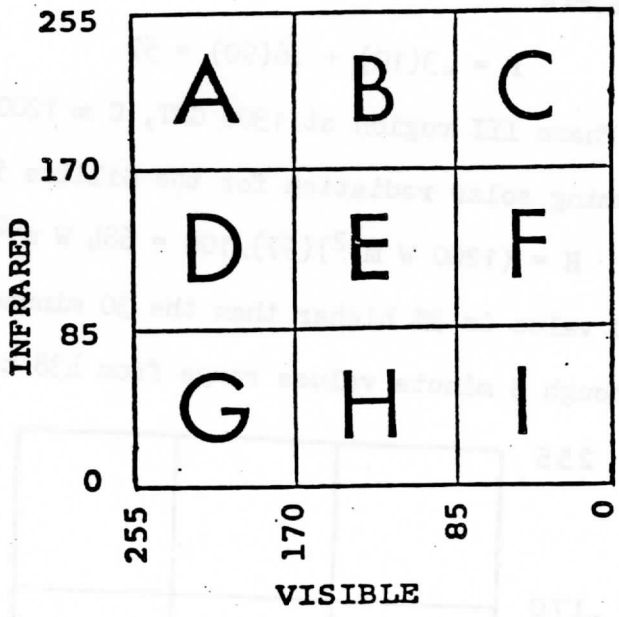

Figure 8: Lettered histogram boxes corresponding to equation (1).

If C is the value of incoming solar radiation under clear-sky conditions, then

$$H = (C)(P)/100 \qquad (2)$$

where H is the predicted value of incoming solar radiation at the earth's

surface. It should be noted that these empirical relationships are based upon GATE Phase III using satellite images for local noon. Data differing in solar zenith angle and/or latitude may yield substantially modified results from those given here.

As an example of the use of the histograms in predicting incoming solar radiation, data from the Gilliss on day 246 is shown in Figure 9. Using the empirical relationships, the percent of possible incoming solar radiation becomes

$$P = .3(10) + .6(90) = 57$$

For the GATE Phase III region at 1300 GMT, $C \approx 1200$ W m^{-2}. Thus, the predicted incoming solar radiation for the Gilliss is

$$H = (1200 \text{ W m}^{-2})(57)/100 = 684 \text{ W m}^{-2}$$

The predicted value is 3% higher than the 30 minute averaged value of 663 W m^{-2}, although 3 minute values range from 438 to 825 W m^{-2}.

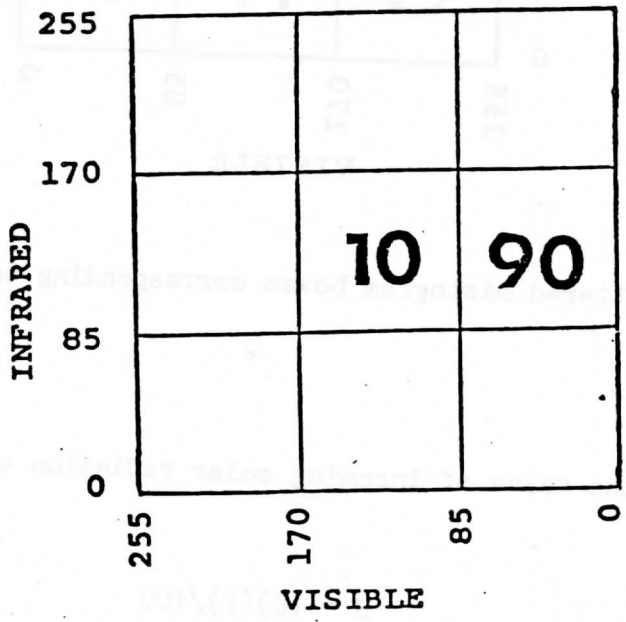

Figure 9: Same as Figure 4 except for the GATE ship Gilliss on day 246.

III. RESULTS

An independent set of 24 histograms was used to predict incoming solar radiation for the four GATE ships during Phase III. The predicted values are listed in Table 1 along with observed 30 minute averaged incoming solar radiation values and percent error.

Two situations may create a large error between predicted and observed values: (a) when all pixels are located in the lower right box I, (b) when pixels are located in boxes H and I only, or F and I only. Both problems occur because the location of data points within a histogram box is not apparent.

When VIS values are very low and IR values are either low or high, clear or thin-cloud conditions exist. If the values are on the high end of the 0 - 85 range, 100% of the pixels will remain in box I even though there is significant reduction in incoming radiation. In the same way, pixel values at or near 85 in one channel, but below 85 in the other, will create an overestimation of incoming radiation if .9 is the coefficient of I in equation (1). Both cases may occur when the field of view contains cumulus clouds smaller than the resolution of the satellite image.

Problem (a) can be alleviated by sub-dividing the histogram into a finer scale and deriving new empirical relationships. For problem (b), it is suggested that the coefficient of I be changed to .7 in equation (1) whenever all points are located either in boxes H and I, or F and I. The results in Table 1 include this correction and are plotted as a scatter diagram in Figure 10.

Table 1

Observed and Predicted Radiation Values
for 24 Histograms During GATE Phase III

Histogram Number		Predicted ($W\ m^{-2}$)	Observed ($W\ m^{-2}$)	Percent Error
1		528	584	9
2		276	311	11
3		360	345	4
4		870	914	5
5	*	1080	700	54
6	*	1080	976	10
7	*	1080	1010	7
8	*	1080	881	22
9		678	797	15
10		600	499	20
11		648	663	2
12	**	756	465	62
13	**	816	594	37
14	*	1080	931	16
15		120	102	17
16		168	155	8
17	*	1080	803	34
18	**	792	610	30
19	*	1080	980	10
20	**	804	859	6
21	**	821	841	2
22	*	1080	971	11
23		720	788	8
24		353	428	17

* all pixels located in box I

** all pixels located either in boxes F and I, or H and I

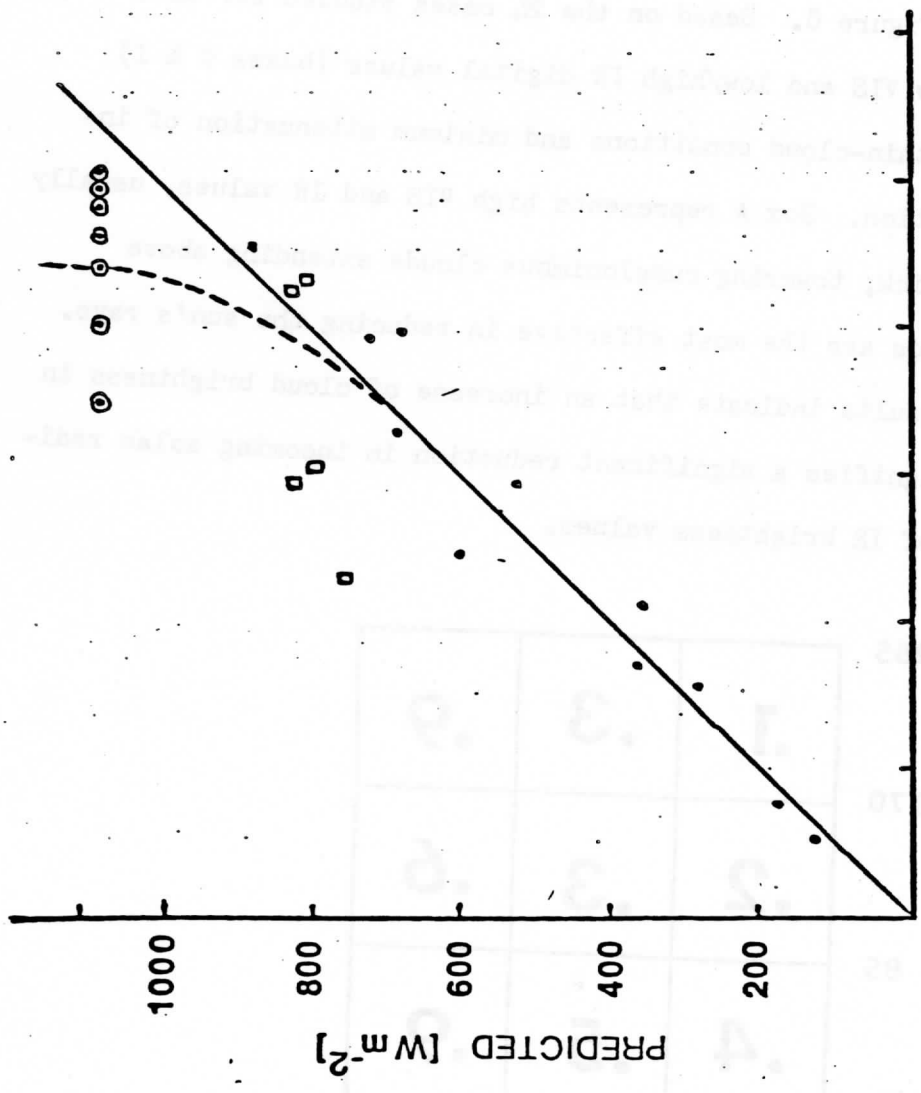

Figure 10: Scatter diagram of predicted vs. observed values of incoming solar radiation for the 24 histograms in Table 1. Dashed line approximates a least-squares fit for the upper half of the diagram. (see text)

Of the 24 cases listed in Table 1, 17 yield predicted values within 18% of observed values. The other 7 cases experienced one of the two aforementioned problems.

Figure 11 shows a histogram and coefficients corresponding to the lettered boxes in Figure 8. Based on the 24 cases studied for GATE Phase III data, low VIS and low/high IR digital values (boxes C & I) indicate clear or thin-cloud conditions and minimum attenuation of incoming solar radiation. Box A represents high VIS and IR values, usually associated with thick, towering cumulonimbus clouds extending above 10 km. These clouds are the most effective in reducing the sun's rays. In general, the results indicate that an increase of cloud brightness in the VIS channel signifies a significant reduction in incoming solar radiation regardless of IR brightness values.

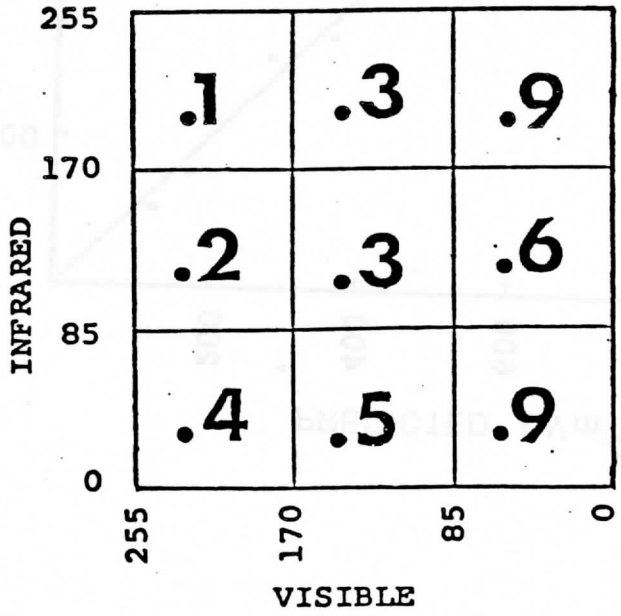

Figure 11: Values of the coefficients corresponding to the lettered boxes in Figure 8.

IV. CONCLUSION

In this study, bi-channel observations of clouds in satellite images have been investigated. Visible and IR digital data, displayed in the form of a two-dimensional histogram, offer a simplified view of the relation between satellite brightness values and incoming solar radiation at the earth's surface.

Twenty-four histograms from 4 GATE ships were used to derive an empirical formula equating the percentage of points in each histogram box to the percentage of incoming radiation reaching a ship's sensor. An independent set of 24 histograms from the GATE area was used to test the derived relationships and over two-thirds of the predicted values were within 18% of observed measurements.

Several conclusions can be made on the basis of this research:

(1) A 3 x 3 two-dimensional histogram of VIS and IR brightness values represents a simplified view of cloud cover, but contains a potentially greater amount of information than observations in only one of the channels.

(2) The histograms may be used with an empirical formula to yield estimates of the percentage of incoming solar radiation reaching the earth's surface. This percentage also represents a description of cloud transmission since the effectiveness of in blocking out the sun's radiation is measured.

(3) The location of data points within a histogram box is not apparent by the method described in this thesis. Problems may

occur when points lie along a division between two boxes, although sub-dividing the histograms into more categories and deriving new empirical relationships could alleviate this.

(4) Based on the coefficients corresponding to the histogram boxes in Figure 11, an increase in the VIS brightness of a region indicates a considerable decrease in cloud transmission regardless of IR brightness values. The most significant decrease in incoming solar radiation occurs with the increase of brightness values in both channels; i.e. the movement of pixels from box I to box E to box A over a given time period. This situation would represent a region undergoing convective activity, resulting in thick, towering cumulonimbus clouds and a major reduction in incoming solar radiation reaching the earth's surface.

Based on the findings of this research, the use of two-dimensional histograms can be explored further. For example, the position of the data points in Figure 10 indicates a non-linear relationship between observed and predicted values when large amounts of incoming solar radiation are recorded. Points in the lower half of the diagram are representative of high VIS and IR values and a different type of cloud cover than points in the upper half. Points in the upper half of the diagram are characterized by low VIS and IR values often associated with scattered cumulus clouds smaller than the resolution of the satellite image.

In order to reduce the percent error between predicted and observed values, an improvement must be made in the prediction of the high values

of incoming solar radiation; i.e. the upper half of the diagram in Figure 10. If a line approximating a least-squares fit is used to represent predicted values (dashed line in Figure 10), the averaged error is reduced by 5% for the entire data set.

What does this suggest about the histograms? Just as the relationship between brightness intensity and cloud thickness is non-linear (see Figure 1), so also is the division of categories in the histogram boxes. Perhaps the VIS brightness value range of 0 - 255 should not be divided into thirds throughout the histogram, but should be staggered for lower IR values as shown in Figure 12. This would help eliminate the problem of data points lying along the division of boxes F and I, or H and I, and considerably reduce percent error between observed and predicted values.

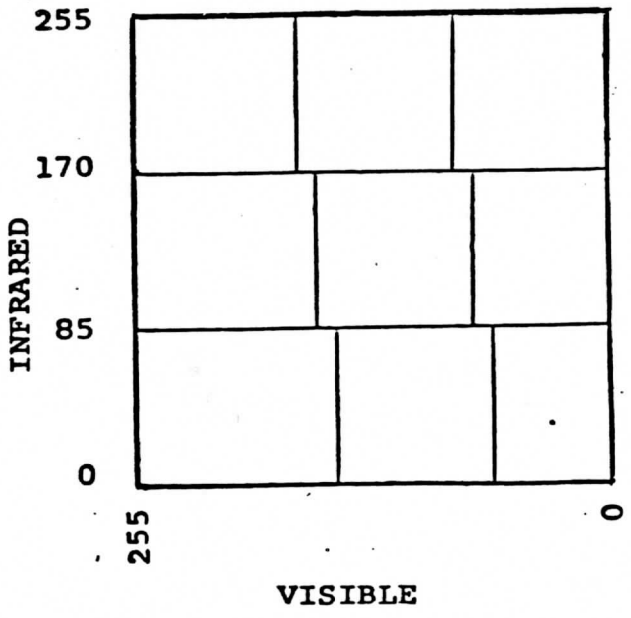

Figure 12: Staggered histogram box configuration which may reduce errors between observed and predicted solar radiation.

The potential use of the histograms is promising because of the ease of data collection. Further experimentation with larger data sets and increased categories within a histogram could lead to greatly reduced errors between observed and predicted surface radiation values. With the extensive global coverage of today's meteorological satellites, it may be possible to utilize two-dimensional histograms to determine incoming solar radiation anywhere on earth.

REFERENCES

Arakawa, A., 1975: Modeling Clouds and Cloud Processes for Use in Climate Models, in The Physical Basis of Climate and Climate Modeling, GARP Publications Series No. 16, World Meteorological Organization, pp. 183 - 197.

Barnes, J.C., 1966: Note on the Use of Satellite Observations to Determine Average Cloudiness over a Region, J. Geophys. Res., 71, 6137.

Bauer, K.G., and J.A. Dutton, 1962: Albedo Variations Measured from an Airplane over Several Types of Surface, J. Geophy. Res., 67, 2367 - 2376.

Bryson, R.A., and G.J. Dittberner, 1976: A Non-Equilibrium Model of Hemispheric Mean Surface Temperature, J. Atmos. Sci., 33, 2094 - 2106.

Budyko, M.I., 1969: The Effect of Solar Variations on the Climate of the Earth, Tellus, 21, 611 - 619.

Clapp, P.F., 1964: Global Cloud Cover for Seasons Using TIROS Nephanalysis, Mon. Wea. Rev., 92, 495 - 507.

Coburn, A.R., 1971: Improved Three Dimensional Nephanalysis Model, AFGWC Technical Memorandum 71-2, Air Force Global Weather Center, Air Weather Service, Offutt AFB, Nebraska, 72 pp.

Cram, R.S., and K.J. Hanson, 1977: The United States B-Scale Surface Radiation Subprogram of GATE: Instrumentation and Data Validation, NOAA Technical Memorandum ERL ARL-65, Air Resources Laboratories, Silver Spring, Maryland, 88 pp.

Holle, R.L., S.W. Leavitt, J. Simpson, R. Biondini, J.W. Snow, 1977:

Cloudiness From Whole-Sky Pictures Taken Aboard 4 U.S. B-Scale Ships, Dept. of Environmental Sciences, Univ. of Virginia.

Hoyt, D.V., 1977: Percent of Possible Sunshine and the Total Cloud Cover, Mon. Wea. Rev., 105, 648 - 651.

Hummel, J.R., and R.A. Reck, 1979: A Global Surface Albedo Model, J. Appl. Met., 18, 239 - 253.

Kasten, F., 1977: Ground Radiation as Affected by Clouds. Proceedings of the Symposium on Radiation In The Atmosphere, Garmisch-Partenkirchen FRG, p. 193.

Kondratyev, K.Y., 1973: Radiation Characteristics of the Atmosphere and the Earth's Surface, Amerind Pub. Co., New Delhi, 580 pp.

Kung, E.C., R.A. Bryson, and D.H. Lenschow, 1964: Study of a Continental Surface Albedo on the Basis of Flight Measurements and Structure of the Earth's Surface Cover Over North America, Mon. Wea. Rev., 92, 543 - 564.

List, R.J., 1971: Smithsonian Meteorological Tables (6th ed.). Smithsonian Institution Press, 527 pp.

Malberg, H., 1973: Comparison of Mean Cloud Cover Obtained by Satellite Photographs and Ground-Based Observations Over Europe and the Atlantic, Mon. Wea. Rev., 101, 893.

Manabe, S., D.G. Hahn, and J.L. Holloway, Jr., 1974: The Seasonal Variation of the Tropical Circulation as Simulated by a Global Model of the Atmosphere, J. Atmos. Sci., 31, 43 - 83.

McKee, T.B., and J.T. Klehr, 1978: Effects of Cloud Shape on Scattered Solar Radiation, Mon. Wea. Rev., 106, 399 - 404.

Mosher, F.R., 1974: SMS Cloud Heights, Space Science and Engineering Center, Univ. of Wisconsin-Madison.

Mosher, F.R., 1979: Flux Variations Across Finite Clouds, Ph.D. dissertation, Univ. of Wisconsin-Madison.

Norris, D.J., 1968: Correlation of Solar Radiation with Clouds, Solar Energy, 12, 107.

Reynolds, D.W., T.B. McKee, and K.S. Danielson, 1978: Effects of Cloud Size and Cloud Particles on Satellite-Observed Reflected Brightness, J. Atmos. Sci., 35, 160 - 164.

Schneider, S.H., 1972: Cloudiness As a Global Climate Feedback Mechanism: The Effects of the Radiation and Surface Temperature of Variations in Cloudiness, J. Atmos. Sci., 29, 1413 - 1422.

Sellers, W., 1973: A New Global Climate Model, J. Appl. Met., 12, 241 - 254.

Sherr, P.E., J.C. Barnes, R.J. Boucher, C.W. Rogers, and W.K. Widger, Jr., 1966: Meteorological Satellite Techniques for the Army, Final Rept., Contract DA 28-043-AMC-01273(E), ARACON Geophysics Division, Concord, Mass. (AD 485-166).

Suomi, V.E., F.R. Mosher, and D.P. Wylie, 1977: Final Report on Phase 1 of Development of Satellite Image Processing Techniques for the First GARP Global Experiment. Contract Report No. NAS 5-23462. SSEC Univ. of Wisconsin, Madison, Wis., 41 pp.

Swartman, R.K., and O. Ogunlade, 1971: Correlation of Solar Radiation with Common Parameters in Toronto, Canada, Solar Energy, 13, 345.

Telegadas, K., and J. London, 1954: A Physical Model of the Northern

Hemisphere Troposphere for Winter and Summer, New York University Final Report on A.F. Cambridge Research Center Contract AF 19 (122) - 165, 55 pp.

World Meteorological Organization, 1965: International Cloud Atlas, Abridged Atlas. World Meteorological Organization, Geneva.

Wyrtki, K., 1966: Reply, J. Geophy. Res., 71, 1760.

An Objective Technique for the Analysis of Cloud Populations

Anne Marie LeBlanc

Space Science and Engineering Center
University of Wisconsin-Madison
1225 West Dayton Street
Madison, Wisconsin 53706

August 1980

Abstract

An objective computer program has been designed which uses visible and infrared digital satellite data as input and produces cloud size and area distributions. The clouds are defined using a point-by-point classification technique, determining three cloud type intervals based on cloud top height: low (surface to 800mb), middle (800 to 500mb), and high (over 500mb). Absolute visible thresholds are used to delineate a cloud/no cloud threshold for low clouds, and thick (convectively active) clouds.

The program was run on a sample data set of eight days from GATE Phase III. Results show small clouds dominating the total number of clouds while large clouds account for most of the area covered by clouds. The high clouds give evidence of a diurnal cycle with a minimum in the early morning hours and maximum cirrus shield coverage in the late afternoon and early evening.

1. Introduction

Cloud populations, size and area distributions are major parameters to be included in energy and radiation budgets, global circulation studies, climate studies and other research. Increased satellite resolution and global coverage has stimulated research to increase the knowledge of clouds, especially in otherwise data scarce regions. Numerous techniques for the classification of cloud types using satellite data have appeared, ranging from a "point-by-point" method (cloud type is determined for each individual element of data set), to the "region" approach (cloud type is determined over an array of data set elements). The scope of these studies has been restricted to cloud typing only. Studies of cloud populations have been done primarily using radar echo data, or aircraft photographs, and have been limited to a specific cloud type, such as cumulus.

The intent of this research is to design an objective computer program which uses visible and infrared digital satellite images as input data, defines clouds according to a given cloud classification technique, counts the number of clouds, the clouds' areas and other parameters, and produces a list of these clouds and their statistics. The advantage of using this objective program lies in the

fact that the type or types of clouds analyzed depends solely on the cloud classification technique chosen by the user. Thus the variety of clouds analyzed can be as large or narrow as the user wishes. To test this program, a simple point-by-point, three level classification scheme was chosen, and two spectral channels (visible and infrared) were used to define cloud type. A normalized visible brightness threshold was also used in this study to delineate the thick or convectively active (precipitating) parts of each cloud. The program was run on a sample data set from the tropical Northeastern Atlantic region and the results compared with other studies. The graphs of cloud size and areal distributions show that small clouds dominated the total number of clouds and the largest clouds accounted for most of the cloud area coverage. These results compare favorably with other cloud population studies, although the satellite results are on a larger scale. The graphs also present evidence of a diurnal change in the high level cloudiness, which in in agreement with the finding of Gray and Jacobson (1977), who presented evidence in support of the existence of a large diurnal cycle of oceanic, deep cumulus convection.

From these results, it appears that large amounts of data (i.e. satellite images) can be analyzed using objective methods to obtain a good cloud census. More

sophisticated cloud-typing techniques could be used in place of the method used here. The program could also be adjusted for use over regions other than the tropical ocean. At present, the method requires on the order of 15 minutes of CPU time to analyze one set of images for one time period. For very large data sets, the cost would be high. Optimization of the program design would very likely streamline the technique and reduce the run-time, and therefore, the cost.

2. Background

Numerous cloud classification techniques have been described, ranging from the point-by-point approach to the region approach. Point-by-point classification techniques using single-channel infrared data or multispectral data have been investigated by Greaves and Chang (1970), Koffler et al. (1973) and Shenk et al. (1976). Greaves and Chang (1970) developed cloud-type signatures for Nimbus-2 cloud data to determine five unique cloud types: cumulus, stratus and/or stratocumulus, altocumulus, cirrus and cumulonimbus. Koffler et al. (1973) used single channel infrared data to discriminate three cloud types according to cloud top height: low clouds (surface to 700 mb), middle clouds (700 to 400 mb), and high clouds (over 400 mb). Shenk et al. (1976) developed a four channel multi-spectral identification technique using Nimbus-3 MRIR measurements to discriminate ten individual cloud types and cloud type combinations.

Cloud population studies have used radar echoes, and aircraft or shipboard camera photographs. Generally only one cloud type is analyzed, usually cumulus. Plank (1969) analyzed primarily small cumuli of the fair weather and cumulus congestus types over the Florida penninsula, from photographs taken from RF-84F photo reconnaissance

aircraft. Holle (1968) related cumulus cloud height distributions over the open ocean to synoptic state and time of data, from photographs taken from a single ship. Lopez (1976) analyzed radar information from several northwestern Atlantic tropical disturbances. Houze and Cheng (1977) analyzed radar echo patterns observed daily during GATE. In all of these studies, however, the areal coverage was limited. The use of satellite data increases the areal coverage possibilities, which (at this time) results in a reduction in the resolution available. The total area coverage is dominated by the large clouds, so the loss of sub-resolution clouds is more important to those studies involving smaller scale dynamics.

The distinction of cloud types according to cloud top height gives no information as to the depth of the cloud. In recent years, brightness thresholds have been used to delineate cloud thickness and rain areas. Kaveney et al. (1977) has shown a direct statistical correlation between cloud thickness and the reflected solar radiation in the visible part of the spectrum (brightness) for NOAA 4 satellite scanning radiometer data. Stout et al. (1979) used a threshold value of brightness (for visible images) and one of coldness (for infrared images) to delineate convectively active clouds.

3. Technique

The intent of the program was to analyze satellite images and generate cloud statistics, thereby reducing the images into a smaller data set without losing vital information contained in them.

The main flow of the program is shown in Figure 1. The main program, or driver, reads in the images and uses the navigation to locate the area of interest. This area is then isolated in a 500 X 672 picture element (pixel) array. Limitations of storage and cost prohibit working with the entire image array at once. Therefore, the array is sub-divided into 280 arrays or boxes, each containing 25 X 48 pixels. For each box, the program calculates the mean visible brightness thresholds to be used (the change in the thresholds from array to array is small enough to allow this approximation), and analyzes the clouds within the box. The image is processed sequentially from left to right, row by row. After the entire image is processed, the program produces a final list of clouds, giving type, area, amount of the cloud area which was classified as "thick", the brightest visible element in the cloud and the earth coordinates of that point. A pictorial image is also produced, in which clear areas are black (0 counts), low clouds are dark gray (75 counts), middle clouds are

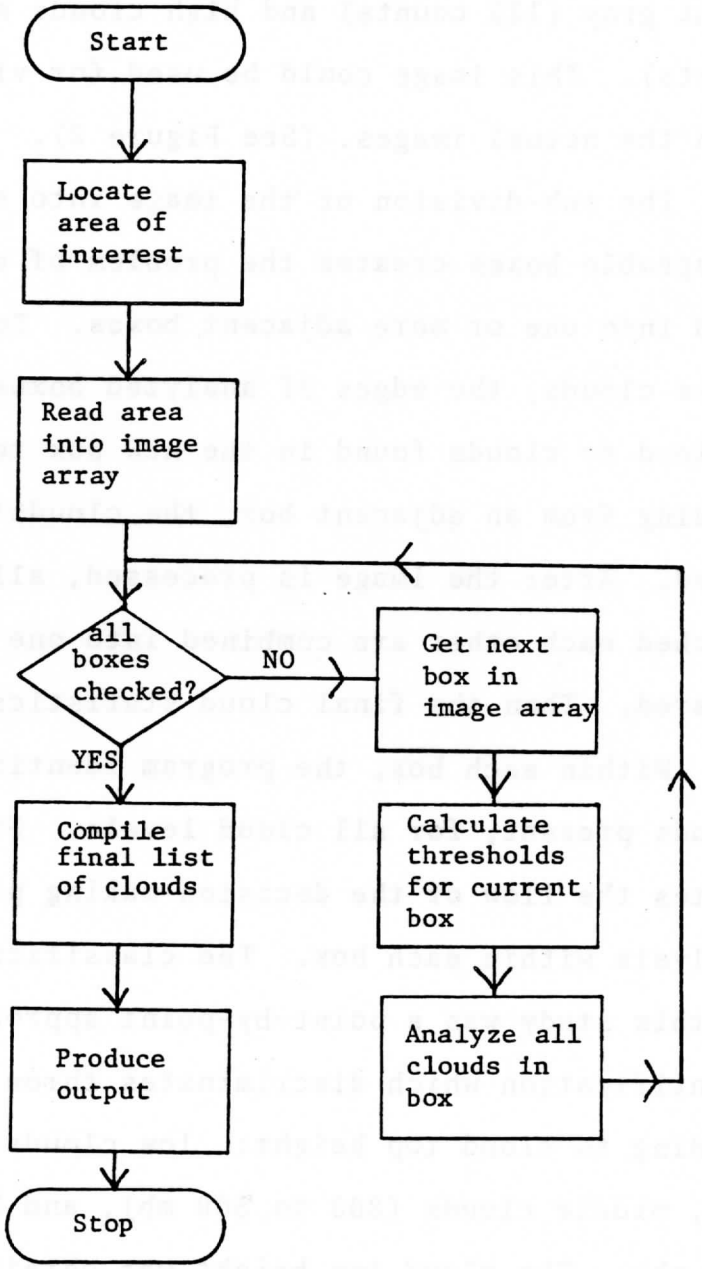

FIGURE 1. Flow diagram for main program.

light gray (125 counts) and high clouds are white (175 counts). This image could be used for visible comparisons with the actual images. (See Figure 2).

The sub-division of the image into smaller, more manageable boxes creates the problem of clouds which extend into one or more adjacent boxes. To keep track of these clouds, the edges of analyzed boxes are saved. If a cloud or clouds found in the new box touch clouds extending from an adjacent box, the clouds' numbers are also saved. After the image is processed, all the clouds which touched each other are combined into one cloud and the rest cleared. Then the final cloud statistics are compiled.

Within each box, the program identifies all of the clouds present, for all cloud levels. Figure 3 illustrates the flow of the decision-making process for cloud analysis within each box. The classification scheme used in this study was a point-by-point approach in cloud type identification which discriminates three cloud types according to cloud top height: low clouds (surface to 800 mb), middle clouds (800 to 500 mb), and high clouds (over 500 mb). The cloud top height was obtained from a program which uses the infrared sensor count to determine the blackbody cloud top temperature. The height was obtained from a standard atmosphere of temperature vs. height, interpolated for latitude and Julian day. The height of

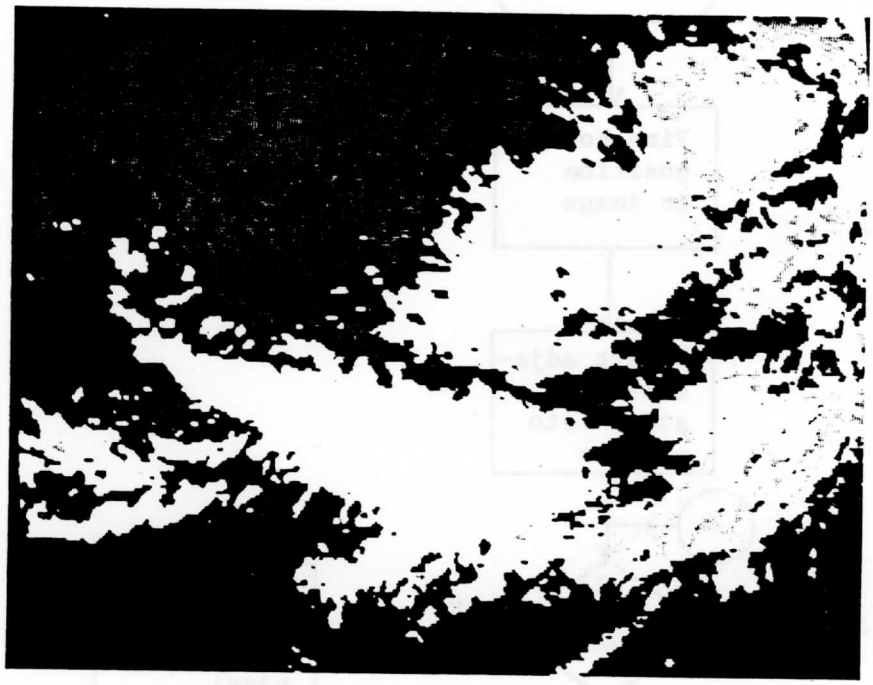

FIGURE 2. Pictorial output of the clouds analyzed on GATE day September 6, 1974, at 150000 GMT.

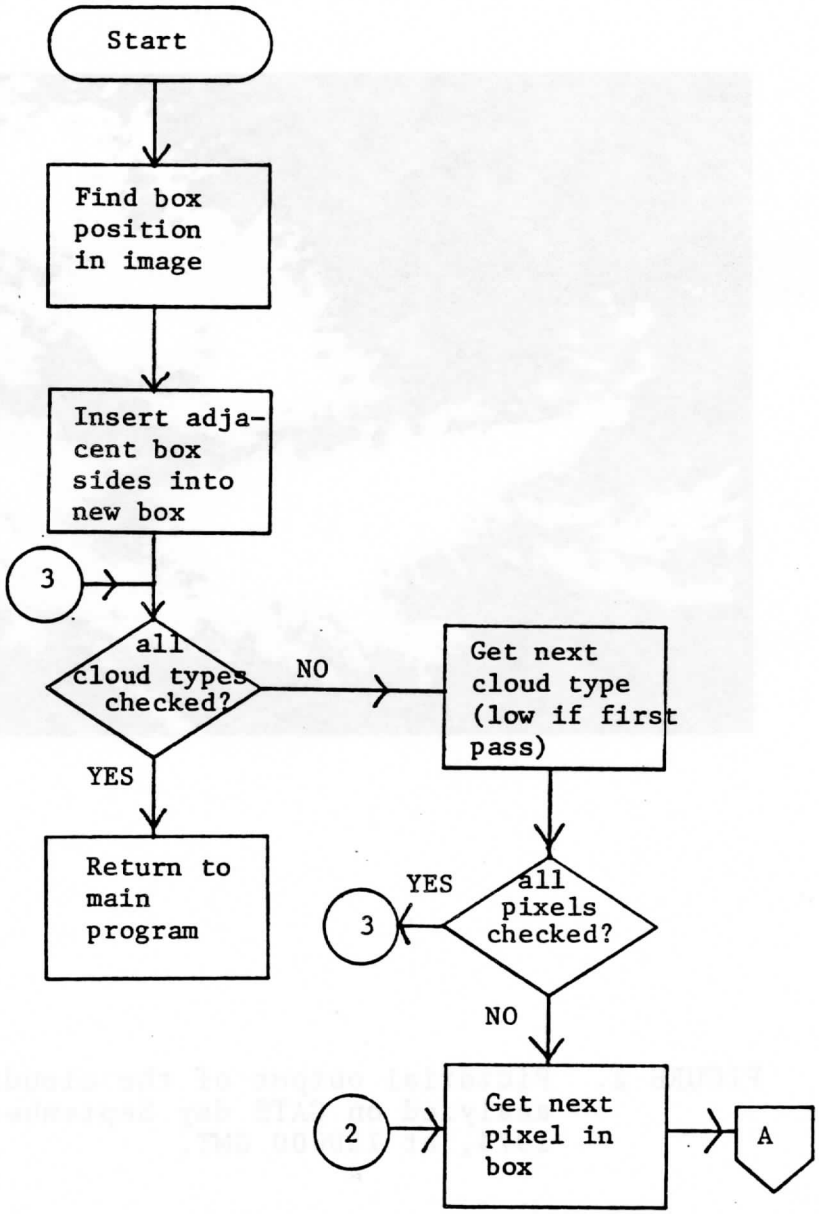

FIGURE 3. Flow diagram for cloud analysis within each box.

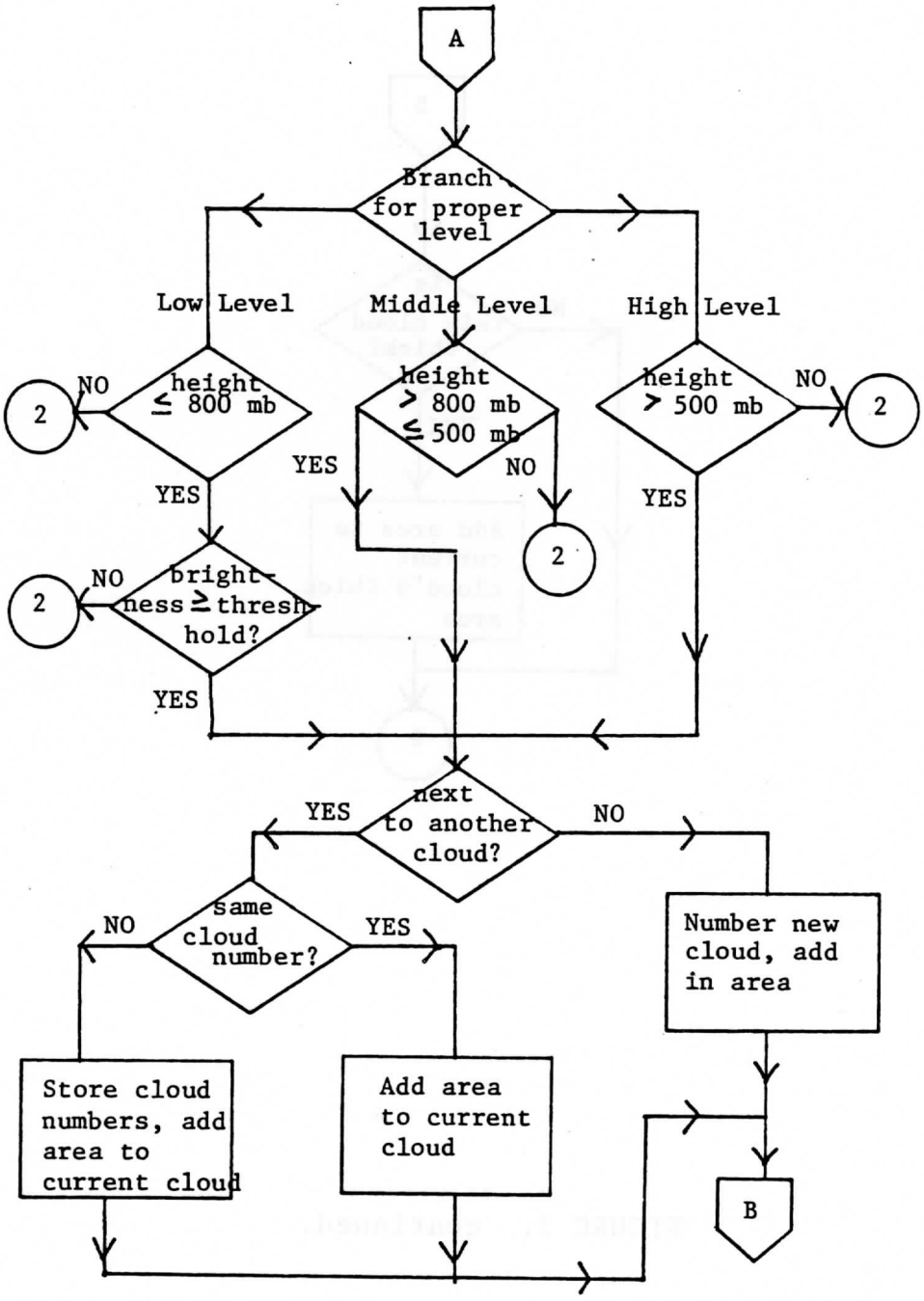

FIGURE 3. continued.

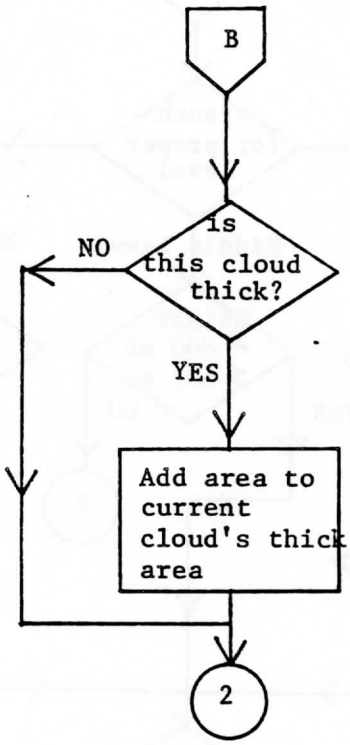

FIGURE 3. continued.

the 500 and 800 mb levels are also calculated using a standard atmosphere of pressure vs. temperature and height, interpolated for latitude and Julian day. Low clouds must also have a digital visible brightness count greater than a calculated cloud/no cloud visible threshold. A new pass is made through the box for each cloud type.

The low cloud/no cloud visible threshold was developed to include clouds with temperatures close to the surface temperature, that could be lost if using only infrared images. Because this study examines an area varying in time, a complication arises in determining this threshold. Sunglint, which is the result of specular reflection of sunlight from the ocean surface, becomes an important factor around midday. The strength of the signal received from sunglint areas by the satellite primarily depends on the number of mirror-like facets which are tilted at the proper angle to reflect light from the sun to the satellite's spin scan camera (Kornfield, 1973). In calm winds, the sea surface is likened to a mirror, and the sunglint area is small but very bright. At higher wind speeds, the sea surface roughness increases, changing the reflective properties of the sea. The sunglint area increases, but the intensity of the reflected light decreases. Cox and Griffith (1979) established

visible thresholds as a function of the distance from the center of the sunglint region as viewed from the SMS-1. Figure 4 depicts their visible clear-sky brightness count threshold as a function of distance from the center of the sunglint pattern. They found the broad, slowly changing portion of the curve, between 400 and 1500 km, centered around a brightness count of 72, corresponding to a system albedo of approximately 14%. This value appeared too high when compared to clear areas in that range in the sample data set, and produced a large drop in low cloudiness at midday. An attempt was made to use a theoretical model for calculating expected sunglint based on satellite and sun position, and surface wind speed and direction. An average surface wind speed and direction taken from GATE ship data for the given date and time did not accurately represent the entire image. For low wind speeds, values of expected sunglint brightness obtained in this manner resulted in unreasonably high brightness values. Because the areal coverage of the 500 X 672 array is approximately ten times greater than the GATE B-scale array used by Cox and Griffith, and both brightness threshold curves generated values that were too high, visible satellite data from cloud-free regions during the eight day period used in this study was collected as a function of distance from the sunglint center. An empirical formula was

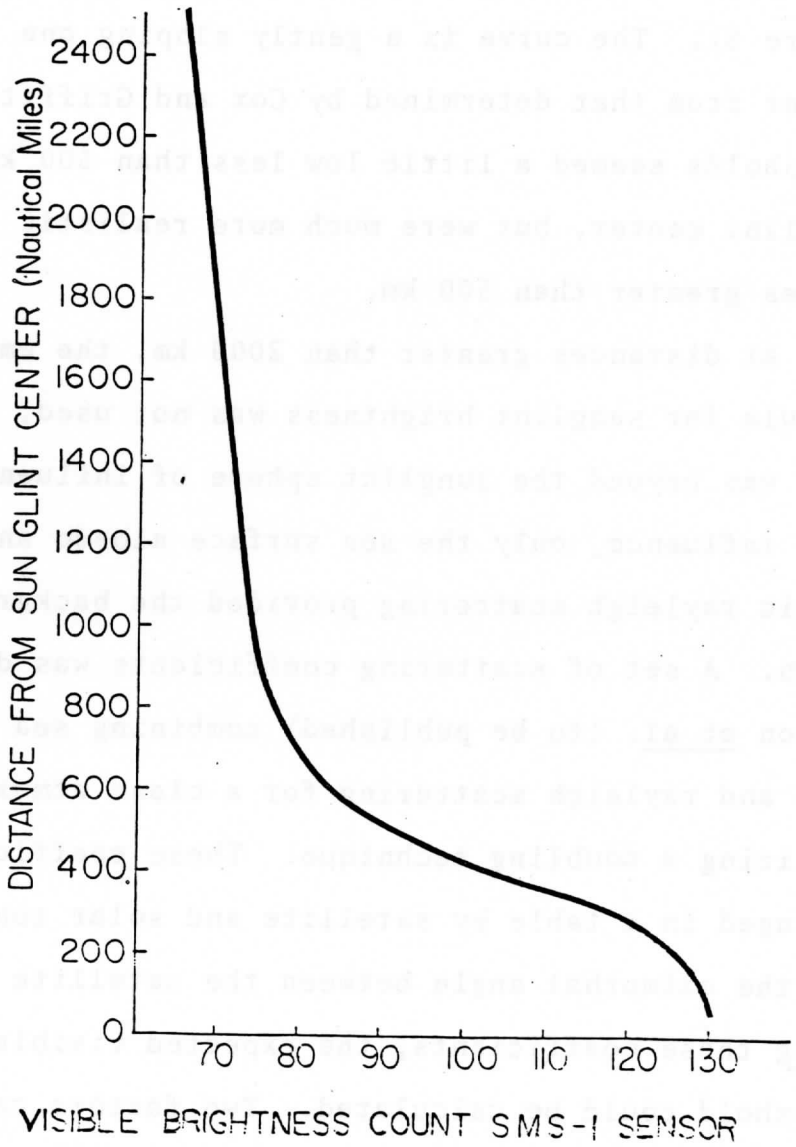

FIGURE 4. Clear sky visible brightness count (SMS-1 satellite) as a function of distance from the sunglint center (From Cox and Griffith, 1979).

calculated as a least squares best fit function (see Figure 5). The curve is a gently sloping one very different from that determined by Cox and Griffith. These thresholds seemed a little low less than 500 km from the sunglint center, but were much more realistic for distances greater than 500 km.

At distances greater than 2000 km, the empirical formula for sunglint brightness was not used, because the area was beyond the sunglint sphere of influence. Beyond that influence, only the sea surface albedo and atmospheric rayleigh scattering provided the background radiation. A set of scattering coefficients was developed by Norton et al. (to be published) combining sea surface albedo and rayleigh scattering for a clean atmosphere, utilizing a doubling technique. These coefficients were arranged in a table by satellite and solar zenith angles, and the azimuthal angle between the satellite and sun. Using these coefficients, the expected visible brightness threshold could be calculated. Two factors can cause this calculated threshold to be inaccurate: 1) turbidity and 2) the presence of sub-resolution cloud fields. The presence of dust and aerosols in the atmosphere over the ocean (common off the west coast of Africa) creates greater scattering and therefore higher thresholds than calculated. Because the amount of dust is not a constant,

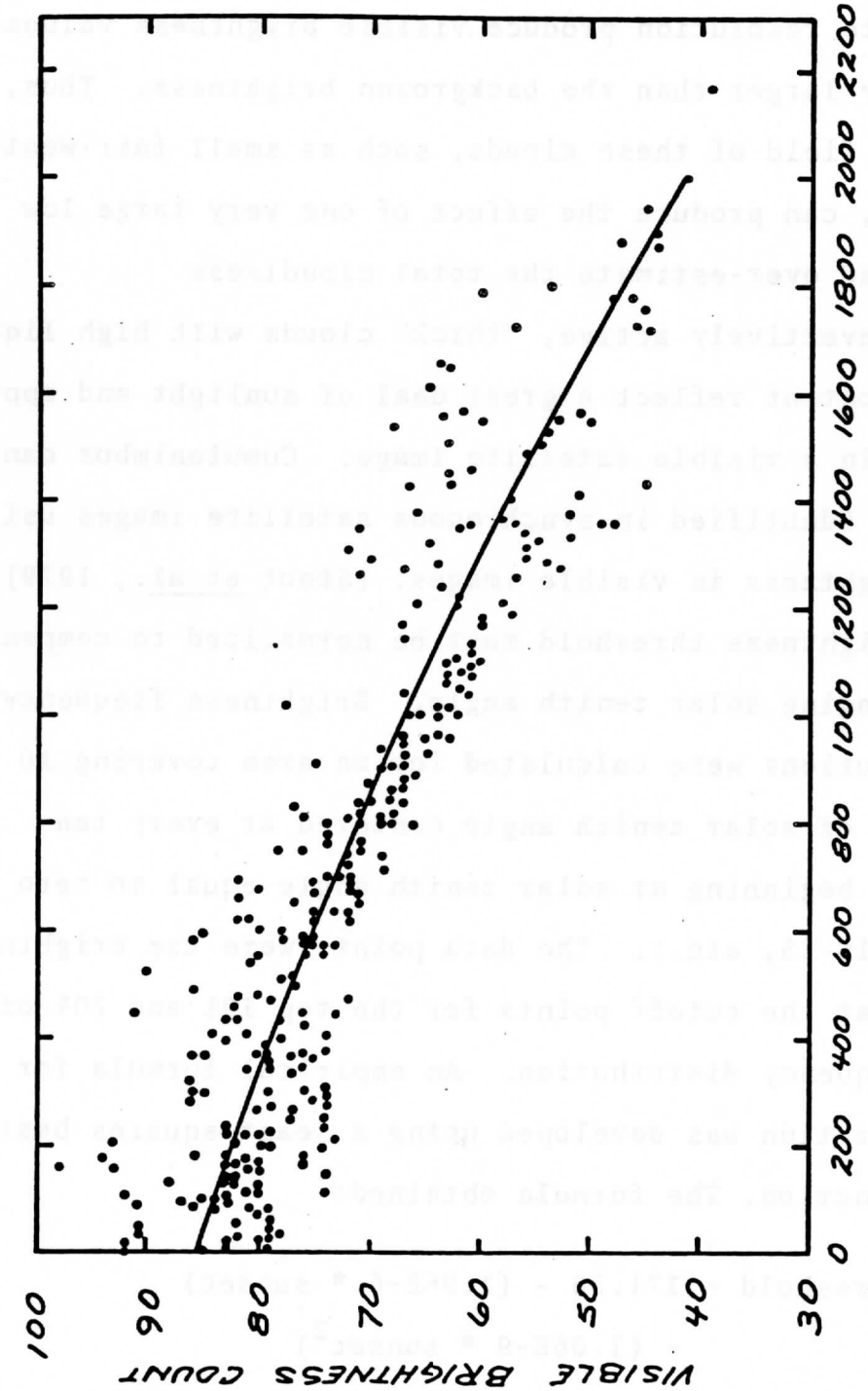

FIGURE 5. Clear sky visible brightness count (SMS-1 satellite) as a function of distance from the sunglint center for the eight test days.

the values are constantly changing. Clouds at or below satellite resolution produce visible brightness values slightly larger than the background brightness. Thus, a large field of these clouds, such as small fair-weather cumulus, can produce the effect of one very large low cloud and over-estimate the total cloudiness.

Convectively active, "thick" clouds with high liquid water content reflect a great deal of sunlight and appear bright in a visible satellite image. Cumulonimbus can be readily identified in synchronous satellite images using the brightness in visible images. (Stout et al., 1979). This brightness threshold must be normalized to compensate for changing solar zenith angle. Brightness frequency distributions were calculated for an area covering 10 degrees of solar zenith angle centered at every ten degrees beginning at solar zenith angle equal to zero (5-15, 15-25, etc.). The data points were the brightness values at the cutoff points for the top 10% and 20% of the frequency distribution. An empirical formula for this normalization was developed using a least squares best-fit function. The formula obtained:

$$\text{threshold} = 171.36 - (1.96\text{E-}6 * \text{sunsec}) - (1.06\text{E-}9 * \text{sunsec}^2)$$

where sunsec = solar zenith angle in seconds

defines a curve illustrated in Figure 6. The value at solar zenith, 171, agrees exceptionally well with the value of 172 used by Stout et al. (1979) to define cloud areas with the maximum correlation to rainfall. This normalization curve also agrees with brightness normalization techniques discussed by Mosher (1979), illustrated in Figure 7.

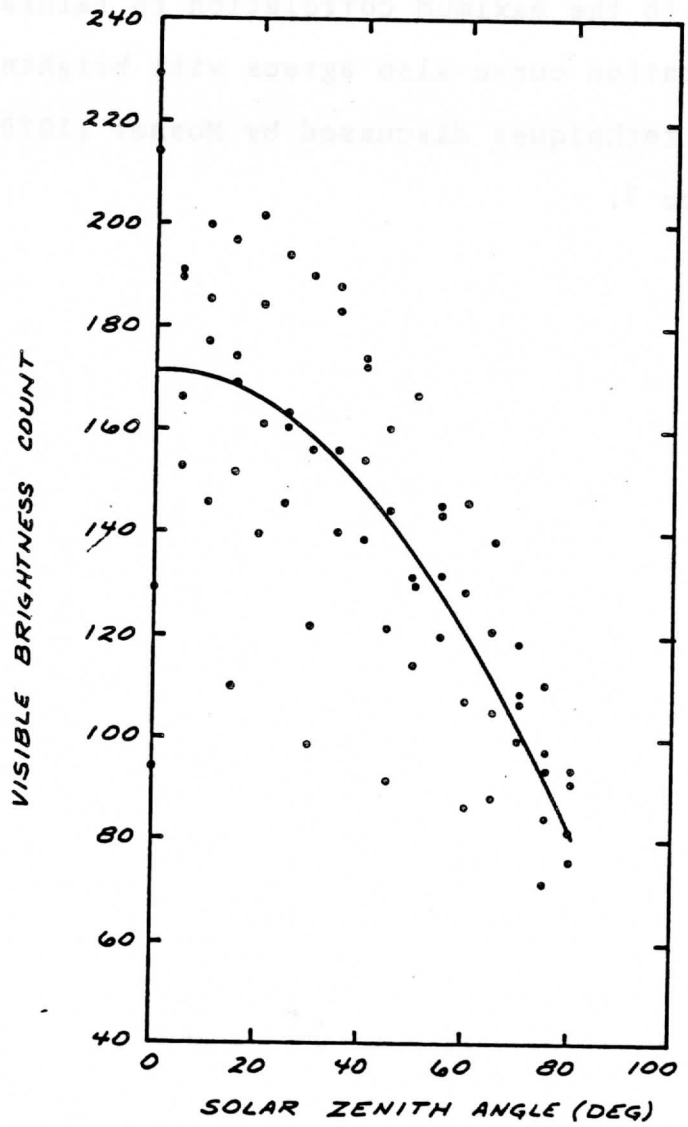

FIGURE 6. Thick cloud visible brightness thresholds as a function of the solar zenith angle.

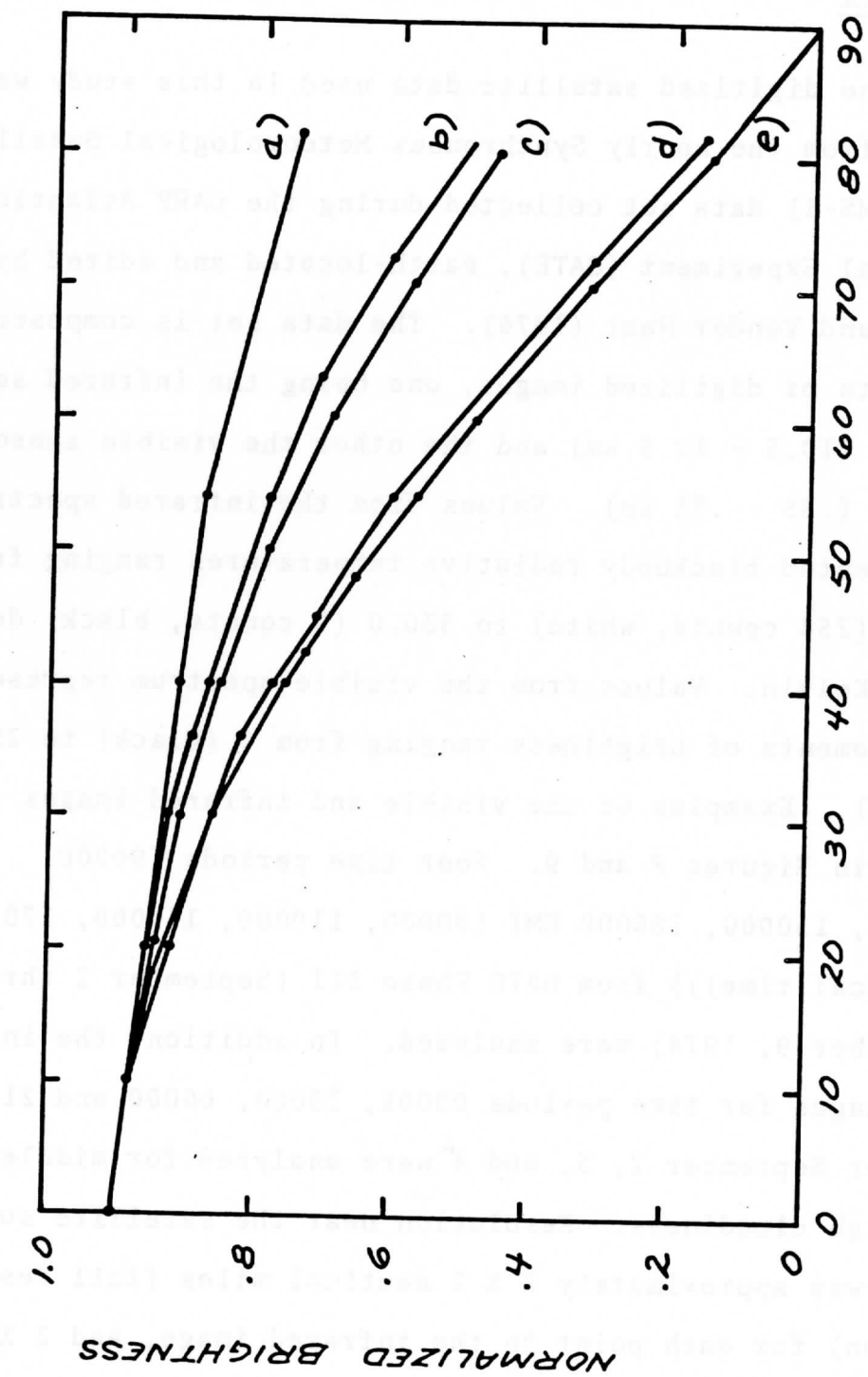

FIGURE 7. Normalized thick cloud visible brightness thresholds as a function of solar zenith angle for a) brightest value on a cube b) brightest value on a cube which is not on the edge c) curve presented in Fig. 6 d) plane parallel clouds and e) cosine of the solar zenith angle.

4. Data

The digitized satellite data used in this study were taken from the hourly Synchronous Meteorological Satellite - 1 (SMS-1) data set collected during the GARP Atlantic Tropical Experiment (GATE), earth-located and edited by Smith and Vonder Haar (1976). The data set is composed of two sets of digitized images, one being the infrared sensor images (10.5 - 12.5 μm) and the other the visible sensor images (.55 - .75 μm). Values from the infrared spectrum represented blackbody radiative temperatures ranging from 164.0 (254 counts, white) to 330.0 (0 counts, black) degrees Kelvin. Values from the visible spectrum represents measurements of brightness ranging from 0 (black) to 255 (white). Examples of the visible and infrared images are shown in Figures 8 and 9. Four time periods (90000, 120000, 150000, 180000 GMT (80000, 110000, 140000, 170000 LT (local time))) from GATE Phase III (September 2 through September 9, 1974) were analyzed. In addition, the infrared images for time periods 00001, 33000, 60000 and 210000 GMT for September 2, 3, and 4 were analyzed for middle and high cloudiness. Resolution near the satellite subpoint was approximately 2 X 2 nautical miles (full resolution) for each point in the infrared image, and 2 X 2 nautical miles (reduced resolution) for each point in the

FIGURE 8. SMS-1 visible satellite image for 120001 GMT, September 4, 1974.

FIGURE 9. SMS-1 infrared satellite image for 120001 GMT, September 4, 1974.

visible image. A 500 X 672 pixel array (1000 X 1344 nm.) was centered at approximately 8° N latitude, 28° W longitude, covering an area from the equator to 16° N latitude, and 18° - 38° W longitude. The navigation used in analyzing the images was developed at the Space Science and Engineering Center, Madison, Wisconsin. The actual data processing was done at the Madison Academic Computing Center, on a Univac 1110 computer.

5. Results

The results of the sample data run will be discussed in two separate sections: 1) the cloud frequency distributions and areal coverage distributions, and 2) the diurnal variation of the high cloudiness and high thick cloudiness. Since a visible threshold was used in the determination of the low cloud type, the sensitivity of this threshold will also be discussed.

A. Frequency and Areal Coverage Distributions

The distributions shown in Figures 10, 11, 12 and 13 are eight day composites of cloud size frequency for 90000, 120000, 150000, and 180000 GMT, respectively. The shape of the frequency distributions are almost identical for all four time periods. The low cloud distribution peaks at the smallest clouds (4 km^2), dropping rapidly with size.

The middle and high level clouds are similar, although different from the low cloud distribution. Both are heavily skewed towards the small clouds, with three generally distinct peaks embedded in the one major peak. The first peak occurs in the 16-20 km^2 interval. This peak is always lower in the high cloud distributions than in the middle cloud distributions. At 180000, the high cloud peak shifted to the 8-12 km^2 size clouds. All

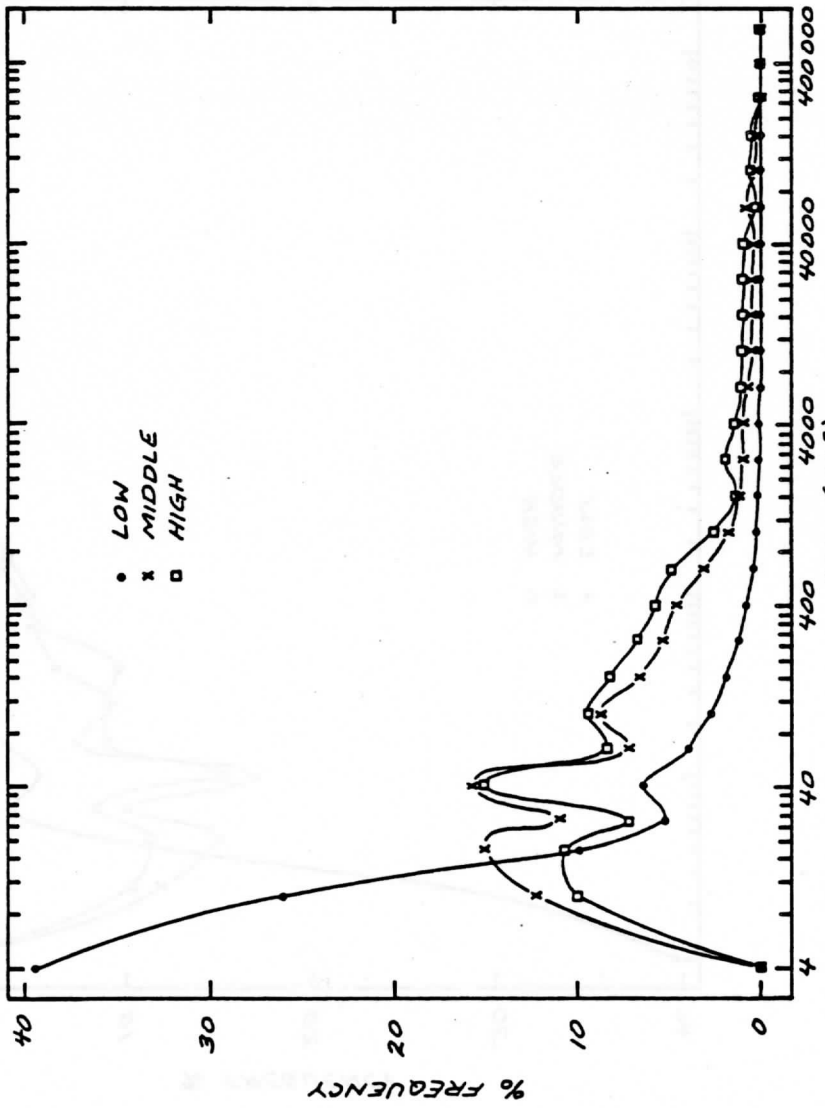

FIGURE 10. Frequency distribution of cloud sizes for eight day composite at 90000 GMT.

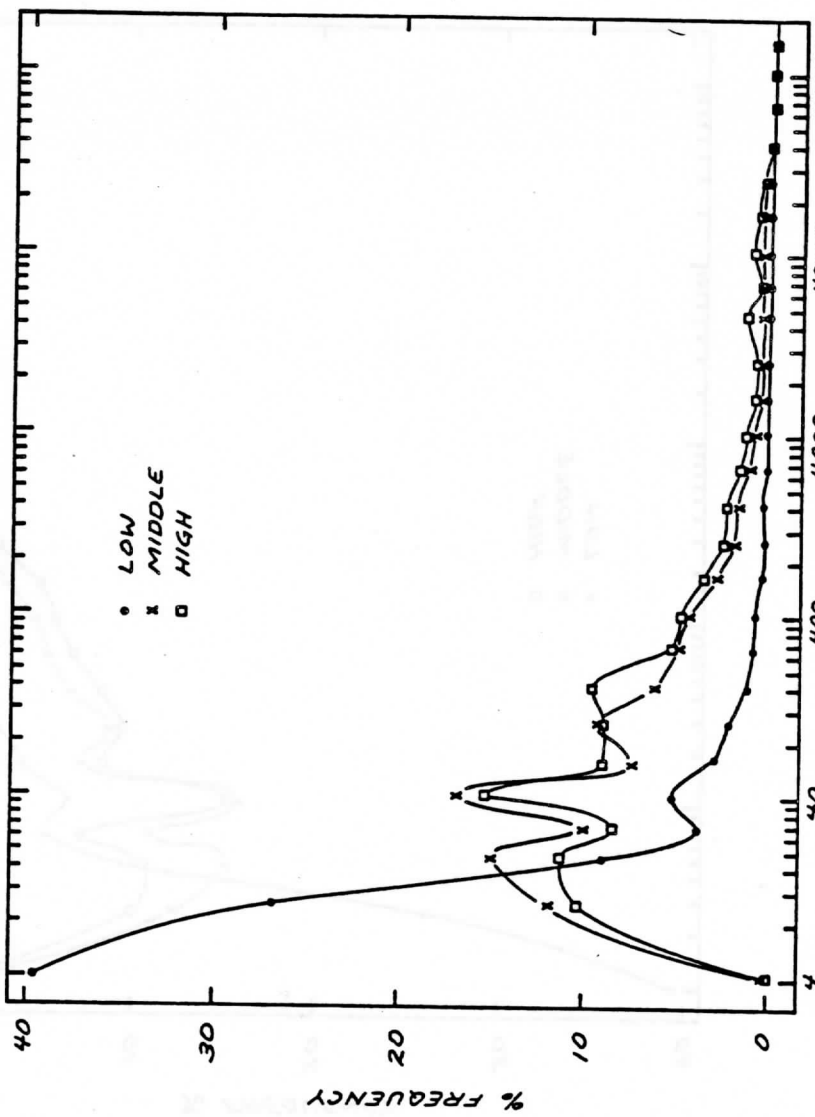

FIGURE 11. Frequency distribution of cloud sizes for eight day composite at 120000 GMT.

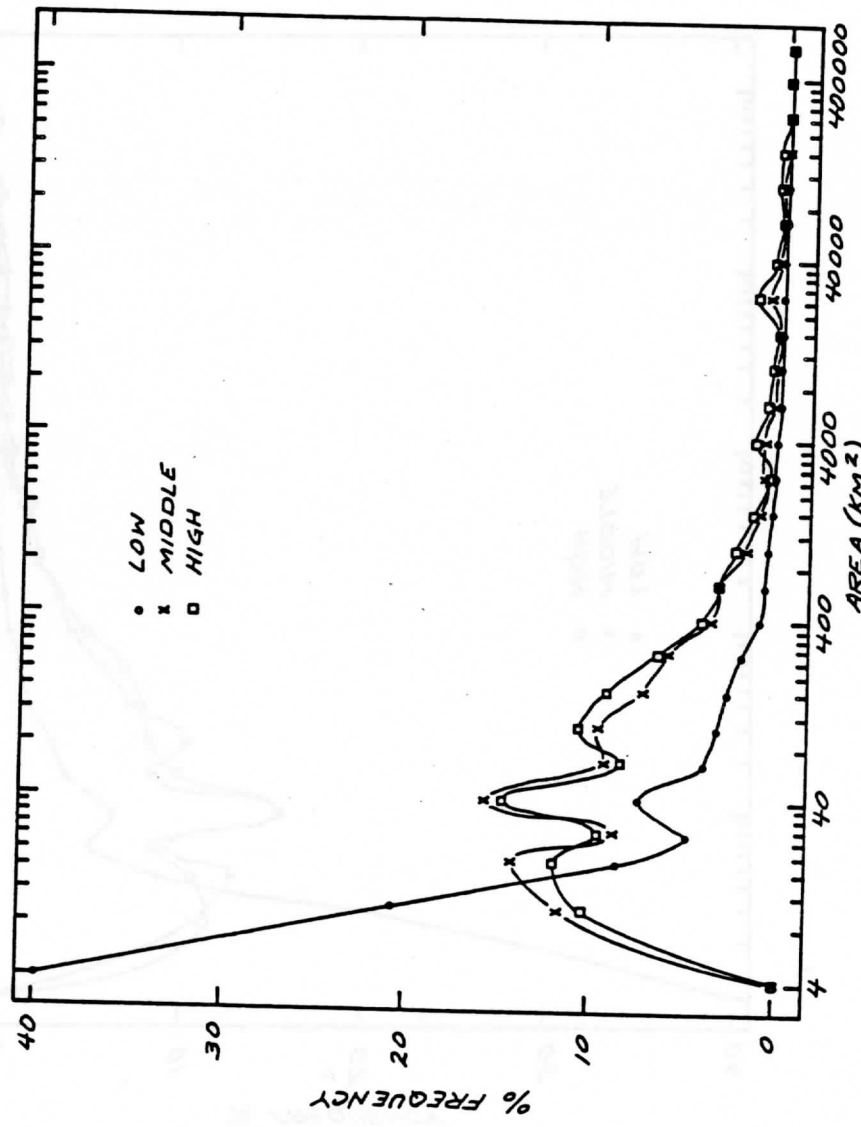

FIGURE 12. Frequency distribution of cloud sizes for eight day composite at 150000 GMT.

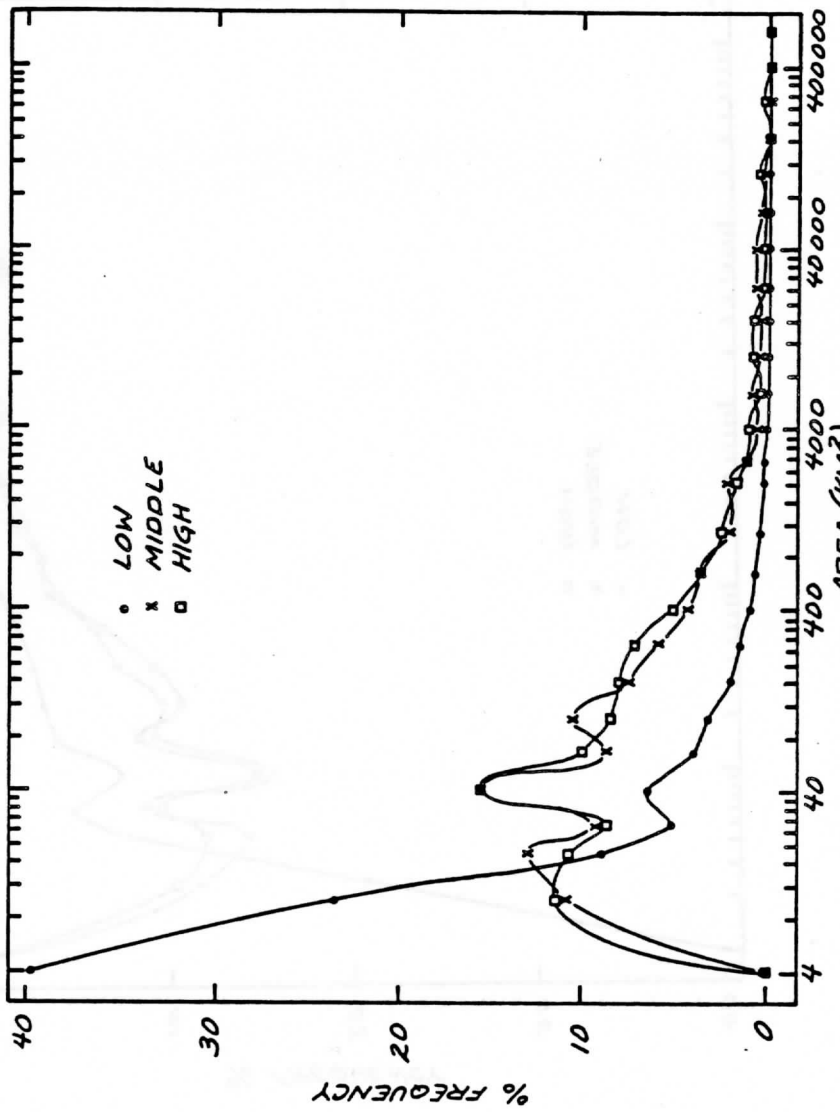

FIGURE 13. Frequency distribution of cloud sizes for eight day composite at 180000 GMT.

distributions show a drop in the 24-28 km^2 interval. The primary peak occurs at 32-48 km^2. The percentage frequency value is almost identical for both cloud levels, around 16%. For the middle cloud level, this peak is only slightly higher than the secondary peak, whose percentage frequency is around 14%. The secondary peak of the high clouds is lower, with a percentage frequency value of approximately 11.5%. The distribution drops off sharply from this peak, with a minor tertiary peak present in the 80-124 km^2 range. This minor peak is not as consistent as the other peaks. This peak in the high level clouds shifts to the 128-196 km^2 range. At 180000, it is not present at all in the high cloud level. There is also a very small peak appearing in the 3000-5000 km^2 range, but it is not always apparent, and is generally more noticeable in the high level clouds. This highly skewed distribution agrees well with the results of Lopez (1976), who found that 60% of the echoes present reached maximum areas less than 31 km^2. These distributions range from 80% for the low cloud level to approximately 35% for the middle and high level clouds, for an average of approximately 55-60%. Houze and Cheng (1977) also found that small echoes less than 100 km^2 dominated the total number of echoes.

The area distributions shown in Figures 14, 15, 16, and 17 are strongly skewed towards the right, or the largest cloud sizes. The peak for the low clouds continues to shift further to the right until 180000, when it shifts back slightly to the left. The bimodal peaks of the middle cloud level shift among the four or five largest cloud size intervals, with no apparent pattern. The high cloud level, which also tends to be bimodal, shifts slightly to the left at 120000, then increasingly shifts to the right at the later hours. These skewed distributions also agree with Lopez (1976), who found that the largest 20% of the radar echoes accounted for about 67% of all shower-covered area, and Houze and Cheng (1977), who found that large echoes (greater than 1000 km^2) accounted for most of the area covered by precipitation. Although radar echoes only analyzed convective patterns, the concept of a few large clouds accounting for most of the areal coverage remains consistent in the much broader view of all clouds presented in this paper.

B. Diurnal Variations

The existence of a diurnal variation in deep cumulus convection led to the examination of the middle and high cloud levels. An apparent diurnal change in the total cloudiness of these levels is present. Brightness norm-

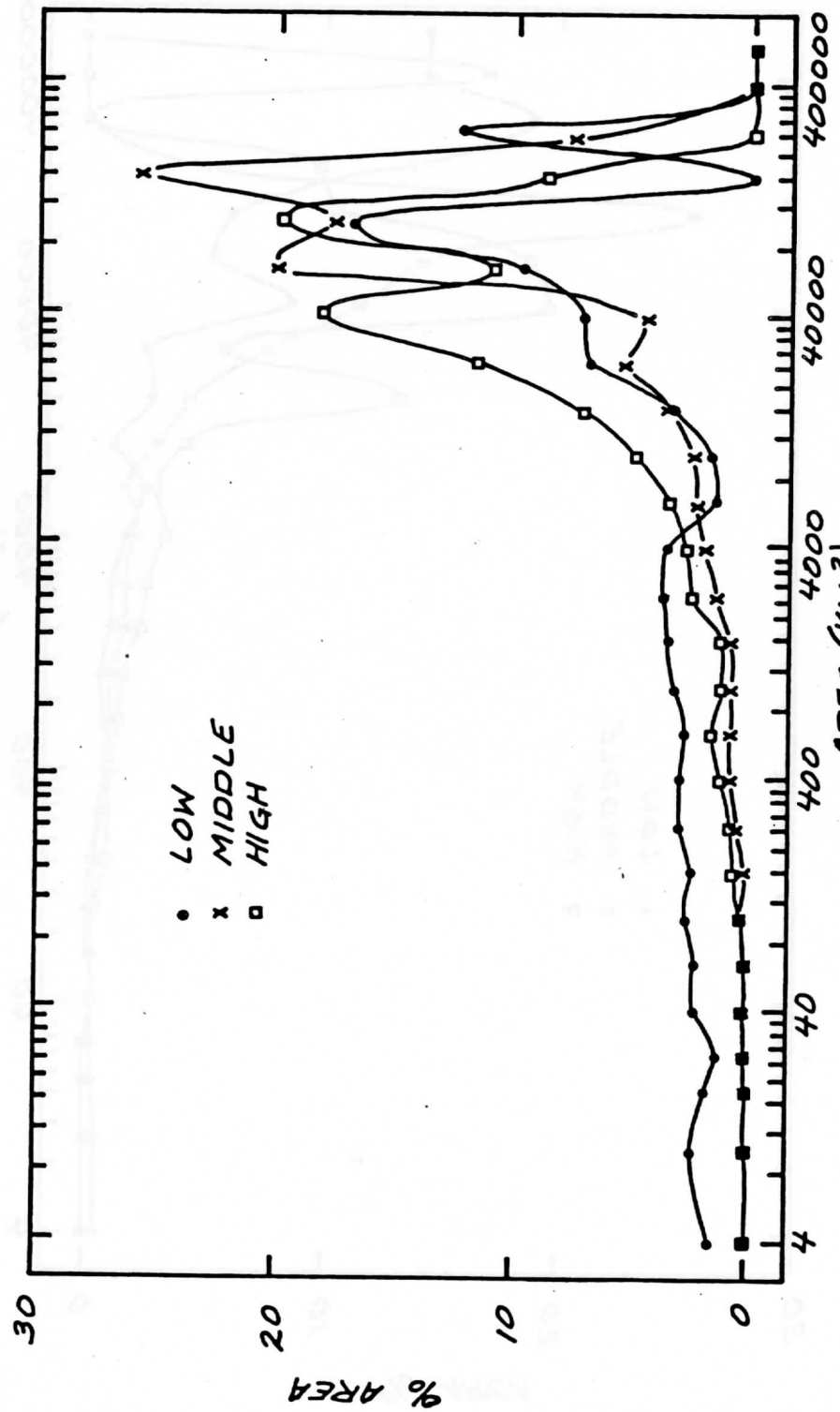

FIGURE 14. Percent of the total area covered at each cloud level by all cloud size intervals for eight day composite at 90000 GMT.

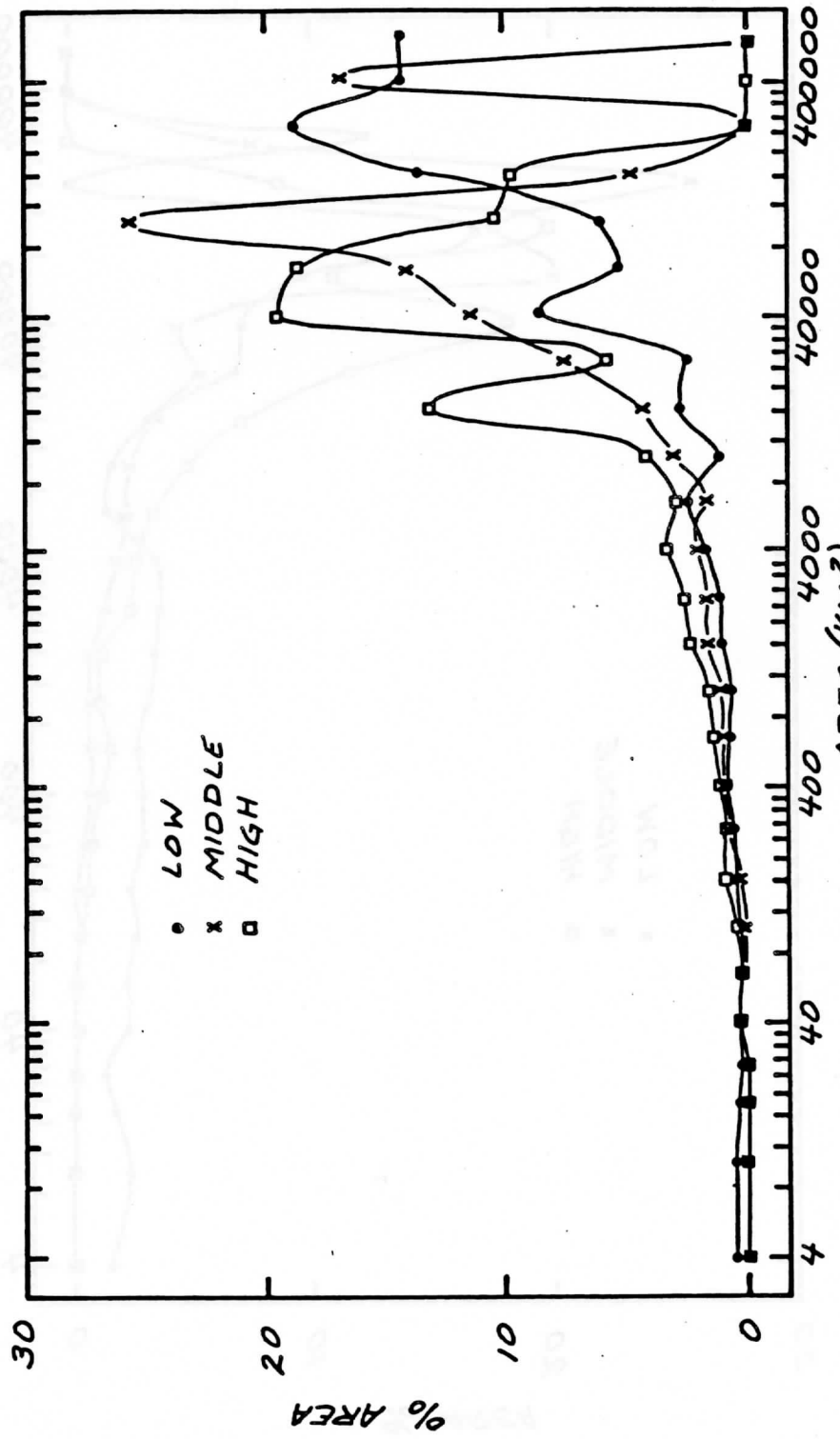

FIGURE 15. Percent of the total area covered at each cloud level by all cloud size intervals for eight day composite at 120000 GMT.

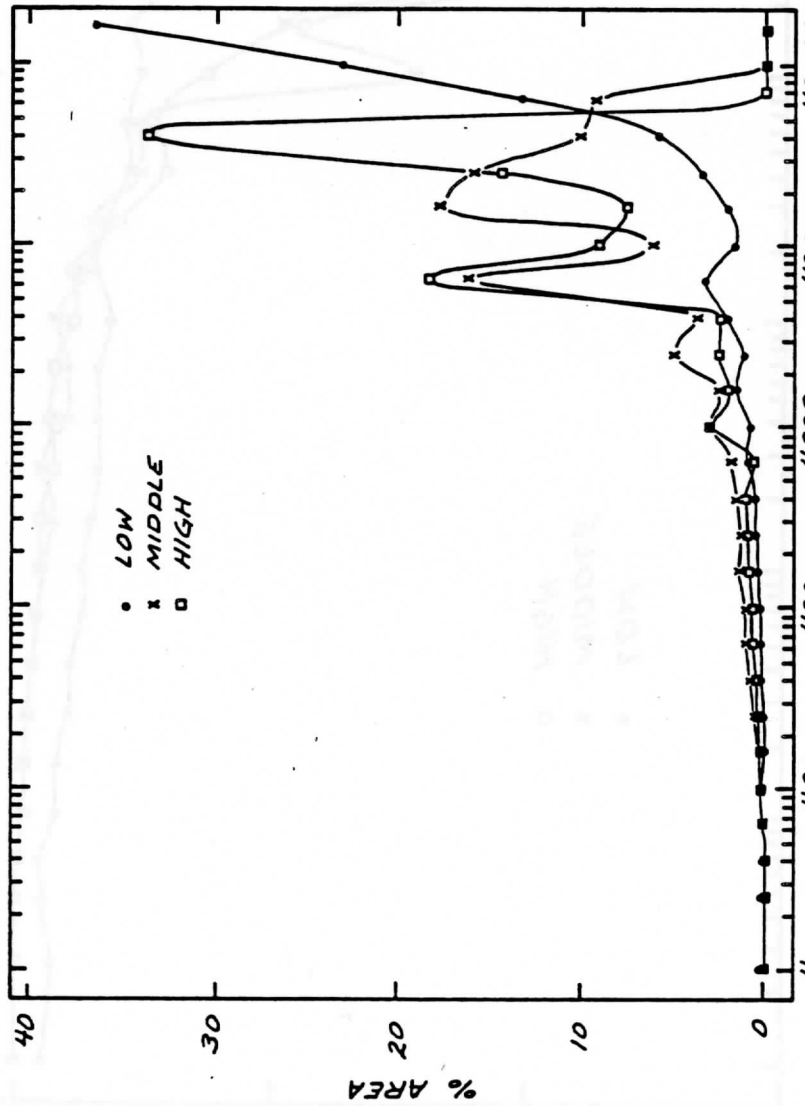

FIGURE 16. Percent of the total area covered at each cloud level by all cloud size intervals for eight day composite at 150000 GMT.

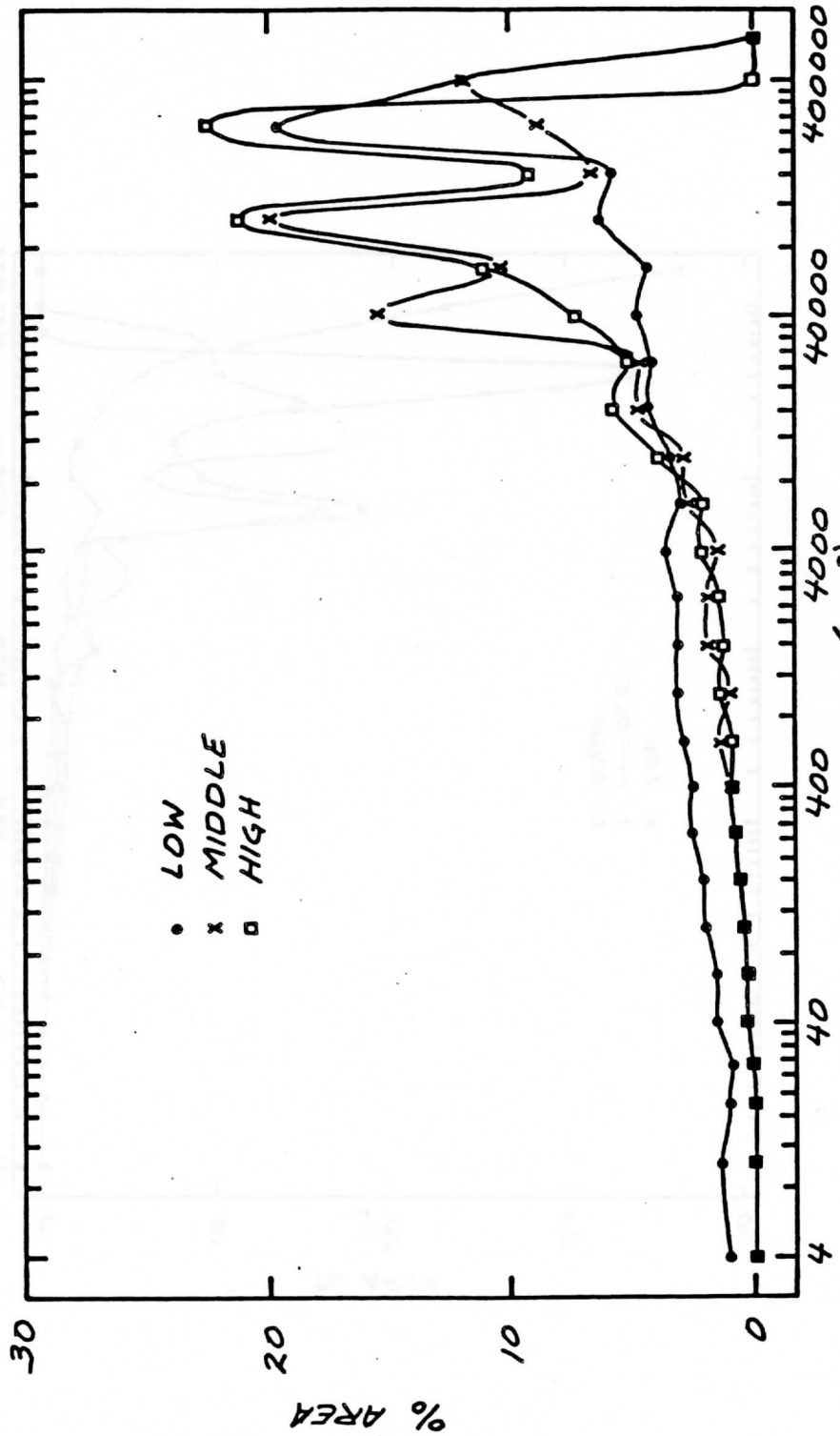

FIGURE 17. Percent of the total area covered at each cloud level by all cloud size intervals for eight day composite at 180000 GMT.

alization was not used in the determination of the total middle and high level cloudiness; therefore, the apparent diurnal change was not an effect of the normalization process. Figure 18 presents the eight day average of the high and middle level cloudiness over the four main time periods. There is a minimum in the amount of high level cloudiness at 120000 (110000 LT), increasing to a maximum at 180000 (170000 LT). The middle level has a maximum at 90000 (80000 LT) and a minimum at 150000 (140000 LT). Both cloud levels show a 5% change in the nine hour period. Figure 19 presents the eight day average of the high and middle level thick cloudiness. Both curves are the same shape, and have a slight peak at 150000 (140000 LT). The overall change in thick cloudiness is approximately 2% for both levels. Thus, it appears that there exists a continuous amount of deep convective activity while the outflow from the deep cores "breathes" over the course of the day. That is, the thick convective cores remain fairly constant while the cirrus shield resulting from increasing (decreasing) convective activity expands (contracts).

In order to better examine this diurnal change, the program was run for GATE days 245, 246, and 247 at 000000, 30000, 60000, and 210000 GMT (230000, 20000, 50000, and 200000 LT) on the infrared image only. Since there was no visible image available, only the total cloudiness could

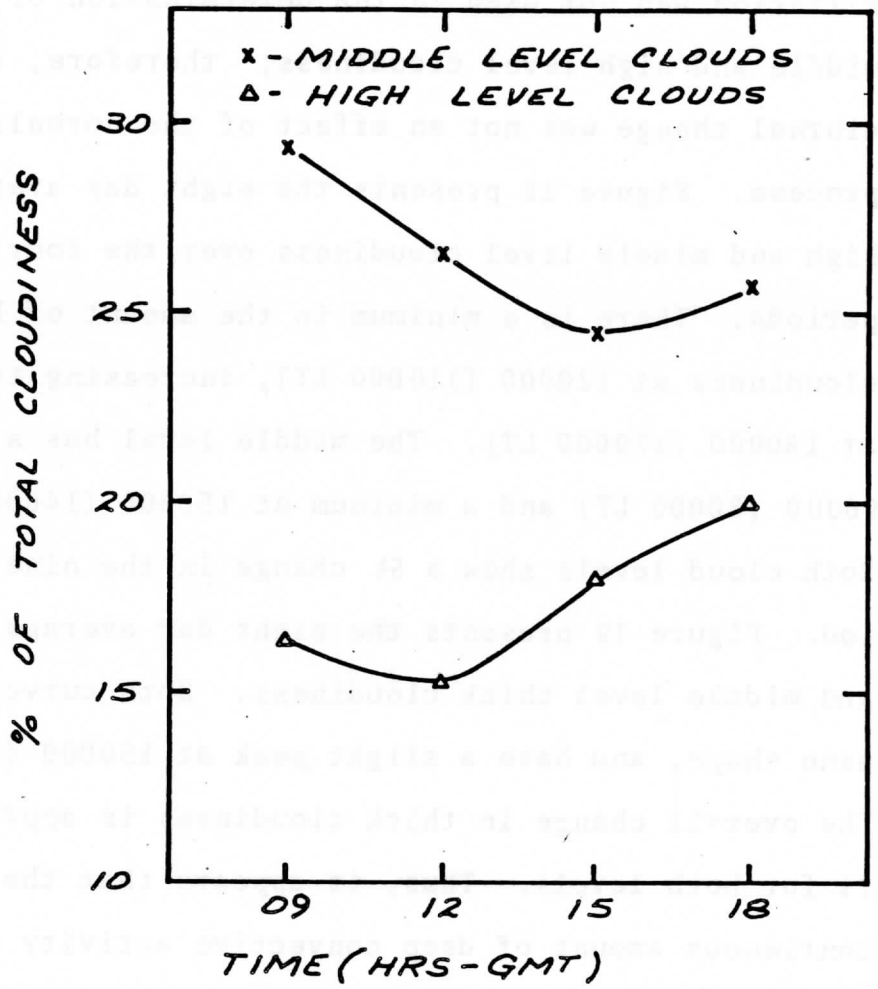

FIGURE 18. Percent of total cloudiness as a function of time for eight day composite.

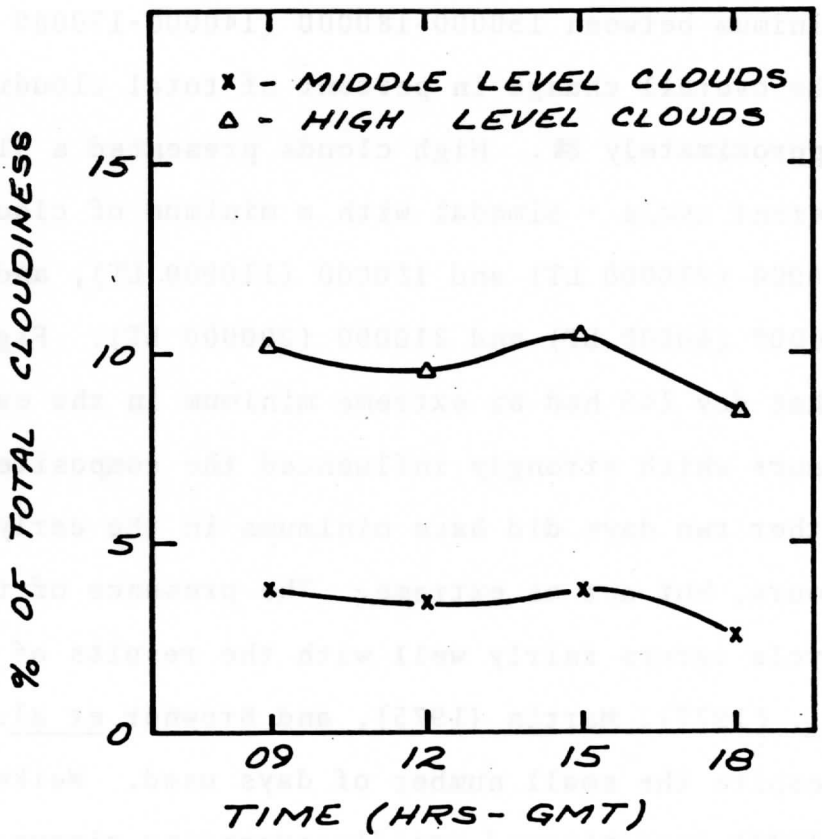

FIGURE 19. Percent of total thick cloudiness as a function of time for eight day composite.

be calculated. Thick clouds could not be analyzed. For these three days, the middle clouds showed a distinct cycle, with a maximum in the very early morning hours, and a minimum between 150000-180000 (140000-170000 LT) hours. The overall change in percent of total cloudiness was approximately 8%. High clouds presented a slightly different cycle - bimodal with a minimum of cloudiness at 00000 (230000 LT) and 120000 (110000 LT), and a maximum at 90000 (80000 LT) and 210000 (200000 LT). Figure 20 shows that day 245 had an extreme minimum in the early morning hours which strongly influenced the composite graph. The other two days did have minimums in the early morning hours, but not as extreme. The presence of this diurnal cycle agrees fairly well with the results of Weikmann et al. (1977), Martin (1975), and Browner et al. (1977), despite the small number of days used. Weikmann et al. (1977) investigated rapidly expanding cirrus shields of cloud clusters within and surrounding the GATE A-B array during GATE with use of geosynchronous satellite data. Nearly twice as many of these rapidly expanding cluster cases occurred between 2300-600 LT as compared with 600-1300 LT or 1300-2000 LT. Martin (1975) has indicated that the time of initial appearance of cloud clusters that later cover an area of more than 1 X 1 degrees in the eastern tropical North Atlantic during the GATE period

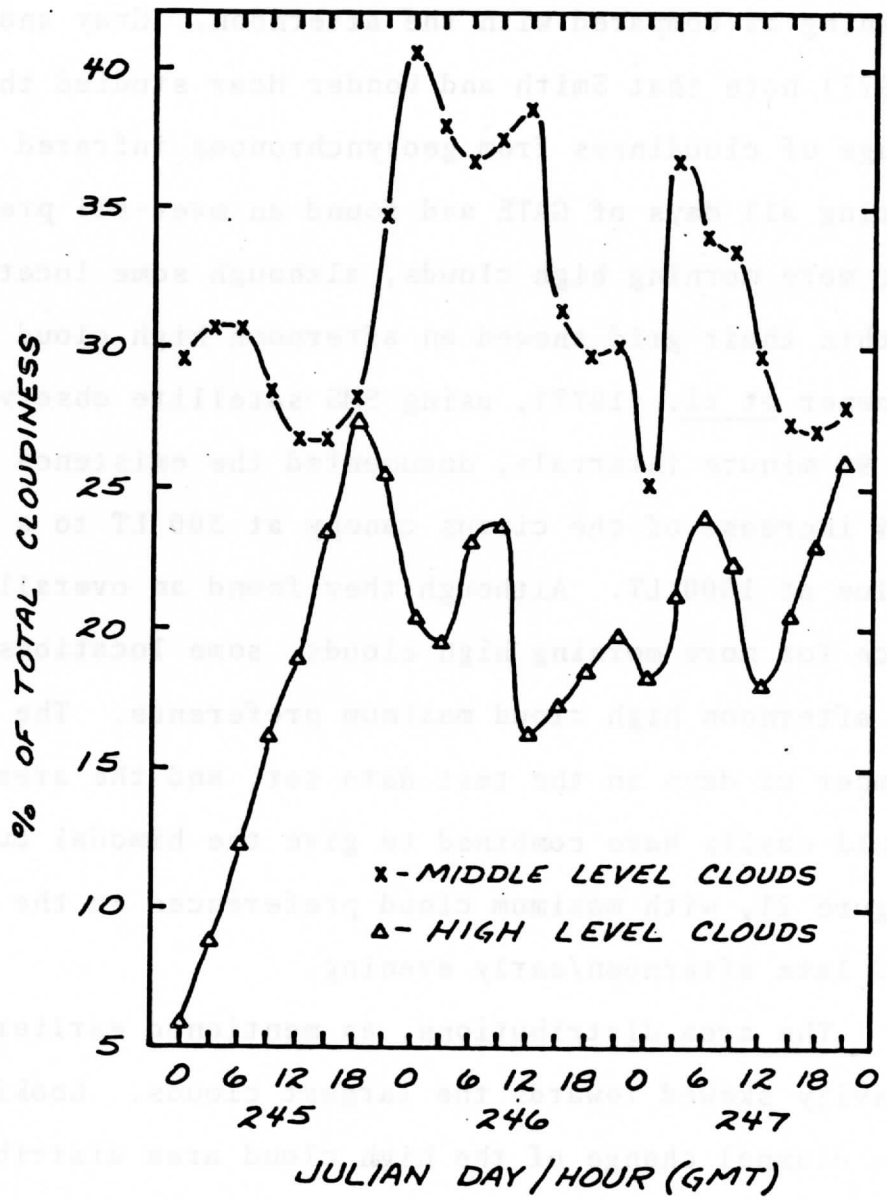

FIGURE 20. Percent of total cloudiness as a function of time for September 2, 3 and 4, 1974.

was nearly twice as frequent during the evening and early morning as compared with the afternoon. Gray and Jacobson (1977) note that Smith and Vonder Haar studied the diurnal range of cloudiness from geosynchronous infrared data during all days of GATE and found an over-all preference for more morning high clouds, although some locations within their grid showed an afternoon high cloud maximum. Browner et al. (1977), using SMS satellite observations at 90 minute intervals, documented the existence of a 50-75% increase of the cirrus canopy at 300 LT to a maximum value at 1500 LT. Although they found an overall preference for more morning high clouds, some locations showed an afternoon high cloud maximum preference. The limited number of days in the test data set, and the area covered could easily have combined to give the bimodal curve of Figure 21, with maximum cloud preferences in the morning and late afternoon/early evening.

The area distributions, as mentioned earlier, are heavily skewed towards the largest clouds. Looking at the diurnal change of the high cloud area distributions in Figure 22 reveals a change in the position of the peak that corresponds to the diurnal change in the total high cloudiness. The small cloud size percentages remain fairly constant. Therefore, the few very large clouds exhibit the "breathing" mentioned earlier.

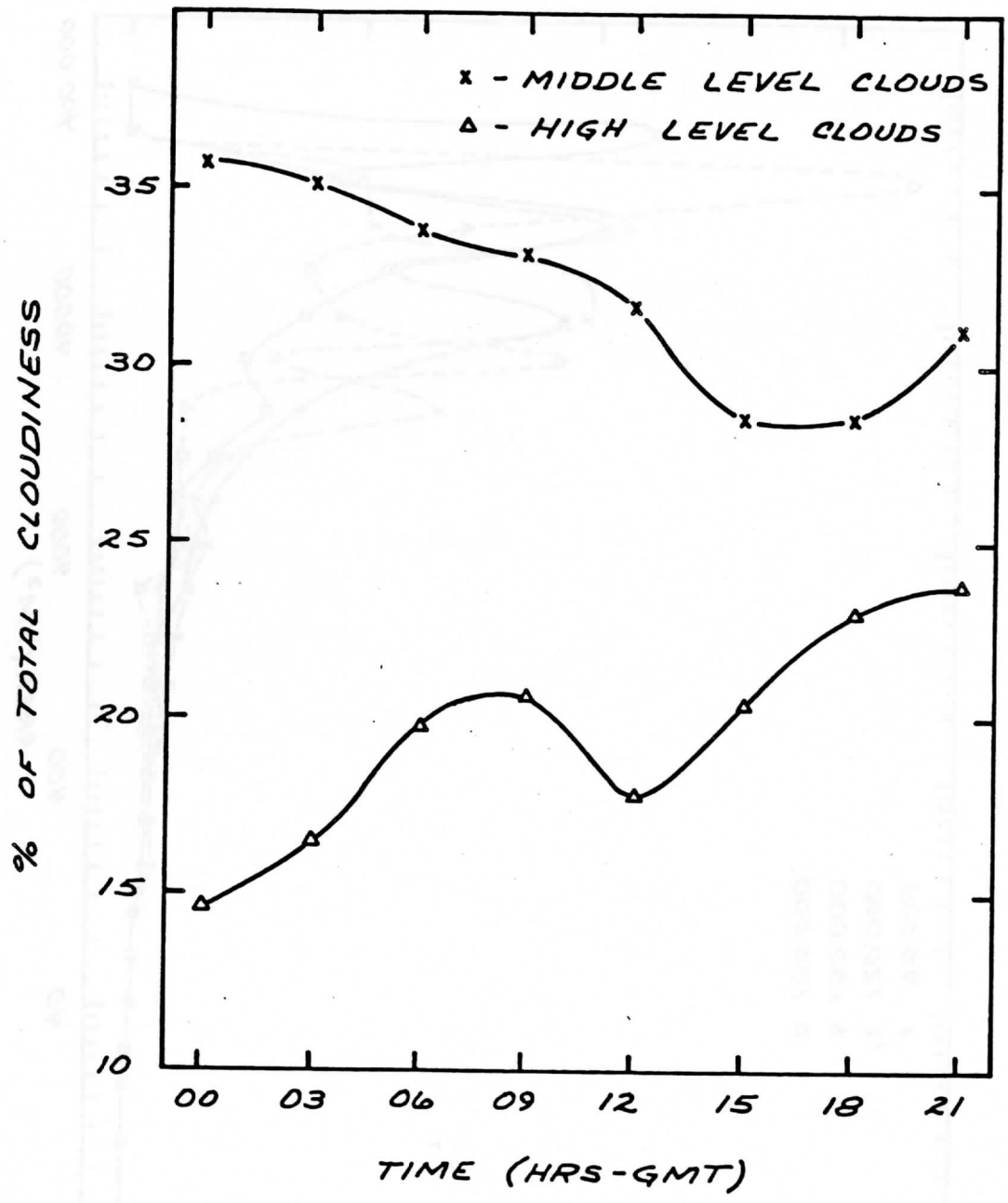

FIGURE 21. Percent of total cloudiness as a function of time for a composite of days September 2, 3, and 4, 1974.

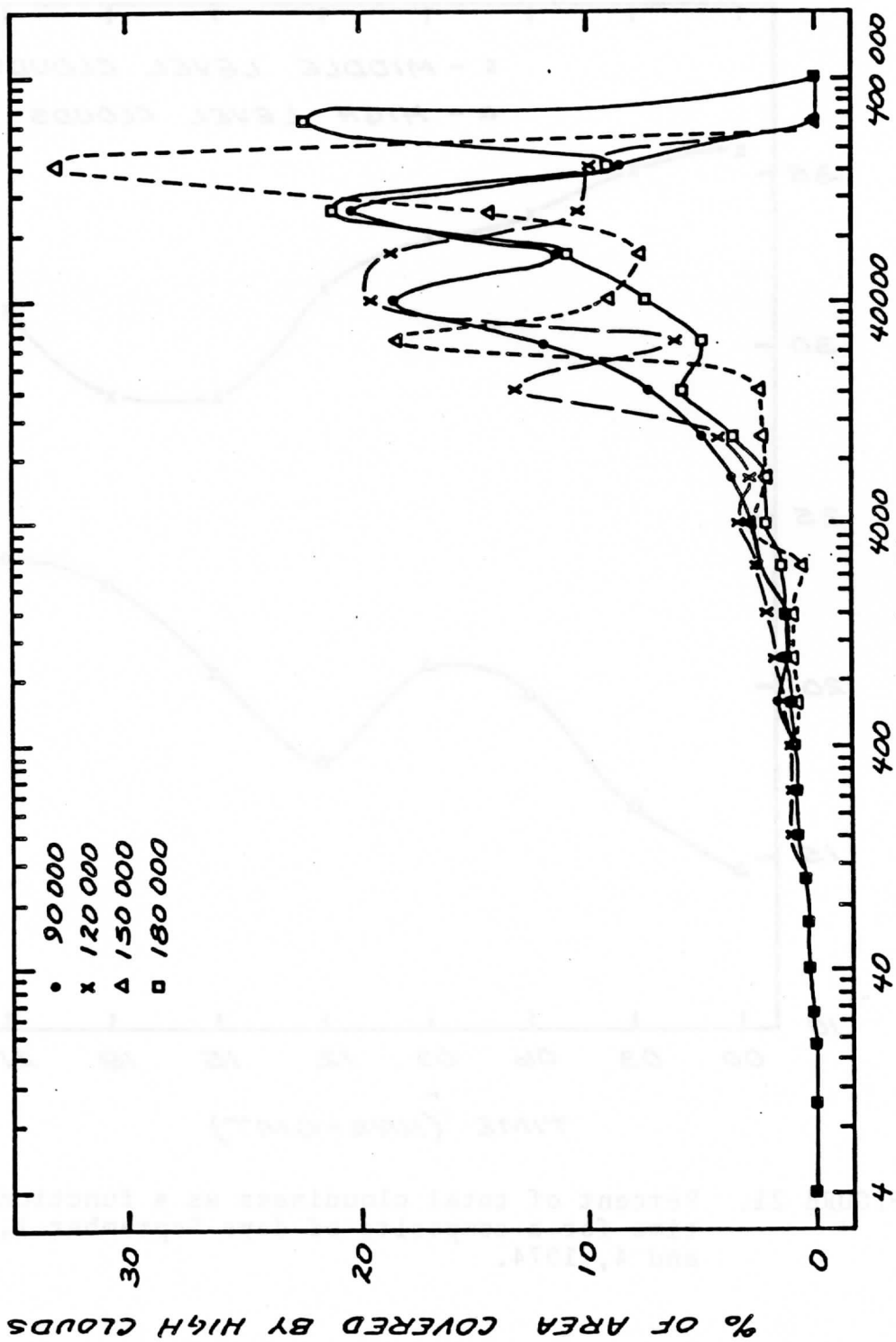

FIGURE 22. Percent of area covered by high clouds for all cloud size intervals, as a function of time for eight day composite.

C. Visible Thresholds

The values of total cloudiness presented in Table 1 show total cloudiness ranging from 50 - 97%. Holle et al. (1977) showed total cloudiness for the GATE Phase III area ranging from 60 - 85%. This is fairly good agreement considering the area covered by this study is about six times greater than that covered in Holle's study. In all cases, the total cloudiness at 120000 and 150000 is often 10-20% greater than that at 90000 and 180000. This increase occurs specifically in the low cloud level. A look at the sensitivity of an absolute visible threshold which was used in the determination of low level clouds is necessary. As mentioned earlier, the cloud typing algorithm used was a simpler model than many now available, and the results presented here reinforce the fact that the use of an absolute visible brightness threshold for cloud/no cloud recognition will not produce accurate results for all time periods. The visible threshold calculated for areas away from the influence of sunglint account for the sea surface albedo and rayleight scattering for a clear atmosphere. The coefficients do not account for the presence of dust or sub-resolution cloud fields.

To test the sensitivity of the visible brightness threshold for low clouds, the calculated threshold was

Table 1

Percent of total cloudiness

Julian Day	Time (GMT)	Level Low	Middle	High	Total
245	90000	13.6	28.5	16.3	58.4
	120000	35.5	26.8	18.9	81.2
	150000	38.8	26.9	23.6	89.4
	180000	19.2	28.2	27.7	75.1
246	90000	13.5	37.5	23.7	74.8
	120000	33.3	38.6	16.2	88.1
	150000	48.6	31.4	17.3	97.2
	180000	22.9	29.9	18.4	71.2
247	90000	16.2	33.6	22.3	72.1
	120000	44.2	29.8	18.1	92.1
	150000	47.8	27.2	20.5	95.5
	180000	27.1	27.1	23.0	77.2
248	90000	26.4	26.3	9.6	62.3
	120000	60.1	18.4	6.8	85.4
	150000	62.2	14.8	8.4	85.3
	180000	37.8	16.6	11.1	65.5
249	90000	20.4	18.2	13.6	52.1
	120000	47.0	20.3	13.3	80.5
	150000	53.6	22.6	14.9	91.1
	180000	29.9	24.7	15.2	69.8
250	90000	18.0	25.8	11.2	55.0
	120000	45.9	24.5	11.5	82.1
	150000	53.2	24.7	16.1	94.0
	180000	23.5	27.3	19.4	70.2
251	90000	14.7	29.9	16.4	60.9
	120000	38.8	26.7	18.0	83.6
	150000	48.4	23.7	22.4	94.5
	180000	19.7	26.6	22.1	68.3
252	90000	11.5	35.1	20.2	66.8
	120000	36.3	28.4	19.2	83.9
	150000	41.2	23.8	22.1	87.2
	180000	14.9	25.0	23.2	63.0

increased by 8, 12, 16, 20 and 24 absolute brightness counts and the program rerun for GATE day 245 at 150000. The maximum addition of 24 counts lifted the brightness threshold close to the level suggested by Cox and Griffith. As can be seen in Table 2, the overall cloudiness dropped about 2-3% with each addition to the visible brightness threshold. That is a drop of about 33% in low cloudiness. As shown in Table 2, the program was also rerun for other days, with the maximum addition of 24 counts. On some of the days, a drop of 50% in low level cloudiness occurred.

In Figure 23, the area distributions for the original threshold, and 8, 16 and 24 counts added to the threshold are plotted. All traces are strongly skewed to the right, but the peak drops steadily to smaller area intervals. There was little change in the very small cloud size intervals. In Figure 24, the cloud size frequency distributions are plotted for the original distributions, and 8, 16 and 24 counts added to the original threshold. The shape of the distributions remain almost constant. It appears, then, that small changes in the visible brightness threshold do not greatly change the cloudiness, but larger brightness changes do result in significant changes in the total cloudiness, and especially in the total low level cloudiness.

Table 2

Low level cloudiness

Julian Day	Time (GMT)	Brightness counts Added to threshold	Percent Cloudiness
245	150000	0	38.8
		8	36.7
		12	34.2
		16	31.8
		20	29.2
		24	26.8
246	150000	0	48.6
		24	23.1
248	150000	0	62.2
		24	32.5
249	150000	0	53.6
		24	30.2

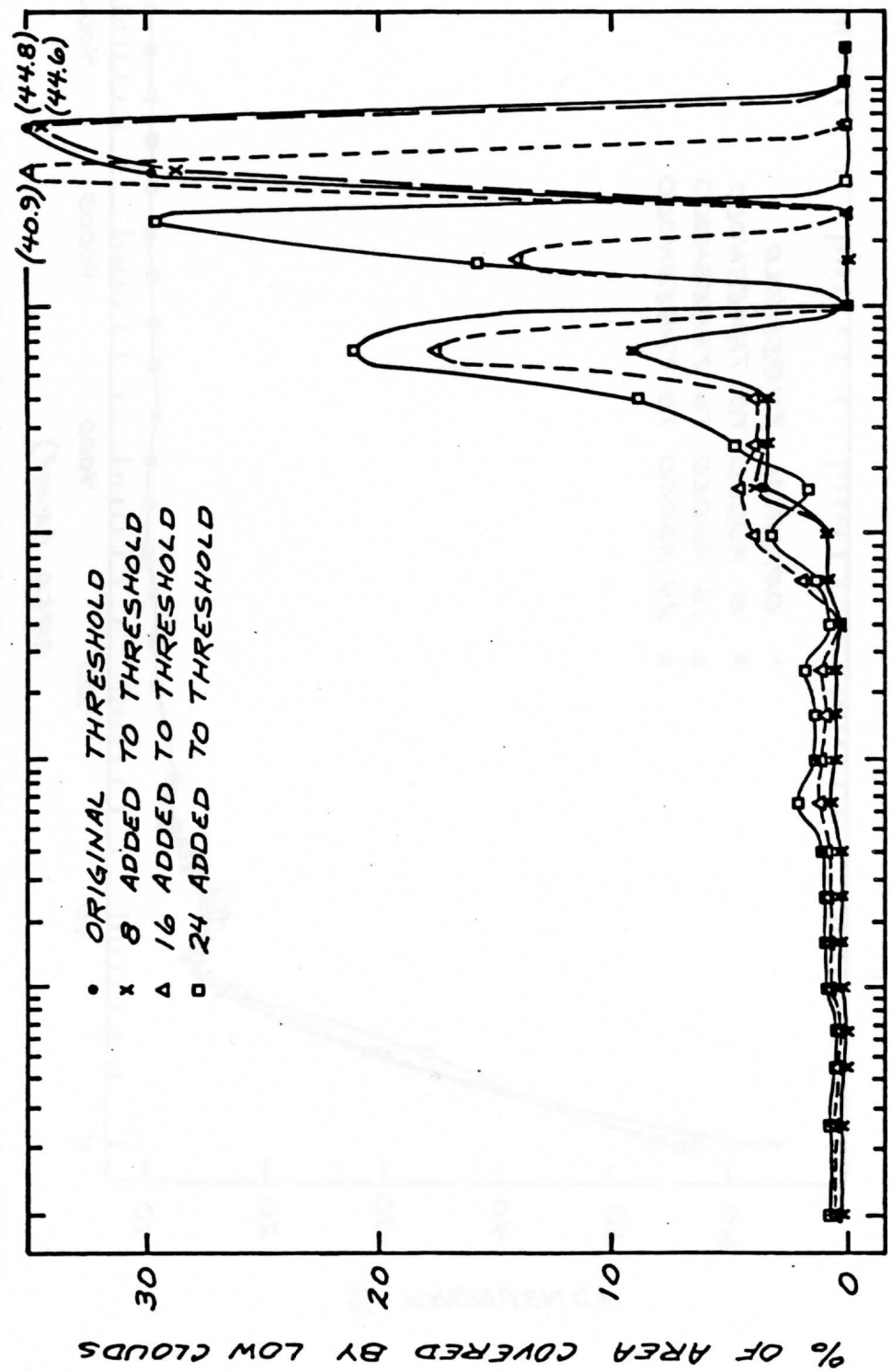

FIGURE 23. Percent of area covered by low clouds for all cloud size intervals, for September 2, 3 and 4, 1974.

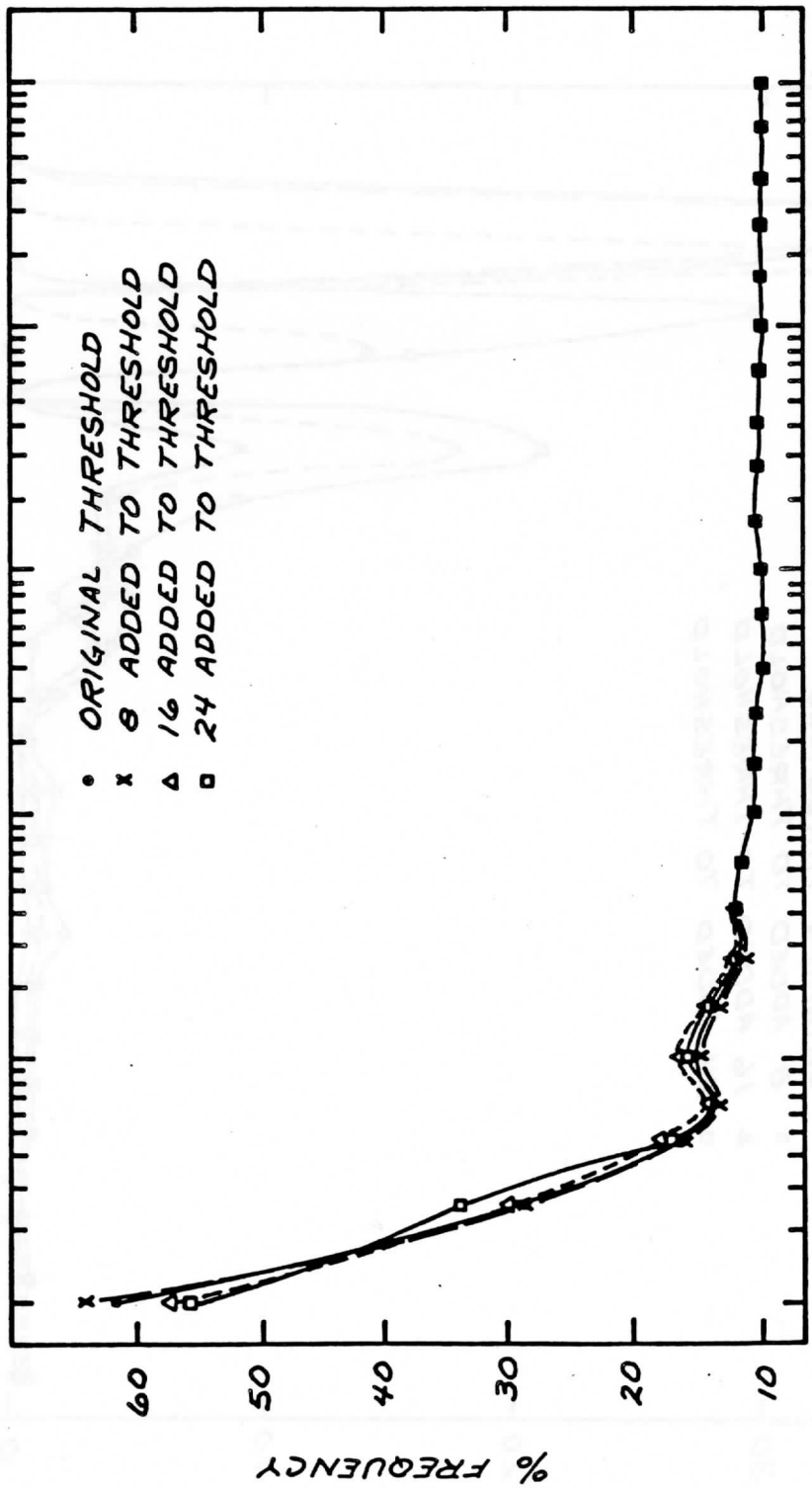

FIGURE 24. Frequency distributions of cloud sizes for September 2, 3, and 4, 1974 at 150000 GMT.

6. Conclusion

An objective technique utilizing geosynchronous orbiting satellite digital data has been presented here. Using a visible and an infrared image as input, cloud types have been discriminated, and the cloud populations measured and analyzed from a sample data set. It was found that small clouds dominated the total number of clouds, while the large clouds accounted for most of the area covered by clouds. This is in good agreement with Lopez (1976) and Houze and Cheng (1977). Analysis of the high cloud populations showed evidence of a diurnal cycle of high cloudiness, with a minimum in the early morning hours and maximum in the late afternoon and early evening. The diurnal change of the size of thick high clouds was minimal, suggesting that the area covered by the deep cores of convective activity remained somewhat constant, while the intensity of the convective activity itself increased in the mid morning hours, resulting in greater upper level outflow and increased high cloudiness in the late afternoon. This is in agreement with the results of Martin (1975), Weikmann et al. (1977) and Browner et al. (1977).

The cloud typing technique used in this program was similar to that used by Koffler et al. (1973), with the additional use of an absolute visible threshold in deter-

mining the presence of low clouds. This resulted in errors due to the presence of sunglint, aerosols in the atmosphere and sub-resolution cloud fields. More sophisticated cloud typing techniques available could be incorporated into this program, resulting in a greater resolution of cloud types and eliminating some problems such as mixed cloud fields, which were not aken into account in this study. In addition, the use of higher resolution images would help eliminate the problem of sub-resolution cloud fields. This would significantly increase the number of small clouds but would have a minor effect on the area distributions of the cloud populations.

The use of a normalized visible brightness threshold in determining thick clouds appeared to be successful, the calculated value in agreement with Stout et al. (1979) and the normalized curve in agreement with the results of Mosher (1979).

The good agreement of these results with other studies offers encouraging support for the objective cloud analysis technique presented here. This is a positive first step towards the use of an objective program for cloud population studies over large areas. In future studies, the technique may be extended for use over land as well as oceanic regions, resulting in a global cloud population data set.

Bibliography

Browner, S., W.L. Woodley and C.G. Griffith, 1977: Diurnal oscillation of the area of cloudiness associated with tropical storms. Mon. Wea. Rev., 105, 856-864.

Cox, S.K. and K.T. Griffith, 1979: Estimates of radiative divergence during Phase III of the GARP Atlantic Tropical Experiment: Part I. Methodology. J. Atmos. Sci., 36, 576-585.

Gray, W.M. and R.W. Jacobson, Jr., 1977: Diurnal variation of deep cumulus convection. Mon. Wea. Rev., 105, 1171-1188.

Greaves, J.I. and D. Chang, 1970: Technique development to permit optimum use of satellite radiation data. Final Report, N62306-69-C-022, Allied Research Associates, Inc., Concord, MASS.

Holle, R.L., 1968: Some aspects of tropical oceanic cloud population, J. Appl. Meteor., 7, 173-183.

Holle, R.L., S. Leavitt, J. Simpson, R. Biondini, and J. Snow, 1977: Cloudiness from whole-sky pictures taken aboard 4 U.S. B-scale ships. Scientific report to the National Science Foundation. Dept. of Environmental Sciences, University of Virginia, Charlottesville, VA.

Houze, R.A. and C. Cheng, 1977: Radar characteristics of tropical convection observed during GATE: Mean properties and trends over the summer season. Mon. Wea. Rev., 105, 964-980.

Kaveney, W.J., R.G. Feddes, K. Kiou, 1977: Statistical inference of cloud thickness from NOAA 4 scanning radiometer data. Mon. Wea. Rev., 105, 99-107.

Koffler, R., A.G. DeCotiis, P. Krishna Rao, 1973: A procedure for estimating cloud amount and height from satellite infrared radiation data. Mon. Wea. Rev., 101, 240-243.

Kornfield, J.I., 1973: On the determination of sea surface wind or stress from sun glint observed by an earth synchronous satellite. Ph.d thesis, University of Wisconsin, Madison, WI.

Lopez, R.E., 1976: Radar characteristics of the cloud populations of tropical disturbances in the Northwest Atlantic. Mon.Wea.Rev., 104, 268-283.

Martin, D.W., 1975: Characteristics of West African and Atlantic cloud clusters. GATE Rep. No. 14, 182-190.

Mosher, F.R., 1979: Visible flux variations across finite clouds. Ph.d thesis, University of Wisconsin, Madison, WI.

Norton, C.C., F.R. Mosher, B. Hinton, D.W. Martin, D. Santek, and W. Kuhlow, (to be published): A model for calculating desert aerosol turbidity over the oceans from geostationary satellite data. J. Appl. Meteor.

Plank, V.G., 1969: The size distribution of cumulus clouds in representative Florida populations. J. Appl. Meteor., 8, 46-67.

Shenk, W.E., R.J. Holub, and R.A. Neff, 1976: A multispectral cloud type identification method developed for tropical ocean areas with Nimbus-3 MRIR measurements. Mon. Wea. Rev., 104, 284-291.

Smith, E. and T.H. Vonder Haar, 1976: Hourly synchronous meteorological satellite-1 (SMS-1) data collected during the GARP Atlantic Tropical Experiment (GATE): Earth located edited data set. Paper no. 291, Dept. of Atmospheric Science, Colorado State University, Fort Collins, Colorado.

Stout, J.E., D.W. Martin, and D.N. Sikdar, 1979: Estimating GATE rainfall with geosynchronous satellite images. Mon. Wea. Rev., 107, 585-598.

Weickmann, H.K., A.B. Long, and L.R. Hoxit, 1977: Some examples of rapidly growing oceanic cumulonimbus clouds. Mon. Wea. Rev., 105, 469-476.

Line Segment Histograms as Part of the Real-Time Satellite-Derived Cloud Climatology

Frederick R. Mosher

Space Science and Engineering Center
University of Wisconsin-Madison
1225 West Dayton Street
Madison, Wisconsin 53706

Line Segment Histograms as Part of the Real-Time Satellite-Derived Cloud Climatology

Frederick R. Mosher
Space Science and Engineering Center
University of Wisconsin - Madison

I. Introduction

Cloud spacial structure is an important parameter which needs to be considered as part of a global cloud climatology program in addition to the cloud's radiative properties. One of the specific requirements of the Oxford (1978) JOC Study Conference on the Parametrization of cloudiness and Radiation for Climate Models was that the cloud climatology include information on cloud size frequency distributions. The Meeting of Representatives of Agencies on the Real-Time Satellite-Derived Cloud Climatology (Balatonalmadi, Hungary, 1980) recommended that histograms of line segment lengths of cloud elements be used to meet this requirement of cloud size distributions. They recommended that a pilot study be undertaken to determine how thresholds would be defined, the amount of data generated, and how the cloud size distribution information can be extracted. This paper is in response to this request for a pilot study.

II. Line Segment Histograms

The real time satellite derived cloud climatology project plans to use several international data procedures to process geostationary satellite data into compacted cloud statistics. An implicit requirement of the data processing system is that all the global processing can be done in real time using modest computer capabilities. This excludes many of the traditional methods of cloud size distribution, such as two dimensional fourier transforms, edge tracing, etc., which require large computers with large amounts of memory. The geostationary satellite data all come from scanning radiometers which transmit one scan of data across the full width of the

earth at a time. A single full earth image of the GOES data represents over 200 megabytes of data. The only way modest computers can process this volume of data in real time is to process one line a time using simple computational algorithms. The line segment histogram techniques should be suitable for processing in real time using modest computers.

A. Threshold Determination

The line segment histogram technique first requires a predetermined cloud/no cloud brightness threshold. When the data exceeds this threshold, a counter is started which counts the number of pixels until the threshold is crossed again in the other direction at the end of the cloud segment. The line segment length information from the counter is stored in a histogram of segment lengths and the process repeated. Since clouds have an approximate log-normal cloud size distribution, the histogram should have a logrithmic length scale to limit the number of size bins to manageable quantities.

The determination of the cloud/no cloud thresholds for line segments is the same problem faced in determining fractional cloud cover using threshold techniques. If one knows the surface brightness (or temperature in the infrared) anything brighter than the surface can be considered covered by cloud. One method of determining the surface brightness is to use a minimum brightness composite. Since the geostationary data is relatively noise free, a minimum brightness composite can be used to determine the surface brightness. A sequence of aligned images are composited using the minimum brightness of each pixel in the sequence. Since the clouds move, but the land doesn't, this is a composite of the holes between the clouds. Figure 1a. shows a visible minimum brightness composite for the month of March 1978 at 18Z. The bright areas around Lake Michigan are snow and ice. Figure 1b shows an infrared minimum brightness composite

for the same time period. The infrared composite is of the warmest temperatures experienced at that time of day during the month. The minimum brightness composites should be made using a sequence of images from the same time of day. This keeps the sun angle constant for the composite visible, and also minimizes the diurnal variations in temperature for the composite infrared image. The time period of the composite should be between five days and one month. The Air Force 3D NEPH analysis using a running 5 day minimum composite. A 5 day composite is adequate to remove clouds from areas of variable weather, but still has some cloud contamination in areas of persistant cloudiness. A one month composite is generally able to remove the clouds from all regions.

One of the problems with a minimum brightness composite is the delination of snow fields which are either created or melt during the time period of the composite. The composite give only the snow fields which are persistant the entire time period. Changing boundaries of snow fields can be interpretated as clouds. If one decreases the time period of the composite to account for these changing snow fields, then areas of persistant cloudiness can be interpretated as being snow fields. Another problem with the infrared composite is that the surface temperature has a larger time variation than does the surface albedo. A 20°C variation of surface temperature for a given time of day is not uncommon over land areas during a month's interval, particularly during the spring and fall. This means that a large delta above the minimum brightness threshold needs to be used in the cloud/no cloud determination to minimize detecting cold land. This can mean that low clouds can be missed in the cloud/no cloud determination. An example of the use of the minimum brightness composite is shown in Figure 2a and b. Figure 2a shows the visible satellite image for March 16. Figure 1a is the visible minimum brightness composite used. Figure 2b shows the clouds which are brighter than the minimum brightness

+12 counts (out of a range of 0-255). Comparisons with airport observations of cloud cover show very good agreement with the satellite determined cloud field except in western Wisconsin which had a snow cover (which melted before the end of the month) which was interpretated as cloud.

The fractional cloud cover determination does not appear to be extremely sensitive to the delta above the minimum brightness composite used to determine the cloud/no cloud threshold. For the data in Figure 2, a delta of 12 resulted in a 69% fractional cloud cover for the area. A delta of 16 resulted in 65%, and a delta of 20 resulted in 62%. For the infrared minimum composite, a delta of 25 (in this range, 1 count=.5°C) resulted in a computed 72% fractional cloud cover. However an analysis of the computed cloud cover showed that some colder land was being counted as cloud. A delta of 30 produced a 66% cloud cover, with a small amount of land incorrectly classifed as cloud. A delta of 40 produced a 53% cloud cover. No land was called cloudy but some of the low clouds were not counted.

B. Line Segment Histograms

The line segment histogram technique was used on several sample areas, and the results compared for visible infrared techniques, and infrared only. The line segment histograms were generated for both high and low clouds. Figure 3 shows one of the areas used for these studies. It is of cellular strata cumulus clouds over the south Atlantic. The clouds were all low in this case. The visible threshold computed a 66% fractional cloud cover while the infrared computed a 59% cloud cover. Figure 4 shows the percent of the computed fractional cloud cover as function of line segment length. The solid lines are for the infrared and the dashed are for the visible. The two kinds of data both indicate that the larger clouds account for most of the cloud area. A comparison of the one dimensional line segment results with a program which computes a two dimensional

cloud size distribution shows that line segment correctly identify the major size properties, but that the line segment histograms tend to spread a two dimensional peak over several line size intervals.

Figure 5 shows the percent of the number of clouds as function of line segment length. The infrared only is the solid line, while the visible is the dashed. The visible data showed that the largest number of clouds were small. This agreed well with the two dimensional results. The infrared missed many of the smaller clouds. This is primarily because the smaller clouds were had temperatures very close to the sea surface temperature.

The brightness of the clouds showed a dependence on the size of the clouds. Figure 6 shows the average visible brightness of the clouds in Figure 3 as a function of line segment length with the solid line. The dashed line is for the low clouds in another region in the ITCZ which had both deep correction and small cummulus clouds. The size of each is about 4 km, so the length scales ranged from 4 km to 1200 km. The figure shows that the larger clouds are significantly brighter. This relationship holds for different types of clouds as is shown by the dashed line. This brightness dependence on cloud scale size is not explained by radiative transfer theory alone. Finite cloud effects in multiple scattering are significant up to optical thickness of 100-500 (in the order of 2 to 50 km at most). The observed brightness dependence in Figure 6 suggests that the larger clouds are either thicker or have an increased liquid water content.

The data volume which is required to store the line segment histograms is minimal. In this study a logarithmic bin size was used successfully. Thirty size bins were used in this study, but it appears that half that number would

be sufficient. The high clouds showed different cloud size characteristics than the low clouds, so separate histograms should be saved for both the high and low clouds. Use of a cumulative frequency histogram for storage of the histogram information with 6 bits/interval makes 15*6 = 90 bits/histogram plus the total number of clouds (16 bits) and the fractional cloud cover for high (8 bits) and low clouds makes a total of 212 bits of data storage required for each data area.

figure 1a
Visible minimum brightness composite for the month of March, 1978 at 18Z.

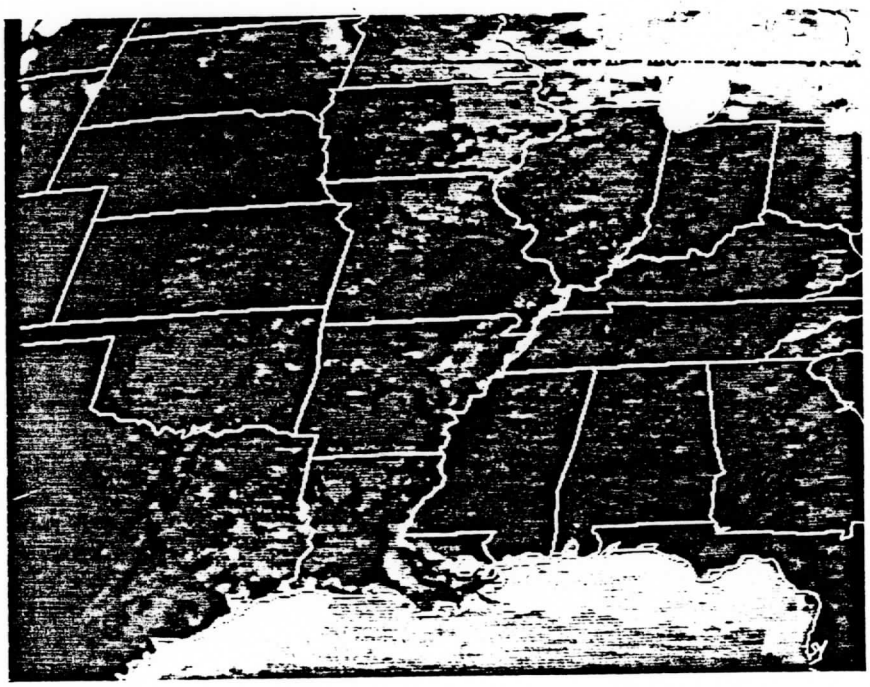

figure 1b
Infrared minimum brightness for the same time period.

figure 2a
Visible geostationary satellite image for March 16, 1978.

figure 2b
Clouds from fig. 2a which are 12 counts brighter then the ground as determined in 1a.

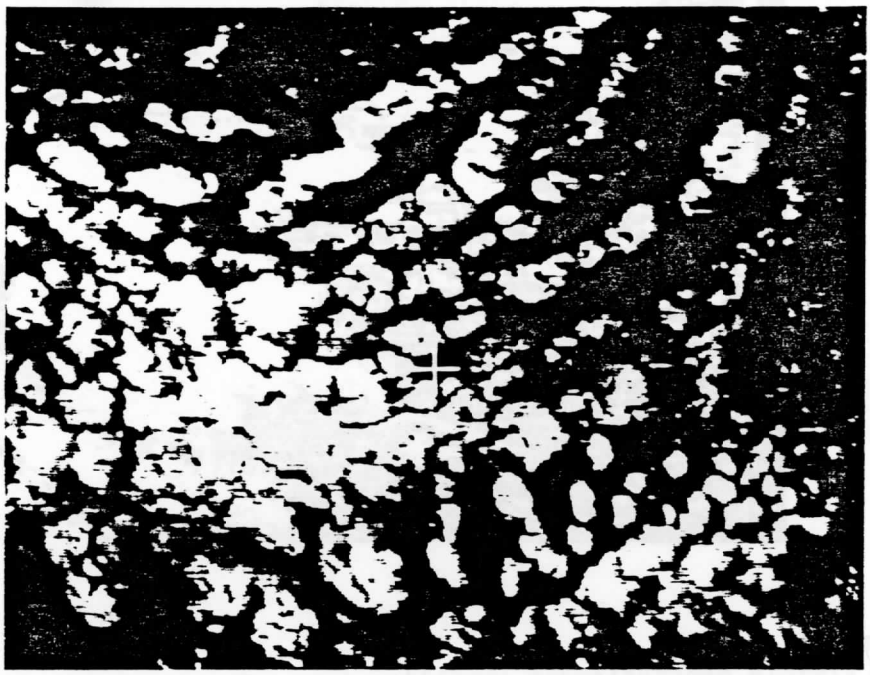

figure 3
Day 249, 1974 15Z showing the clouds over the south Atlantic used in analysis of line segment histograms.

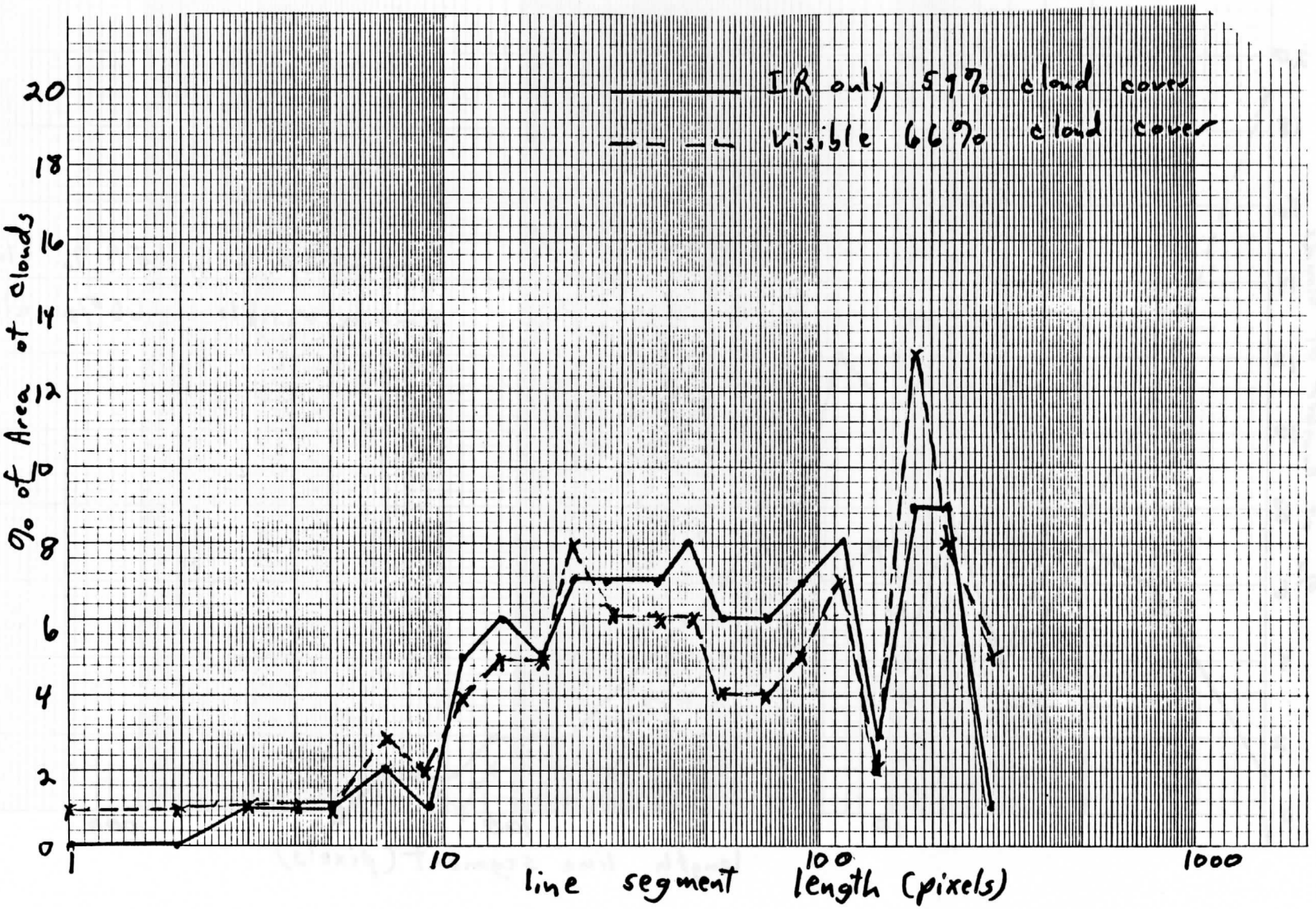

figure 4
The percent of the area of cloudy region as a function of line segment length.

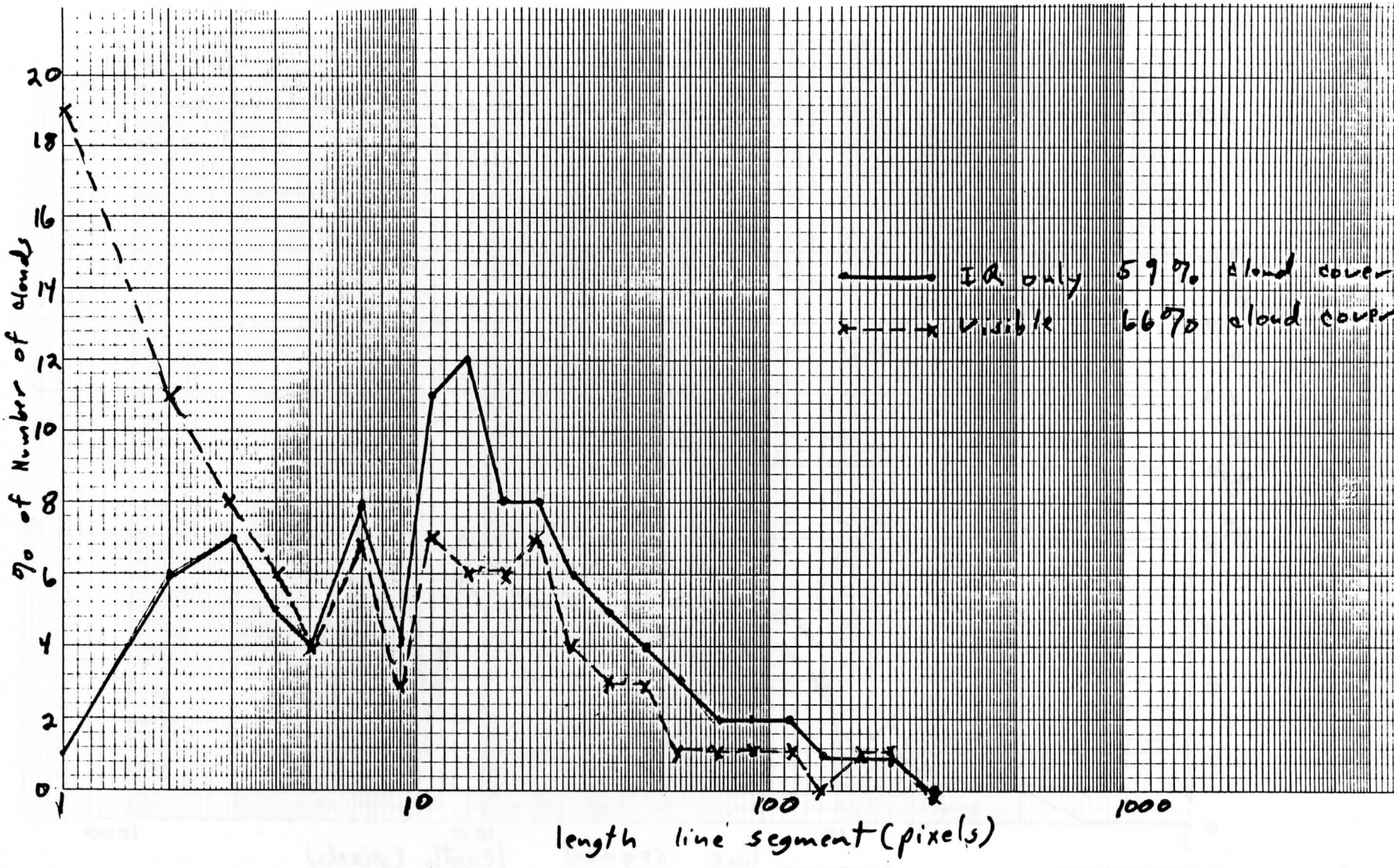

figure 5
The percent of the number of clouds as a function of line segment length.

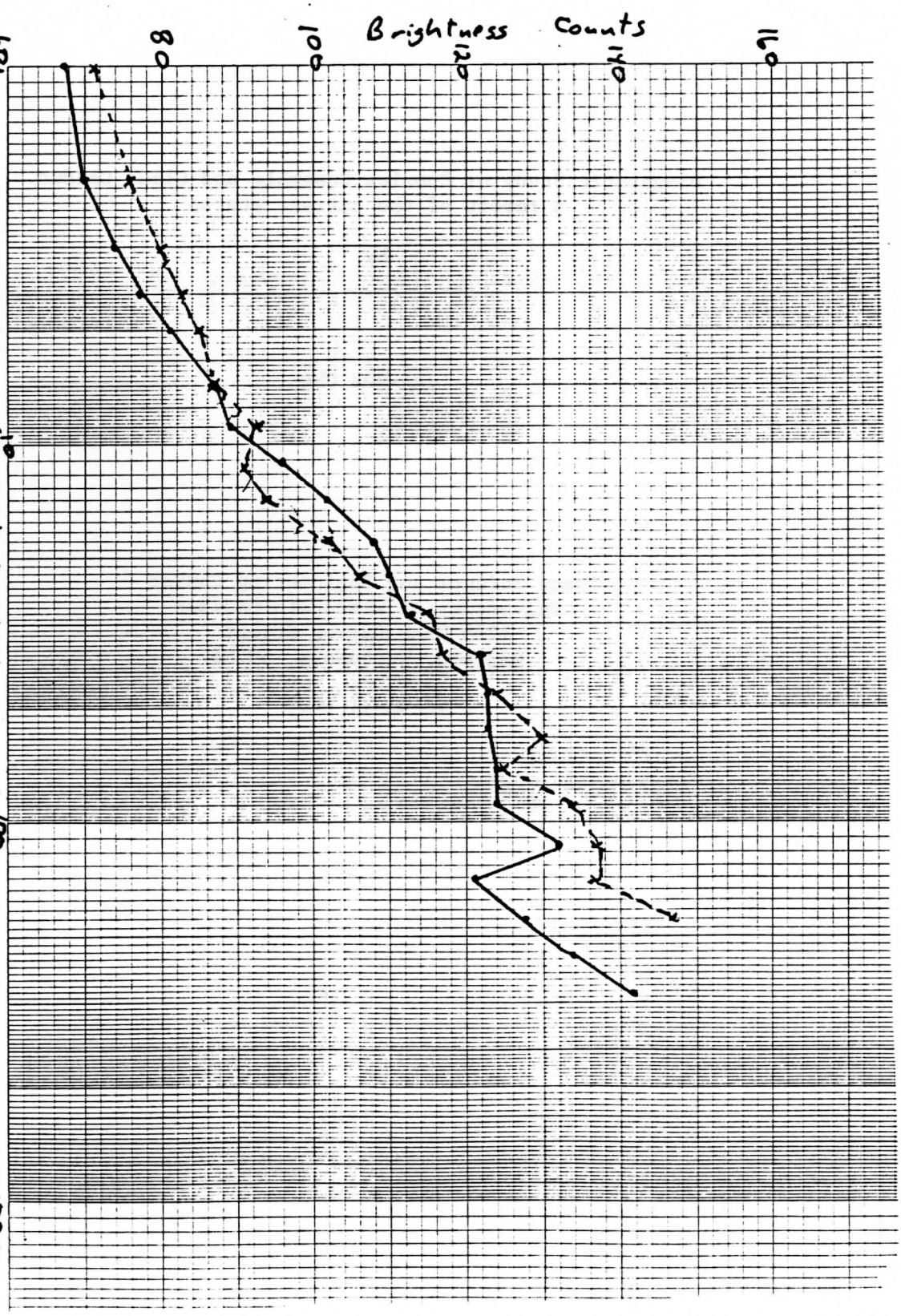

figure 6

The dependence of the average brightness of low clouds on cloud length for two different synoptic situations. The solid line is for a strata-cumulus case while the dashed is for a mixture of deep convection and small trade cumulus.

Diagnostic Study of Cumulus Ensemble and Cloud Census
A report of the current status

by

Jan-Hwa Chu

Space Science and Engineering Center
University of Wisconsin-Madison
1225 West Dayton Street
Madison, Wisconsin 53706

10 April 1979

Diagnostic Study of Cumulus Ensemble and Cloud Census

A report of the current status

by

Jan-Hwa Chu
Space Science and Engineering Center
The University of Wisconsin, Madison

10 April 1979

1. Introduction

Cloud census were needed to varify the cumulus cloud mass flux obtained by diagnostic study of cumulus ensemble. The diagnostic study, in turn, offers an interpretation to the cloud census.

The goals of this research are to estimate the spatial and temporal variations of convective cloud mass flux by using the data observed during the phase III of GATE, and to compare these variations with the type and amount of cloud deduced from GOES satellite cloud pictures.

2. Processing of Wind data

We used upper air and surface wind data of forteen ships in the GATE A/B- and B- scale area during the period from 31 August to 18 September (from Julian day 242 to 262), 1974, so called the phase III of GATE. Fig. 1 and Table 1 shows the nested formation of ships and their nominal positions, respectively. The characteristics of this data set are that 1) the reported data were sampled over a limited twenty day period and a limited oceanic area, 2) the sampling rate in the vertical is very high compared to the rate in the horizontal, 3) the data points were irregular spaced in time and space, the data may be under sampled for squalls and convective clouds but over sampled for the synoptic features, such as lower tropospheric

easterly wave and monsoon, in which they are imbedded, 4) the acquisition of data were made by different instrumentations, method of corrections and interpolations, the data may contain instrument bias and human errors (Reeves et al., 1976).

A substantial effort initiated by Dr. K. Ooyama at National Center for Atmospheric Research and his collaborators (Prof. S. Esbensen, Oregon State University and Dr. J. H. Chu, University of Wisconsin) had gone into developing techniques for analysis of the data set. One of the unique features of the techniques is the use of Ooyama's optimal representation scheme, which two-dimensionally and simultaneously interpolates and filters irregularly spaced data. Ooyama's forthcoming paper will contain a detail discussion of the objective analysis (personal communication, 1979). Ooyama and Esbensen (1977) applied the techniques to the height-time analysis of the ship data to determine the nature and probable causes of data error. They found that the variance of wind measured by radar has less high-frequency (<12 hour) noise than it measured by NAVAID system, and the winds below 950 mb are less reliable than those above it. Using two-day and longer low-pass filtered wind data, they noticed that winds varied systematically in height and space, but the difference between NAVAID winds and radar winds remains. They computed power spectra of vorticity and divergence by using A/B- scale winds (radar wind) and by using B- scale winds (NAVAID winds, with the exception of the Vanguard), the results shown the noise in the B- scale short-period variations. Their analysis of intercomparison data revealed that the A/B- scale ships reported tropopause at a pressure from 5 mh to 15 mb lower than the B- scale ships, and the A/B- scale ships reported a height-dependent temperature at about 1 K higher than the B- scale

ships. Similar problems on humidity field were found.

From these studies, we realized several reasons for the poor quality of reported data that could be improved. We used the following method iteratively to correct the wind data. First, analyze the maps of previously processed (12 hour filtered) winds of all the ships at twenty-one levels from sea surface (assumed to be 1012 mb) to 70 mb on three hourly intervals to identify suspicious data and to pinpoint the corresponding data of individual soundings. Second, delete the suspicious data, or replace them with better estimates taken from the wind maps and the WMO surface hourly reports, carefully matching with vertical profiles of reported winds of individual sounding. Third, re-analyze the corrected data set in filtered time-height format, and return to the first step. The task involved was essentially a man-machine interactive process of data analysis. Temperature and moisture data have been edited by the similar method at Oregon State University. This edited data set, soon will be obtained, is our primary data.

3. Preliminary results

The effort of wind data editing was rewarded with generally consistent wind data between A/B- scale ships (radar wind) and B- scale ships (NAVAID wind). Fig. 2a, b and 2c, d shown, as an example, the differences of variance spectra among reported wind, 12 hr filtered winds before correction of data and after correction for Vanguard (radar wind) and Researcher (NAVAID wind). The correction suppressed the variance in the period interval from 12 hour to 2- day more than those in the other periods.

Time averaged wind variations along -23.5 longitude are shown in Fig. 3.

The easterly has a maximum in the south at 200 mb level and decreases toward north. Secondary easterly peaks locate around 600 mb and 500 mb at 12° N and 7° N, respectively. A westerly maximum centered around 950 mb level at 8° N. The time variations of easterly are strong at 150 mb and at 635 mb levels. Northerly is found below 850 mb level, wind directions have more vertical variations at the south than that at the north. The time variations of meridional winds are strong around 200- mb and 635- mb levels. Fig. 2 shows the spatial variation of time averaged winds from Krenkel to Priboy.

We computed the variances of ship wind and concluded that the total variances (sum of variances with period greater than 12 hr) have a primary peak around 160 mb level and a secondary one around 635 mb level. The partial variance in the time interval from 2- to 8- day (e- band) has a peak around 635 mb level for all ship winds, the variances of northern ships are stronger than those of southern. On the same level, the partial variances in the interval from 12- hour to 2- day (d-band), from 8- to 16- day (1- band) and about 16- day period (trend) are small compare to those of the e- band. The situation is different at 160 mb level, there the partial variances of the e- band and of the lower frequency (sum of 1- band and trend) have similar magnitude, partial variance of d-band is smaller than them. Figs. 2b and 2d, as an example, shows the vertical profiles of these partial variances of Vanguard and Researcher.

Fig. 5 shown the 2- day low-pass filtered winds, a wavy variation of wind centered around 600-mb level, its amplitude increases northward, speed of propagation is about 7° lat/day. There are also wavy variations centered around 200 mb level, with high inter-ship correlations. The wave with

period 4- to 6- days centered around 700 mb were studied by Thompson et al., 1979 .

Fig. 6 shows the 8- day low-pass filtered winds, a easterly maximum around 200 mb level has a phase propagation with a speed of 7°/1.5 day, and with an unclear ten day period, similar pattern are recognized in northerly. There are easterly and northerly peaks around 600 mb level. Wind variations in the lower layer may resemble the cross equatorial flow and monsoonal flow. The phase III GATE A/B- scale data are too short to explore these phenomena with longer periods of variations.

As for the derived data set, we used the primary wind data to compute vertical component of relative vorticity, horizontal divergence and vertical p- velocity in seven subregions (Fig. 1 and Table 2) of GATE A/B- scale area by using Bellamy's method. We observed an inphase relation between strong upward motion in the B7 area and large amount of areal rainfall (Figs. 7a and b). Since the corrected wind were used, the time averaged vertical p-velocity of B7 area has a improved mass balance compare to previous results obtained by Ooyama and Esbensen (1977). Figs. 8a and 8b show the time-height sections of 2 day low-pass filtered relative vorticity and vertical p-velocity in NW4, B7 and SW4 subregions. Vorticity centers around 700 mb show wavy pattern, and it takes one day to propagate northwestward through these subregions. The Bellamy's method, however, assumes a linear variation of wind between ships. The imbalance of mass in E5 and W4 subregions were mainly attributed to this assumption. We than assumed that winds may be represented by a polynomial surface defined over the A/B- scale area. The results shown an improvement of mass balance in E5 and W4 regions (Fig. 9b). The regional differences of vertical

p-velocity and vorticity are shown in Figs. 9 and 10. The polynomial surfaces, defined over the entire area of interest and obtained from data points with irregular spacing, can neither distinctly nor homogenously represent the spatial variations of winds. That may distort the phenomena with a scale smaller than the entire area or with preferably geographical orientation. These experiments demonstrated the need of a spatially de-aliasing scheme, in order to interpolate the spatially under-sampled data (Ooyama, personnal communication). To design such a shceme, it requires not only nested data points but also sufficiently long time series for meaningful statistics of data.

The other alternative is to make corrections on the divergence computed by using Bellamy's method, in order to insure the mass balance. The vertical distribution of the corrective amount was determined subjectively with the aliasing error in mind. Then the amount of corrections of all subregions on each level will be used to adjust the divergent part of winds on every data point. It is implicitly assumed that the signals associated with vorticity are stronger than those with divergence, that were frequently observed during phase III of GATE. A similar method was proposed by Fankhauser (1974) and used by Smith et al. (1975). Since only the divergent part of wind was mutually adjusted, the resulting winds at each data point will not completely lose their geographical characteristics. An advantage of this method is to obtain the mass balance and consistent wind fields which is crucial for budget studies. A disadvantage is to leave the problem of spatial aliasing unsolved.

4. Future works

We are going to compute the large-scale thermodynamic and moisture budget, after we receive the data from Prof. S. Esbensen.

REFERENCES

1. Fankhauser, J.C., 1974: The deviation of consistent fields of wind and geopotential height from mesoscale rawinsonde data. J. Appl. Meteor., 13, 634-646.

2. Hudlow, M. and F. Marks, 1977: Echo statistics and rainfall. Report of the U.S. GATE Central Program Workshop, 25 July - 12 August 1977, Nat. Center for Atmos. Res., 215 - 236.

3. Ooyama, K. and S. Esbensen, 1977: Rawinsonde data quality. Report of the U.S. GATE Central Program Workshop, 25 July - 12 August 1977, Nat. Center for Atmos. Res., 131 - 163.

4. Reeves, R.W., S. Williams, E. Rasmusson, D. Acheson, T. Carpenter, and J. Rasmusson, 1976: GATE convection subprogram data center -- analysis of rawinsonde intercomparison data. NOAA Technical Report, EDS 20, 75 pp.

5. Smith, C., E. Zipser, S. Daggupatz and L. Sapp, 1975: An experiment in tropical mesoscale analysis: part 1. Mon. Wea. Rev., 103, 878-- 892.

6. Thompson, R., P. Steven, R. Ernest and R. Reed, 1979: Structure and properties of synoptic-scale wave disturbances in the intertropical convergence zone of the Eastern Atlantic. J. Atmos. Sci., 36, 53 - 72.

LIST OF TABLES

Table 1

Ship Name	Ship No.	Nominal position Lat.°N	Lon.°W	Approximate period of observation made at nominal position (Julian Day)
Korolov	8	12.00	-23.50	243.0-262.0
Priboy	13	10.50	-27.50	243.3-261.3
Poryv	9	10.50	-20.00	242.0-262.0
Vanguard	2	10.00	-23.50	242.3-250.0, 250.8-261.7
Gillis	7	9.25	-24.80	242.0-262.0
Quadra	3	9.00	-22.50	242.0-262.0
Vize	1	8.50	-23.50	243.0-258.8, 259.8-261.2
Dallas	16	8.50	-23.50	242.0-260.0
Bidassoa	6	7.75	-24.80	242.0-262.0
Oceano-grapher	4	7.75	-22.20	242.0-262.0
Researcher	5	7.00	-23.50	242.0-262.0
Okean	12	6.50	-27.00	242.0-262.0
Krenkel	10	6.50	-20.00	242.0-243.5, 245.5-262.0
Zubov	11	5.00	-23.50	242.0-261.0

Table 2

ID of subregions	Name of subregions	ID of ships enclosing the subregion	Area $(km)^2$
B7	B-scale septilateral area	2-7-6-5-4-16-3	63266
NE4	Northeast Tetragon	3-9-8-2	66623
NW4	Northwest Tetragon	2-8-13-7	62225
W4	West Tetragon	7-13-12-6	73689
SW4	Southwest Tetragon	6-12-11-5	62846
SE4	Southeast Tetragon	5-11-10-4	62846
E5	East pentagon	4-10-9-3-16	77275
AB6	A/B-scale hexagon	11-10-9-8-13-12	468869

LIST OF FIGURES

Fig. 8. The time-height section of 2-day low-pass filtered relative vorticity and vertical p-velocity (omega) in NW4, B7 and SW4 subregions, a) vorticity, b) omega.

Fig. 9. Time averaged (day 243 to 261) vertical p-velocity of a) NW4 and NE4 subregions, b) W4, B7 and E5 subregions, c) SW4 and SE4 regions. Unit: 10^{-4} mbs^{-1}.

Fig. 10. Same as Fig. 9 except for vorticity. Unit: 10^{-6}s^{-1}.

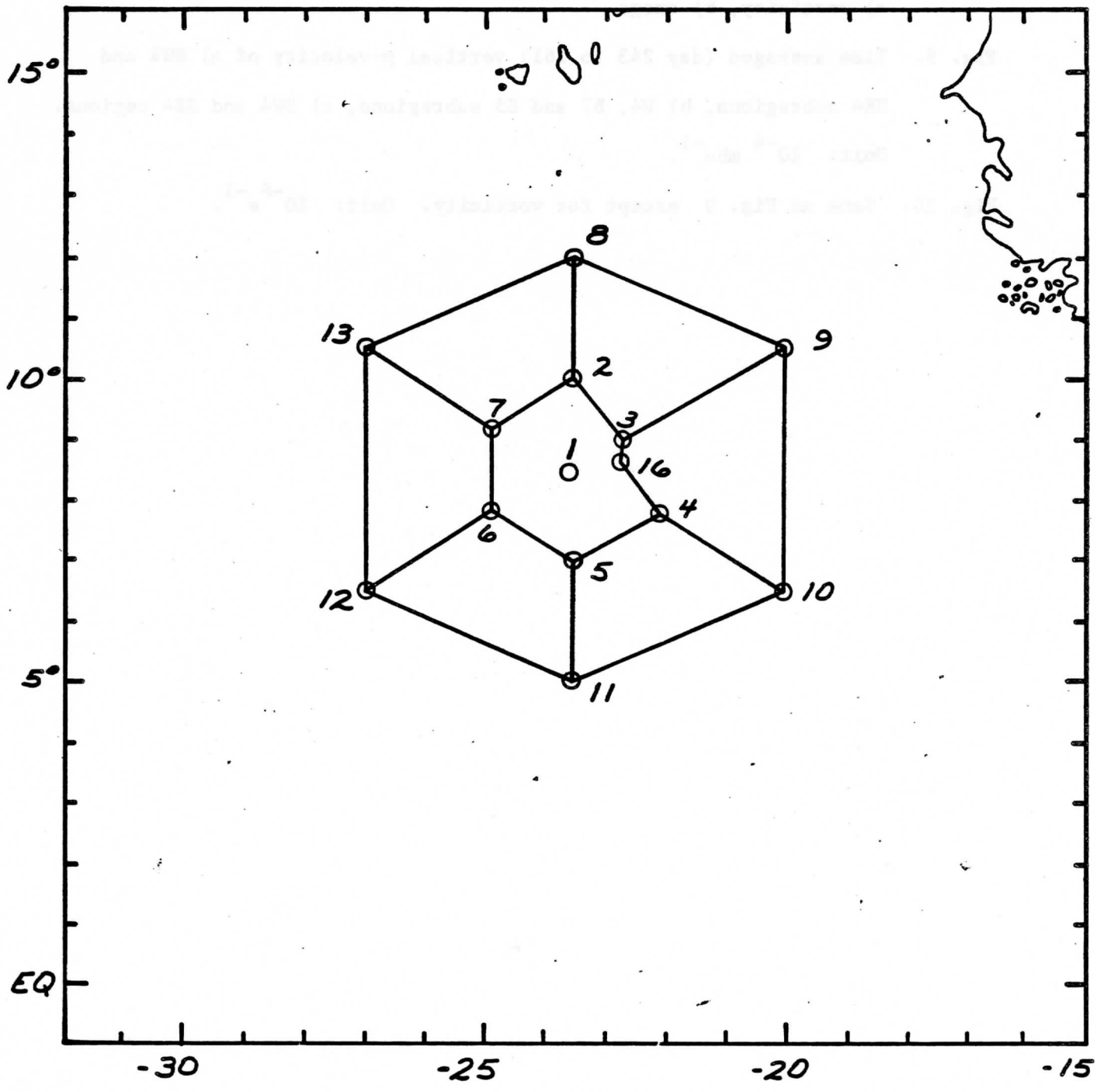

FIG. 1

VARIANCE SPECTRA VANGUARD

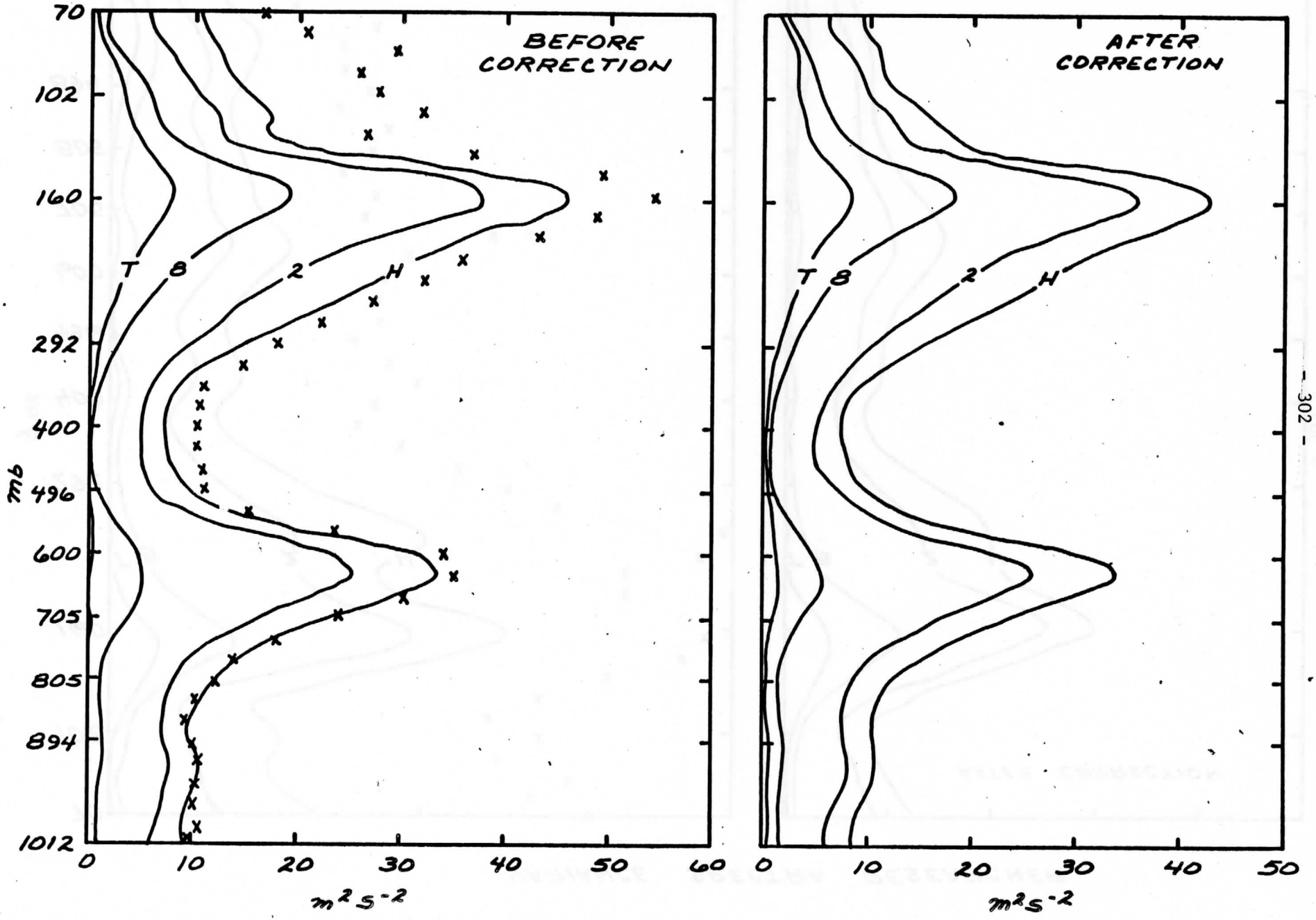

FIG. 2a

FIG. 2b

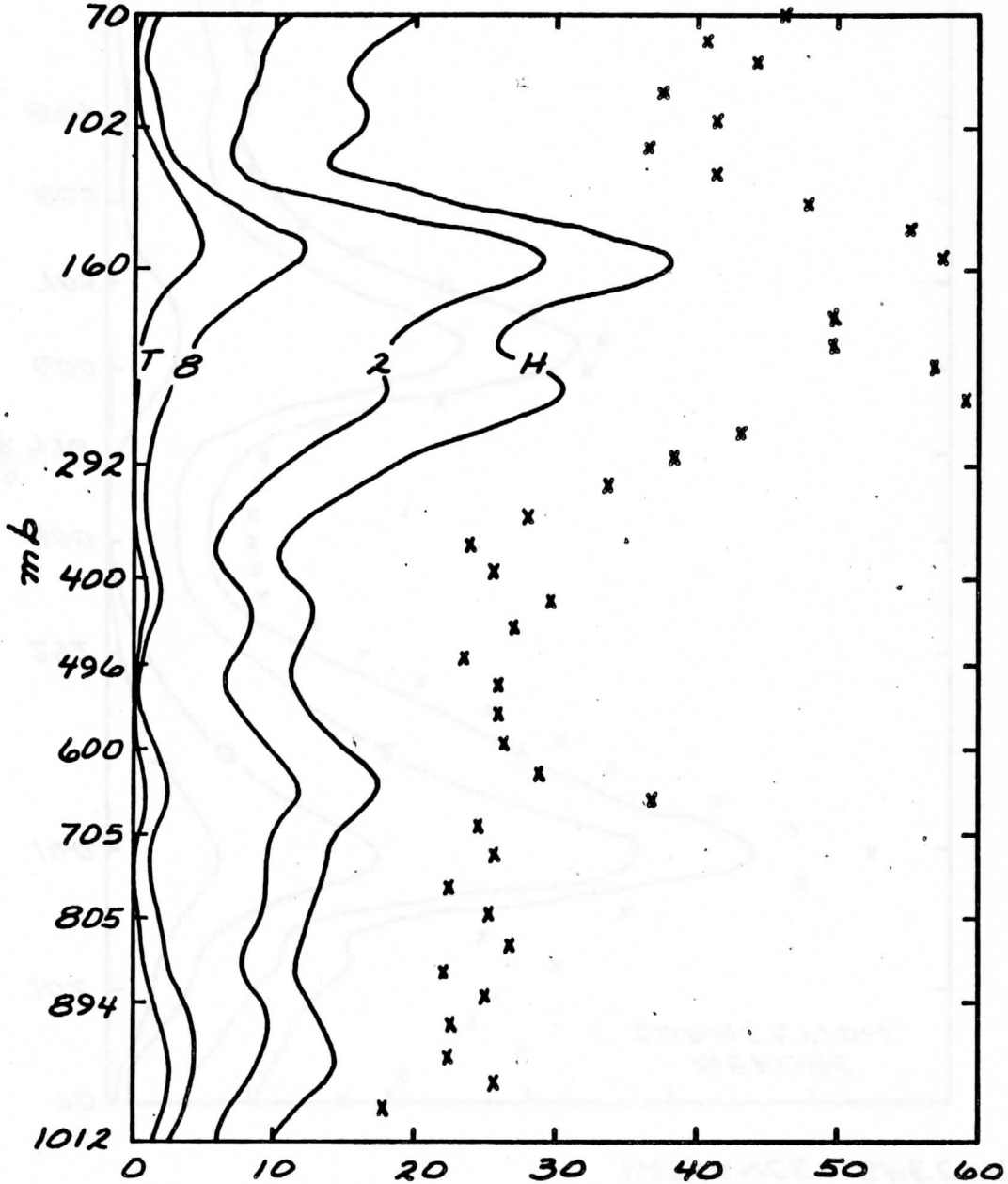
70
102
160
292
400
496
600
705
805
894
1012
mb
T
8
2
H
0
10
20
30
40
50
60
m²s⁻²

Fig 2c

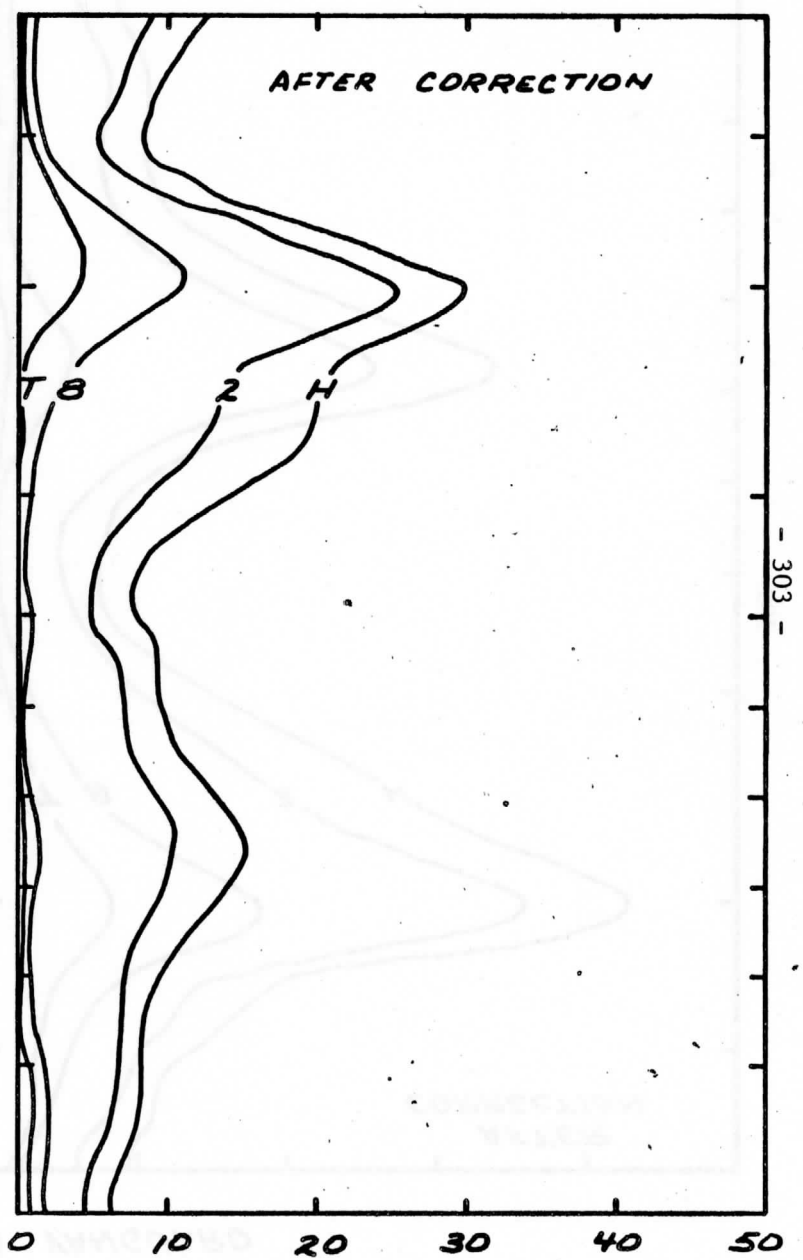
AFTER CORRECTION
T
8
2
H
0
10
20
30
40
50
m²s⁻²

Fig 2d

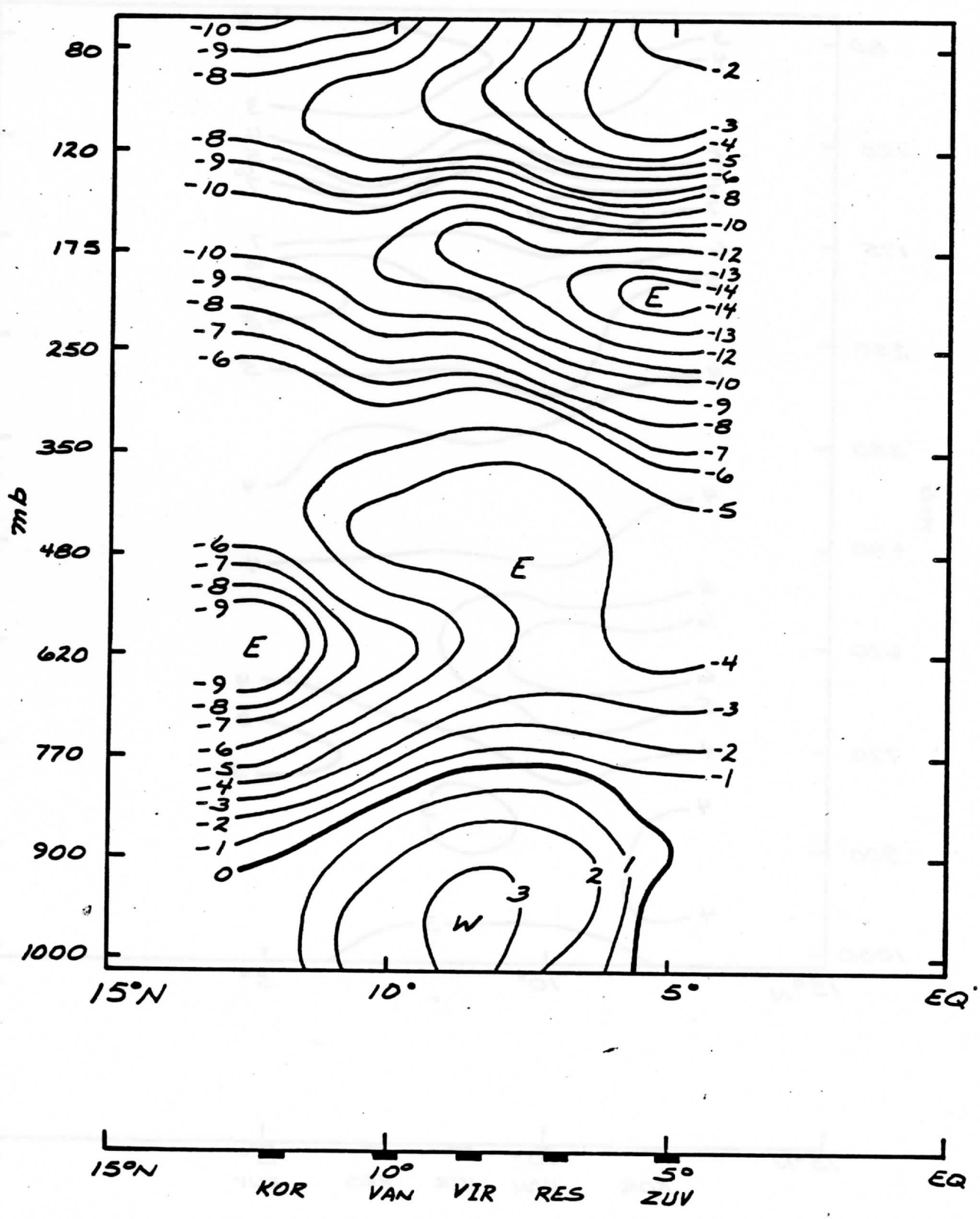
80
120
175
250
350
480
620
770
900
1000
mb
15°N
10°
5°
EQ
E
W
KOR
VAN
VIR
RES
ZUV

FIG. 3a

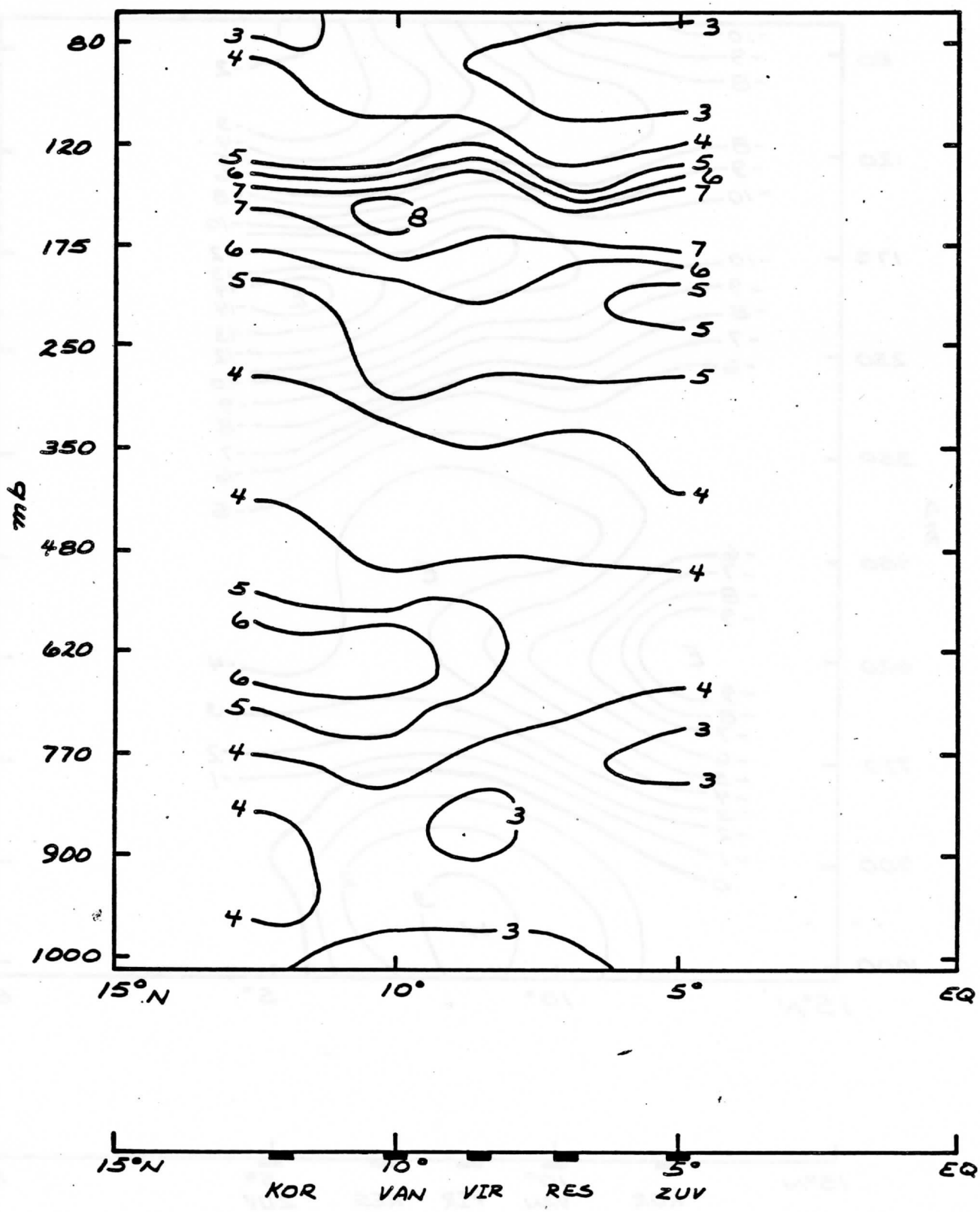
80
120
175
250
350
480
620
770
900
1000
mb
15°N
10°
5°
EQ
KOR
VAN
VIR
RES
ZUV

FIG. 3b

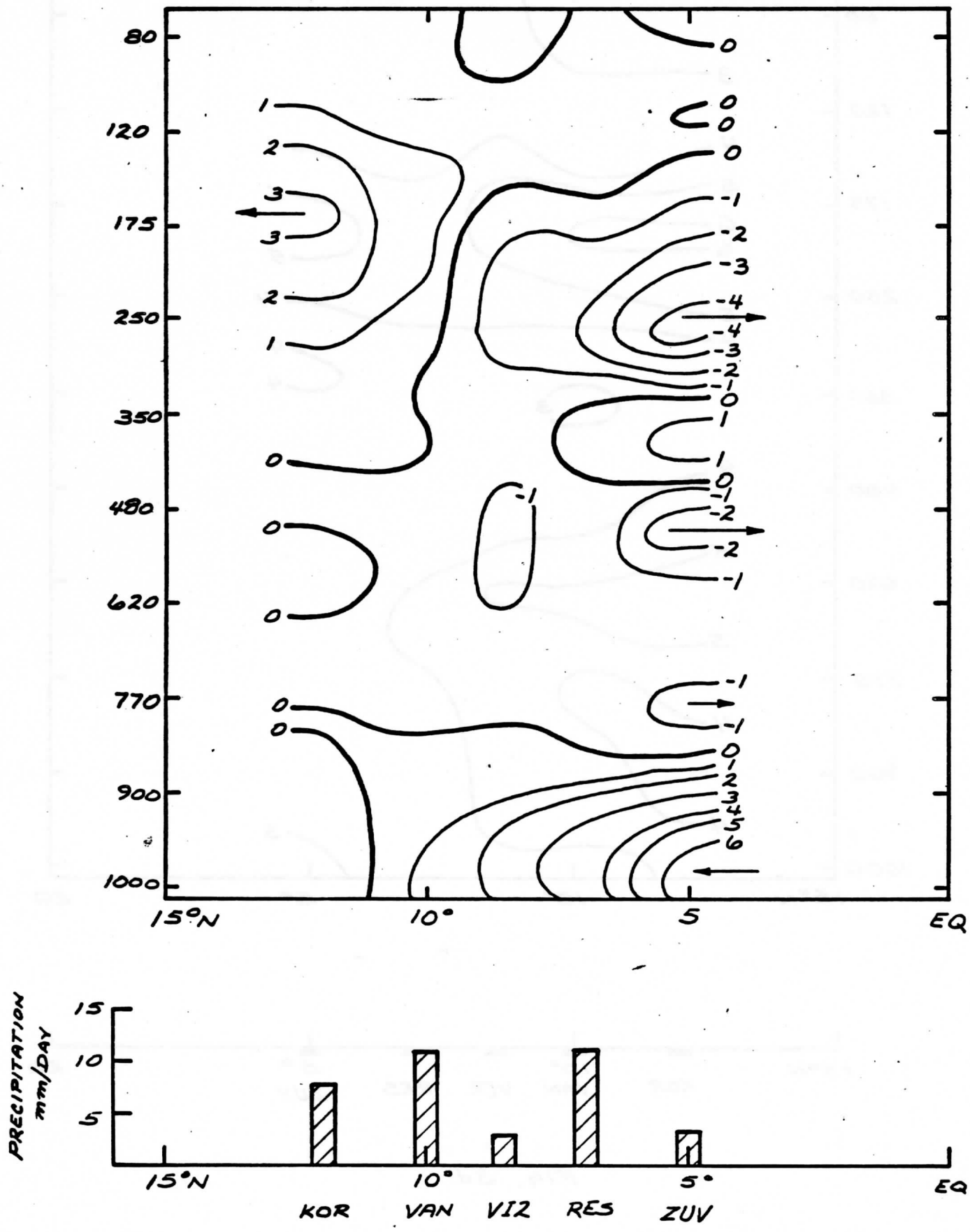
80
120
175
250
350
480
620
770
900
1000
15°N
10°
5
EQ
PRECIPITATION mm/DAY
15
10
5
15°N
10°
5°
EQ
KOR
VAN
VIZ
RES
ZUV

FIG. 3c

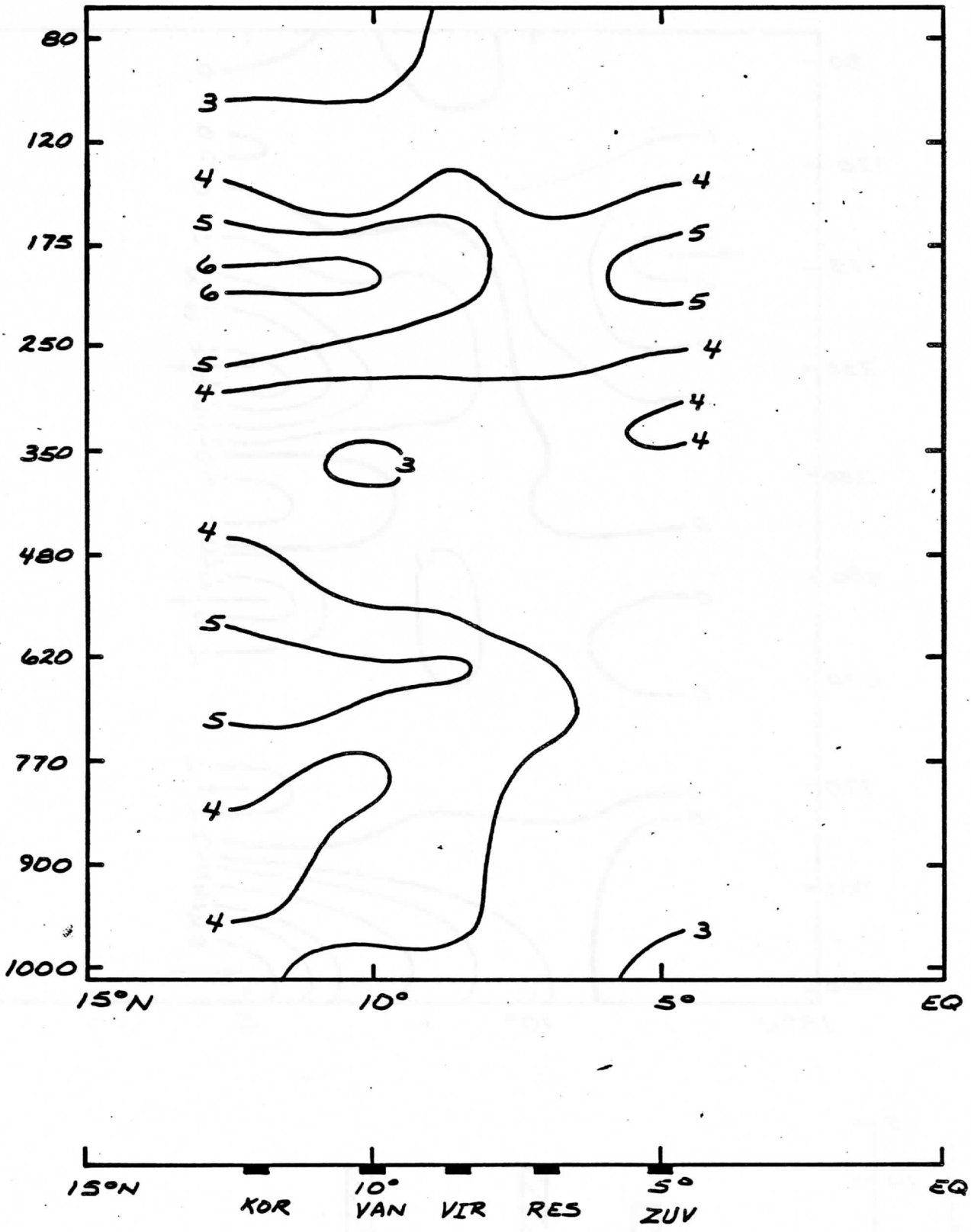
80
120
175
250
350
480
620
770
900
1000
15°N
10°
5°
EQ
3
4
5
6
6
4
5
5
5
4
4
4
4
3
4
5
5
4
4
3
15°N
10°
5°
EQ
KOR
VAN
VIR
RES
ZUV

FIG. 3d

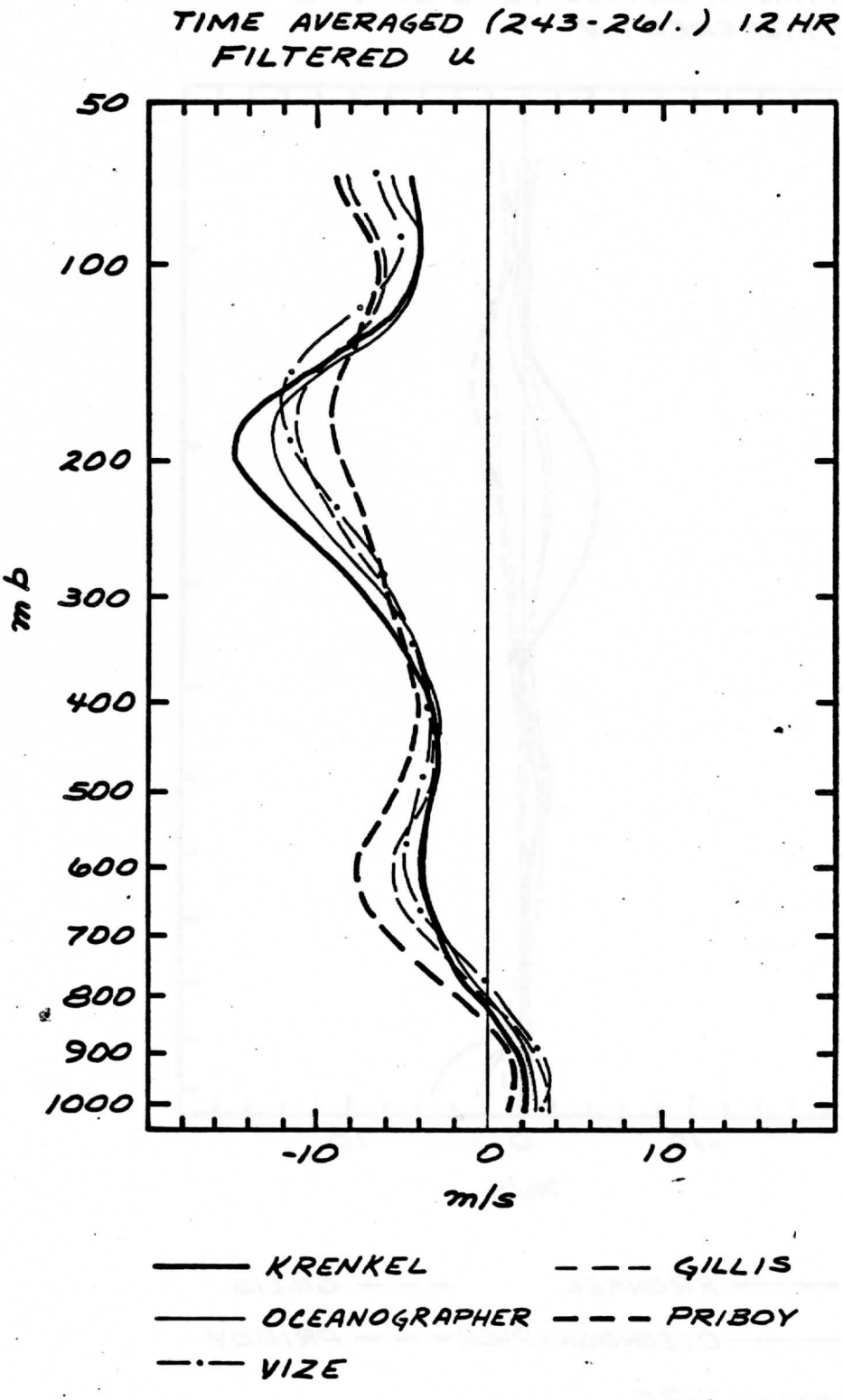
TIME AVERAGED (243-261.) 12 HR
FILTERED u
50
100
200
300
400
500
600
700
800
900
1000
mb
-10
0
10
m/s
KRENKEL
GILLIS
OCEANOGRAPHER
PRIBOY
VIZE

FIG. 4a

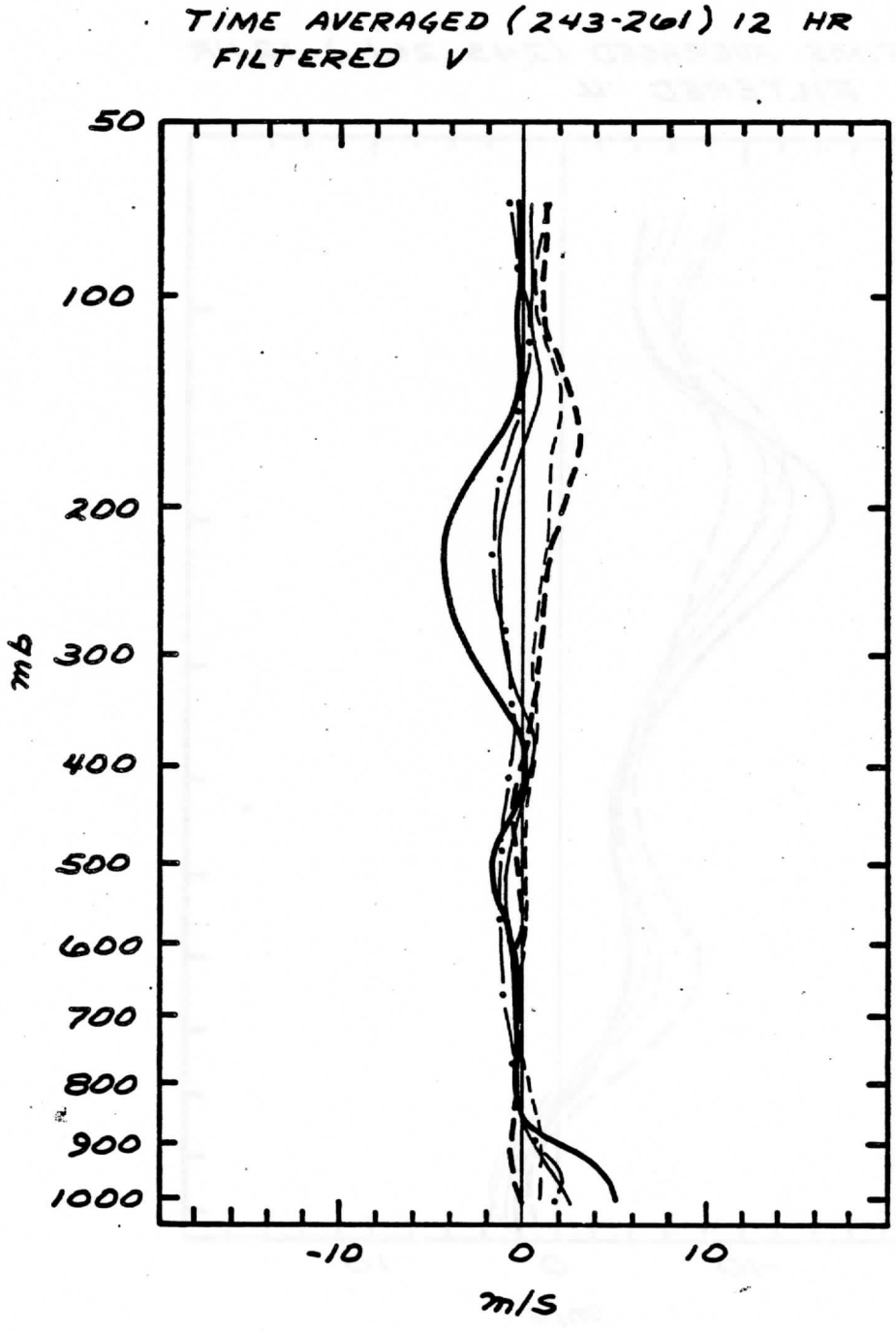
TIME AVERAGED (243-261) 12 HR
FILTERED V
50
100
200
300
400
500
600
700
800
900
1000
mb
-10
0
10
m/s
KRENKEL
GILLIS
OCEANOGRAPHER
PRIBOY
VIZE

FIG. 46

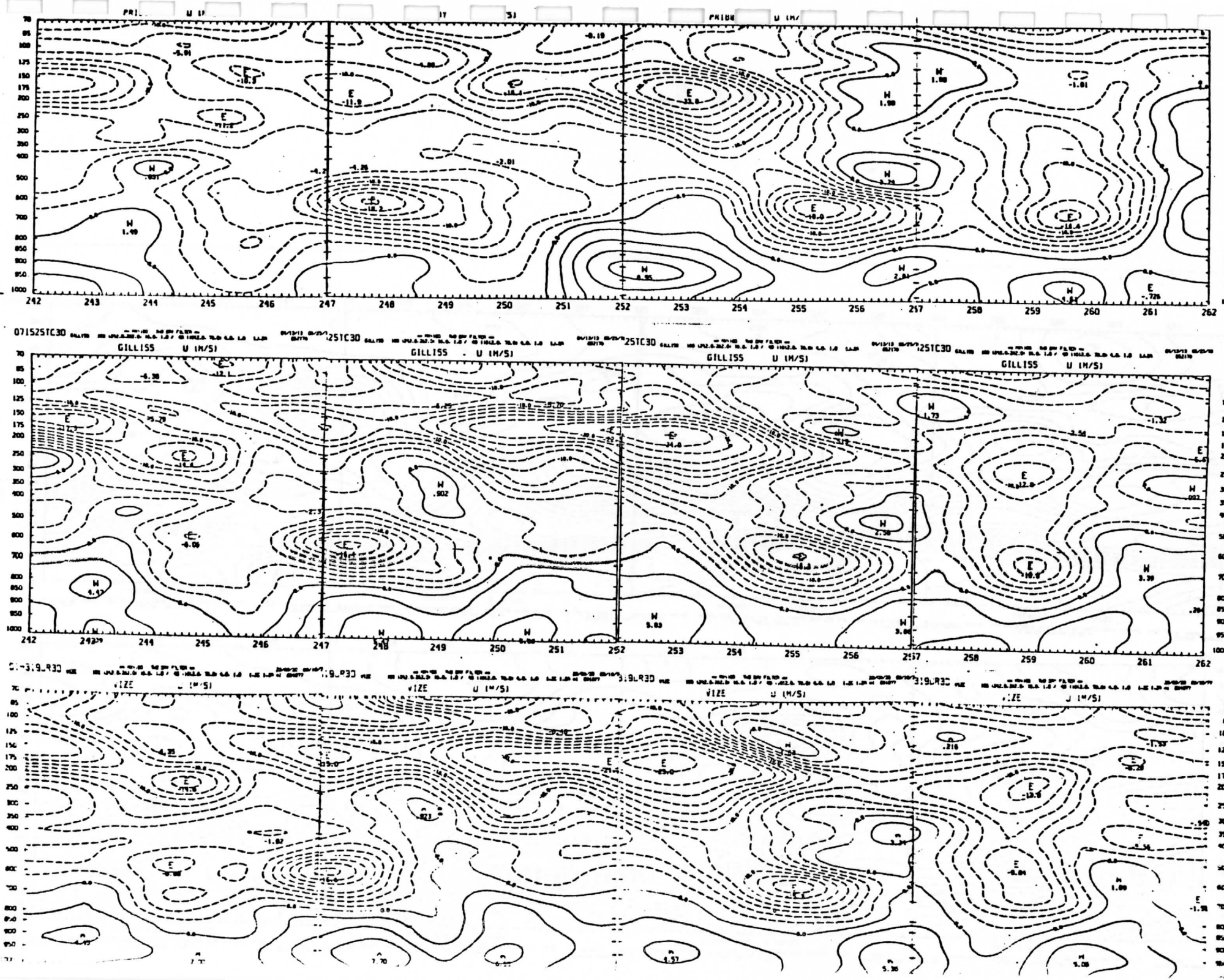
GILLISS U (M/S)
242 243 244 245 246 247 248 249 250 251 252 253 254 255 256 257 258 259 260 261 262

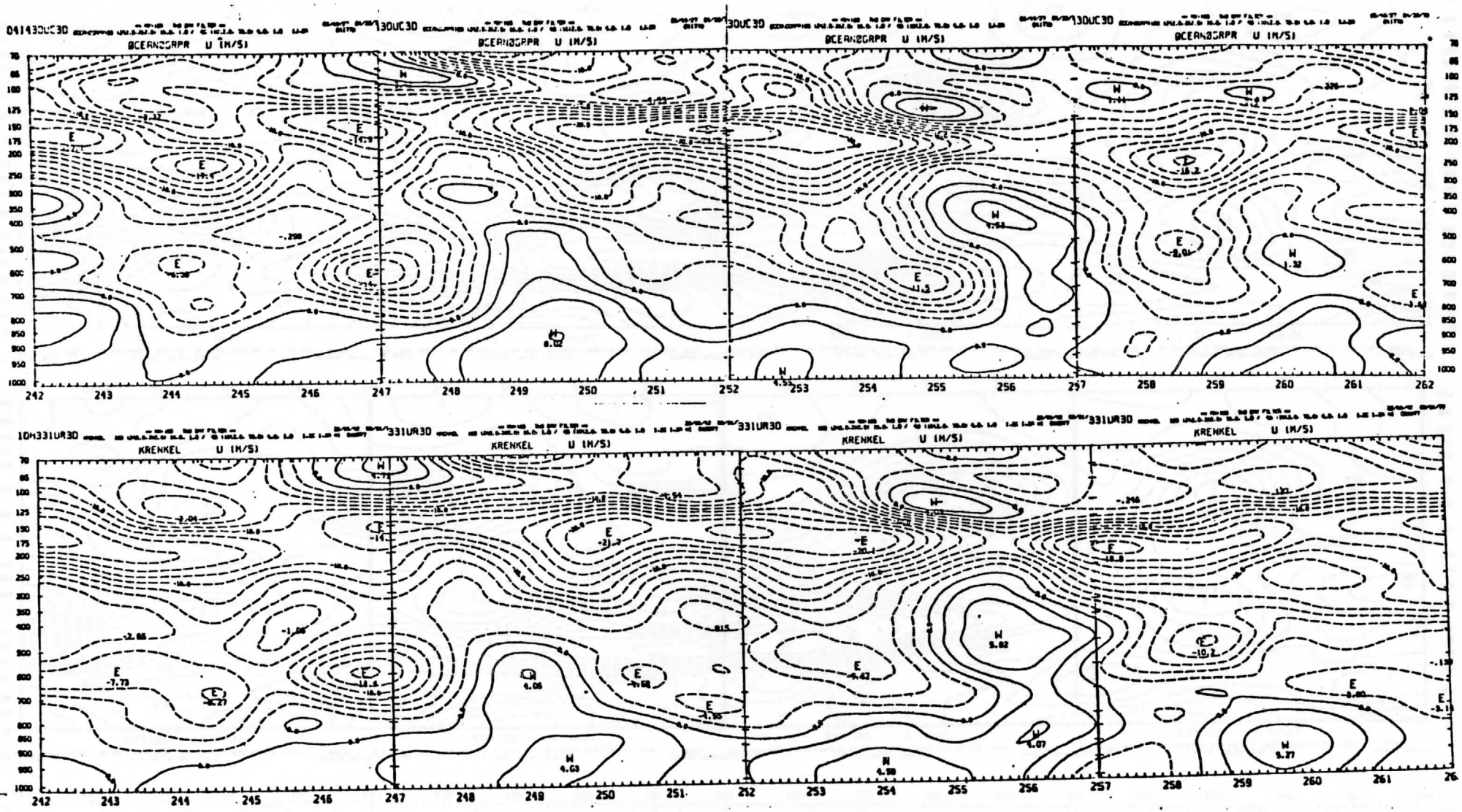

Fig. 5a

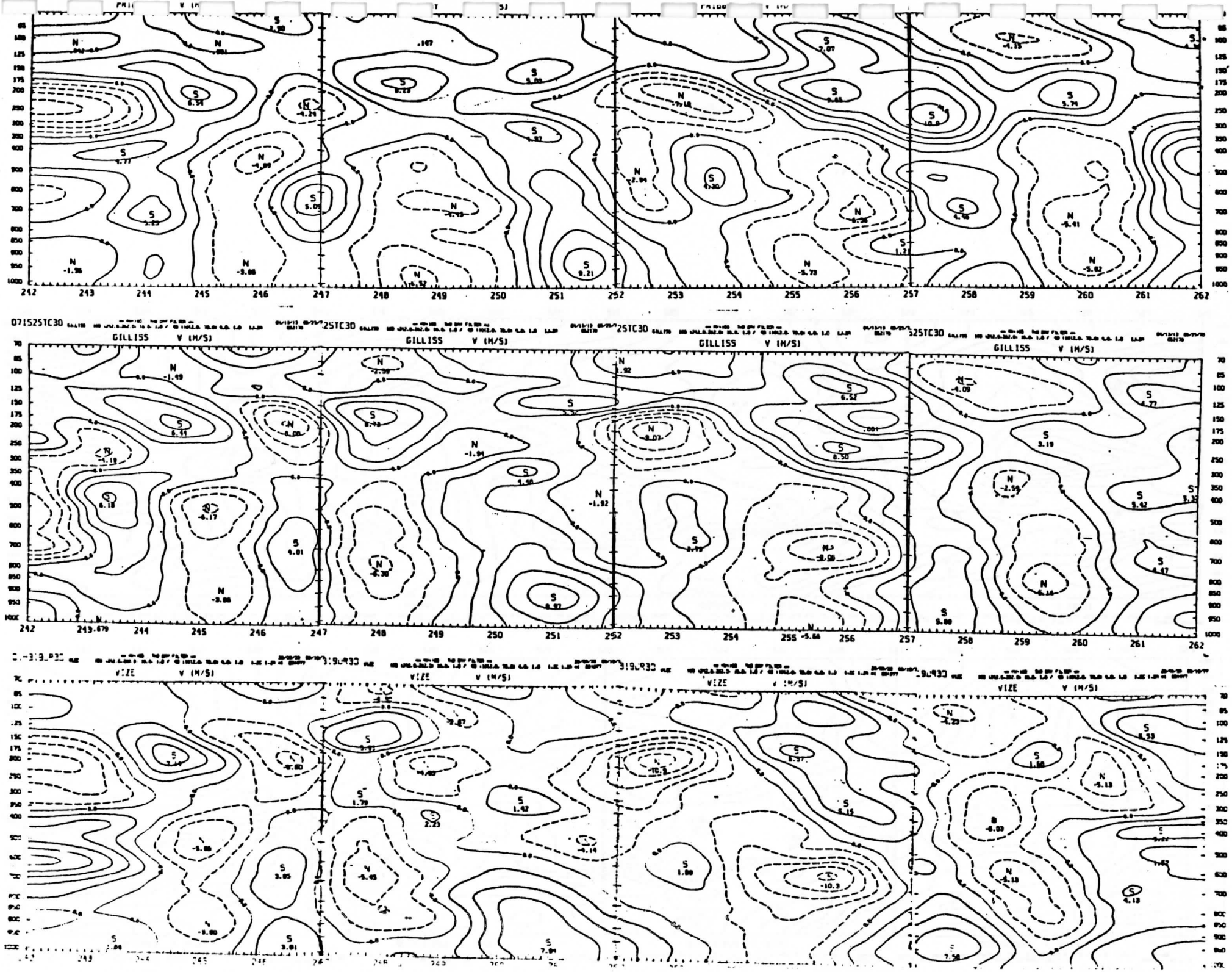
GILLISS V (M/S)
242 243 244 245 246 247 248 249 250 251 252 253 254 255 256 257 258 259 260 261 262

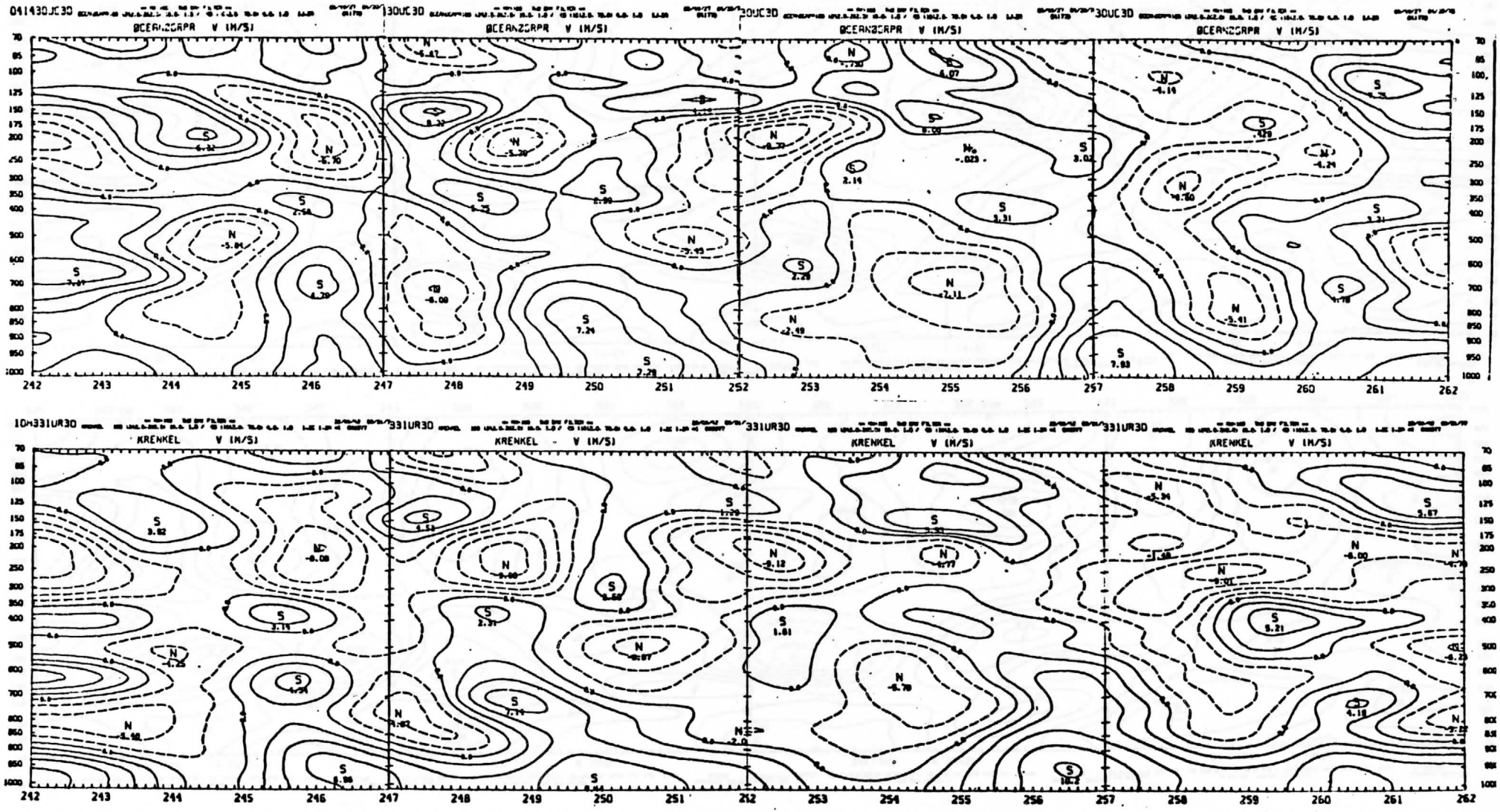
041430UC3D
30UC3D
30UC3D
30UC3D
OCEANZORPR V (M/S)
OCEANZORPR V (M/S)
OCEANZORPR V (M/S)
OCEANZORPR V (M/S)
10H331UR3D
331UR3D
331UR3D
331UR3D
KRENKEL V (M/S)
KRENKEL V (M/S)
KRENKEL V (M/S)
KRENKEL V (M/S)

Fig. 5 b

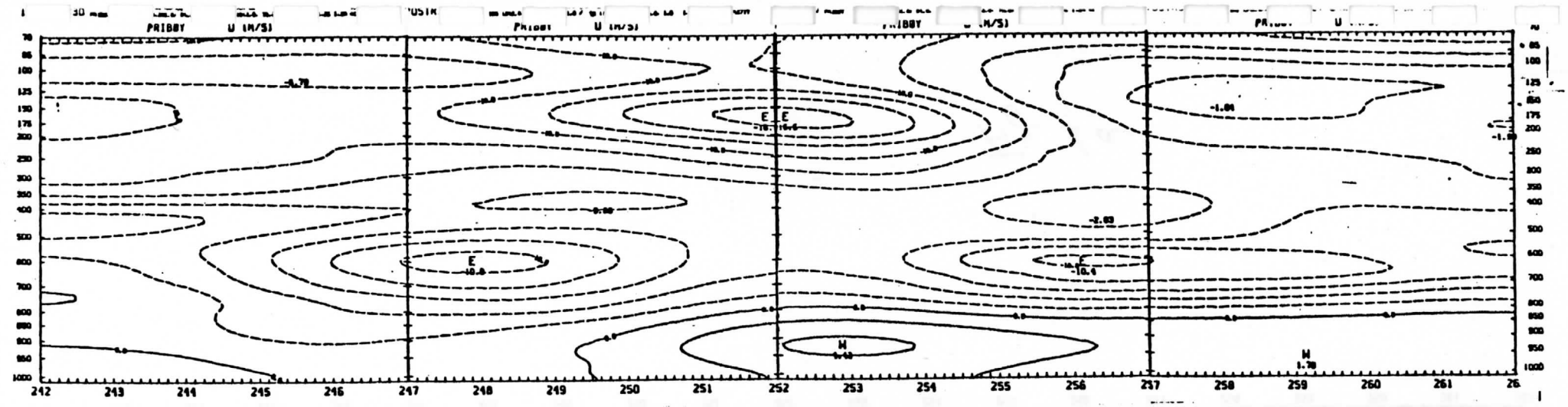
PRIBBY U (M/S)
PRIBBY U (M/S)
PRIBBY U (M/S)
PRIBBY U (M/S)

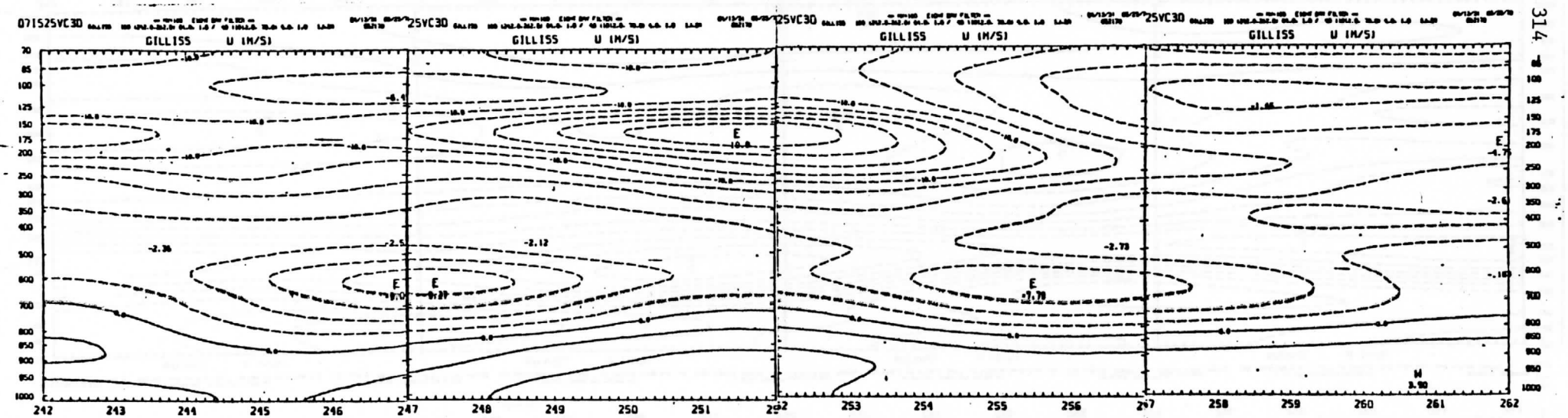
071525VC30
GILLISS U (M/S)
25VC30
GILLISS U (M/S)
25VC30
GILLISS U (M/S)
25VC30
GILLISS U (M/S)

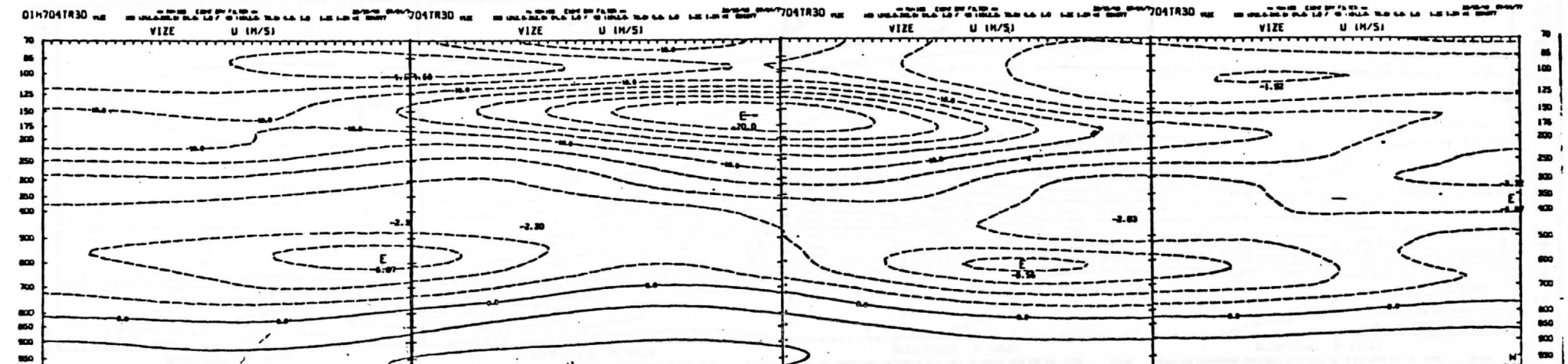
01H704TR30
VIZE U (M/S)
704TR30
VIZE U (M/S)
704TR30
VIZE U (M/S)
704TR30
VIZE U (M/S)

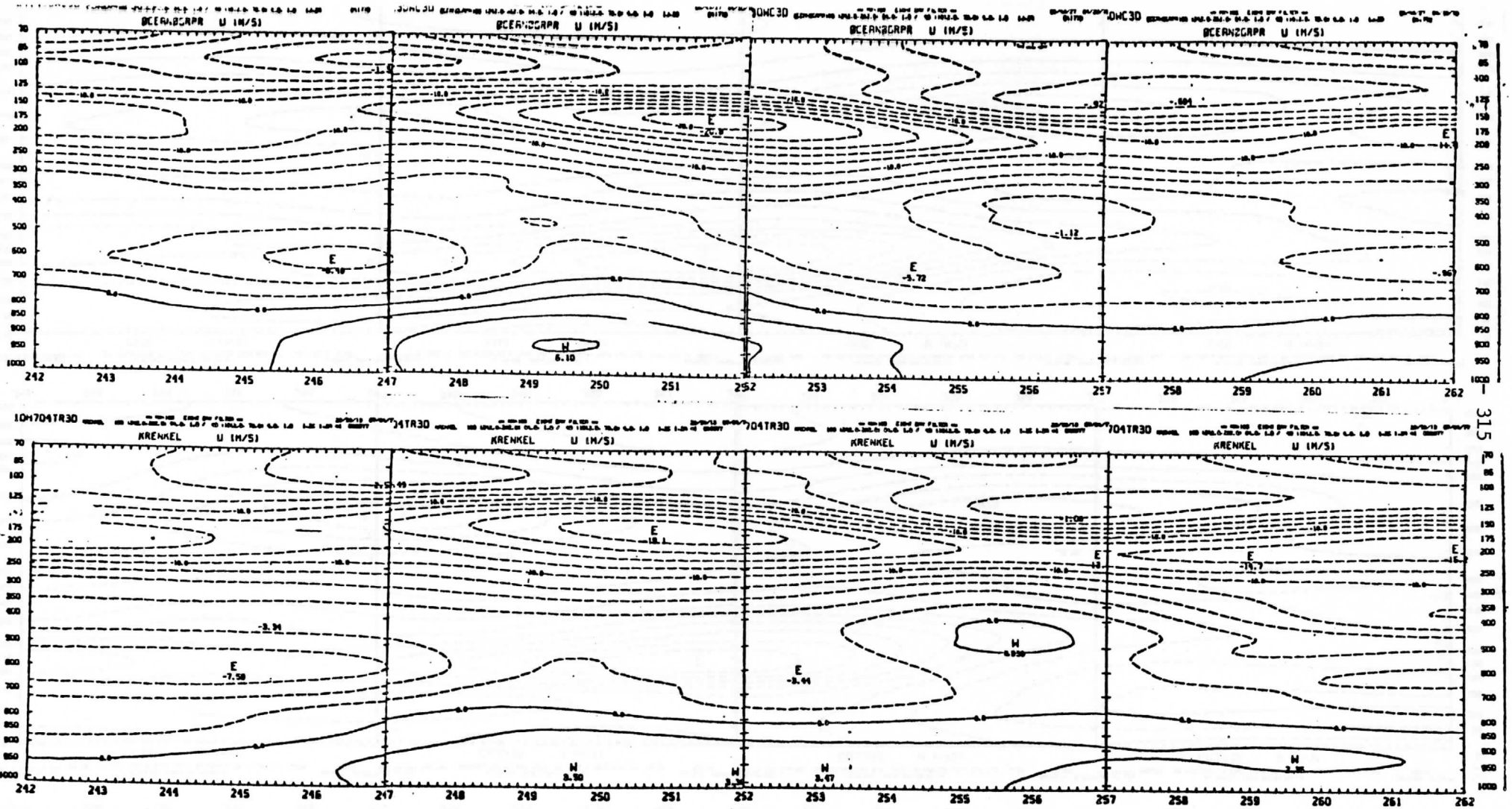
OCEANOGRAPH U (M/S)
KRENKEL U (M/S)
242 243 244 245 246 247 248 249 250 251 252 253 254 255 256 257 258 259 260 261 262

315

Fig. 6a

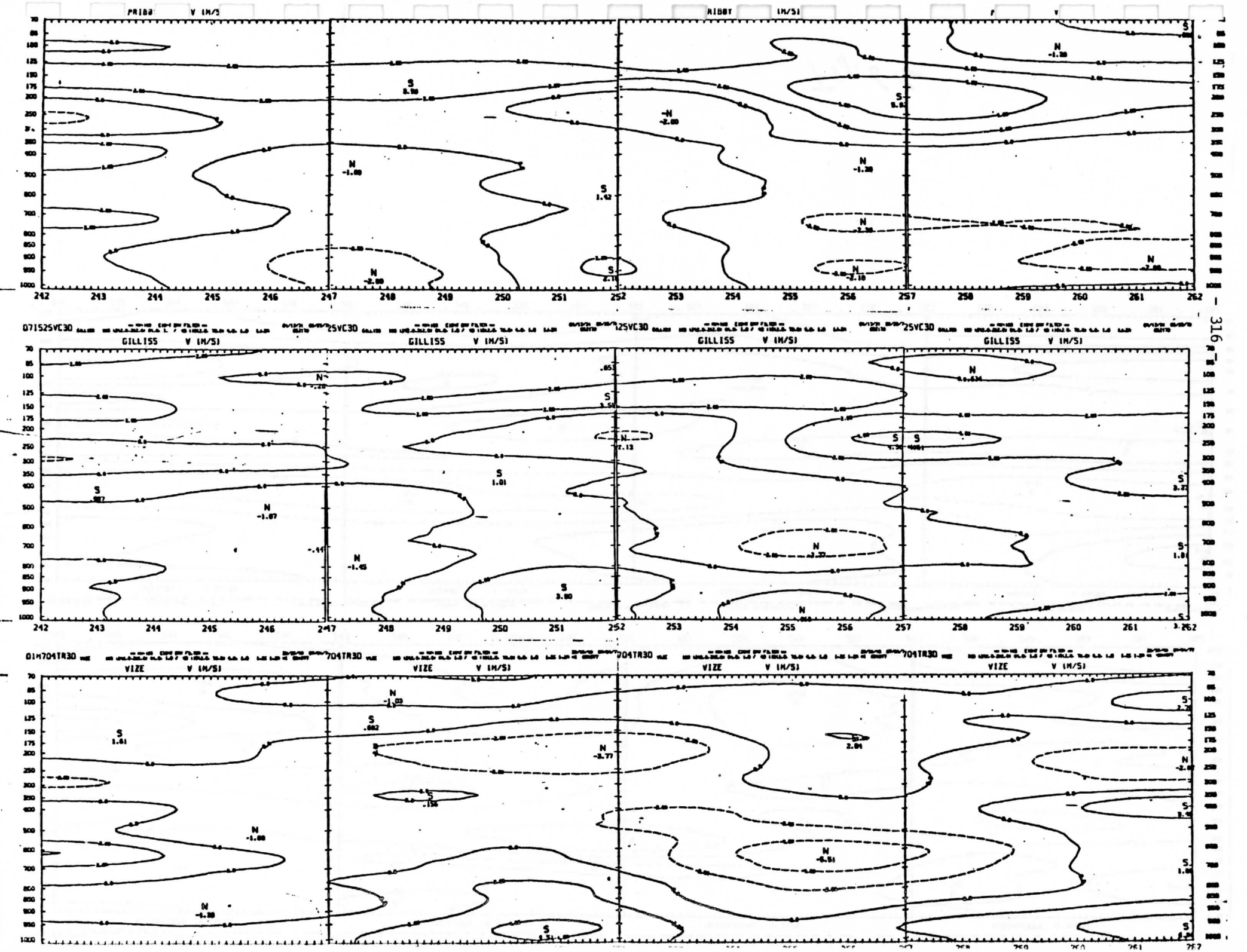
PRIBB V (M/S)
RIBBT (M/S)
GILLISS V (M/S)
VIZE V (M/S)

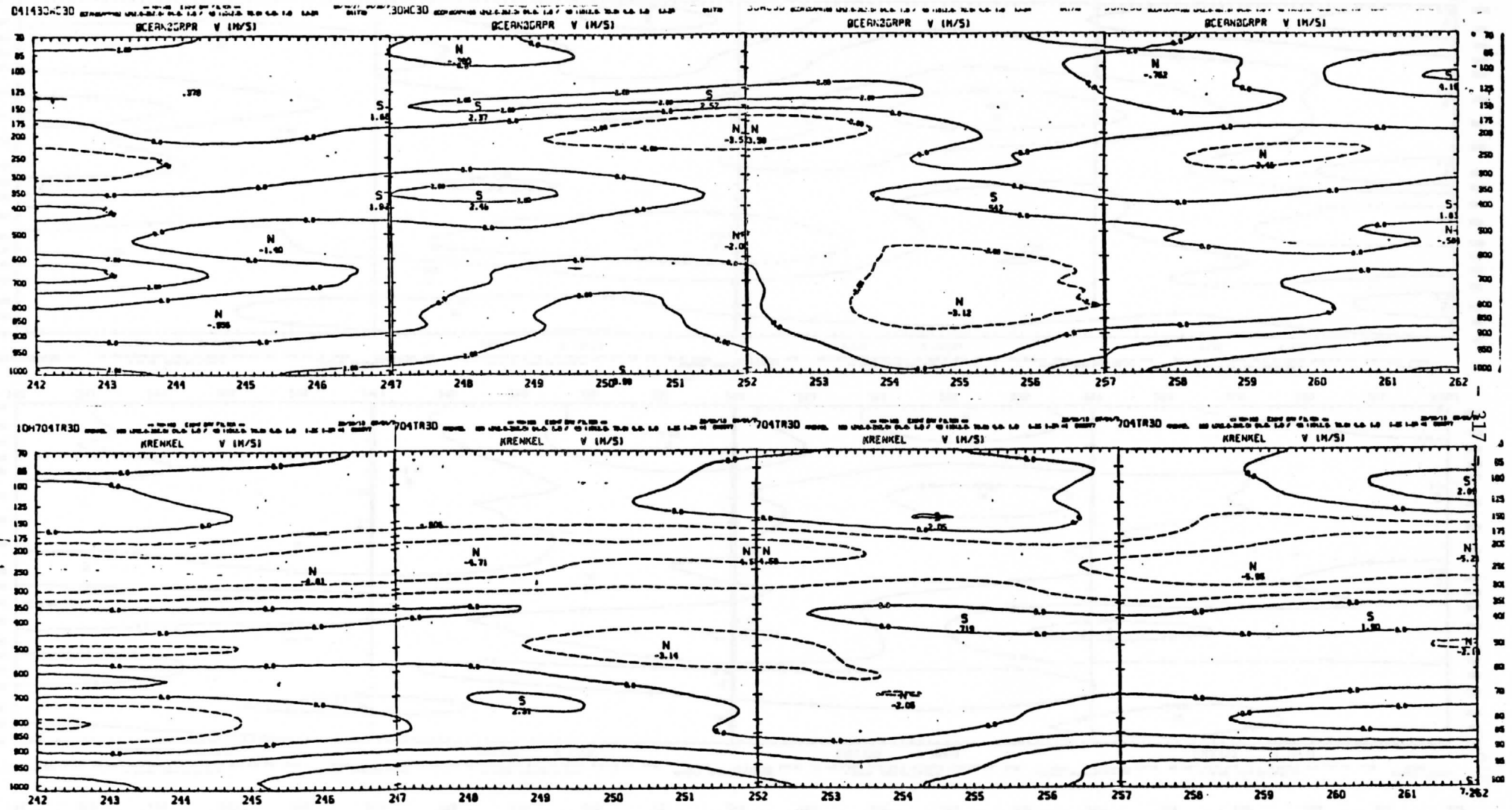
OCEAN3GRPR V (M/S)
OCEAN3GRPR V (M/S)
OCEAN3GRPR V (M/S)
OCEAN3GRPR V (M/S)
KRENKEL V (M/S)
KRENKEL V (M/S)
KRENKEL V (M/S)
KRENKEL V (M/S)

Fig. 6 b

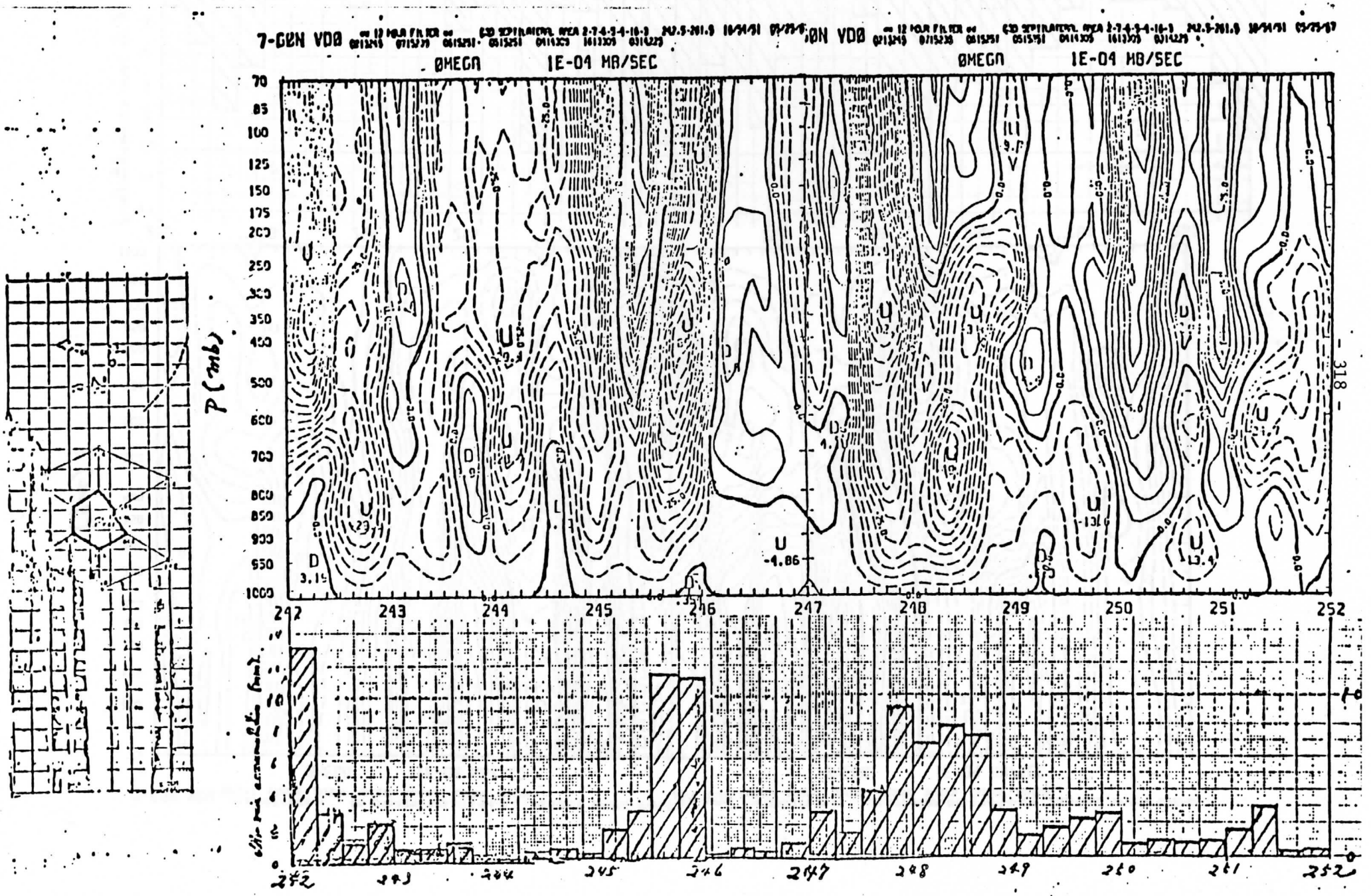

Fig 7a

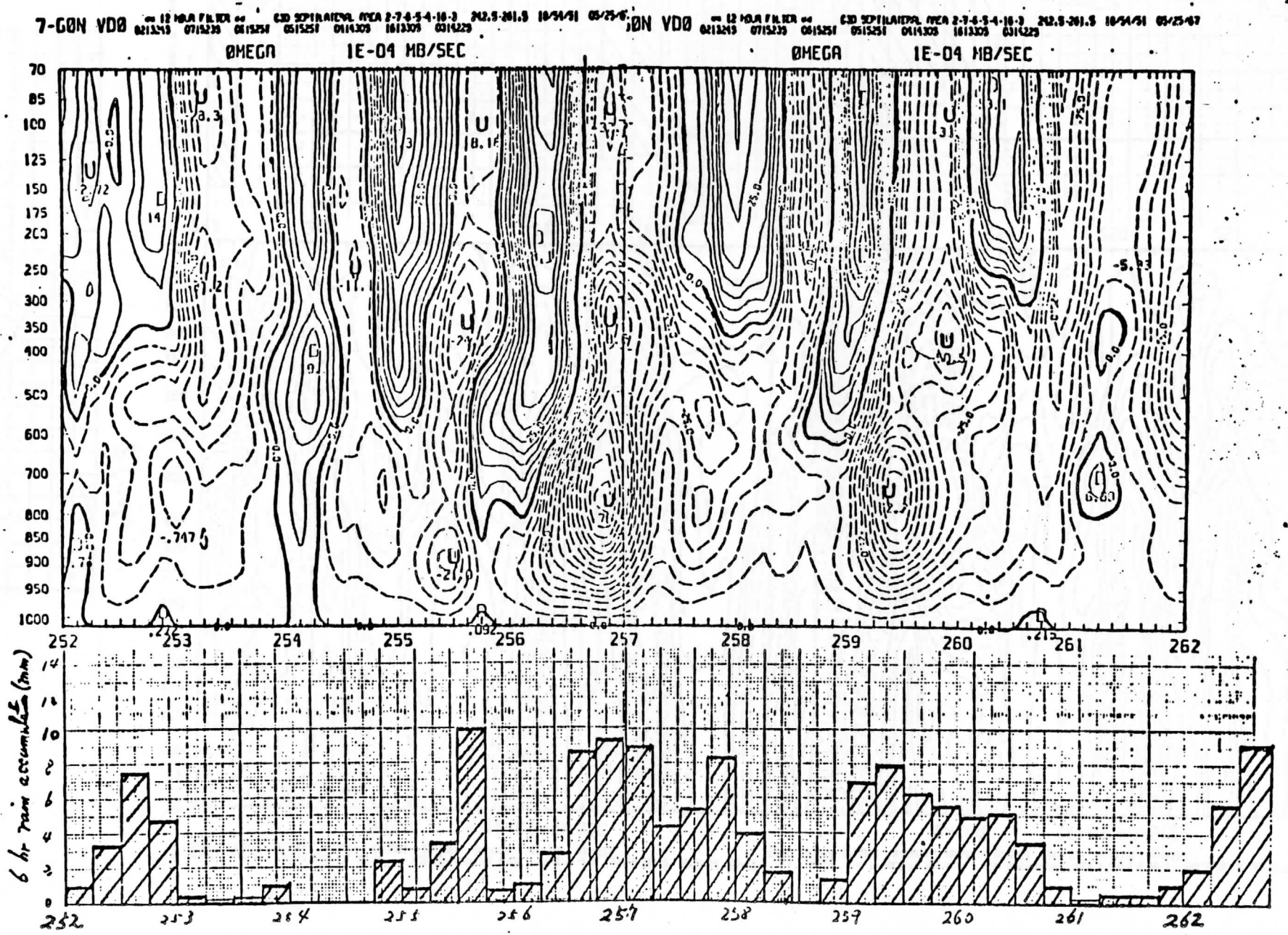
7-GØN VDØ
ØMEGA 1E-04 MB/SEC
JØN VDØ
ØMEGA 1E-04 MB/SEC
P (mb)
70
85
100
125
150
175
200
250
300
350
400
500
600
700
800
850
900
950
1000
252
253
254
255
256
257
258
259
260
261
262
6 hr rain accumulation (mm)
DAY

Fig. 16

Relative Vorticity ($10^{-6} s^{-1}$)

NW-4

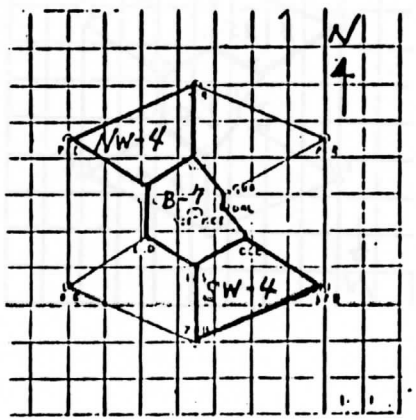

SW-4

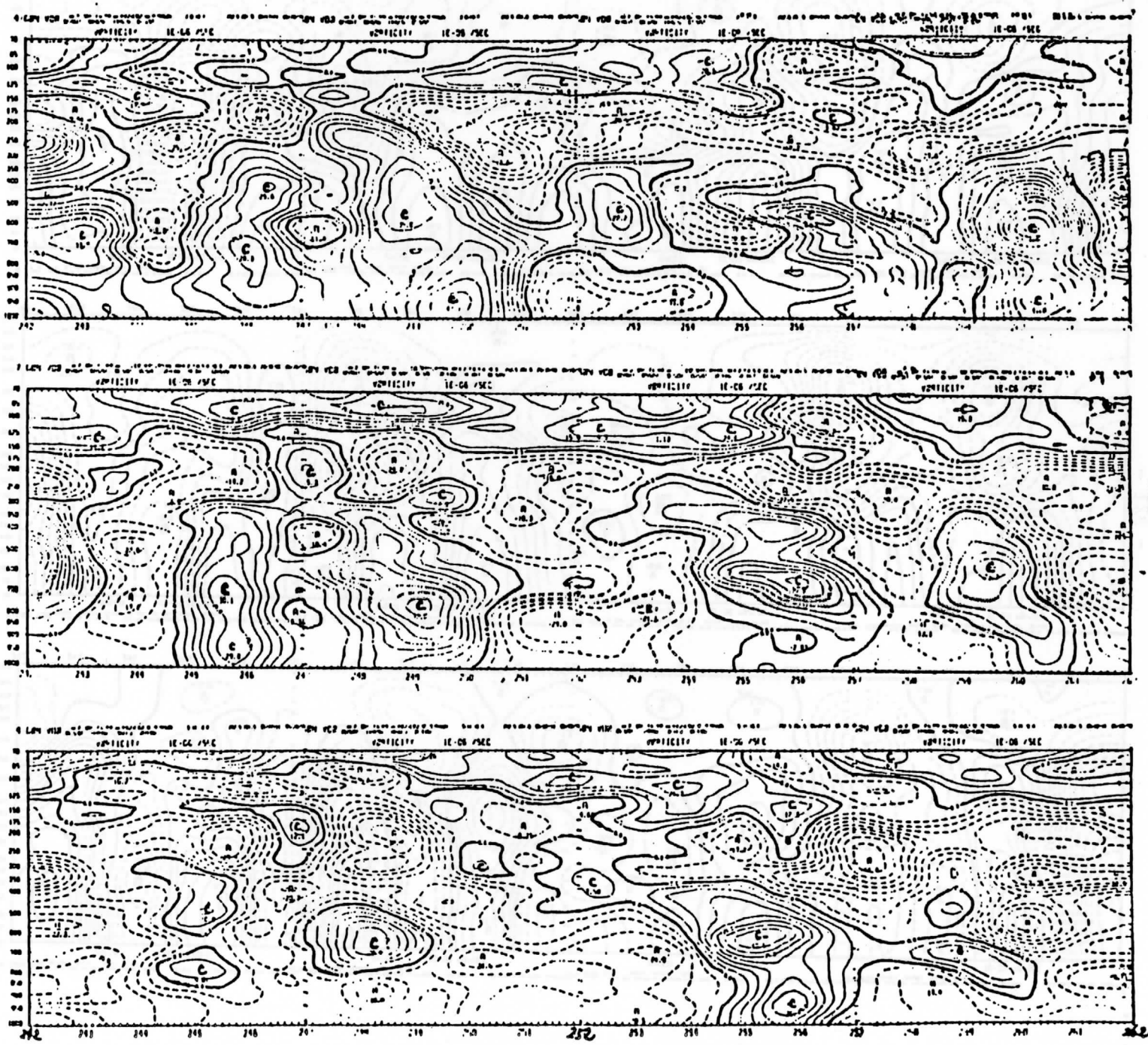

DAY

Fig. 5a

Omega (10^{-4} mb s^{-1})

NW-4

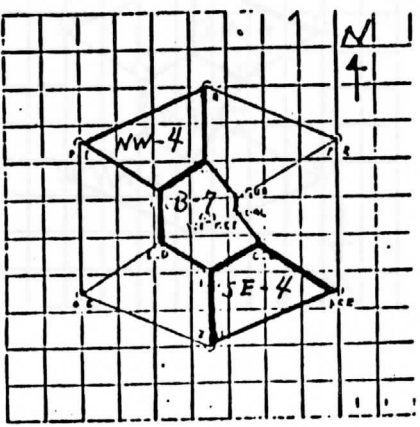

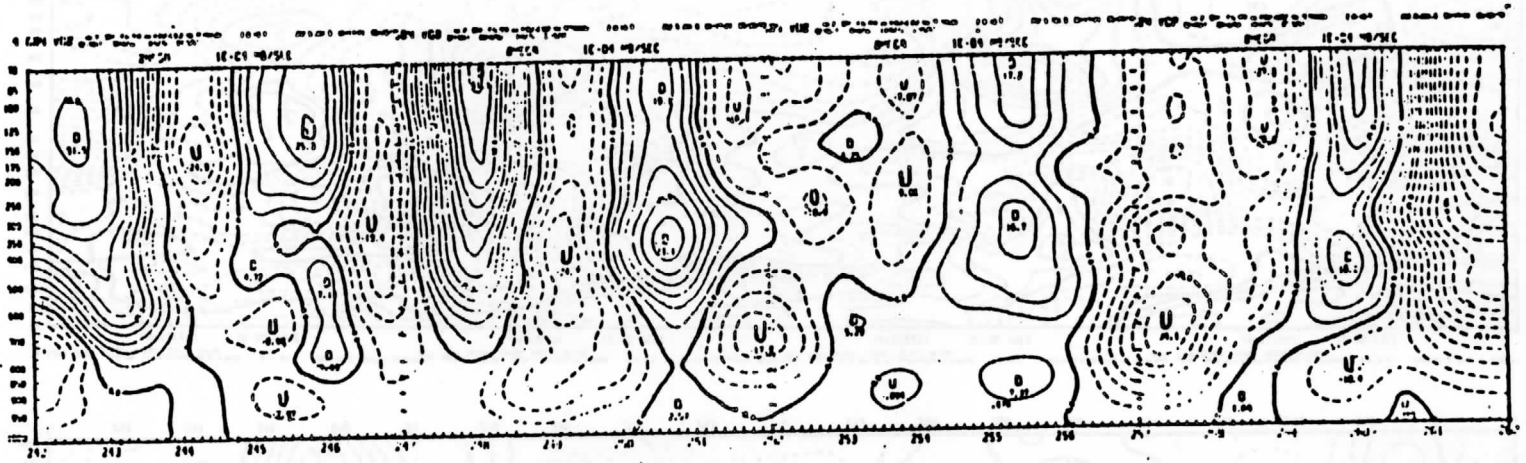

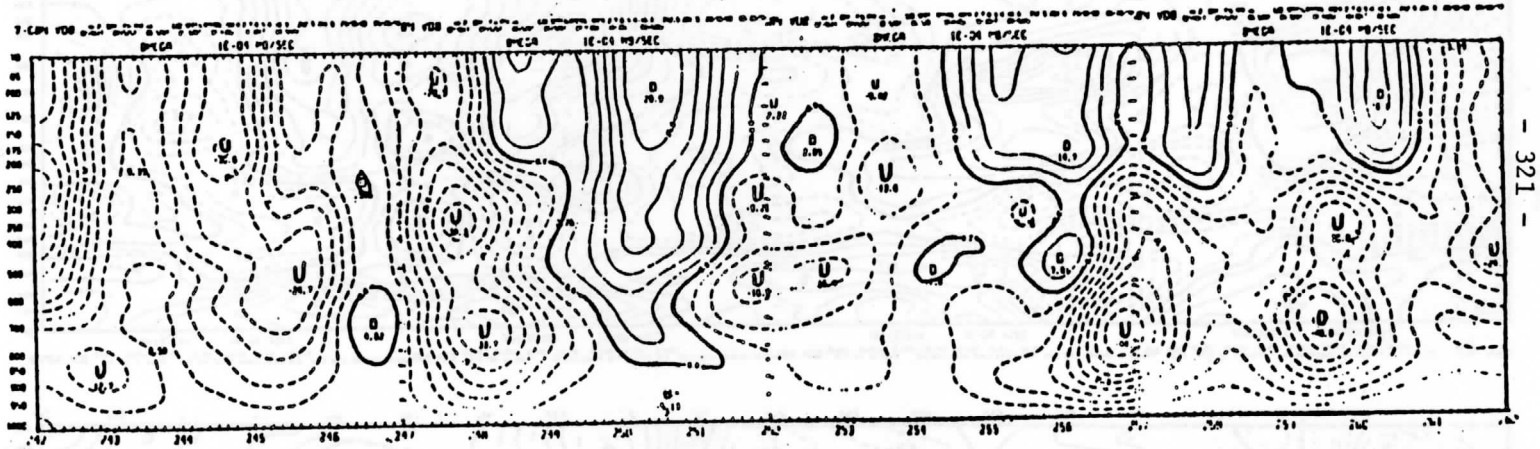

SE-4

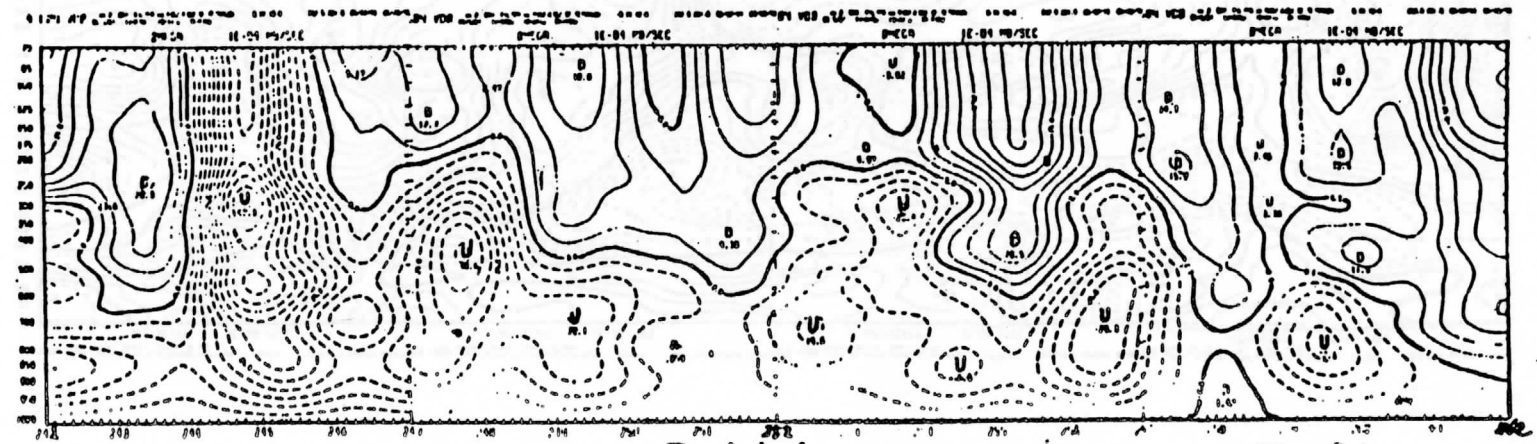

DAY

Fig 3b

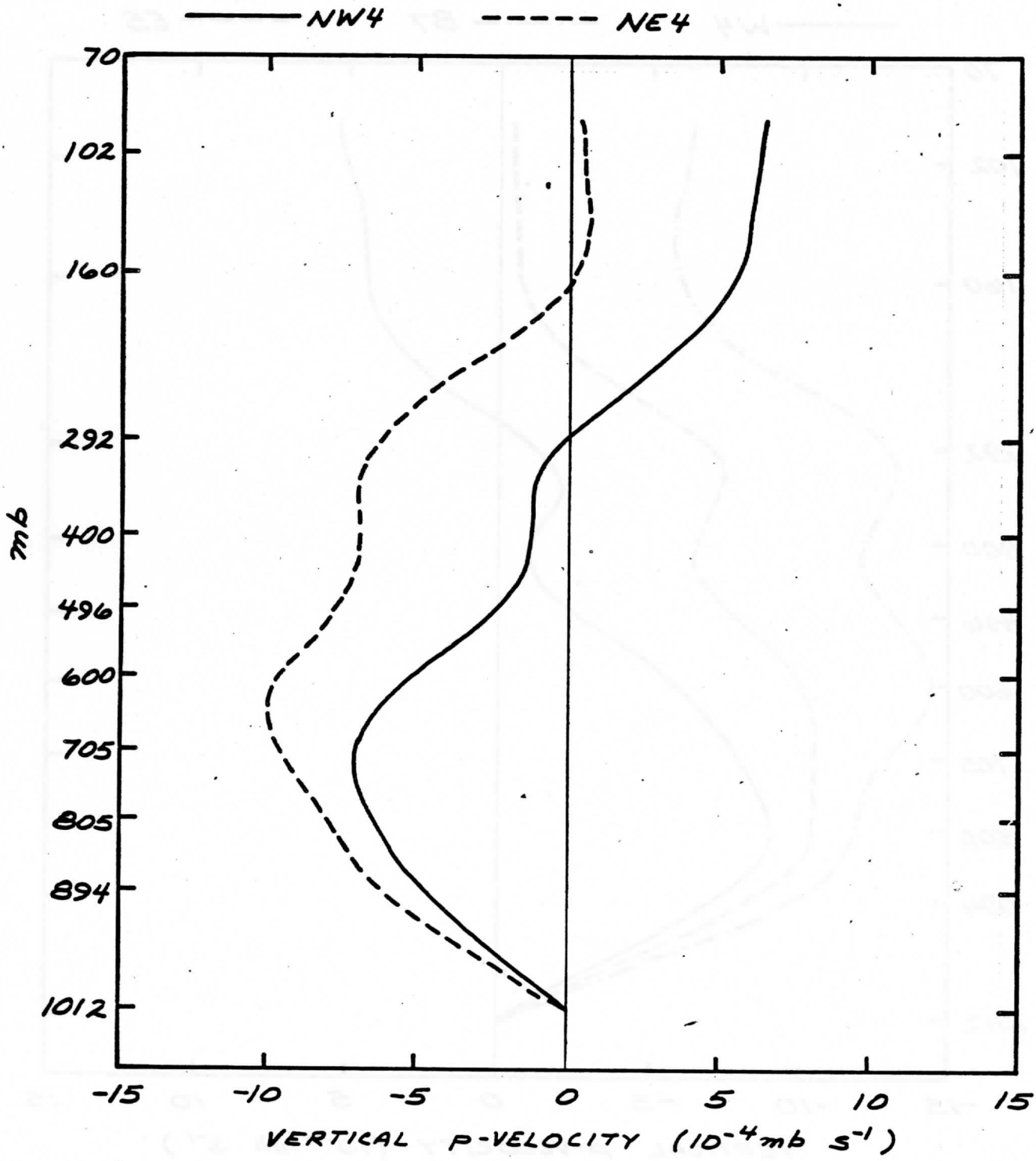
NW4
NE4
70
102
160
292
400
496
600
705
805
894
1012
mb
-15
-10
-5
0
5
10
15
VERTICAL P-VELOCITY (10^{-4} mb s^{-1})

FIG. 9a

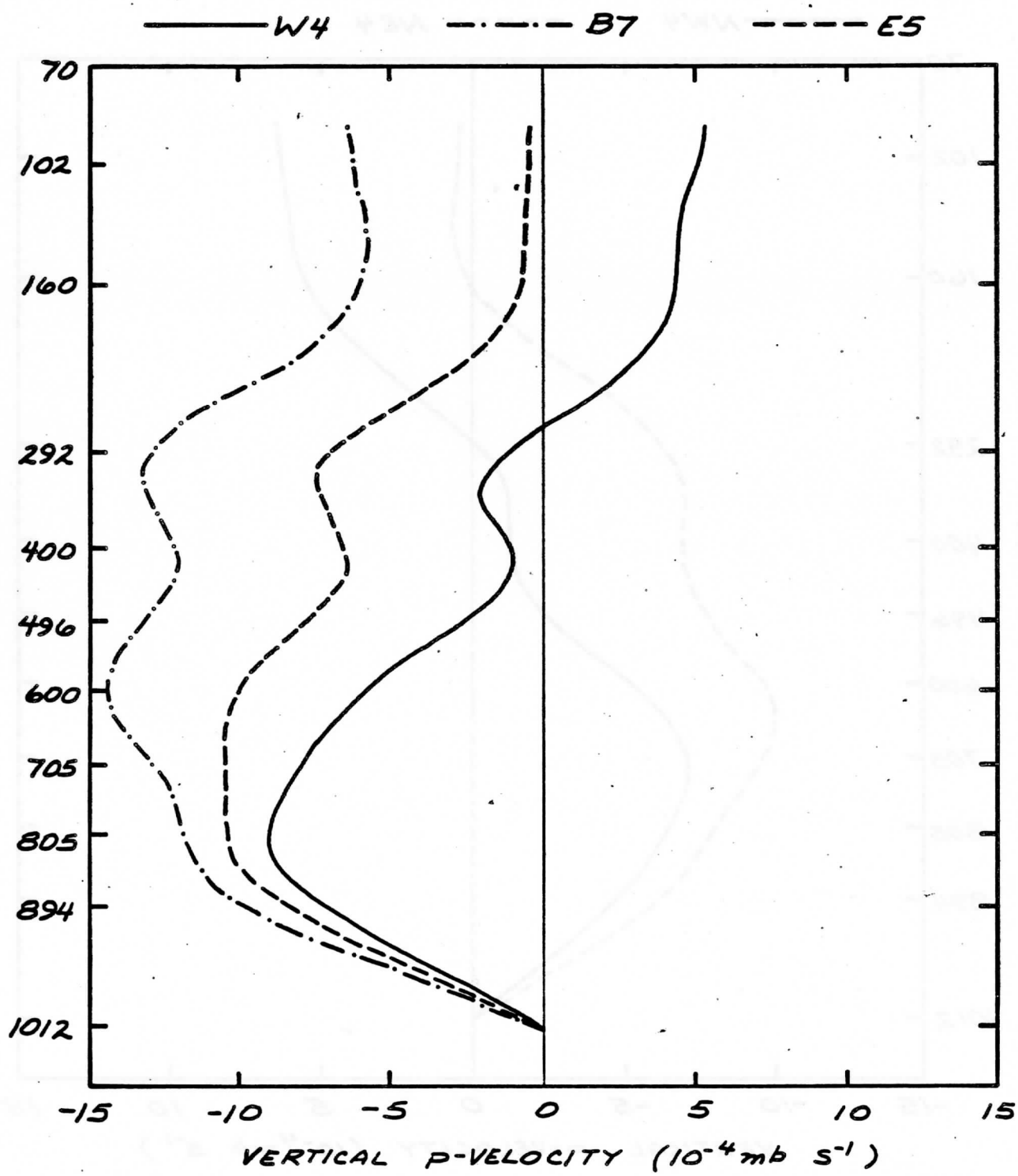
W4
B7
E5
70
102
160
292
400
496
600
705
805
894
1012
-15
-10
-5
0
5
10
15
VERTICAL p-VELOCITY (10^{-4} mb s^{-1})

FIG. 9b

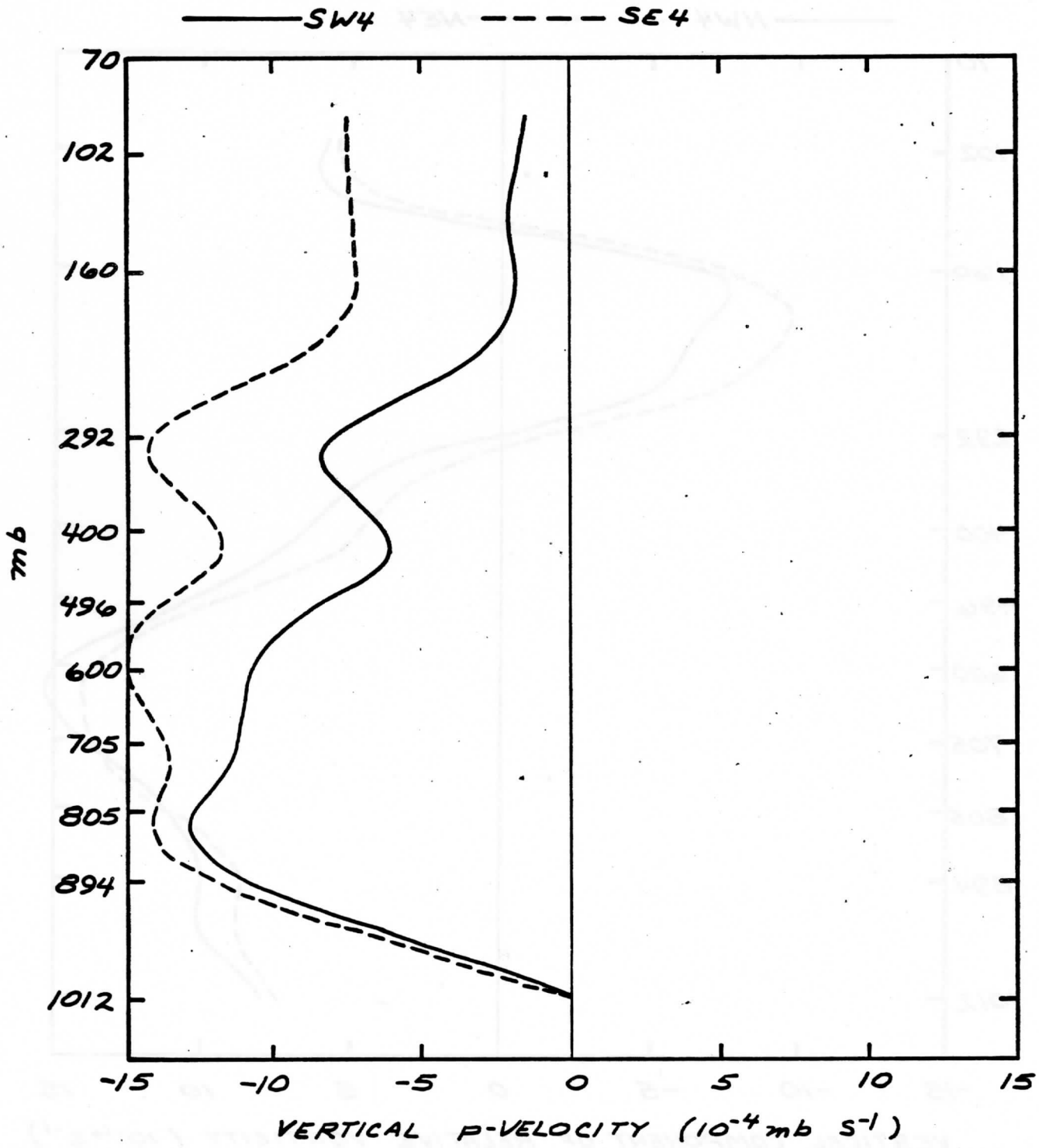
SW4
SE4
70
102
160
292
400
496
600
705
805
894
1012
mb
-15
-10
-5
0
5
10
15
VERTICAL p-VELOCITY (10^{-4} mb s^{-1})

FIG. 9c

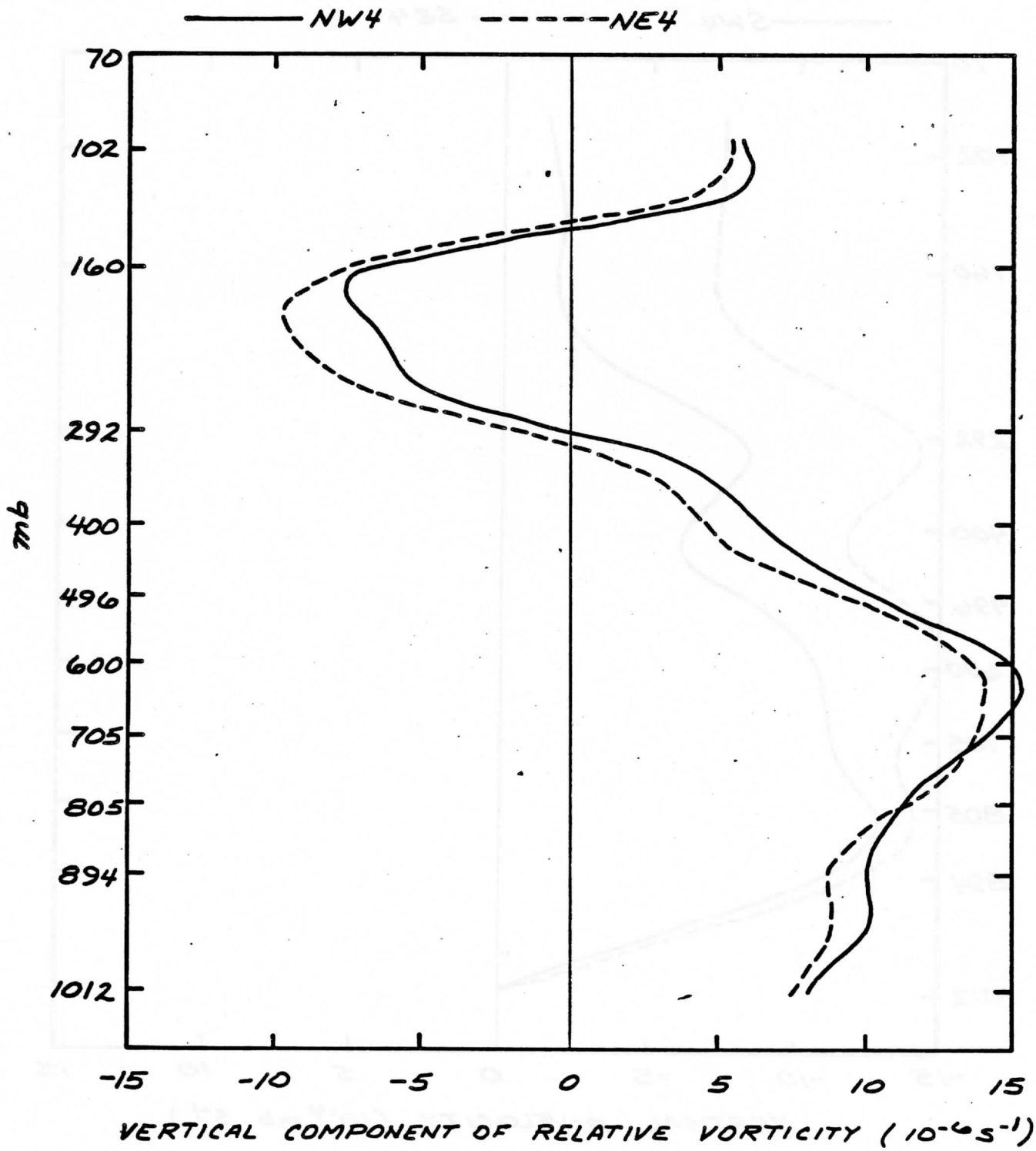
NW4
NE4
70
102
160
292
400
496
600
705
805
894
1012
mb
-15
-10
-5
0
5
10
15
VERTICAL COMPONENT OF RELATIVE VORTICITY ($10^{-6} s^{-1}$)

FIG. 10a

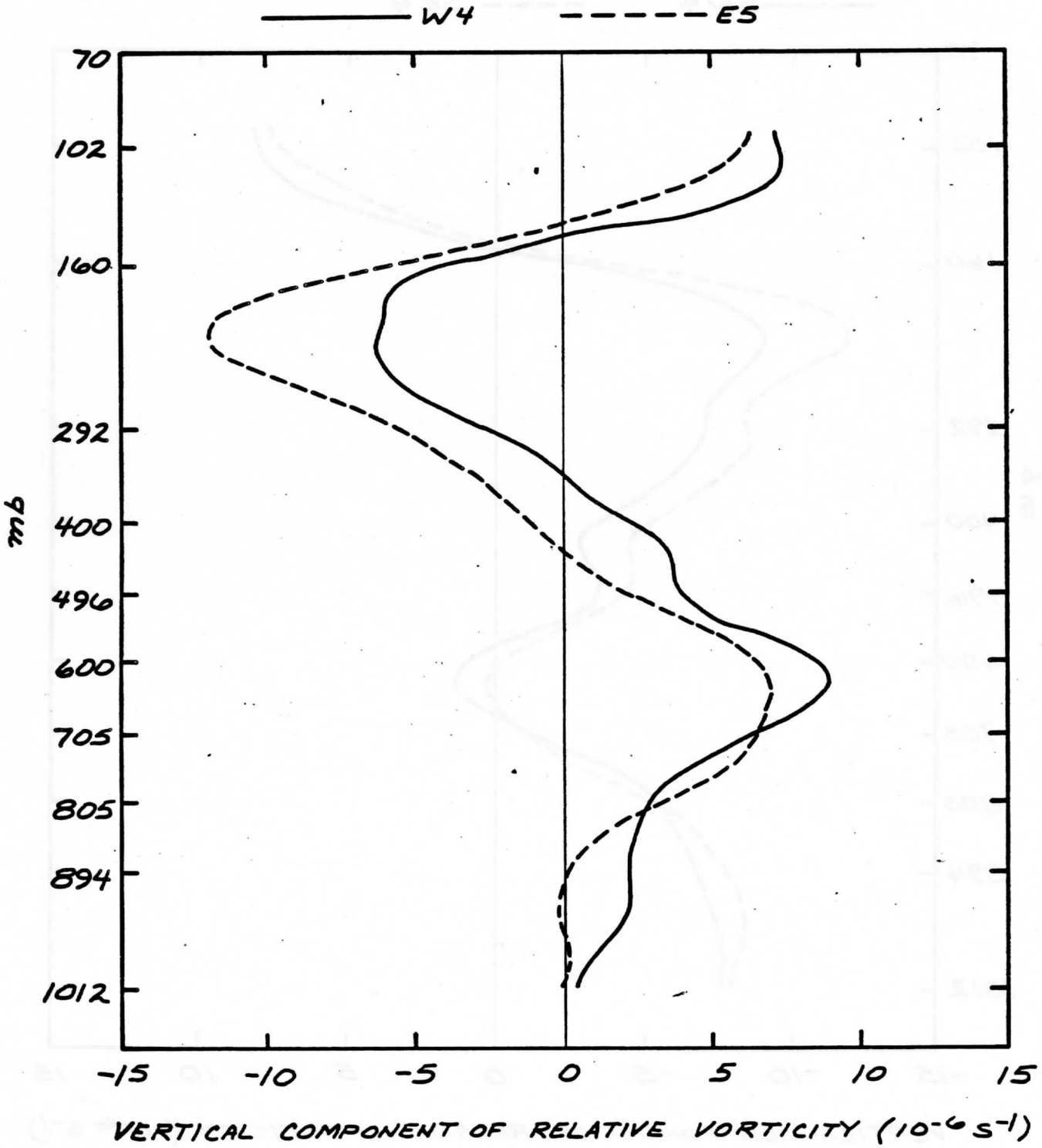
W4
ES
70
102
160
292
400
496
600
705
805
894
1012
mb
-15
-10
-5
0
5
10
15
VERTICAL COMPONENT OF RELATIVE VORTICITY (10^{-6} s^{-1})

FIG. 10 b

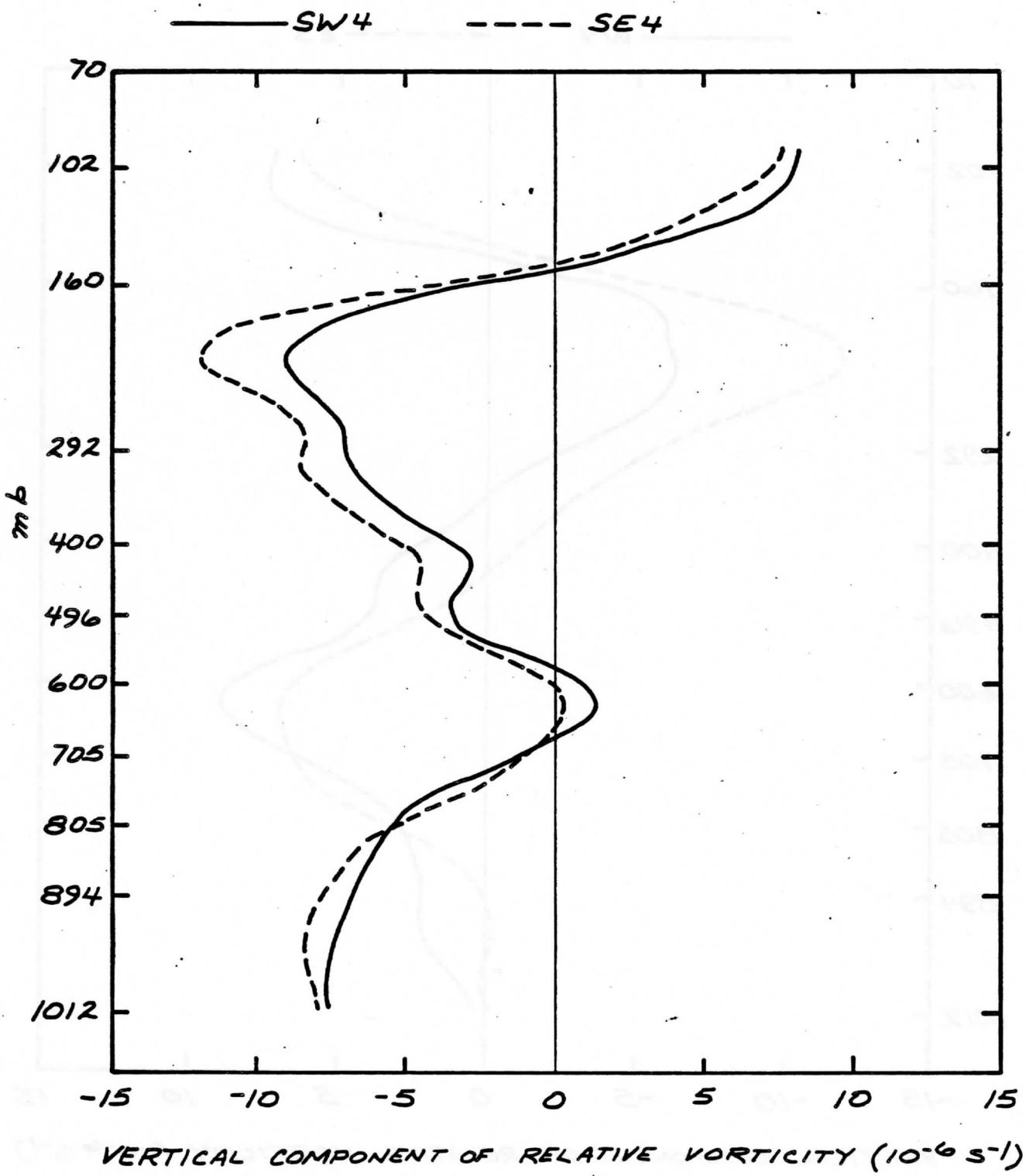
SW4
SE4
70
102
160
292
400
496
600
705
805
894
1012
mb
-15
-10
-5
0
5
10
15
VERTICAL COMPONENT OF RELATIVE VORTICITY (10^{-6} s^{-1})

FIG. 10 c

HEAT AND MOISTURE BUDGETS IN THE ENVIRONMENT OF CONVECTIVE SYSTEMS OVER THE GATE B-AREA

by

Jan-Hwa Chu
Space Science and Engineering Center
University of Wisconsin
Madison, WI 53706

Katsuyuki Ooyama
National Hurricane Research Laboratory
National Oceanic and Atmospheric Administration
Coral Gables, FL 33146

and

Steven K. Esbensen
Department of Atmospheric Sciences
Oregon State University
Corvallis, OR 97331

September 1981

ABSTRACT

The heat and moisture budgets in the environment of convective systems are computed by using the objectively analyzed wind fields, mechanically interpolated thermodynamic fields and modeled radiative divergence representing the B-area during the Phase III of GARP Atlantic Tropical Experiment (GATE). This is the first time after the field phase of GATE, the B-array upper air wind data has been successfully used together with the A/B-array wind to calculate the B-scale thermodynamic budgets. Results indicate a general agreement between the phase averaged values of diagnosed eddy fluxes of heat and moisture energy at the surface and the corresponding independent measurements. The time dependent behavior of these diagnosed fluxes well represents the situations associated with significant amounts of precipitation measured by radar.

The B-scale apparent heat source, apparent moisture sink and vertical eddy flux of total heat energy are compared with several previous studies which mainly used A/B-scale upper level winds. It is an indication of improvement that the results of B-scale budgets contain more clear information concerning the convective activities than that of A/B-scale budgets. These results from B-scale budgets are composited according to the phases of five-and-a-half wave disturbances on 700 mb, in order to compare with previous studies. The standard deviations of apparent heat source and apparent moisture sink at each wave phase are displayed to reveal the variability among these disturbances. The merits and defects of this method of composite are discussed.

I. Introduction

GATE was designed to collect a nested data set for a study of physical interactions between the cumulus convection and its large-scale environment. The Convective Subprogram Data Center (CSDC) (EDS, 1975) edited the Phase III A/B-and B-array ships upper-air and surface data. This data were used in many, by now familiar, studies: determination of the mean state of the atmosphere, studies of the structure and energetic of the composited easterly wave (Reed, 1978, Thompson et al., 1979); determination of cloud properties by using the data of composited wave (Johnson, 1978, 1980) and the data during individual times (Nitta, 1977, 1978; Cho et al., 1979); a time resolution analysis of the kinematic fields and the vertically integrated thermodynamic budgets (Reeves et al., 1979, Frank, 1979), and studies of organized convective systems (Ogura et al., 1979). Most of these studies used a quadratic surface to represent the spatial variations of wind, temperature and moisture data, the choice of that surface is a compromise one in view of the qualities of data (Ooyama and Esbensen, 1977), the number of independent measurements and the computational stability of uniquely determining those coefficients of the surface. The quadratic surface represents only one extreme over the analysis area and is equivalent to a spatial filter which filters out any variations with scales smaller than the area. The first derivative fields of the quadratic surface, such as divergence fields, over the A/B- and B-area have the same value, because of the two concentric areas which are similar in their geometric shapes. Ogura et al. (1979), on the other hand, use Cressman's successive corrections method with predetermined weighting function and the method of cubic spline under tension to analyse the fields. They used temperature and humidity data from all A/B- and B-scale ships, and winds from the A/B-scale ships and the Vanguard ship as the primary data set. The closest distance between ships

is about 50 km for both temperature and humidity and 150 km for wind. They discussed the space-time structures associated with deep convection episode. The presence of distinct low-level convergence during the initial stage of the development of deep convective systems and their spatial association have been established.

These studies have undoubtedly enriched our information on diagnostic features of the interactions between the synoptic-scale and the convective scale. Nonetheless, the results from these studies also revealed that more detailed information in space and time are needed to define the scale dependence of budget computations (Greenfield and Fein, 1977).

In this study, the B-scale heat and moisture budgets are computed using wind field analyzed by an objective scheme, temperature and mixing ratio fields analyzed by a mechanical method of surface fitting and radiation data provided by Cox at the Colorado State University. The period of study is from 00Z, 30 August to 00Z, 19 September 1974, namely, the Phase III of GATE. Data of the first and last days were discarded when time mean is computed because many observations were lacking.

2. Data

An improved objective method of space-time data analysis had been developed by Ooyama, one of the authors. This method uses a bi-cubic B-spline function on regular spaced nodes to represent a field, it two-dimensionally interpolates and filters irregularly spaced data. The analysis skill of this method is derived from the statistical information of the ships' data and is integrated into the spatial interpolation. Thus, this method was designed to take full advantage of the nested GATE A/B- and B-scale data in order to preserve both temporal and spatial continuties of the observed disturbances and to eliminate the the spatial aliasing due to the undersampling of the small scale phenomena, such as convection. This method had been applied to

A/B- and B-array ship wind data which were edited by CSDC and further corrected by the authors. The final wind data set used in this study represents 450 km, 100 mb and 12 hour filtered field which are approximately equivalent to the 225 km, 50 mb and 6 hour running averaged field. The data are represented on 41 pressure levels from 1012 mb to 70 mb, there are 19 x 19 grids (Fig. 1) on each of the pressure surface and total 161 grids in time with 3 hour intervals.

Analysis of the A/B- and B-array ship upper-air moisture and temperature data indicated that there are ship-to-ship bias on the time averaged fields and unrealistic information among their time deviation fields (Ooyama and Esbensen, 1977). One of the authors (E) has already removed the obviously erroneous data in the deviation fields of the data.

For the time being we used the following steps to obtain the field of mixing ratio (q) from the edited ship data: first, replace ship Vize's (ship no. 1 on Fig. 1) time mean q by a spatial average of time mean q at ships 2, 3, 4, 5 and 7 with weighting which is proportional to the inverse of relative distance, and then replace ship Bidassoa's (ship no. 6) time mean q by the spatial average of q at ships 1, 5, 7 and 12. Second, use a linear surface to represent the time mean q field and use a quadratic surface to represent the band-pass filtered q field, the filter picks up signals with the period from 12 hours to the mean. These surfaces were determined by using least square method with equal weight for each ship data. The same method was used for ships' temperature data except the Zubov's (ship no. 11) temperatures above 208 mb were also discarded in the first step. The temperature and mixing ratio fields analyzed by the method of mechnical surface fitting represents 1000 km, 100 mb and 12 hour filtered fields. The first step was used to eliminate the obvious ship-to-ship bias on the time mean T and q, and the second step does not necessarily imply that the spatial

variations of time mean fields are less than that of the banded field. The treatment of the thermodynamic data is not as rational as that of the wind. Because the physical bases linking between these selected surfaces and the spatial variations of data were not studied carefully. However, it is adequate for the thermodynamic budget studies over the B-area, because the vertical advection term is the dominate one in the budget components.

The gridded hourly radiation data computed by Cox and Griffith (1979 a, b) consists of ten vertical layers from 1000 to 100 mb and represents A/B-area with 1/2 degree latitude as grid distance. The GATE radar precipitation available from Hudlow and Patterson (1979) and the B-area ships' hourly surface observations were used to compute the surface sensible and latent heat fluxes.

3. Results

a. Vertical p-velocity and static energy

The time mean of mass balanced vertical p-velocity ω, averaged over these grids representing B-area and A/B-area (Fig. 1) and their standard deviations are shown in Figure 2. The mean ω of B-area and A/B-area at 102 mb without mass balance imposed is 1.35×10^{-4} mb/s and 0.98×10^{-4} mb/s, respectively. Both values are less than that obtained by Reeves et al. (1979). The time mean profiles of ω for two areas are similar, both have maximum and a secondary peak at 650 mb and 350 mb. The A/B-area ω is very similar to those obtained by Nitta (1978) and Reeves et al. (1979). Two layers of time mean convergence, the lower one is between 1012 mb and 800 mb levels and the middle one is between 430 mb and 370 mb levels, contribute to the vertical profile of ω. The main difference between B-area and A/B-area ω is their time variabilities, especially within the layer between 800 mb and 300 mb levels. Such a difference reveals that the statistically optimal analysis method designed by

Ooyama has an advantage over the method of quadratic surface fitting. The standard deviation of ω for A/B-area is about 30% less than that obtained by Reeves et al. (1979). The power spectra of B-area ω (not shown) confirms that the diurnal variation of ω contributes significant power to the total variance. Here the standard deviation was used only to measure the time variability of the parameter and regardless of the shape of its histogram.

The time mean vertical profiles of the dry static energy $\bar{s}$, moist static energy $\bar{h}$ and saturation moist static energy $\bar{h}^*$ representing B-area are shown in Figure 3. The $\bar{h}$ is much greater than $\bar{s}$ in the lower troposphere where moisture concentrates. The profile of $\bar{h}$ has a minimum at 650 mb. The standard deviations of $\bar{s}$ and $\bar{h}$ are one to two order of magnitude smaller than their time means, that is contrary to the characteristics of time variations of vertical p-velocity. The vertical gradient of $\bar{h}^*$ is a gross measure of static stability of satureated air whenever the hydrostatic approximation is valid or the non-acoustic motion is considered. The mean $\bar{h}^*$ shows three neutral layers around 400 mb, 600 mb and 800 mb levels. The mean unstable layer extends from the surface up to 600 mb. Figure 3 also shows that the vertical profiles of mean $\bar{s}$, $\bar{h}$, and $\bar{h}^*$ in the GATE area and those in the Marshall Island area (Yanai et al., 1973) are different in two ways: first, GATE area has systematically lower values of $\bar{s}$, $\bar{h}$, and $\bar{h}^*$ throughout the entire troposphere; second, the atmosphere in the GATE area is more thermodynamically stable below 600 mb. Similar facts were pointed out by Gray (1977) and Thompson et al. (1979).

b. Apparent heat source, apparent moisture sink and net radiation

Following Yanai et al. (1973), the apparent heat source Q_1 and apparent moisture sink Q_2 consist of the local change, horizontal and vertical advections of dry static energy and of moist energy, respectively. The time mean

profiles of those terms and the net heating rate due to the radiation Q_R are shown in Figures 4a and b. The vertical advection terms are dominant in both heat and moisture budgets, and an accurate vertical p-velocity is a key factor for determining these terms. The horizontal advection of temperature has a maximum at the upper troposphere owing to the strong wind there, and the horizontal advection of moisture energy has a peak around 700 mb because of drier air being advected into the B-area by the easterlies between 500 and 800 mb and by the low level monsoonal flow below 900 mb. A similar conclusion was found by Frank (1979). In the cloud layer, the cumulus convection is hypothesized as the mechanism to consume moisture Q_2 as fuel and to convert the fuel into heat Q_1. The magnitudes of Q_1 and Q_2 are different from the results computed by Nitta (1978) and Thompson et al. (1979). This difference is ascribed to the different methods by which wind fields and vertical p-velocity were analyzed. The standard deviations of Q_1 is due to the time variations of the local change and the vertical advection of $\bar{s}$ in the upper troposphere, and of the vertical p-velocity. The standard deviation of Q_2 is due to time variations of the local change of moisture in the layer below 400 mb and of the vertical advection of moist energy. The diurnal variation of net radiation has a sizable magnitude of 0.5 to 1.0 Deg.C/day (Gray and Jacobson 1979), and is the major part of the standard deviation of Q_R (Fig. 4a).

Several studies computed the heat and moisture budgets for individual periods, only one case was used to compare with the result from current study. Figure 5 shows the time averaged vertical profiles of B-area vertical p-velocity together with apparent heat source and moisture sink during the period from 00Z, 7 September (Day 250.000) to 18Z, 8 September (Day 251.750) this period was classified as relatively undisturbed case by Cho et al. (1979), according to the phase of a wave disturbance, the infrared imageries of

satellite cloud pictures and the surface precipitation measurements.

In Figure 5, B-area ascending motion is found below 400 mb with a maximum and a secondary peak around 670 mb and 900 mb, respectively. The magnitude of this motion is much weaker than the mean ascending motion during the Phase III (Fig. 2). Two distinct layers of positive Q_2 representing the drying effect locate from 800 mb to 400 mb and from 950 mb to 800 mb. The positive Q_1 corresponding to warming effect is found from the surface up to 400 mb. These results obtained with the newly analyzed wind data are physically realistic when one imagines that the major convective activities during a weakly disturbed period are confined below 400 mb and hypothesizes that the collective effects from these convective clouds are net drying and warming. The results show clear improvement over that of previous studies. Using different net radiation data, both studies computed the surface eddy flux of total heat energy, the value of current study is 181 W/m^2 and that of Cho et al. (1979, Table 1) is 179 W/m^2. The agreement between these vertically integrated fluxes is very close and perhaps somewhat fortuitous in view of the quite different vertical profiles of ω, Q_1 and Q_2 of this study and that of Cho et al. (1979, Figures 6 and 7). It is important to mention that an agreement on the surface eddy fluxes of total heat energy does not warrent an agreement on the vertical distributions of apparent heat source or apparent moisture sink.

C. Vertical eddy fluxes of heat and moisture energy

The vertical eddy flux of heat energy F_s, of moisture energy F_{Lq} and of total heat energy F_h are computed by the vertical integration of $Q_1 - Q_R$, Q_2 and $Q_1 - Q_2 - Q_R$, respectively. These eddy fluxes are assumed to be zero at 102 mb level near the tropopause. Figure 6 shows the time mean profiles of these fluxes. Both F_s and F_{Lq} have maximum near the surface and decrease upward. They almost vanish above 250 mb level. A positive F_h indicates an

upward heat transport which is postulated as the collective effects of sugrid-scale cumulus convection. The mean profile of F_h has a maximum (150.2 W/m^2) at 800 mb level and a secondary peak (138.7 W/m^2) at the surface. This maximum value is 20 W/m^2 greater than that of phase averaged F_h of the composite wave (Thompson et al., 1979, Figure 20a).

Three time averaged vertical profiles of B-scale vertical eddy flux of total heat energy F_h are shown in Figure 7, for the purpose of comparing with the A/B-scale F_h during the three periods studied by Nitta (1977). These periods were classified according to the activities of cloud clusters and the magnitude of A/B-scale vertical p-velocity, namely, mature stage, decayed stage and unorganized cluster stage. Figure 7 depicts that the F_h during the stage of mature cloud cluster is two to three times greater than that of the decayed stage within the layer from 900 mb to 400 mb; a significant amount of F_h still remain above 400 mb level. The positive F_h of the unorganized cloud cluster stage is due to the vertical transport of the net heat energy of the shallow convective cloud below 600 mb. The small negative values of F_h over a deep layer indicate an uncertainty on the order of 10 W/m^2. Two obvious differences between the B-scale F_h of this study and the A/B-scale F_h (Nitta, 1977, Figure 8) are noticed; first, the maximum of B-scale F_h during the mature stage is 45% greater than that of the A/B-scale F_h; second, the values of B-scale F_h of decayed stage and of unorganized stage are more similar than that of A/B-scale F_h of these two stages. Since the averaged area of GATE active cloud cluster, viewed from the infrared satellite cloud picture, is compatible with the B-scale area, the B-scale F_h certainly represents clearer information associated with cloud cluster than the A/B-scale F_h does. Thus, the current data set is especially suitable to study the interactions between cloud cluster and its large-scale environment.

Following Nitta (1972) and Yanai et al. (1973), the surface values of these vertical fluxes, F_{so}, F_{Lqo} and F_{ho}, are approximately equal to the surface measurements of $LP_o + S_o$, $L(P_o - E_o)$ and $LE_o + S_o$, respectively, where L is latent heat of condensation, P_o is the precipitation amount obtained from the B-area radar rainfall data (Hudlow and Patterson, 1979, area No. 10), E_o and S_o are the surface fluxes of evaporation and sensible heat which were computed by using the bulk aerodynamic formulas to the hourly surface observations of seven B-area ships and then taking spatial and temporal averages. Businger and Sengnin (1977) suggested that the bulk coefficients for E_o and S_o are 1.6×10^{-3} and 1.4×10^{-3}, respectively. For comparison, the mean fluxes are summarized as following: $F_{so}/(LP_o + S_o) = 407./375.$, $F_{Lqo}/L(P_o - E_o) = 268./249.$, $F_{ho}/(LE_o + S_o) = 139./126.$, where all units are W/m^2. The diagnosed mean energy fluxes are 10% greater than the mean "ground truth".

The three hourly surface fluxes of heat, moisture and net heat energy together with their corresponding ground truth are shown in Figures 8a, b, and c. In view of the time variations of F_{so} and F_{Lqo}, it is concluded that the B-area budgets do represent the situations associated with significant amount of precipitation. The most obvious disagreement occured around days 251 and 252. A disturbance with period about 2.5 Day moved through the A/B-area according to Thompson et al. (1979). Nitta (1978) pointed out that the meridional component of wind associated with this disturbance is weaker than those of the others because of the center of this disturbance locates far northward from the A/B-area. In this study, significant amounts of cloudiness and precipitation were found to be in phase with a secondary ascending portion associated with the disturbance but not the primary one. The standard deviations of F_{so} and F_{Lqo} are 344.8 W/m^2 and 343.8 W/m^2 and that of $LP_o + S_o$ and $L(P_o - E_o)$ are 397.9 W/m^2 and 380.3 W/m^2. The time variability of vertical

p-velocity almost determines the variations of F_{so} and F_{Lqo}, and the precipitation P_o dominates heat and moisture energy fluxes. The similar content of Figure 8a but for the A/B-scale was shown by Frank (1979, Figure 6) and of Figure 8b by Thompson et al. (1979, Figure 24). Despite a close agreement on the gross features in those figures, it is unfeasible to compare them in detail.

The net heat flux at the surface F_{ho} is essentially the difference between two large values of F_{so} and F_{Lqo}, its standard deviation is 165.4 W/m^2 and is much greater than 38.6 W/m^2, the standard deviation of $LE_o + S_o$. Figure 8c together with a scatter diagram (not shown) of F_{ho} versus $LE_o + S_o$ indicate the unrealistic features: there are 29 cases of negative F_{ho} out of a total 145 cases, 39 cases of large values of F_{ho} exceeding 250 W/m^2 and 10 cases of small positive values of F_{ho}. The range of error is possible to guess but is not meaningful because many sources of errors associated with data, methods of data analysis and of budget computations are unknown or uncertain. However, this puzzling fact should not hamper further study using the results from budget computation, under the conditions that the results were scrutinized in order to discard the obviously erroneous and suspicious results, then average or composite methods can be used to sharpen the information content of the results.

d. Analysis of stratified data

In order to compare some results of current study with that of Thompson et al. (1979), the heat and moistrue budgets were further stratified according to wave phases designated by them. These phases had been verified using the 2- to 8- day band-pass filtered meridional components of winds on 700 mb, a remarkable agreement was found except for a trough passing the B-area on day

256, 09Z which is six hours earlier than that assigned by Thompson et al. (1979). Figures 9a and b show the cross-sections of the apparent heat source Q_1 and its standard deviation for each wave phase. The maximum of Q_1 of 9.0 Deg.C/Day is found at 700 mb level in the trough and the magnitude of Q_1 decreases toward the ridges. In the upper troposphere the Q_1 is negative except for the wave phase 3. Q_1 has a minimum of -3.5 Deg.C/Day at 175 mb level in the wave phase 7, this is too large to count for the radiative cooling effects and is considered as error. The standard deviations of Q_1 have significant values within the middle layer in the wave phases 1 to 5. The cross-sections of the apparent moisture sink Q_2 and its standard deviations are shown in Figures 10a and b. The maximum of Q_2 is 11.3 Deg.C/Day and happens at 900 mb in the wave phase 3. Standard deviation of Q_2 shows maximum at wave phase N. Both cross sections of Q_1 and Q_2 are similar to the results computed by Thompson et al. (1979), except the heights of maximum Q_1 and Q_2 of this study are lower by 100 mb at trough and 20 mb at wave phase 3 than that of theirs. The net heat energy flux F_h has a maximum of 275 W/m^2 on 773 mb at wave phase 3, the value is about 30 W/m^2 greater than that obtained by Thompson et al. (1979, Figure 20a). The net radiative heating rates Q_R for composite wave had been discussed by Johnson (1980), here we only report that the standard deviations of Q_R exceed 1 Deg.C/Day between the layers from 530 mb to 300 mb in wave phases from 3 to 7. Comparing Figure 9a with Figure 10a, it is found that the axis of maximum Q_1 has little vertical tilt, but the axis of maximum Q_2 clearly tilts eastward with height at the wave phases 3, T and 5. Similar features were also depicted by the composite results of Thompson et al. (1979), however, these features are not common among wave disturbances; it was found that these features exist only during the two phases of trough around days 245.625 and 256.500 by inspecting the time-height cross sections of Q_2 (not shown).

The surface fluxes F_{so}, F_{Lqo} of each wave phase are shown in Figure 11 and compare with the results of Thompson et al. (1979, Tables 3 to 6) and of Johnson (1980, Table 2). By and large, results from those studies well resemble the ground truth. F_{so}, F_{Lqo} and F_{ho} of the current study have good agreement with the ground truth at wave phases N to 5 and 7. Thompson et al. (1979) used the radiation data from Gray and Jacobson (1977) and Johnson (1980) used radiation data from Cox and Griffith (1979b) for the computation of F_{ho}, the latter achieved good agreement with $LE_o + S_o$ at wave phases 6 to R, 1 and T. It is concluded that both of the B-scale and A/B-scale heat and moisture budgets are able to reflect the signature of composite wave, however, the B-scale budget is generally more reliable in the phases N, 3, T and 5 where the precipitation rates are high (Thompson et al., 1979, Figure 18).

4. Conclusions and Discussions

The GATE B-area heat and moisture budgets are computed using the newly analyzed wind field, the thermodynamic data and Cox and Griffith's gridded radiation data during the Phase III. This is the first time B-scale wind fields were used to study the thermodynamic budgets and the vertically integrated energy fluxes. The vertical p-velocities of B-scale and A/B-scale have similar time mean values of the Phase III but different standard deviations. The time averaged vertical eddy fluxes of heat and moisture energy at the surface agree within 10% of the corresponding surface measurements. The time dependent behavior of both eddy fluxes reflect the situations associated with strong convectivities. The B-scale heat and moisture budgets of this study contain more clear information concerning the convective activities than that of A/B-scale budgets obtained in previous studies. The individual period averaged apparent heat source and apparent moisture sinks show realistic vertical distributions. The surface eddy flux of total heat energy were composited

according to the phases of wave disturbances; results show a close agreement with the sum of surface eddy fluxes of latent and sensible heat at the trough region of the composite wave. It is fair to state that a definite improvement on the thermodynamic budgets is found by using this data set.

A unique potential of this set of data lies in their rich and detailed information content, such as the spatial variations of wind fields associated with convective systems, such data enables us to study the spatial distributions of the budget components and to answer the question concerning the scale dependent of budget computations, particularly A/B- and B-scale.

The aforementioned mechanical method of surface fitting are far from satisfactory. First of all the temporal and spatial characteristics of the temperature and mixing ratio fields are different from that of the wind, and have to be studied so as to confirm the basis linking the surface and the spatial variations of data together or to make statistically optimal interpolation in space. The full potential of this data can then be enhanced for the purpose of studying the physical interactions between the convection and its large-scale environment.

During the course of this study, we realized that the composite method employed by Thompson et al. (1979) is a powerful way to enhance the common features associated with the traveling easterly waves in the layer of maximum wave amplitude. Certain impression one may gather from the composite wave is that the horizontal velocity fields have great symmetry with respect to the location of trough, the vertical p-velocity around the trough has two peaks on 350 mb and 775 mb respectively, the relative vorticity at wave trough decreases upward by $30 \times 10^{-6} s^{-1}$ from 700 mb to 200 mb and each phase of the

composite wave lasts for about eleven hours. However, we learned that certain primary variables describing the state of the individual wave, such as the period of wave, the location of extreme vertical motion and relative vorticity associated with wave phases, are quite different from the corresponding composite results. It is known that the wave phase N during Day 255 persisted about thirty hours. In addition, since the averaged wavelength is about three to four times greater than the size of the A/B-area, the composite results is a synthesis of the snapshot pictures describing a portion of the somewhat different five-and-a-half wave disturbances. When the composite wave was interpreted as statistic result, the overall confidence to the wave might not be as high as one hoped. Therefore, each individual wave deserves a detail case study. Furthermore, the other alternative methods of composite, such as composite according to the stage of convective events (William and Gray, 1973; Frank, 1978) and the convective code (Martin, 1975), may well be worthwhile to explore in order to make good use of the valuable potential of this data.

Acknowledgements

Special gratitude is due to Dr. David W. Martin at Space Science and Engineering Center (SSEC), University of Wisconsin at Madison, for his encouragement throughout the course of this work and his careful improvements on the manuscript. Thanks also extended to Mr. Cecil Lo at SSEC for his invaluable design in data processing and programming. The radiation data was kindly made available by Dr. Martin from Professor Stephen K. Cox of the Colorado State University. This research was supported by the National Science Foundation under Grants ATM78-05951 and ATM80-20895 and by the National Aeronautics and Space Administration under Contract NAS5-23462 to the University of Wisconsin at Madison, and National Science Foundation Grant ATM78-18805 to the Oregon State University.

REFERENCES

Businger, J., and W. Sequin, 1977: Transport across the air-sea interface: Sea-air surface fluxes of latent and sensible heat and momentum. Report of the U.S. GATE Central Program Workshop, NCAR, Boulder, Colorado, 441-453. [Available from the GATE Project Office, NOAA, Rockville, MD.]

Cho, H.-R., R. Bloxam and L. Cheng, 1979: GATE A/B-scale budget analysis. Atmos. Ocean, 17, 60-76.

Cox, S. K., and K. T. Griffith, 1979a: Estimates of radiative divergence during phase III of GARP Atlantic tropical Experiment: Part I. Methodology. J. Atmos. Sci., 36, 576-585.

_____, _____, 1979b: Estimates of radiative divergence during phase III of the GARP Atlantic Tropical Experiment: Part II. Analysis of phase III results. J. Atmos. Sci., 36, 568-601.

EDS, 1975: GATE Data Catalogue. National Climatic Center, EDS/NOAA, Asheville, N.C.

Frank, W., 1978: The life cycles of GATE convective systems. J. Atmos. Sci., 35, 1256-1264.

_____, 1979: Individual time period analysis over the GATE ship array. Mon. Wea. Rev., 107, 1600-1616.

Gray, W., 1977: Mean state and typical conditions. Report of the U. S. GATE Central Program Workshop, NCAR, Boulder, Colorado, 199-213. [Available from the GATE Project Office, NOAA, Rockeville, MD.]

_____, and R. Jacobson, Jr., 1977: Dirunal variation of deep cumulus convection. Mon. Wea. Rev., 105, 1171-1188.

Greenfield, R. S. and J. S. Fein, 1979: The global atmospheric research program's Atlantic Tropical Experiment. Rev. Geophys. Space Phys., 17, 1762-1772.

Hudlow, M. D. and V. L. Patterson, 1979: GATE radar rainfall atlas. NOAA Special Report, 155 pp.

Johnson, R. H., 1978: Cumulus transports in a tropical wave composite for phase 3 of GATE. J. Atmos. Sci., 35, 484-494.

_____, 1980: Diagnosis of convective and mesoscale motions during phase 3 of GATE. J. Atmos. Sci., 37, 733-753.

Martin, D. W., 1975: A satellite convective code. GATE Report No. 14, Vol. 2, WMO, 176-181.

Nitta, Tsu., 1972: Energy budget of wave disturbances over the Marshall Islands during the years of 1956 and 1958. J. Meteor. Soc. Japan, 50, 71-84.

_____, 1977: Reponse of cumulus updraft and downdraft to GATE A/B-scale motion system. J. Atmos. Sci., 34, 1163-1186.

_____, 1978: A diagnostic study of interaction of cumulus updrafts and downdrafts with large-scale motions in GATE. J. Meteor. Soc. Japan, 56, 232-241.

Ogura, Y., Y.-L. Chen, J. Russell and S.-T. Soong, 1979: On the formation of organized convective systems observed over the eastern Atlantic. Mon. Wea. Rev., 107, 426-441.

Ooyama, K. and S. Esbensen, 1977: Rawinsonde data quality. Report of the U.S. GATE Central Program Workshop, NCAR, Boulder, CO, 131-163. [Available from the GATE Project Office, NOAA, Rockville, MD.]

Reed, R. J., 1978: The Structure and Behavior of Easterly Waves Over West Africa and the Atlantic. Meteorology Over the Tropic Oceans. ed. D. B. Shaw (Great Britain: Royal Meteorological Society,1978) pp.57-71.

Reeves, R., C. Ropelewski and M. Hudlow, 1979: Relationships between large-scale motion and convective precipitation during GATE. Mon. Wea. Rev., 107, 1154-1168.

Thompson, R., P. Steven, R. Ernest and R. Reed, 1979: Structure and properties of synoptic-scale wave disturbances in the intertropical convergence zone of the eastern Atlantic. J. Atmos. Sci., 36, 53-72.

William, K. T. and W. M. Gray, 1973: Statistical analysis of satellite-observed trade wind cloud clusters in the western north Pacific. Tellus, xxv, 4, 313-336.

Yanai, M., S. Esbensen, and J.-H. Chu, 1973: Determination of bulk properties of tropical cloud clusters from large-scale heat and moisture budgets. J. Atmos. Sci., 30, 611-627.

LIST OF FIGURES

$-\bar{\omega}\delta\bar{Lq}/\delta p$. The dashed line is the standard deviation of Q_2.

Fig. 5. Time mean profiles of B-scale vertical p-velocity ω (thick solid line, unit: 10^{-4} mb/s) and of apparent heat source Q_1 and apparent moisture sink Q_2 (light solid line and dashed line, units: Deg. C/Day), averaged over the period from 00Z, 7 September to 18Z, 8 September during the Phase III of GATE. This period was chosen after Cho et al. (1979).

Fig. 6. Time mean profiles of B-area averaged vertical eddy fluxes of heat energy F_s (dashed line), of moisture energy F_{Lq} (dotted line) and of total heat energy F_h (solid line). Unit is Cal/Cm^2/Day or W/m^2. The arrows and numbers on the abscissa are the corresponding surface measurements of $LP_o + S_o$ (dashed arrow), $L(P_o - E_o)$ dotted arrow) and $LE_o + S_o$ (solid arrow).

Fig. 7. Three vertical profiles of time averaged B-scale net heat energy flux F_h during three periods, namely, mature stage of cloud cluster (09–18Z, 5 September and 06–15Z, 12 September, solid line), decayed stage of cloud cluster (18Z, 12 September - 03Z, 13 September, thin, solid line) and unorganized cloud cluster stage (00Z, 6 September - 00Z, 7 September, dashed line). These periods were chosen after Nitta (1977).

Fig. 8.. The time series of three hourly diagnosed surface fluxes (solid line) and the corresponding surface measurements (dashed line). Unit 10^3 cal/cm^2/day and 10^2 W/m^2. (a) F_{so} and $LP_o + S_o$, (b) F_{Lqo} and $L(P_o - E_o)$, and (c) F_{ho} and $LE_o + S_o$.

Fig. 9. (a) Height-wave phase cross section of the apparent heat source Q_1 for composite wave. Unit: Deg. C/day. The symbols on abscissa are wave phases of composite wave; the R, N, T, and S are the phase of ridge, maximum northerlies, trough and maximum southerlies on 700 mb, the 1, 3, 5, and 7 indicate the intermediate phases. These symbols are after Thompson et al. (1979). (b) Standard deviations of Q_1 at every wave phase.

Fig. 10. (a) and (b) are the same as in Figure 7a and b except for the apparent moisture sink Q_2.

Fig. 11. A comparison between surface measurements (light solid line) of composite wave and different diagnostic studies of the surface fluxes, they are the results from current study (thick solid line), from Thompson et al. (1979, dashed line) and Johnson (1980, plotted only on the lowest panel, dotted line). Units: W/m^2.

Fig. 1

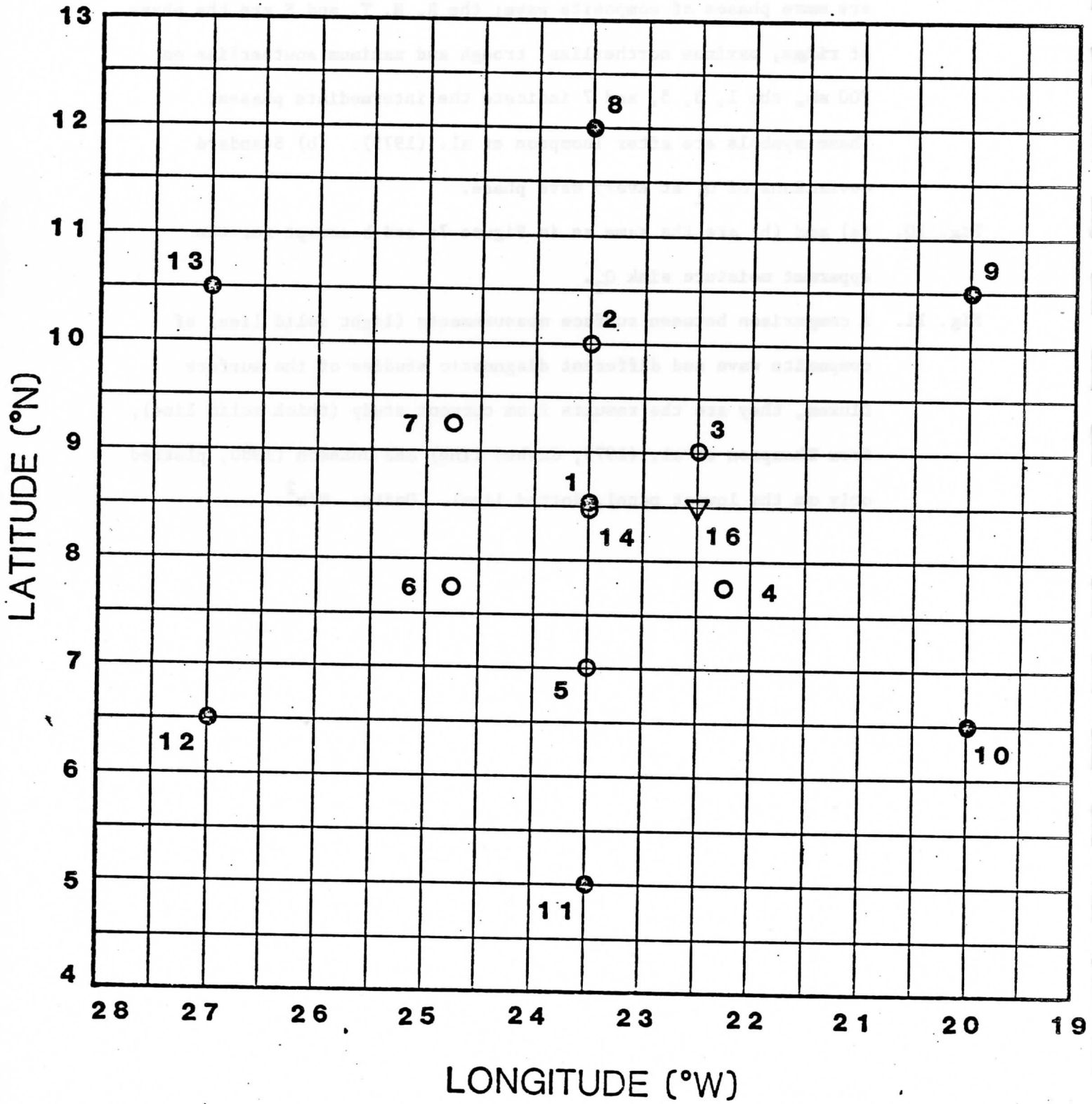
13
12
11
10
9
8
7
6
5
4
LATITUDE (°N)
28
27
26
25
24
23
22
21
20
19
LONGITUDE (°W)
8
13
9
2
7
3
1
14
16
6
4
5
12
10
11

Fig. 2

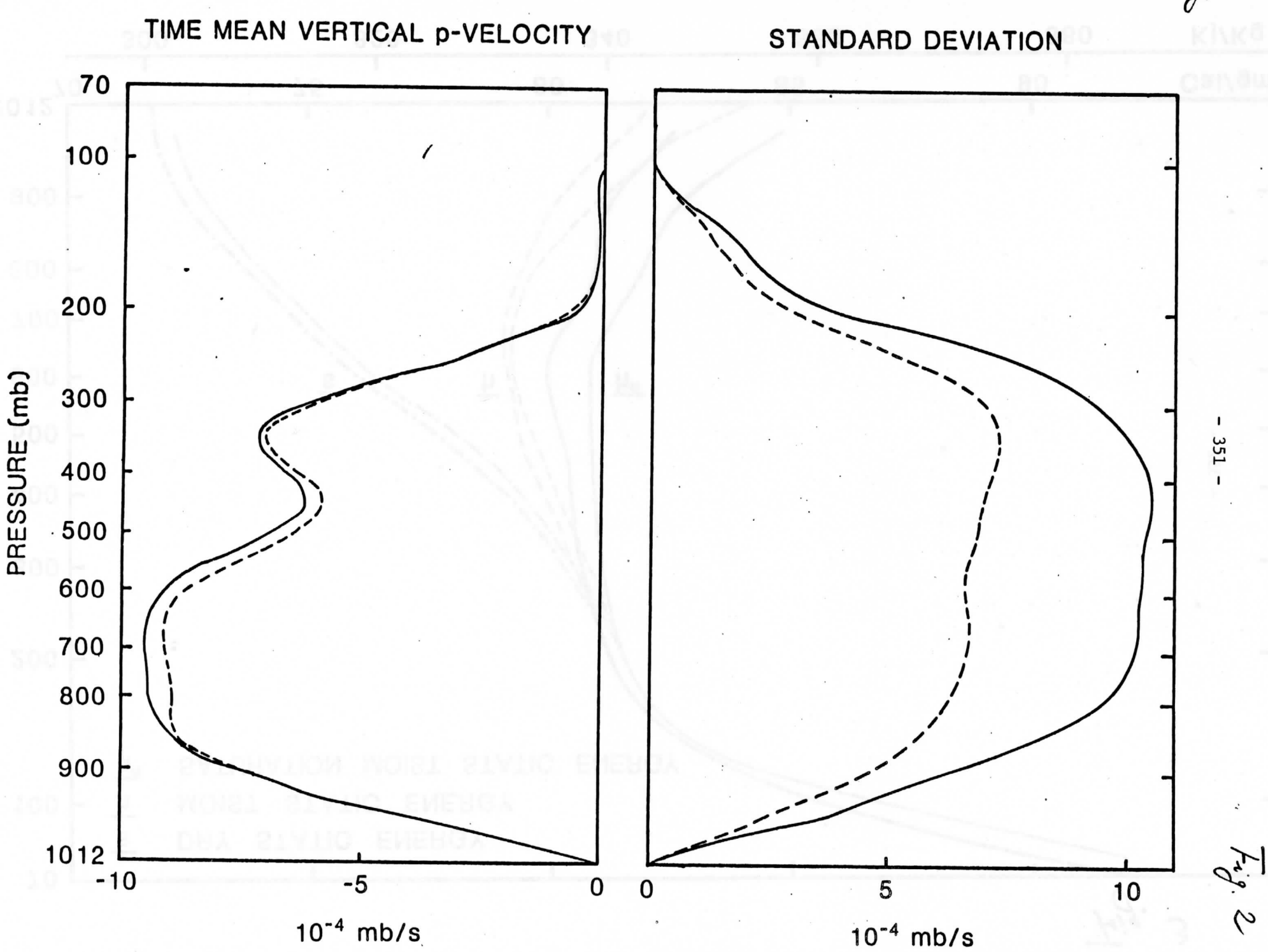
TIME MEAN VERTICAL p-VELOCITY
STANDARD DEVIATION
PRESSURE (mb)
70
100
200
300
400
500
600
700
800
900
1012
-10
-5
0
0
5
10
10^{-4} mb/s
10^{-4} mb/s

Fig. 2

Fig. 3

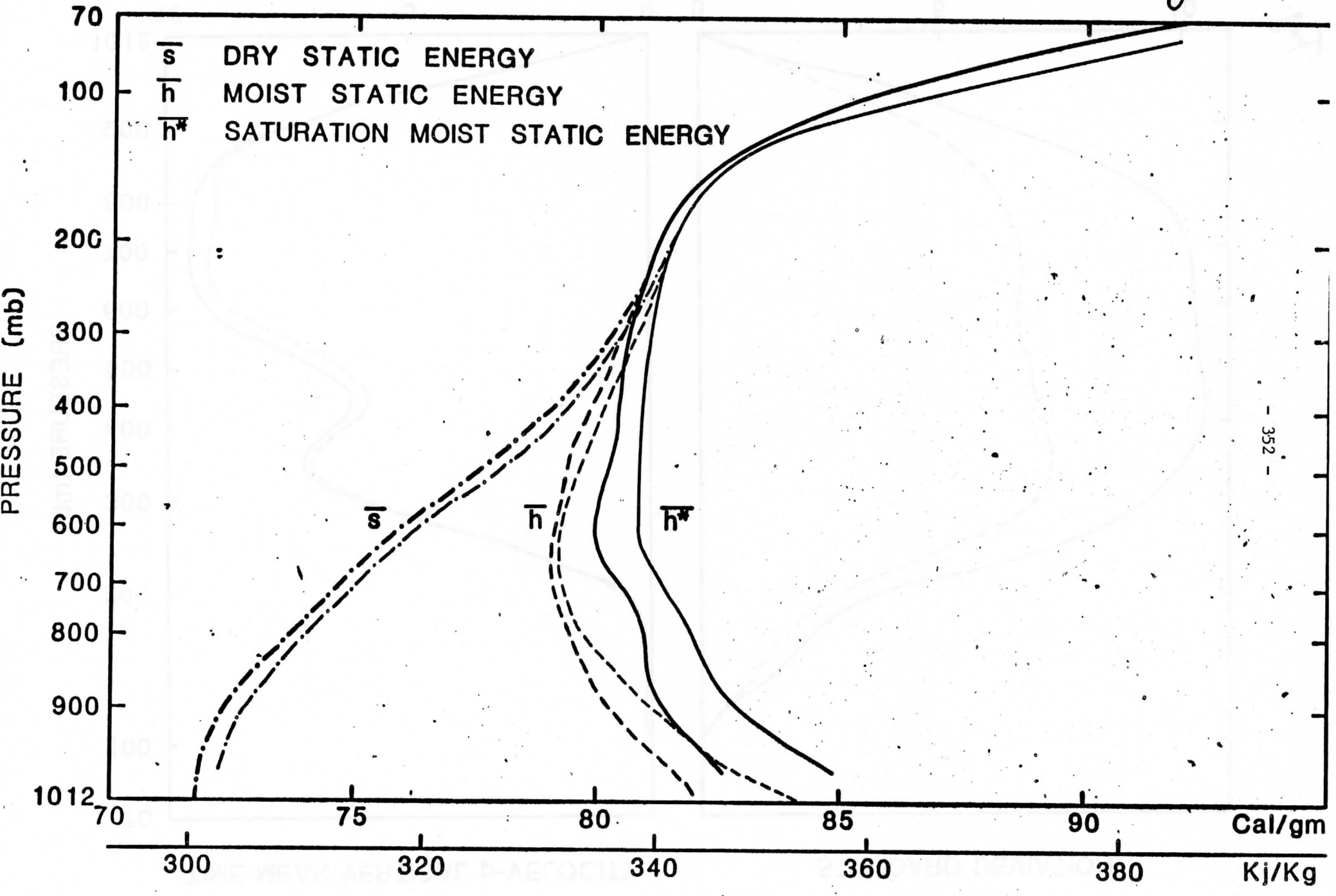
$\overline{s}$ DRY STATIC ENERGY
$\overline{h}$ MOIST STATIC ENERGY
$\overline{h^*}$ SATURATION MOIST STATIC ENERGY
PRESSURE (mb)
70
100
200
300
400
500
600
700
800
900
1012
$\overline{s}$
$\overline{h}$
$\overline{h^*}$
70
75
80
85
90
Cal/gm
300
320
340
360
380
Kj/Kg

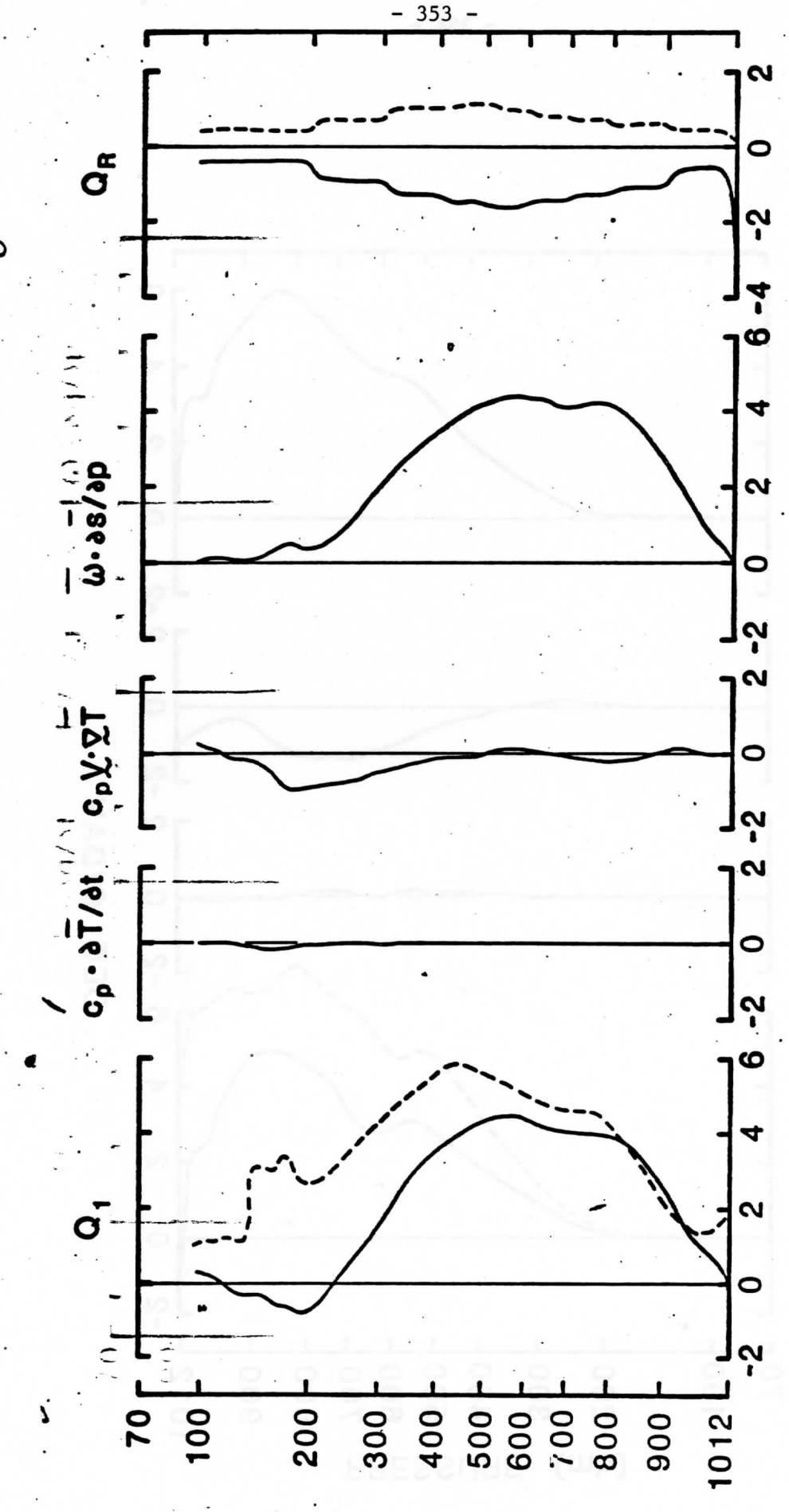
Q1
$c_p \cdot \partial\bar{T}/\partial t$
$c_p\bar{V}\cdot\nabla\bar{T}$
$\bar{\omega}\cdot\partial\bar{s}/\partial p$
Q_R
PRESSURE (mb)
70
100
200
300
400
500
600
700
800
900
1012
-2 0 2 4 6
-2 0 2
-2 0 2
-2 0 2 4 6
-4 -2 0 2
DEG C/DAY

Fig. 4a

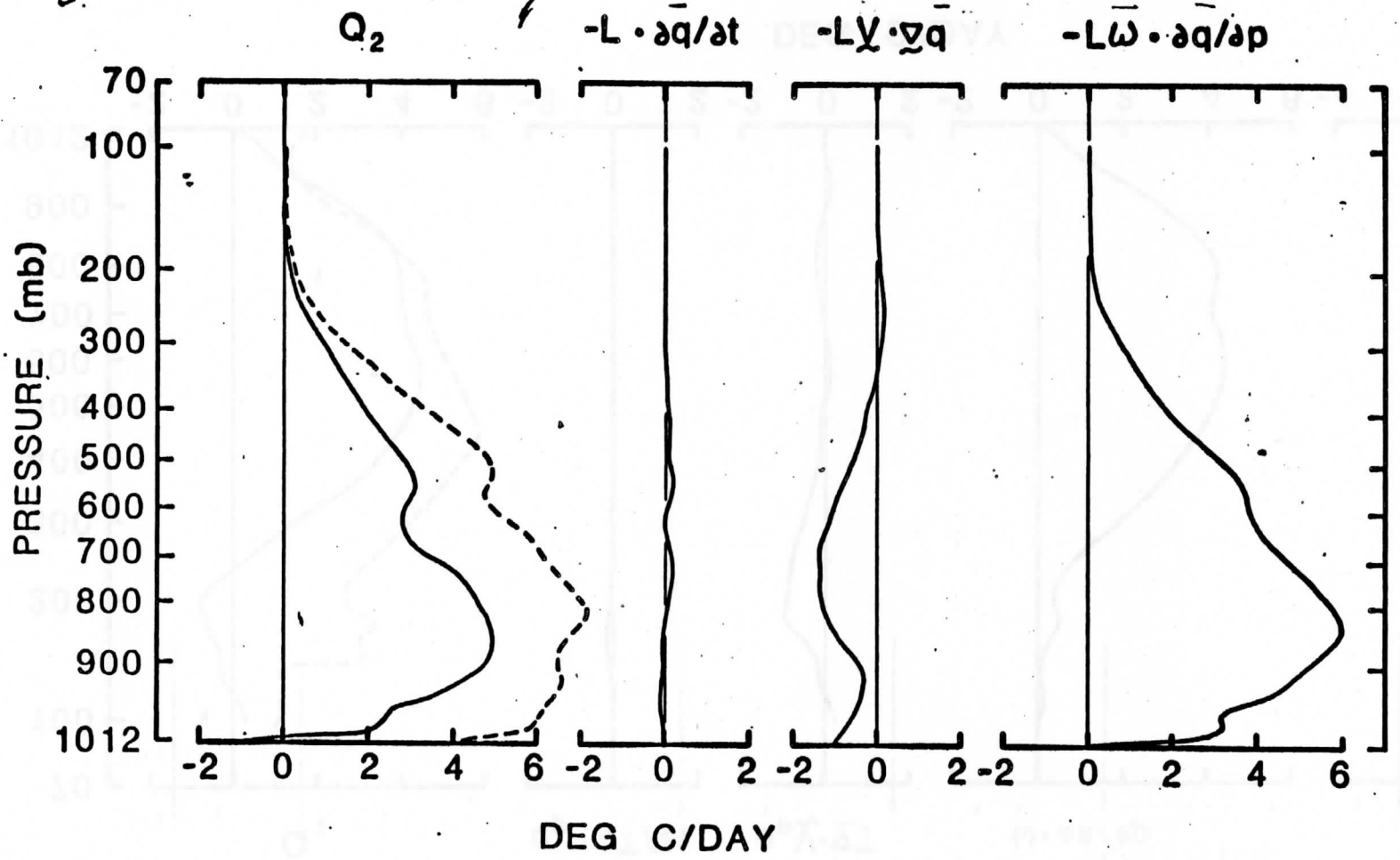
Q_2
$-L \cdot \partial\bar{q}/\partial t$
$-L\bar{V} \cdot \nabla\bar{q}$
$-L\bar{\omega} \cdot \partial\bar{q}/\partial p$
PRESSURE (mb)
70
100
200
300
400
500
600
700
800
900
1012
-2 0 2 4 6
-2 0 2
-2 0 2
-2 0 2 4 6
DEG C/DAY

Fig. 4a

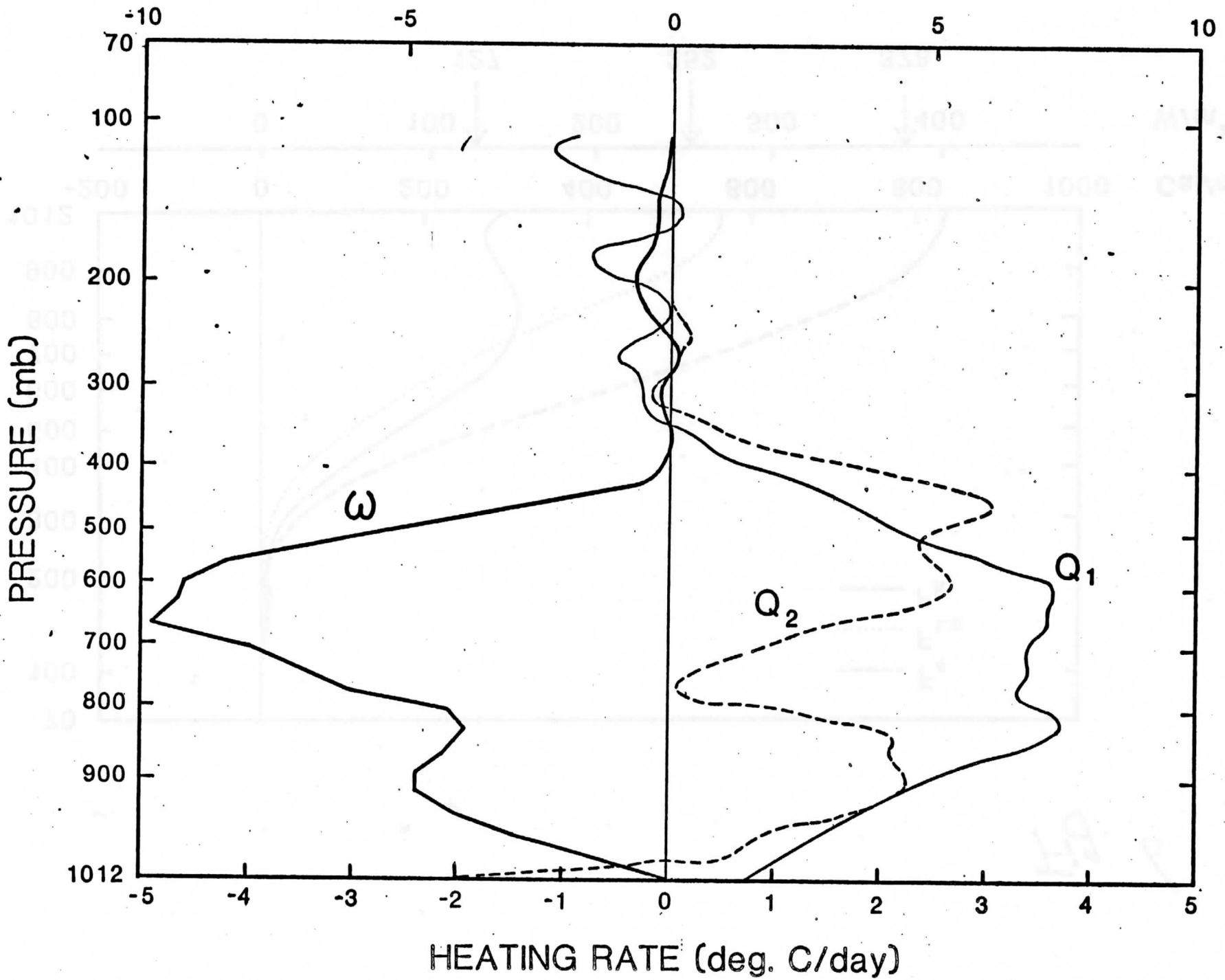
VERTICAL p-VELOCITY ω (10⁻⁴ mb/s)
-10
-5
0
5
10
70
100
200
300
400
500
600
700
800
900
1012
PRESSURE (mb)
ω
Q1
Q2
-5
-4
-3
-2
-1
0
1
2
3
4
5
HEATING RATE (deg. C/day)

fig. 3

Fig. 6

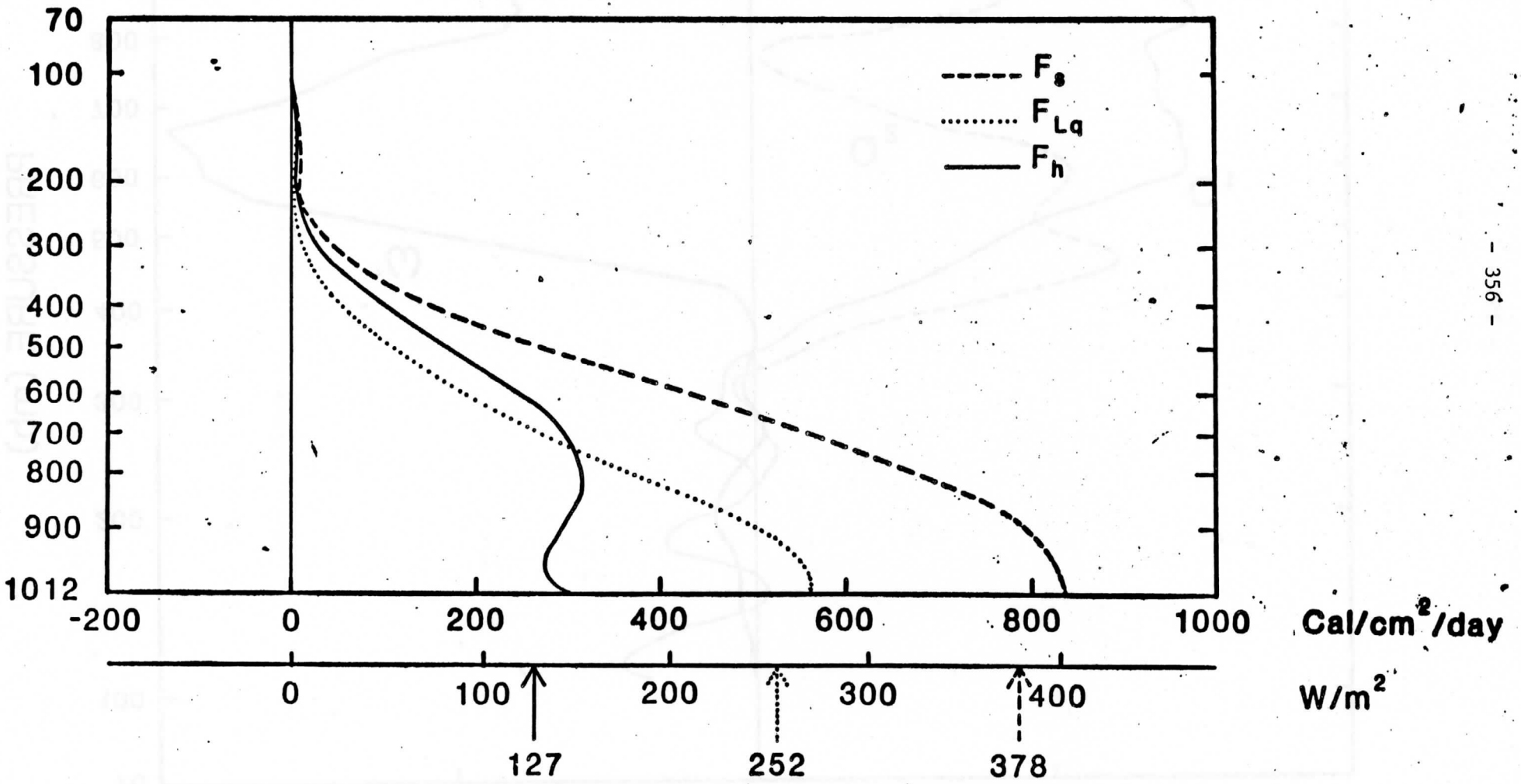
70
100
200
300
400
500
600
700
800
900
1012
F_s
F_{Lq}
F_h
-200
0
200
400
600
800
1000
Cal/cm²/day
0
100
200
300
400
W/m²
127
252
378

Fig. 7

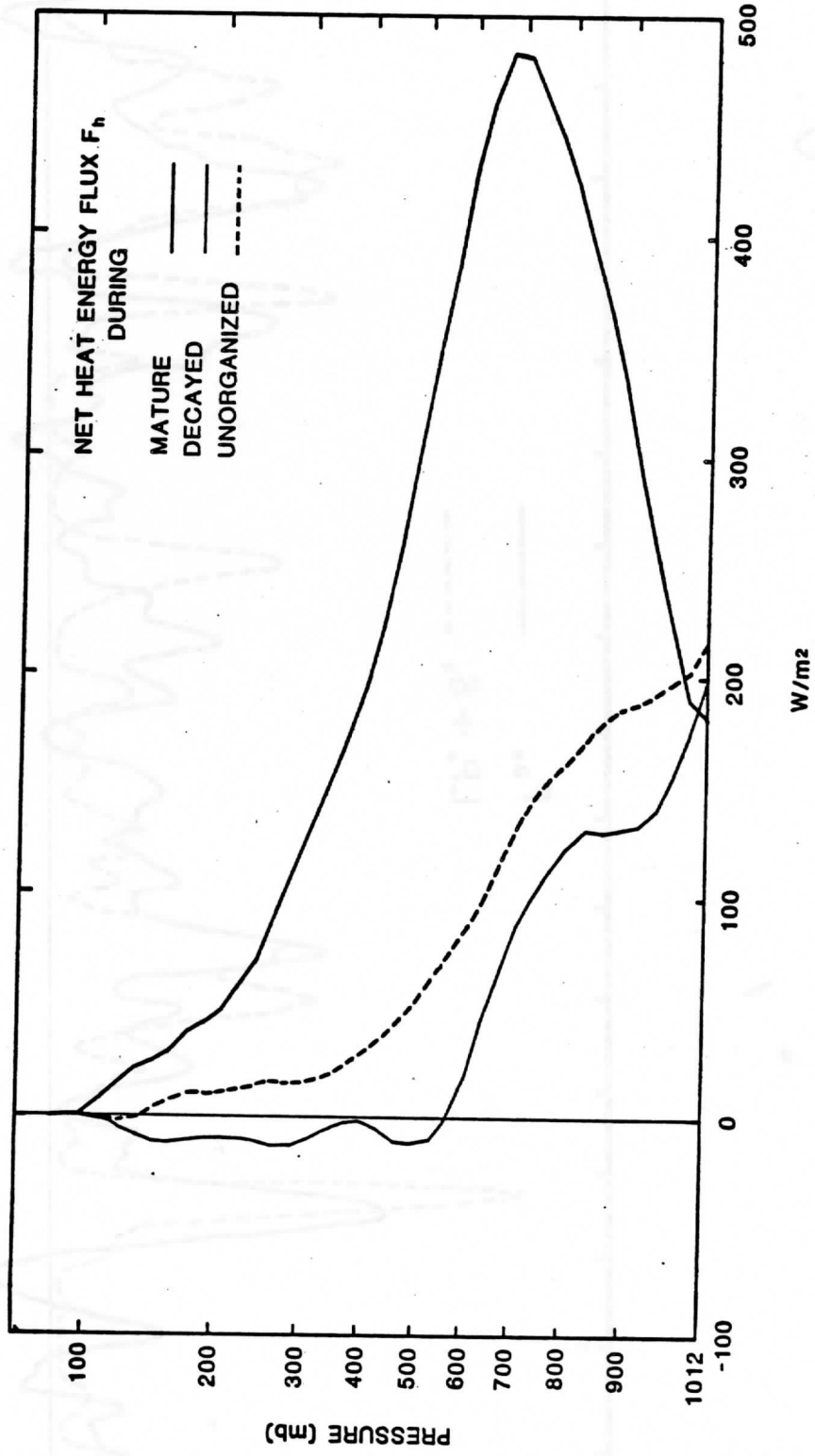
NET HEAT ENERGY FLUX F_h
DURING
MATURE
DECAYED
UNORGANIZED
PRESSURE (mb)
100
200
300
400
500
600
700
800
900
1012
500
400
300
200
100
0
-100
W/m²

Fig. 8a

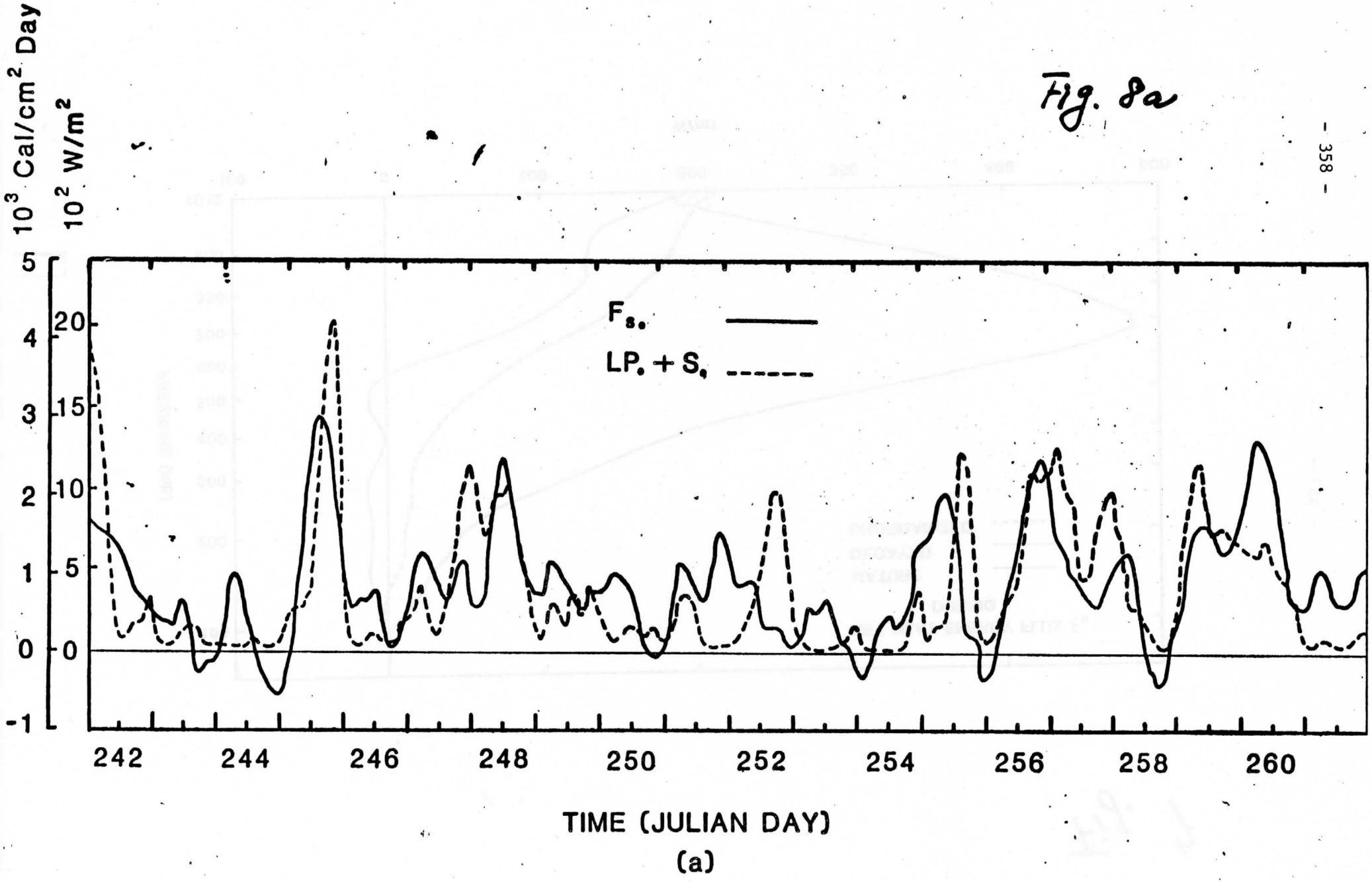
10^3 Cal/cm^2 Day
10^2 W/m^2
5
4
3
2
1
0
-1
20
15
10
5
0
$F_{s\downarrow}$
$LP_\uparrow + S_\uparrow$
242
244
246
248
250
252
254
256
258
260
TIME (JULIAN DAY)

(a)

Fig. 8b

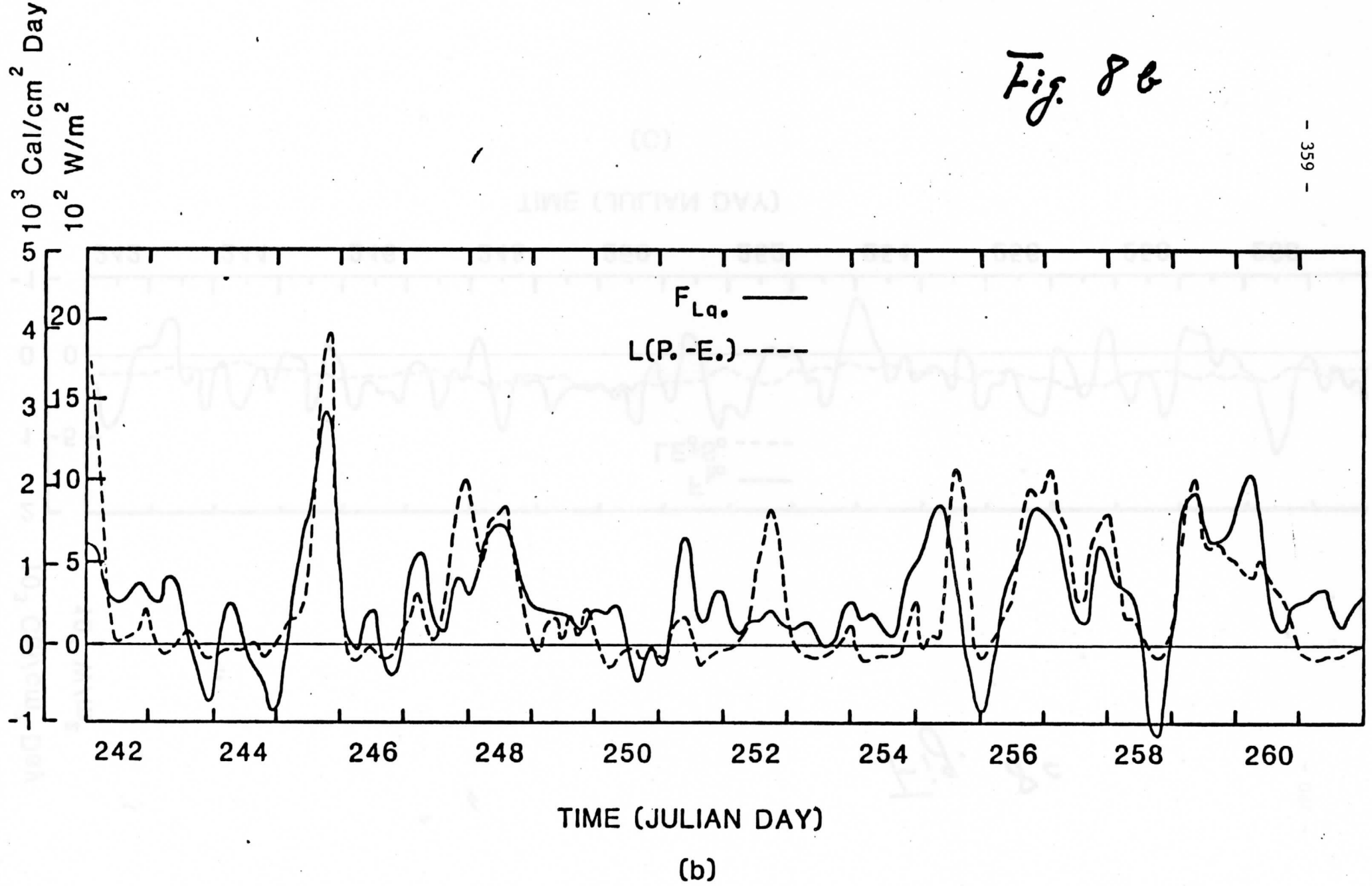
10^3 Cal/cm^2 Day
10^2 W/m^2
5
4
3
2
1
0
-1
20
15
10
5
0
$F_{Lq.}$
L(P.-E.)
242
244
246
248
250
252
254
256
258
260
TIME (JULIAN DAY)

(b)

Fig. 8c

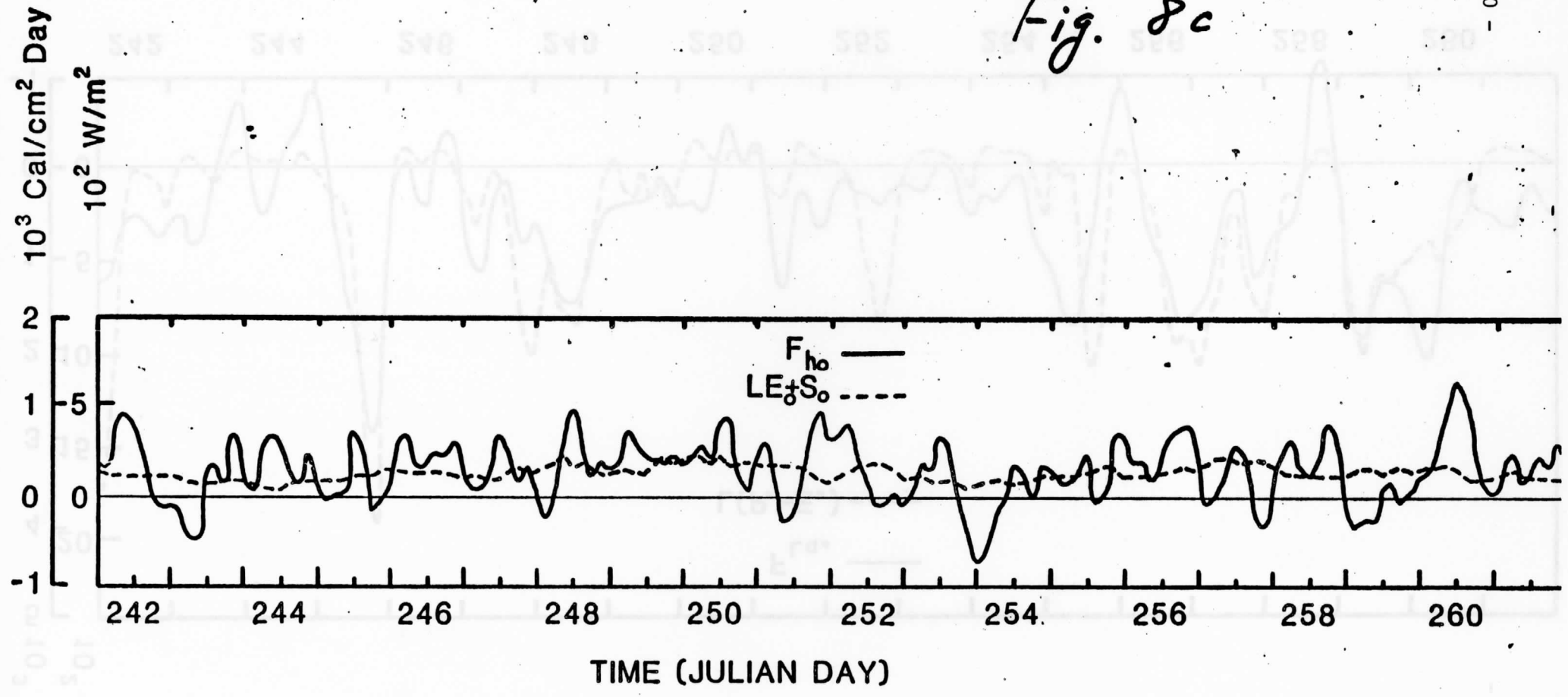
10^3 Cal/cm^2 Day
10^2 W/m^2
2
1.5
1
0
-1
F_{ho}
$LE_{\delta}S_o$
242
244
246
248
250
252
254
256
258
260
TIME (JULIAN DAY)

(C)

Fig. 9

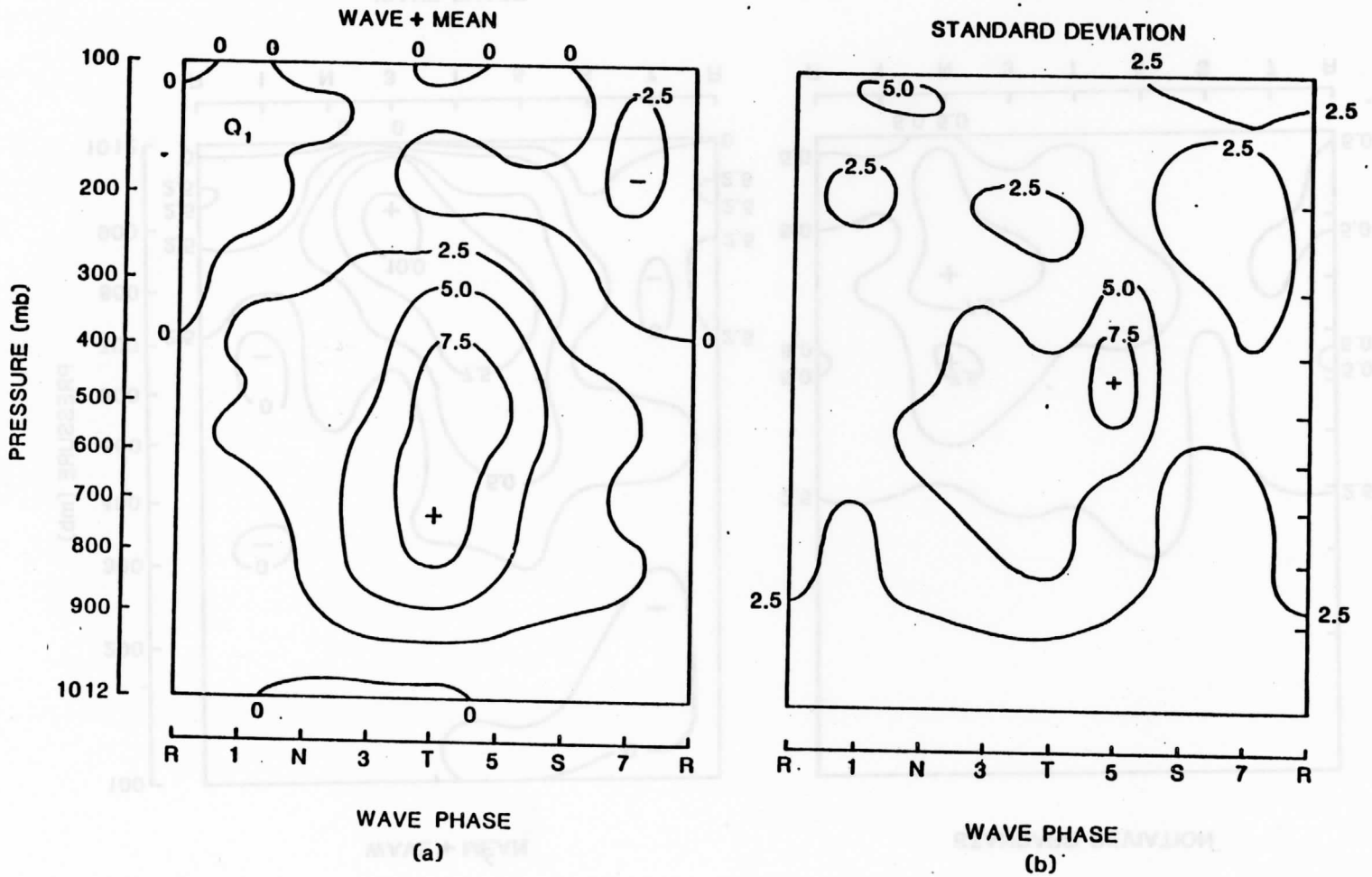
WAVE + MEAN
PRESSURE (mb)
100
200
300
400
500
600
700
800
900
1012
Q_1
0
2.5
5.0
7.5
R 1 N 3 T 5 S 7 R
WAVE PHASE
(a)
STANDARD DEVIATION
2.5
5.0
7.5
R 1 N 3 T 5 S 7 R
WAVE PHASE
(b)

Fig. 1a

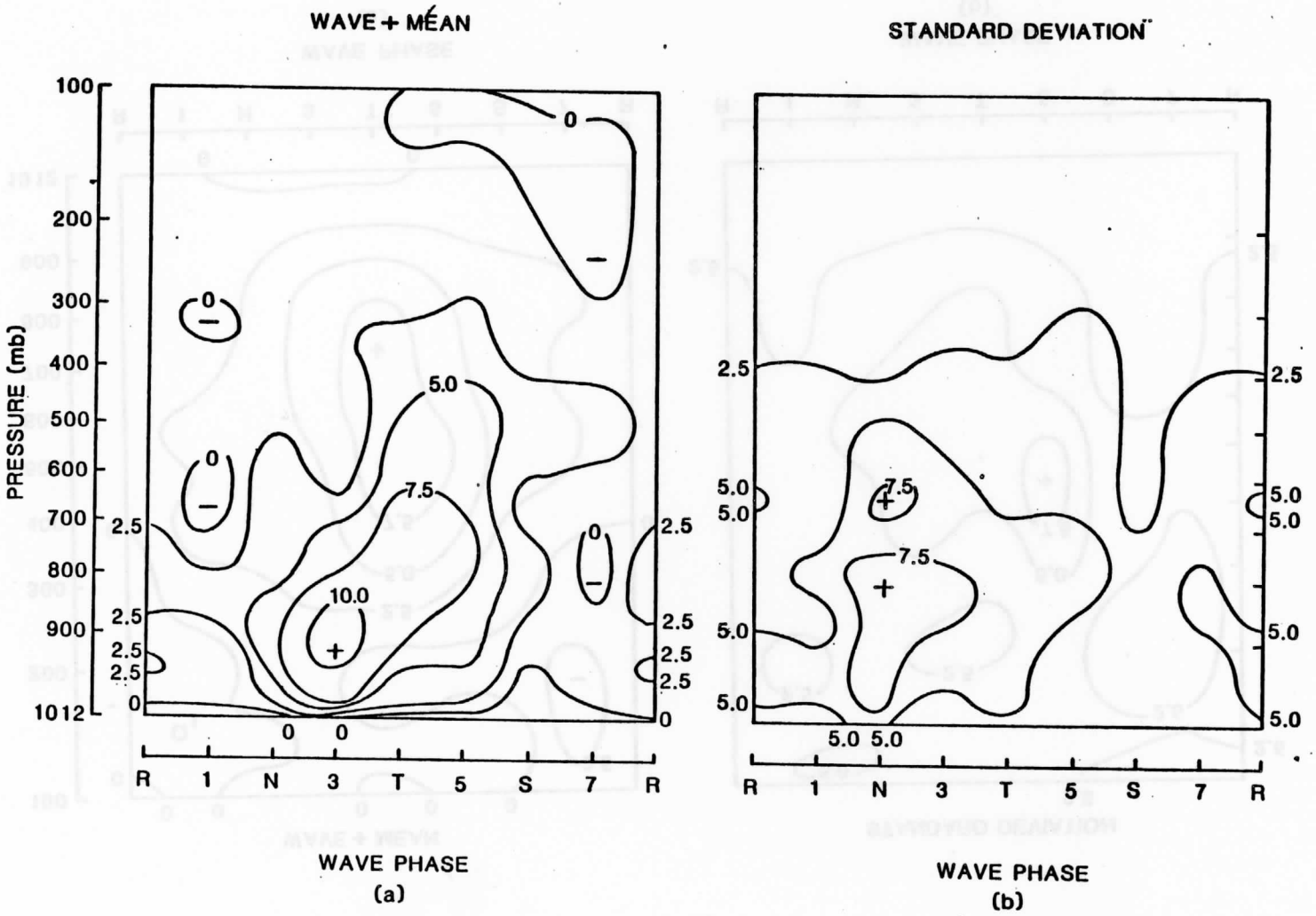
WAVE + MEAN
STANDARD DEVIATION
PRESSURE (mb)
100
200
300
400
500
600
700
800
900
1012
0
5.0
7.5
10.0
2.5
R 1 N 3 T 5 S 7 R
WAVE PHASE
(a)
WAVE PHASE
(b)

Fig. 11

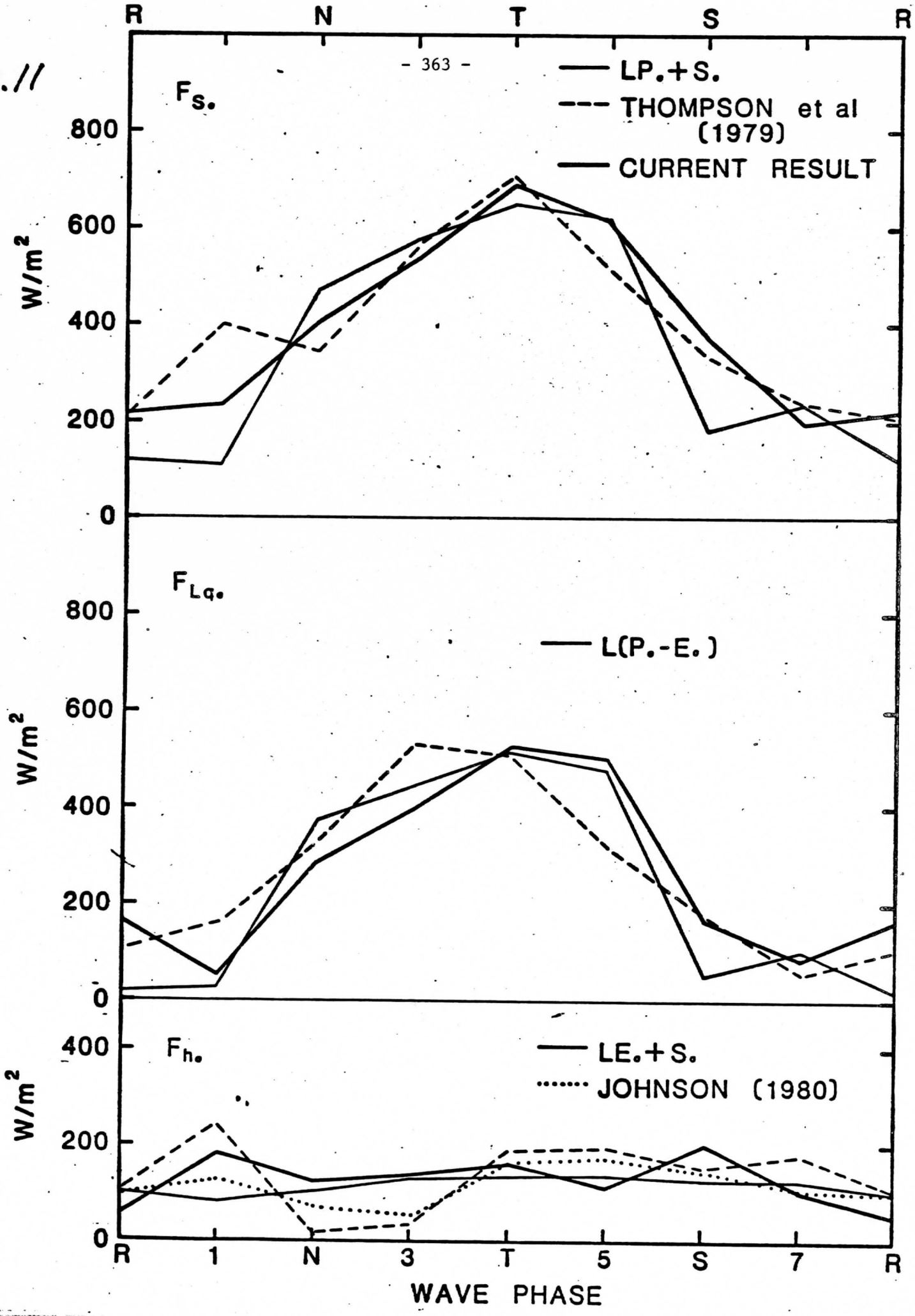
R
N
T
S
R
$F_{s.}$
LP.+S.
THOMPSON et al (1979)
CURRENT RESULT
800
600
400
200
0
W/m²
$F_{Lq.}$
L(P.-E.)
800
600
400
200
0
W/m²
$F_{h.}$
LE.+S.
JOHNSON (1980)
400
200
0
W/m²
R
1
N
3
T
5
S
7
R
WAVE PHASE